

Proton Beam Writing

Dissertation

zur Erlangung des mathematisch-naturwissenschaftlichen Doktorgrades

"Doctor rerum naturalium"

der Georg-August-Universität Göttingen im Promotionsprogramm ProPhys

der Georg-August University School of Science (GAUSS)

vorgelegt von

Alrik Stegmaier

aus Rostock

Göttingen, 2022

Betreuungsausschuss

Prof. Dr. Hans. C. Hofsäss, II. Physikalisches Institut, Georg-August Universität Göttingen

Prof. Dr. Peter E. Blöchl, Department of Applied Theoretical Physics, Technische Universität Clausthal

Prof. Dr. Andres Tilgner, Institut für Geophysik, Georg-August Universität Göttingen

Mitglieder der Prüfungskommission

Referent: Prof. Dr. Hans. C. Hofsäss, II. Physikalisches Institut, Georg-August Universität Göttingen

Korreferent: Prof. Dr. Andreas Tilgner, II. Physikalisches Institut, Georg-August Universität Göttingen

Weitere Mitglieder der Prüfungskommission

Prof. Dr. Peter E. Blöchl, Department of Applied Theoretical Physics, Technische Universität Clausthal

Prof. Dr. Stan Lai, II. Physikalisches Institut, Georg-August Universität Göttingen

Prof. Dr. Stefan Mathias, I. Physikalisches Institut, Georg-August Universität Göttingen

PD Dr. Jörn Große-Knetter, II. Physikalisches Institut, Georg-August Universität Göttingen

Tag der mündlichen Prüfung: 29. 03. 2022

Abstract

Proton beam writing (PBW) is a mask-less 3D structuring method that uses a focused, relatively high energy Proton beam, followed by an etching step to create free standing 2D and 3D structures in a large variety of target materials. During the irradiation step, defects are created locally in the target material that influence the etching behavior of the second step. The flexibility, high resolution and ability to perform rapid prototyping of micro-electro-mechanical systems makes PBW an interesting area of investigation. However, producing 3D structures reliably and predictably as well as limited theoretical understanding of many of the complicated aspects of PBW are some of the challenges that PBW faces.

This work extends the knowledge of this complicated process in many key areas, including the stopping (slowing down and radiation damage) of fast particles in matter and the etching of the final 3D structures. For this new models are developed, simulations are performed and key experiments are used to test and improve the new approaches. New aspects of the etching process during PBW of Gallium Arsenide are also uncovered and discussed.

Further more, progress on many practical aspects of PBW was made. These include ion beam optics optimization, beam-line design, target design and accelerator upgrades to the accelerator facilities in Göttingen. Additionally, new software tools for PBW were also developed and employed successfully.

Contents

1. Introduction	6
1.1. MEMS	7
1.2. The theoretical foundation of Proton beam writing	13
1.3. The experimental steps of Proton beam writing	16
1.4. Comparison with similar techniques	17
1.5. History of PBW and state of the art	21
2. PBW facilities in Göttingen	23
2.1. Overview	23
2.2. Ion source	25
2.2.1. Sputtering model of the SNICS	27
2.2.2. Thermodynamic considerations	31
2.3. Tandem accelerator	33
2.4. Micro-beam-line	35
2.4.1. General layout	35
2.4.2. Lens System	39
2.5. Irradiation chamber	41
2.6. Sample holder	42
2.7. Irradiation process	47
2.7.1. Beam size optimization	47
2.7.2. Beam size measurement	48
2.7.3. Irradiation plan	50
2.7.3.1. Optimization of irradiation points	51
2.7.3.2. Beam time optimization	52
3. The irradiation process	53
3.1. Stopping	53
3.1.1. General considerations	53
3.1.2. Nuclear stopping	64
3.1.2.1. High velocity limit	65
3.1.2.2. Low velocity limit	70
3.1.3. Electronic stopping	75
3.1.3.1. Stopping of point charges	75
3.1.3.2. Effective charge	77
3.1.3.3. Bond relaxation	80
3.1.3.4. Delta-Electrons and spatial extend	83
3.2. Defect production	84

Contents

3.3. Defect evolution	85
3.3.1. Resists and polymers	86
4. Etching	88
4.1. Chemical equilibrium	90
4.2. Rate equations	92
4.3. Reaction drift diffusion models	94
4.3.1. Poisson's equation	94
4.3.2. Defects	96
4.3.3. Mobility model	97
4.3.4. Band structure and Fermi-Dirac statistics	101
4.3.5. Current densities	103
4.4. Deformation	103
5. PBW in Gallium Arsenide	112
5.1. Radiation damage	112
5.2. Etching	115
5.3. Simulations in comparison to experiments	130
6. Computational Quantum Chemistry	134
7. Summary	148
8. Discussion and Outlook	149
Bibliography	151
A. Basis sets	184

1. Introduction

Proton beam writing (PBW) is a relatively new, mask-less, direct-write lithographic process for patterning and 3D structuring of semiconductors, photo resists, ceramics and some organic materials at micro- and nano-dimensions, using a focused beam of Protons of often relatively high energy (500 keV to 3 MeV per Proton) [298]. In PBW a target material is locally exposed to the beam and defects are created in it through collisions of the Protons with the target and the resulting collision cascade. This alters the target material properties locally. For the creation of 3D structures, in a second step, either the defect rich material or the defect poor material is selectively removed, leaving behind a structured surface (a more detailed view of this is discussed in sec. 1.2 on page 13). If the process is well controlled, almost arbitrarily shaped 3D structures with measurements between a few nanometers up to fractions of a millimeter can be produced relatively quickly and without the need to use a mask or coating the target material in a resist. This allows for the rapid prototyping of 3D micro- and nano-structures at costs and speeds that are often better than common structuring methods as discussed in sec. 1.3 on page 16 and 1.4 on page 17. Alternatively, the change in material properties alone (without etching) can also be very useful, for example for the creation of buried light wave guides in fused silica [19] or the creation of color centers [187].

PBW as a 3D structuring method is being researched at several places around the world, among them the Georg-August University of Göttingen, the Institute for Nuclear Research in Debrecen and the Center for Ion Beam Applications in Singapore. Increasing the experimentally achievable resolution, novel applications and target materials as well as an improved theoretical understanding and simulation of the complex processes involved are topics in this research. Despite this, open questions about many practical aspects of PBW, such as repeatability, reliability, predictability and economics of the process hinder its wider application and industrial use [165].

This work expands the theoretical foundation of the process as well as improving practical aspects of the irradiation and etching steps. This allows for a more efficient production of 3D structures, as well as better repeatability, reliability and predictability of the process. The theoretical models developed here also allow to design novel irradiation and etching techniques as well as a better understanding on how to transfer PBW to new materials and for already structured as well as complex layered targets.

In the following a discussion of micro-electrical-mechanical systems (MEMS) and their production, the primary application for PBW, a short review of the theoretical foundation, practical aspects and the history of Proton beam writing will be given, as well as a description of the current state of the art and a comparison with similar structuring techniques. In chap. 2 on page 23 the PBW facilities in Göttingen, that is the accelerator, target chamber and associated systems, are described and their recent upgrades are

1. Introduction

presented. Chap. 3 on page 53 focuses on the irradiation process, the slowing down of the Protons in the target as well as the changes in the target material. Chap. 4 on page 88 discusses the etching process and resulting 3D structures. In chap. 6 on page 134 the recent progress on the research on PBW in Gallium Arsenide is presented. This includes a more detailed understanding of the electrochemistry and improved simulations of the PBW in this material. Chap. 6 on page 134 focuses on the computational quantum chemical methods employed throughout this work. In the final chapters the results are summarized, discussed and an outlook is provided.

1.1. MEMS

While the high resolution and aspect ratio of PBW allows it to be used for many applications, the primary use of PBW is the prototyping of MEMS and other 3D structures similar to them. Micro-electro-mechanical systems, or MEMS for short, are microscopic, mostly free standing 3D structures that combine electrical and mechanical systems on the 1 to 100 μm scale. The production of such devices already started in the 1960ies with systems like the resonant gate transistors from Westinghouse [176], but the term MEMS was only coined in a proposal to DARPA in 1986 [103]. It has only been in the recent decades though, that MEMS have come into widespread use [91]. MEMS have been described as one of the most impressive technological topics of the recent years, due to their rapid development and potential applications in consumer products and industrial applications [315]. Fig. 1.1 on the following page shows the number of scientific publications mentioning MEMS as found by `scholar.google.com` and the three most important publishers of these papers. The large number of active authors on this wide field of research is visible as well as a strong upward trend in the number of yearly publications mentioning MEMS since 2000. In the years 2014 to 2016 the number of new academic articles seems to have peaked on this field, however the number of papers in high quality journals still continues to rise (for example `nature.com` rising from 107 publications in 2014 to 323 in 2021), showing a maturation process of the technology.

1. Introduction

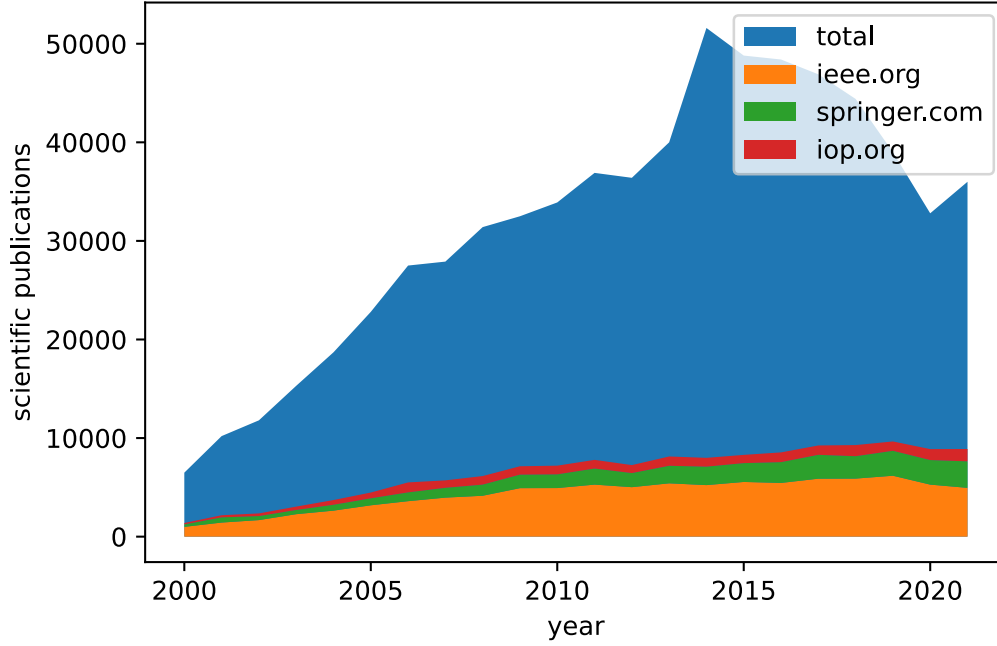


Figure 1.1.: Number of scientific publications mentioning MEMS as indexed by `scholar.google.com` by year of publication in total and by the three largest publishers in the field.

MEMS are not simply a continuation of the trend for miniaturization and higher efficiency as observed in transistor production for example. Instead they can be described more closely as the effort to apply the batch fabrication techniques and economics of scale to a variety of typically macroscopic, electromechanical systems. This effort has not only lead to a miniaturization of some traditional sensors, actuators and machine components by a few orders of magnitude, often accompanied by an increase of performance, but also to a development of entirely new systems [108]. Fig. 1.2 on the next page shows the first MEMS design by Harvey Nathanson from 1965 in comparison to modern design for a tunable coupling dual cavity for photonic integrated circuits from 2010.

1. Introduction

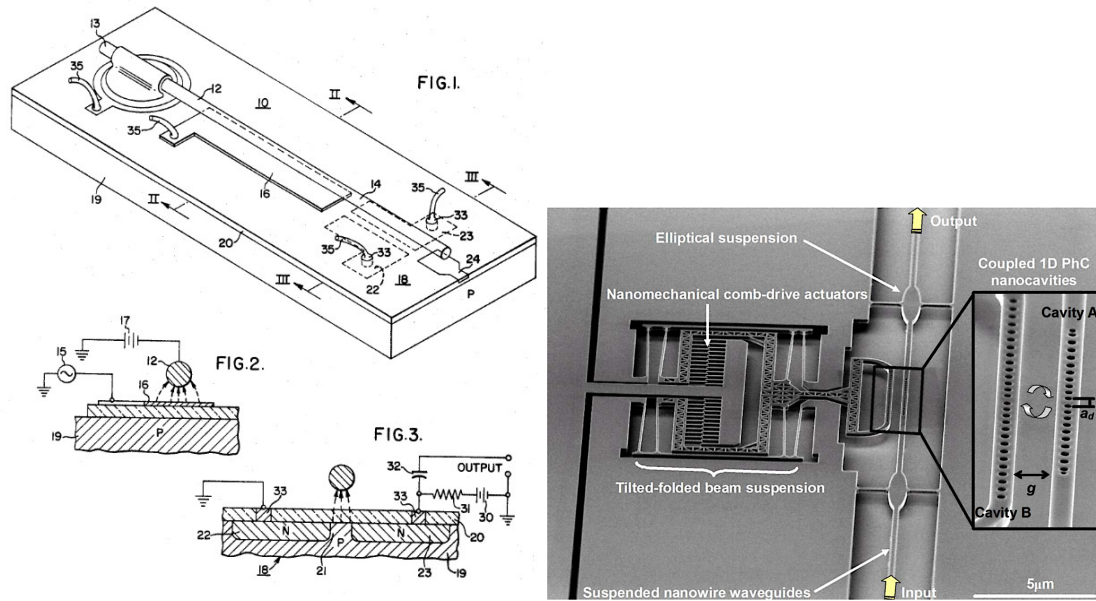


Figure 1.2.: The first MEMS design, a resonant gate transistor, as published in a patent in 1965 (left) [177], in comparison to a modern design for a tunable coupling dual cavity for photonic integrated circuits from 2010 [47].

MEMS can be used for a large variety of applications. Among them are the use as [91, 148, 55]:

- ink jet heads in thermal and piezoelectric ink jet printer heads
- Silicon microphones and microspeakers
- pressure sensors
- accelerometers
- gyroscopes
- magnetometers
- inertial navigation sensor packages
- optical components in optical switches, micro-spectrometers, adaptive optics, LiDARs, projection displays and laser TV, head mounted displays
- thermal sensing and imaging sensors
- micro-fluidic components in inhalers, micro-pumps, micro-valves, micro-needles or point of care tests

1. Introduction

- radio-frequency components in switches, radar and communication devices, antennas and surface and bulk acoustic wave filters
- oscillators and resonators
- micro tips for atomic force microscopes as well as probes for automatic test equipment
- flow meters
- humidity-, bio- and chemo-sensors
- ultra-sound transducers and fingerprint sensors
- labs on a chip
- energy harvesters (devices that can provide energy from mechanical or electromagnetic sources)

As such it comes to no surprise that in the last decade MEMS have become increasingly common and important in many modern electronic devices, despite many technological challenges. Improvements in the production methods continue to expand the possible applications, with demand for MEMS also rising steadily. The largest markets for MEMS are shown in tab. 1.1 together with an indication of past and likely future growth. The by far largest market are consumer products, covering more than half of the total market for MEMS. Among the MEMS products, radio frequency components made up the largest market share with more than 2 billion US\$ alone. The growth of the MEMS markets was also not negatively affected by the COVID-19 pandemic. The largest manufacturers for MEMS in the world are the Robert Bosch and Broadcom companies, together making up about 24 % of the total market [55].

market	change since 2014	size in 2020 [billion US\$]	expected change until 2026
consumer	+27 %	7.13	+7.9 %
automotive	-35 %	2.03	+5.8 %
industrial	+31 %	1.47	+6.0 %
medical	+27 %	0.80	+6.7 %
defense and aerospace	+45 %	0.55	+4.5 %
telecommunication	-75 %	0.06	+17 %
total	+9.1 %	12.1	+7.2 %

Table 1.1.: Markets for MEMS products in 2020 and their relative change since 2014 as well as their predicted growth until 2026 [55].

Typical material choices for MEMS are silicon or other semiconductor materials, polymers, glasses, metals or ceramics [148, 101]. The material is typically chosen depending on the desired application and available manufacturing methods. The most important

1. Introduction

material for MEMS is therefore Silicon, as it allows to use the mature and readily available Silicon manufacturing technology and enables easy integration of MEMS with other IC components [101].

The production methods for MEMS are as diverse as the materials that are used. The traditional production methods for MEMS are [101]:

- Bulk micro machining with wet chemical etching, where a mask layer is deposited and patterned on the substrate. Afterwards the substrate is etched away at the exposed areas by a liquid state etchant. Depending on the etchant and substrate, anisotropic or isotropic etching is possible.
- Bulk micro machining with a gas phase etchant, where the liquid etchant is replaced by a gas mixture.
- Deep reactive ion etching (DRIE), where after the creation of the initial mask, repeated applications of a reactive plasma and polymer coating are used to etch the material away. The Bosch process on Silicon is one of the most used variations of this.
- Surface micro machining, where a mask is used to deposit material in the exposed substrate areas. Repeated mask application, material deposition and polishing build up layers on the surface. A mask removal step at the end creates the final 3D structures.
- “Lithographie Galvanoformung Abformung” (LIGA, engl.: lithography, electroplating and molding) uses a UV, X-ray or synchrotron radiation source to expose PMMA on a substrate through a mask. The radiation exposed material is removed afterwards, creating a mask with smooth side-walls. The substrate is electroplated through the exposed areas of the PMMA mask and the mask is removed, creating the 3D structure.
- Hot embossing uses a patterned tool that is impressed into the surface of a heated substrate (often a polymer heated up to slightly above its glass transition temperature) to create a structured imprint.
- Electro-discharge micro machining (micro-EDM) uses a conductive working electrode that is brought in close proximity of a conductive substrate with a dielectric liquid separating them. High voltage pulses cause electric breakdown discharges and remove substrate material.
- Laser micro machining, where a laser is used to directly machine the substrate. Depending on the type of laser and substrate, thermal processes like evaporation or melting, or non-thermal processes like photo-ablation can be used to machine the substrate. An alternative version of this method uses a mask on the substrate surface.

1. Introduction

- Focused ion beam (FIB) micro machining, where a focused beam of ions with a few keV to several hundred keV is used to sputter selected areas of the target away. Additionally, the FIB can also be used for ion-induced deposition, lithography, implantation doping, mask repair, device repair and device diagnostics.
- Electrochemical fabrication (EFAB), where an elastic mask is held against the substrate surface and by electroplating a material is deposited through it. A protective coat can then be applied and polished to produce a level surface. The process is then repeated multiple times with different masks to produce complex structures layer by layer. In the end the protected material is removed and the final 3D structure is created.

Particularly interesting are production methods for MEMS from semiconductor materials with high resolution, smooth side walls and large aspect ratios. Aspect ratios in this context is the ratio of the maximum depth of the produced structures to the lateral resolution. Especially for research applications and micro-fluidics, high aspect ratios and smooth side walls are often required. Of the production methods mentioned, the DRIE, LIGA and hot embossing methods are typically used when high aspect ratios are required [193].

For DRIE two variations of the main process are common: a cryogenic process and the Bosch process [292]. In both processes a mask is applied to the top of the substrate where the semiconductor substrate is to be protected from the etching solution. In the cryogenic process the semiconductor substrate is cooled down so much that the etching reactions at the material surface become highly selective in their etching direction. This leads to an etching of the exposed semiconductor areas almost exclusively in the normal direction to the surface of the substrate. With this process aspect ratios from 47.5:1 [279] to about 120:1 [192] are reported but the process has still several challenges to overcome (such as the cracking of the masks on the wafers at the extreme cold or the deposition of etching products on the material or electrode) until it can be used in mass production of MEMS elements. In the Bosch process a reactive high frequency plasma is generated and accelerated towards the semiconductor surface where anisotropic etching occurs. In a second step all the surface of the semiconductor material is coated by a polymer passivation layer. Then the steps are repeated until the required etch depth is reached. With this, aspect ratios from 30-60:1 (for $2.3 - 0.13 \mu\text{m}$ wide trenches, [1]) up to 160:1 (for $0.25 \mu\text{m}$ wide trenches [192]) have been reported. In contrast to the cryogenic process, the Bosch process (and improved variants thereof) is used in mass production. For comparison, the related FIB milling process was observed to produce aspect ratios of up to 8:1 in Silicon [105].

For LIGA either conductive substances are used or a conductive layer is applied to the surface of the substance. Additionally the surface is coated in a layer of X-ray or UV sensitive positive tone resist (like PMMA or SU-8). The resist is then exposed through a mask to either UV light, X-rays or synchrotron radiation. When the resist is developed, the areas that were exposed to the highly energetic photons are removed and left behind is a 3D structure that is filled with metal through a galvanic process. The remaining resist is then removed. From there several options exist. On the one hand it is possible

1. Introduction

to further modify the metallic structure through etching and form the final product from it. On the other hand the metallic structure can be used as a molding shape for another process. In particular, micro scale thermoforming, micro injection molding or (vacuum) hot embossing. Generally aspect ratios like 50:1 are possible with LIGA [76].

For hot embossing a template that was produced with another method, for example LIGA, is pressed against the surface of a heated substrate, creating an imprint that can be used as a MEMS. The materials of choice are often polymers or metals. Hot embossing usually allows for aspect ratios of 0.1-10:1 [197], however aspect ratios of 25-40:1 have been achieved with micro casting, a type of hot embossing that uses metal alloy sheets and silicon templates [221].

In comparison to these three methods, PBW can be used in a larger variety of different materials, such as organic and inorganic semiconductors, resists and some insulators. Under ideal conditions aspect ratios of up to 120:1 have been demonstrated [111].

1.2. The theoretical foundation of Proton beam writing

As mentioned in the introduction, the experimental procedure of Proton beam writing generally consists of the two primary steps of sample irradiation with Protons and etching with an appropriate etchant. In the following, a closer look at these processes in the two most important target material categories, semiconductors and resists, will be given.

In semiconductors, the most important effect of Proton irradiation is the creation of defects, that is vacancies, interstitial atoms and (in case of multi-component semiconductor compounds [52]) anti-sites, where an atom of an incorrect species occupies a lattice site instead of the atom of the species that occupies the site in an undamaged crystal [285]. When the semiconductor material is submerged in an etchant and a voltage is applied, it is etched electrochemically and the introduced defects hinder the motion of charge carriers through the sample. Additionally the defects can also act as a local dopant. Both effects together are used to control the etching process at the sample surface by applying a voltage across it. In formerly (before the irradiation with Protons) p-doped material, the electrical conduction is dominated by the motion of holes in the valence bands of the semiconductor. The holes are required for the etching process at the surface of the material, where they help breaking the bonds of the atoms at the surface. As such, the irradiated areas act like an obstacle for the motion of the holes to the surface and are etched much slower than the unirradiated bulk of the material. In formerly n-type material the process is a little more subtle. Here the concentration of holes in the bulk is very low in comparison to the concentration of Electrons and electrical conduction is dominated by the motion of Electrons in the conduction bands of the semiconductor. In the irradiated areas, however, the defects introduce doping levels in the band gap and the material behaves more like intrinsic (in case of Gallium Arsenide for example) or p-doped (in case of Silicon) material. This causes a generation and conduction of holes to the surface of the material that is significantly larger in the irradiated regions than in the unirradiated areas. This in turn causes preferential etching of the irradiated regions of the material [298].

1. Introduction

Resists often mostly consist of relatively large molecular chains that are loosely bound to each other and have to ability to form strong bonds between each other, or break these bonds, when an activation energy is supplied to them. Some resists also consist of short molecular chains that can form longer chains or complex networks. One of the effects of Proton irradiation is the excitation of Electrons, which can in turn create reactive sites in some of the molecules of the resist. These reactive sites can cause the molecule to break up (also called chain scission) or cause the molecule to form bonds with another molecule of the resist (also called cross-linking). Usually both effects occur with a certain probability, but, depending on the chemistry of the resist and the irradiation dose, one of them is dominant. After the chemical reactions, the resulting material can be more soluble in an appropriate developer for a positive resist (when chain scission was the dominant process) or less soluble for a negative resists (when cross-linking was dominant). As such, immersion into the developer will create structures caused by the local alteration of the soluability of the resist from the creation of reactive sites [298].

Fig. 1.3 on the next page shows a simple outline of these two steps for semiconductors and resists. This description is only a rough outline of the complex processes that take place in Proton beam writing and more detailed descriptions are provided in chap. 3 on page 53 and chap. 4 on page 88.

1. Introduction

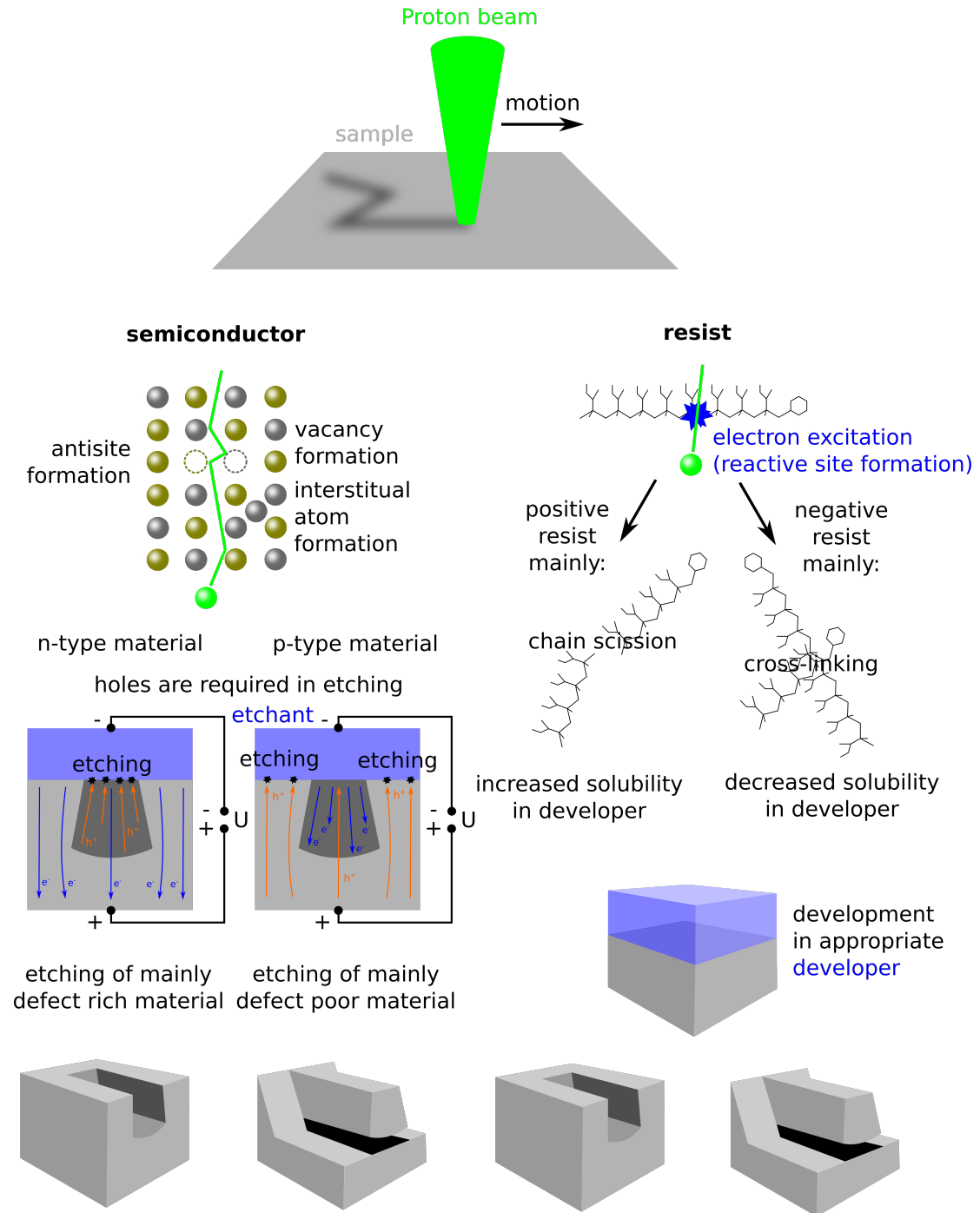


Figure 1.3.: Outline of the two primary steps of Proton beam writing in semiconductors (left) and resists (right). Both materials are modified in some way by Proton irradiation and can be selected such that either only defect rich or only defect poor material is removed in etching.

1. Introduction

Besides the material choice, there are also two different target compositions that can be structured: thin films and bulk materials. In bulk structuring, the entire collision cascade of the Protons is in the material that is sensitive to Proton beam writing. The resulting 3D structure, if it is etched entirely down, will be as deep as the collision cascade can reach into the target and be as wide as the collision cascade at the widest point. In thin film irradiation only the part of the collision cascade that lies within the film results in structuring, with the rest of the material chosen in such a way that it remains inert in etching the thin film. This first part of the collision cascade is often relatively narrow in comparison to the whole cascade thus allowing for the simple production of very high aspect ratio (ration of the depth of the structure to its width) structures.

As shown in this work, it is also possible to use channeling in certain crystalline targets to create a more narrow collision cascade even in bulk material irradiation. Further, it is possible to use targets that were doped differently in certain areas to create 3D masks within the target that can be used to effectively control the etching and create complex structures that would normally require several more production steps.

1.3. The experimental steps of Proton beam writing

While the previous description provides a good theoretical overview of the two step process of Proton beam writing, in practice, however, the experimental procedure can be described more accurately by six steps:

1. Sample preparation
2. Accelerator setup
3. Focusing lenses tuning
4. Sample irradiation
5. Etching of sample
6. Post-processing

Sample preparation often consists of doping of the sample material (if neccessary), cutting the samples to shape, cleaning of the samples, heat treatment, application of electrical contacts (if neccessary) and mounting them in the target chamber of the accelerator. In a next step the accelerator is set up, that is, the ion source is brought up to its operating current and temperature, the acceleration voltage is tuned to the required value and the electric and magnetic lenses and steerers are tuned to provide as much ion beam current as possible to the target chamber. Following this, the magnetic lenses that focus the Proton beam are tuned to focus the Proton beam to a point that is sufficiently small in size. This is done by finely adjusting their positions and currents and measuring the beam spot size on a scintillator or with the help of a metal grid in the target chamber. At this point the sample can be irradiated. This happens by either moving the beam accross the sample or the sample through the beam according to a pre-computed irradiation plan.

1. Introduction

After the irradiation, the accelerator can be shut down and the samples are moved from the target chamber to an etching chamber. The etching chamber typically needs to be filled with processing chemicals, electric contacts need to be connected (if necessary) and the chamber equipped with sensors to record and control the etching process. Then the samples are etched either chemically or electrochemically. In the post-processing step the samples are cleaned from etching residuals and the 3D structure can be seen for the first time under a microscope (either an optical or scanning Electron microscope). Depending on the purpose of the samples, heat treatments, application of front contacts, other measurements or even several more cycles of irradiation and etching may follow.

All together, roughly at least 2 person working days are currently required to produce a single 3D structured sample in a well equipped and prepared facility like the micro-beam-line at MaRPel in Göttingen or at CIBA in Singapore. This is relatively fast for prototyping of arbitrary structures. However, since the process can not yet be efficiently parallelized, mass production of 3D structures with this procedure is impractical.

1.4. Comparison with similar techniques

In comparison to similar direct write techniques, specifically Electron beam or ion beam lithography, Protons as projectiles offer some unique advantages and disadvantages. While it takes much more effort to create and focus a Proton beam of similar target penetration power (or penetration depth) to an Electron beam, Protons are also about 1836 times more massive than Electrons and as such, travel much straighter than them when penetrating materials, as Electrons necessarily scatter at 90 degree angles with respect to each other [298]. This property allows for the fabrication of 3D structures with high aspect ratios, low line edge roughness and smooth side walls with Protons, which is often more difficult to achieve with Electron beams. Only in very thin layers and in comparison with other methods like reactive ion etching, Electrons can produce comparably smooth and high aspect structures to Protons. Simulations have also indicated that Proton beams exhibit only very minimal proximity effects (that is: exposure of the surrounding material via secondary Electrons) since on average the secondary Electrons produced in Proton-Electron collisions in the target material at practical Proton energies have low energies and therefore also very little range in the target [282]. In comparison to Electrons, Protons are also much more easily able to displace target atoms, in particular at the end of their range, thereby increasing the localized damage. In some materials (like Silicon) the creation of point defects in the form of displaced atoms and vacancies in the crystal structure even is the primary method of modification. In thin film resists, where Electron lithography and PBW are best comparable, an exposure of about 30-150 $\frac{nAs}{mm^2}$ is often required for PBW, while Electron irradiation requires about 80-100 times larger doses [298]. However, Electron sources are also commonly about 6 orders of magnitude brighter than Proton sources [112].

The advantages of Proton beams are shared with heavier projectiles (like Helium or Carbon ions), however the ability of the target material to resist ion beam penetration (the so called stopping power) is greater for heavier ions than the one for Protons. Additionally

1. Introduction

the specific charge (nuclear charge divided by nuclear mass) is lower for heavier projectiles. This has the effect that higher projectile energies are necessary to create structures of the same depth as Protons in the target substrate. The increased projectile energies in turn require much larger (more energetic) accelerators, which necessitate larger and more difficult to optimize focusing lenses as well.

Fig. 1.4 on the following page shows 100 simulated projectile trajectories created by a point like Electron-, Proton- and Argon-beam of comparable penetration power (reaching a depth of about 20 to 30 μm) in the three materials PMMA, Silicon and Gallium Arsenide. These three materials are common target substrates in PBW. The relatively curved paths of the Electrons is apparent, just like the increased energy required to implant Argon as deep as the Protons in the targets. Also shown are secondary particles created in the collisions. Note that these are more energetic (longer ranged) if created by heavier projectiles. The simulations were performed with Casino 3.3 [56] and SRIM 2013 [318] (both some of the most commonly used simulators in their respective domains). For Casino, a work function of 5 eV, 4.85 eV and 4.69 eV was used for the three materials and a plasmon energy of 23.09 eV, 31.05 eV and 44.17 eV [322]. The Electrons showed a back-scattering rate of about 30%, while none of the ions were backscattered.

1. Introduction

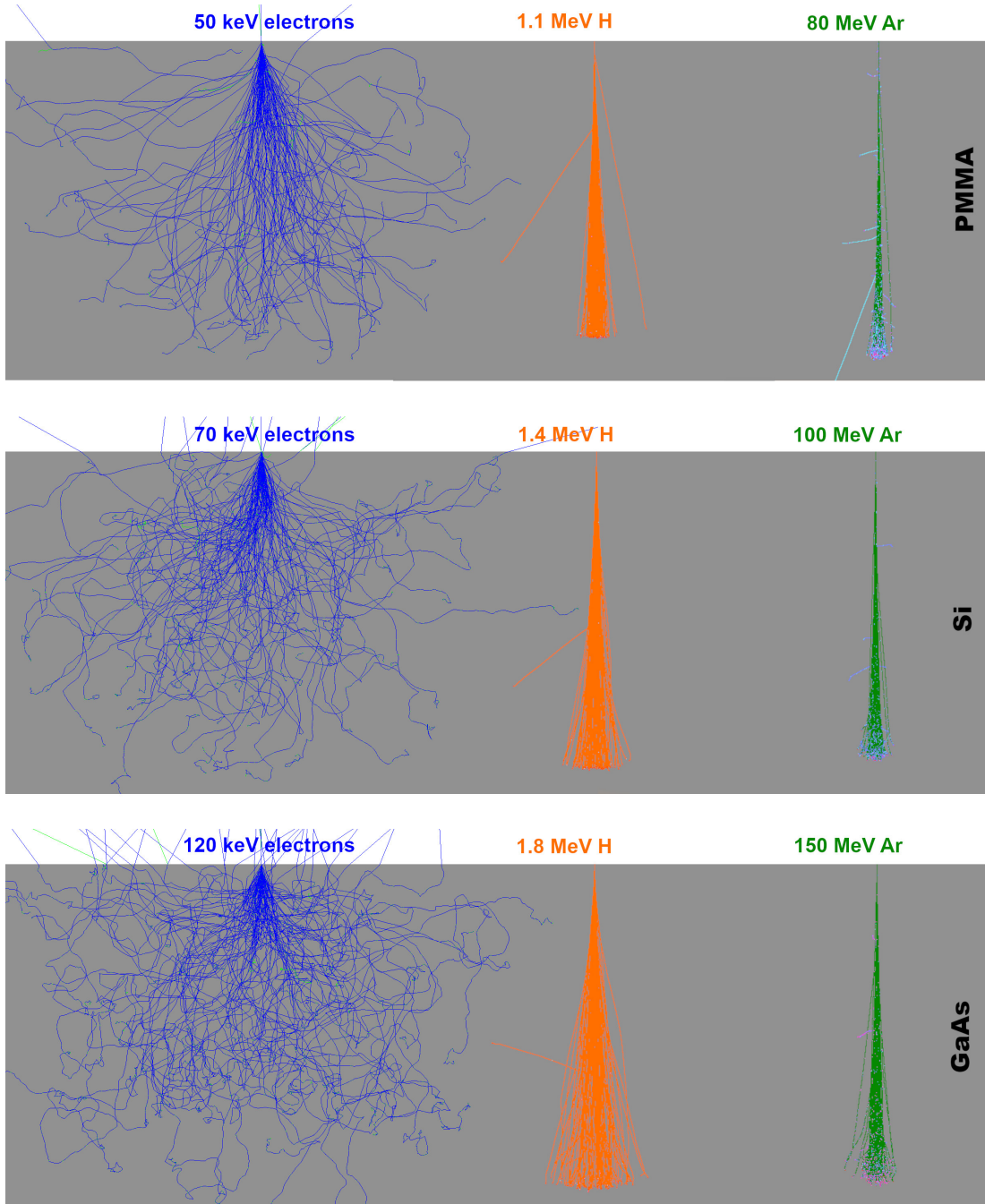


Figure 1.4.: Simulated trajectories of 100 projectiles (Electrons, Protons and Argon) in PMMA, Silicon and Gallium Arsenide. The gray layer represents a 30 μm thick layer of the target material and the particle energies are selected such that a majority of the layer is penetrated. The fanned out structure of Electron paths in the target are visible as well as the high particle energies required for the Argon beam to reach the required depths.

1. Introduction

Comparing the case of Proton and Argon irradiation of Gallium Arsenide, SRIM predicts a production of 44.4 vacancies per 1.8 MeV Proton, while 20400 vacancies are predicted to be produced per 150 MeV Argon ion (both have approximately the same range in the target). The Argon projectiles are expected to have a standard deviation of about 7900 target vacancies per ion. This is a relative coefficient of variation of about 39%. If the same number of Protons are used to produce the vacancies of a single 150 MeV Argon projectile (about 460), they are expected to have a standard deviation of 980 in the number of vacancies produced, or a relative coefficient of variation of about 5%. This shows that Proton irradiation can offer a more homogeneous target irradiation at low fluences. This comes at the cost of more implanted Hydrogen (in comparison to Argon) in the target though. For these simulations a lattice binding energy of 3 eV and a displacement energy of 25 eV per atom were used. These numbers are more closely examined in chap. 3.2 on page 84.

It was also found that Protons allowed for much looser tolerances on the exposure variations while at the same time offering a smaller span of doses within a single ion track as compared to He or C ions in the resist PMMA. Void formation and stress-induced surface roughening were also reduced for Protons [183]. This hints at a potential of Protons as a more precise tool for structure generation than heavier ions.

For nanostructures, PBW can also be compared to the otherwise slightly less related methods of deep ultraviolet (DUV), extreme ultraviolet (EUV) and focused ion beam (FIB) lithography. DUV and EUV lithography use masks in their process and are therefore able to be used efficiently in large volume production methods, while PBW does not require masks and can thereby save the cost and effort of mask creation for small volume production of nanostructures. Large scale production with PBW could still be possible though if PBW is used to write stamps or molds and combined with nanoimprinting and pattern transfer [304, 196]. DUV and EUV lithography often require specially developed, amplified resists. PBW in contrast can also be performed in these materials but is not limited to them. Additionally, the energy deposition (radiation damage) of Protons is roughly constant except for an about tenfold increase at the end of their range (more on this in sec. 3 on page 53), while photons show exponential decay as a function of penetration depth. This allows for the direct production of very different structures by Protons as compared to photons. The range of Protons in the target structure is also easily controllable by the energy of the projectiles, while this is relatively difficult for photons. This allows for the creation of multi-level structures in a single layer of resist (which would be very difficult in DUV or EUV lithography).

The process of material modification in FIB lithography is very different than for PBW. In FIB, heavy ions are used to sputter (remove) atoms from the surface of the target substrate. Conventional FIB has a sputter rate of about 1-10 atoms per projectile. This is about one million times less efficient than the removal rate of PBW. This slower rate is, however, somewhat offset by the much higher brightness of FIB sources. It is also slightly more difficult to produce structures with overhangs (for example bridge-like structures) for FIB techniques than for PBW, where this is routinely done. FIB lithography is also more flexible than PBW in the target material selection, as all solid materials can be sputtered to some extent by a heavy ion beam of appropriate energy [8].

1. Introduction

Other related techniques to PBW are so called ion projection (IP) lithography methods, where, similar to photon lithography methods, a mask or stencil is used and projected with the help of electrostatic reduction optics onto a substrate. Many of the advantages of PBW, like the high resolution, target material choices and high aspect ratios are shared by these techniques, however in mass production IP lithography has to compete with DUV and EUV lithography, which tend to be more cost effective, while for rapid prototyping and low scale production the required expensive mask/stencil production step makes it currently uncompetitive with traditional production methods [296].

1.5. History of PBW and state of the art

Eventhough implantation isolation and radiation damage of semiconductors by Proton beams has long been known (see for example [195] for a review of this process in III-V compound semiconductors and [250, 264] for silicon) and Proton beams have also been used to expose photoresists for the use as masks (see for example [239]) as well as being directly structured through Protons with the help of masks [227], one of the earliest examples of PBW was performed in the University of Oxford at the Nuclear Physics Laboratory only in 1993, where a 3 MeV Proton beam with a diameter of about 200 nm was used to create channels in PMMA that was carefully etched afterwards resulting in channels of about 125 μm depth and widths of as low as 2 μm [35], hinting at an aspect ratio (depth of structure to diameter of structure) of the method of at least 50:1. Following this, several laboratories have adopted the method, including the University of Singapore in 1997 [256], the Ruder Boskovic Institut in Zagreb (Croatia) in 1999 [203] and the Institute of Nuclear Research of the Hungarian Academy of Science (Debrecen) in 2003 [213]. The first experiments with PBW were performed in resists until the process was transfered to inorganic semiconductor materials. Tab. 1.2 on the next page gives an overview of the materials where Proton beam writing has been experimentally demonstrated in some of the early experiments. As it can be seen, roughly one new target material was added each year since 1999.

1. Introduction

materials	type	location	year	
PMMA	resist	Oxford	1993	[35]
PMGI and SU-8	resist	Singapore	1999	[113]
Silicon	semiconductor	Zagreb	1999	[203]
CR-39 and Foturan	resist	Debrecen	2003	[213]
PTFE	resist	Surrey	2005	[78]
GaAs	semiconductor	Surrey	2005	[165]
HSQ	resist	Singapore	2006	[114]
TADep	resist	Athens/Debrecen	2008	[45]
InP	semiconductor	Leipzig	2009	[160]

Table 1.2.: Overview of some of the early experiments and the materials in which Proton beam writing was successfully demonstrated as well as the time and place this happened.

Besides the transfer to new target substrates, there has been considerable effort to produce ever smaller structures with ever increasing aspect ratios. The potential of Proton beam writing to produce very small structures, shown theoretically to be as small as 3 nm in PMMA [74], was recognized relatively early, but reaching this limit is experimentally difficult. Over the years, ion beam optics, ion sources and accelerator designs were improved to obtain smaller beam spots at increased beam current on the target substrate in an effort to reach these predicted limits and compete with the resolution of Electron beam and EUV lithography. From the 200 nm beam in 1993, in 2003 it was already possible to reach spot sizes as low as $35 \times 75 \text{ nm}^2$ for 1 MeV Protons at beam currents of about 1.6 fA at the facilities in Singapore [297]. This improved to spot sizes as low as $19 \times 30 \text{ nm}^2$ in 2012 [112]. Which in turn, improved to spot sizes as low as $9.3 \times 32 \text{ nm}^2$ for 1 MeV Protons at currents of about 2 fA with essentially the same setup but improved tuning algorithms for the ion lenses [309].

In practice the smallest structures produced to date were lines with a diameter of 19 nm (in HSQ [310]) and the structures with the highest aspect ratios were lines in thin films with an aspect ratio of greater than 160 [111].

2. PBW facilities in Göttingen

2.1. Overview

The large accelerator hall in the faculty of physics, located at the 2nd institute of physics in Göttingen, houses two large accelerators: IONAS (a 500 keV Walton-Cockroft accelerator from HVEE [283]) and MaRPel. Of these, only MaRPel is equipped with a micro-beamline. MaRPel is a 3 MV-Pelletron 9-SDH2 tandem accelerator manufactured by NEC that was originally used at the Max-Planck Institute for nuclear physics in Heidelberg and was transported to and set up in the 2nd institute for physics at the Georg-August Universität Göttingen around the turn of the millienium [238, 284]. Here it remains until this day and is mostly used for material analysis, material modification, ion source development and teaching with light and intermediately heavy ions in the energy range from slightly below 1 MeV up to 9 MeV for some ions. The general layout of MaRPel has been previously published [238] and the accelerator is also shown in its current state in fig. 2.1 on the following page.

2. PBW facilities in Göttingen

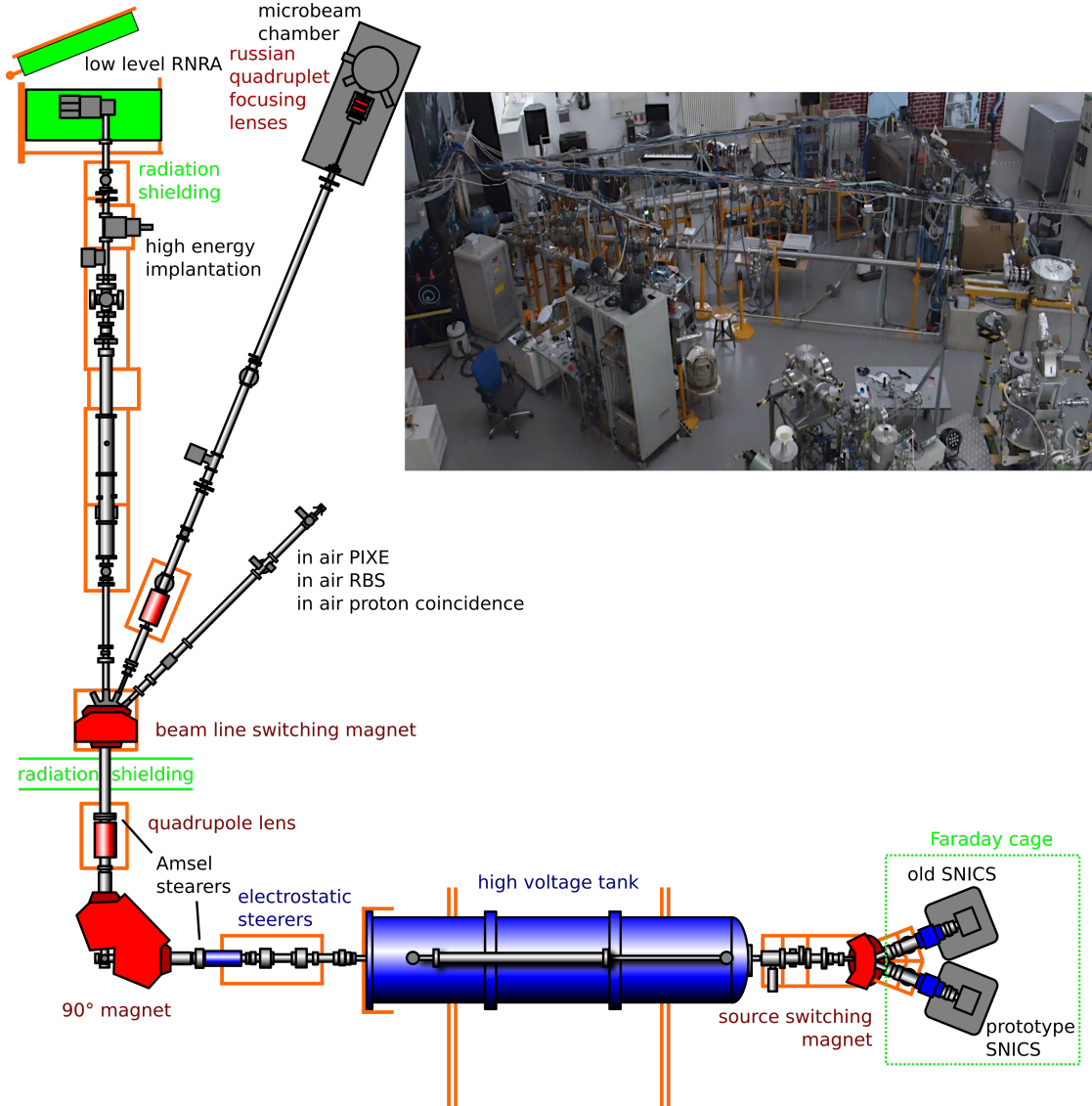


Figure 2.1.: Overview of the Pelletron MaRPel and a photo of the beam-lines in their current configuration. The ion beam is generated in the SNICS, accelerated to high energy in the high voltage tank and guided to one of three experiment beam-lines. The middle beam-line ends with the micro-beam chamber where PBW is performed.

Negatively charged ions leave one of the two ion sources and are guided by a switching magnet into the high energy beam-line. Here they are accelerated towards the center of the high pressure tank with a voltage in the megavolt range. Reaching this point, the ions enter a small tube filled with a low pressure stripper gas (Nitrogen) where they collide with the gas and in a stochastic process lose several Electrons. The now positively charged ions are accelerated again with the same positively charged voltage. This is the origin of

2. PBW facilities in Göttingen

the name “tandem accelerator”. The high energy ion beam leaves the high pressure tank towards a 90° mass separation magnet that also acts as a tunable energy filter. After the 90° mass separation magnet, the beam leaves the radiation shielding of the accelerator and is guided by a beam-line switching magnet into one out of three currently set up beam-lines:

- The RNRA (Resonant Nuclear Reaction Analysis) beam-line, which contains a chamber for high energy ion implantation as well as a specially shielded, low level RNRA setup.
- The micro-beam-line, which contains focusing lenses and a chamber for PBW as well as micro-beam analysis
- The in air PIXE (Proton Induced X-ray Emission) beam-line that allows for an extraction of the beam into air, where it can be used for PIXE, RBS and Hydrogen coincidence spectroscopy on samples that would not survive a vacuum.

PBW in Göttingen is only performed at the micro-beam-line of MaRPel. In the following sections the components will be discussed in some detail in the order in which a projectile passes them.

2.2. Ion source

The ion source used for PBW is a so called SNICS (Source of Negative Ions by Caesium Sputtering) [163, 251, 161, 42, 20, 162]. In this source, a heated Caesium bath is connected to the vacuum of the source chamber. This creates a very thin (about 10^{-6} mbar) Caesium atmosphere. On the ionizer, a heated, positively charged Tantalum surface, the Caesium vapour is partially ionized and repelled towards the cathode. The ionizer has about 200W of heating power which corresponds to an effective temperature in the order of $900-1000^\circ\text{C}$. The cathode, being under a negative potential in comparison to the chamber, is sputtered by the positive Caesium ions. It is commonly assumed [254] that due to the cooling of the cathode, a thin, slightly negatively charged Caesium layer forms on its surface, which the sputtered cathode material passes through. Upon collisions with the Caesium vapor, free Electrons are created which can stick to the freshly sputtered material, creating negatively charged ions. Since Electrons have a preference to stick to atoms with a greater Electron affinity, they tend to recombine mostly with the sputtered cathode material instead of the low Electron affinity Caesium atoms. This, besides the good sputtering yield of the comparatively heavy ion and the low evaporation temperature, is the primary reason for using Caesium as a working gas in the source. It should be noted that some more modern descriptions of the SNICS are slightly more nuanced but hold a similar view [13]. In any case: the produced, negatively charged ions are then repelled out the source. On the SNICS, a magnet is placed that diverts Electrons to the side but allows heavier ions to pass almost unaffected. The reduction of the free Electron content in the beam reduces the amount of x-rays generated in the higher energy sections of the beam-line. Fig. 2.2 on the next page shows a schematic view of the modified SNICS source used in Göttingen.

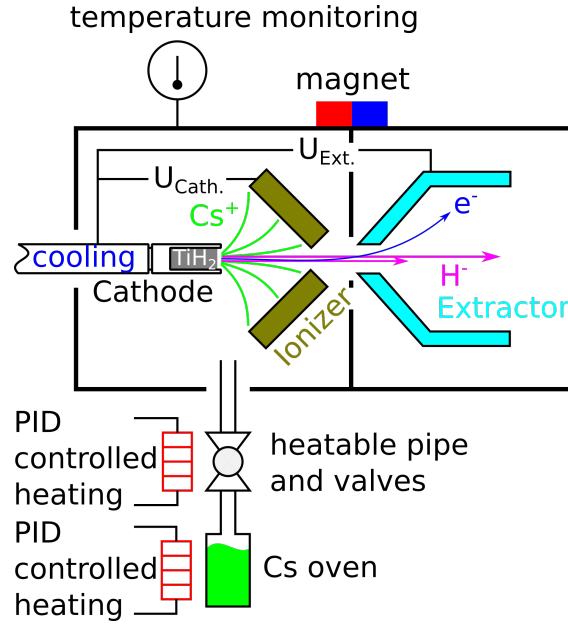


Figure 2.2.: Schematic representation of the SNICS (ion source) used for PBW in Göttingen. The source works by ionizing Cs atoms and accelerating them towards a cooled cathode, where a sputtering process generates negatively charged ions that are accelerated out of the source.

Some modifications were carried out on the SNICS. The applied voltages were modified to the configuration shown in the picture and a PID controller for the heating of the chamber walls was installed. Several cleanings of the vacuum components were performed and a heater for the valve to the Cs chamber was installed. All this allows for much easier and finer control of the chamber temperature and makes the operation of the source more reliable. Additionally, a new mode of operation for the source was developed and successfully used for several years. This new “low temperature” mode can be contrasted to two modes of source operation that were described in the literature [145]: the “burping” mode and the “high temperature” mode.

In the “burping” mode, a large amount of Cs is introduced into the chamber. This Cs can then form a puddle at the bottom of the chamber where it is slowly evaporated by the heat from the heater of the source. This allows for a fine control of the Cs pressure in the source but it is very difficult to not introduce too much Cs so that the source performance is reduced again. This mode of operation also has some disadvantages during maintenance, as there is always a considerable amount of Cs in the source region that oxidizes and needs to be removed when the source is exposed to air.

In the “high temperature” mode, the source is heated up to much higher temperatures than in the “burping” mode. Here the Cs can no longer form any reservoir in the chamber and instead needs to be supplied continuously and in reasonably large amounts from the oven. As such, the Cs pressure in the chamber is largely controlled by the oven heater. This avoids some of the disadvantages of the “burping” mode, however this causes the

2. PBW facilities in Göttingen

entire source to behave rather sluggish and makes the entire source very sensitive to small variations in the oven temperature. This in turn makes the source hard to control in this mode, even for skilled operators.

It turns out that the manufacturer recommended continuous supply of Cs from the oven is not necessary. NEC also assumes that the source is always started from cold (room) temperatures, where the start up time is about 1-3 hours until a large current is reached. This long start up time is not related to the heating of the Cs oven but rather the heating of the components in the source and the corresponding redistribution of Cs on the surfaces.

In the newly developed “low temperature” mode, the source is never fully cooled down. Instead it is held at a standby temperature when out of use and brought up to an operation temperature within 10 to 15 min when used. This means that the source is effectively started up to operating pressure by the small amounts of Cs that are condensed on some of the surfaces on the source before startup. This “reservoir” in the source was found to be large enough for several days of continuous operation without refilling the Cs from the oven. On occasion the source area is refilled with Cs from the oven. For this PID controlled heating elements are used at both the Cs oven and the valve leading to the chamber, where the PID control was newly installed. Once the source is filled up again, the valve is closed. The source can be used for several months in this way, since the SNICS is not continuously used. A disadvantage of this mode of operation is a slightly reduced maximum beam current.

The cathode material that is used for the creation of negative Hydrogen ions in Göttingen is made up of a pressed titanium hydride (TiH_2) powder that also contains an equal amount of Silver in the form of a fine powder. The Silver was found to increase the efficiency (maximum extractable stable current) of the cathode by a factor of two [237]. A similar improvement was also found for the beam current for KCN cathodes [238].

The previously mentioned view of the charge transfer process at the cathode surface might, however, be a bit too simplistic, considering the deposited energy (and therefore effective temperature) by the Caesium ions at the surface of the cathode and the sputter rate of cathode material. In the following two sections the processes at the surface of a SNICS are discussed and contrasted. The first one argues from the point of view of a sputtering process that takes place at the surface of the cathode, whereas the second view considers the thermodynamics of the TiH_2 as a source of the negatively charged Hydrogen.

2.2.1. Sputtering model of the SNICS

To understand the behaviour of the SNICS, a series of sputtering simulations were carried out with SRIM. For this 10'000 Cs atoms at different energies were set to be colliding with a cathode of different compositions. These compositions were always set to equal amounts of TiH_2 and Ag with a varying content of Cs, such that the sputtering rate of Cs was one sputtered Cs atom per projectile, approximating the quasi-static equilibrium conditions at the surface. The density of the cathode material is determined by a linear interpolation between the densities of TiH_2 , Ag and Cs at room temperatures. The surface layer thickness is approximately the mean implantation depth of the Cs atoms

2. *PBW facilities in Göttingen*

at the given energy and target composition. Due to a lack of better values, the lattice binding energies are set to 0 and the surface binding energies set to the atomization enthalpies of the elements (4.88 eV for Ti, 2.25 eV for H, 2.95 eV for Ag, 0.78 eV for Cs [90]). The results of these simulations are summarized in tab. 2.1 on the following page. It should be noted that recent research points to more realistic approaches for sputtering processes than the simulations with SRIM can provide [98, 99], but since the calculations performed here are more for a qualitative understanding of the conditions at the SNICS surface and the impact angles of the projectiles are orthogonal to the surface, the SRIM simulations are deemed sufficiently accurate for the discussion here.

2. PBW facilities in Göttingen

Cs energy [keV]	0.22	0.5	1	2	5	10	20	50	100
conc. in surf. layer [TiH ₂ : Ag : Cs]	0:0:1	1:1:0.9	1:1:0.5	1:1:0.3	1:1:0.18	1:1:0.13	1:1:0.11	1:1:0.1	1:1:0.09
surf. layer thickness [Å]	44	22	26	32	45	62	91	160	262
eff. density at surf. [$\frac{\text{g}}{\text{cm}^3}$]	1.93	5.51	6.08	6.44	6.69	6.80	6.85	6.87	6.90
tot. sputter yield [atoms/projectile]	1	1.52	2.13	3.14	5.19	6.89	8.63	10.4	11.5
mean energy of sputtered H [eV/atom]	-	2.48	4.22	5.92	9.79	15.0	22.0	38.1	54.7
mean energy of sputtered atoms [eV/atom]	7.15	7.69	10.1	13.8	18.9	25.1	35.4	56.3	80.7

Table 2.1.: Properties of the sputtering process in the cathode as a function of the Cs energy as roughly estimated with SRIM. Shown are the surface layer properties and sputtering details as a function of the Cs ion energies.

2. PBW facilities in Göttingen

On average the Cs projectiles deposit about 98 to at most 99 % of their energy at the cathode under the simulated conditions and only less than about 2% is carried away by the sputtered atoms. This means several hundred eV of energy are deposited in surface layers in the order of 100 Angstrom or less per keV energy Cs atom. Even with cooling of the cathode this is such a high local energy density that it seems unlikely that a liquid or condensed Cs layer would be able to survive the collision cascades. Also visible from the simulations: in the practical energy range of up to 100 keV, the sputtering yield and the mean kinetic energy of the sputtered Hydrogen atoms increases continuously. Below about 0.32 keV initial kinetic energy of the Cs projectiles the total sputter yield drops below 1, meaning that the source is expected to not emit Hydrogen by sputtering at the quasi-static equilibrium conditions assumed here. It is also visible that at the lower energies simulated here both the active surface layer thickness decreases and the Cs content increases within it. This means that at the limit of very low projectile energies the model of a Cs layer at the surface through which sputtered atoms need to pass becomes feasible. At higher and more realistic energies, however, the surface layer can be understood more like a material with a content of about 10% or less Cs. As such only every tenth (or less) collision between a sputtered atom and an atom in the target will involve a Cs atom. This means that the simplistic picture for the efficient charge transfer between Cs and sputtered atoms needs to be modified.

The amount of usable negatively charged Hydrogen ions by sputtering can be estimated by free energy considerations, if we assume the sputtered Hydrogen as an interacting gas at a temperature that is determined by the mean kinetic energy of the sputtered ions. For this we use the energies from tab. 2.3 on the next page. Tab. 2.2 shows the yield of negatively charged Hydrogen per Cs ion. It should be noted that for the creation of a negatively charged ion additionally an Electron needs to be removed from the cathode, thus incurring an energy penalty.

Electron affinity [eV]	sputter yield of H ⁻ per Cs atom							
	$E = 0.5$ keV	1 keV	2 keV	5 keV	10 keV	20 keV	50 keV	100 keV
4.0	0.18	0.33	0.53	0.91	1.20	1.48	1.75	1.92
2.0	0.25	0.40	0.61	0.99	1.27	1.54	1.79	1.96
1.0	0.30	0.44	0.65	1.03	1.30	1.57	1.81	1.97
0.5	0.32	0.46	0.67	1.05	1.32	1.58	1.82	1.98
0.0	0.34	0.48	0.69	1.07	1.34	1.60	1.83	1.99

Table 2.2.: Sputtering yield of negatively charged Hydrogen as a function of Cs kinetic energy and Electron affinity of the negatively charged target from the approximations discussed in the text.

Eventhough the approximation of the sputtered atoms as an interacting gas with an effective temperature is relatively crude, the trend of increased Hydrogen yield with increased Cs energy that was observed from the sputtering simulation is even further amplified. As such, it is clear that higher Cs energies and to a smaller extend lower Electron affinities in the target improve the effective Hydrogen current that is usable in

2. PBW facilities in Göttingen

the accelerator. Tab. 2.3 shows some of the Electron affinities and for comparison also ionization potentials of some of the atoms in the SNICS. As shown, both Titanium and Caesium have Electron affinities below 0.5 eV and are ideally suited for the creation of negatively charged Hydrogen (with an Electron affinity above 0.75 eV). Silver in this context would hinder the formation of Hydrogen anions, but it improves both the heat and electrical conductivity of the otherwise non-conductive cathode. Considering these effects, Carbon or Aluminium might be considered in future experiments as well, as they both have lower Electron affinities (thus capturing less Electrons than Silver), good heat and electrical conduction and as an added benefit can capture Oxygen atoms in the source volume that might otherwise oxidize the Cs vapour, in case of Carbon possibly even more efficiently than Titanium (TiO has a bond energy of about 642 kJ/mol, CO 1072 kJ/mol and AlO 507 kJ/mol [202]).

atom	ionization potential [eV]	Electron affinity [eV]
H	13.598	0.754
Ti	6.828	0.079
Ag	7.576	1.302
Cs	3.894	0.472

Table 2.3.: Atoms in the collision cascade of the SNICS with Titanium Hydride (and Silver) filling and their ionization potentials and Electron affinities [90] in comparison.

This simple sputtering model of the SNICS can therefore explain the kinetic energy threshold of the Caesium in the source that is observed experimentally, the rise of the source current with increased kinetic energy of the Caesium ions as well as motivate why Ti and Cs are good choices for use in the source. It can however not easily explain the occurrence of a maximum of the beam current at a comparatively low value of a few keV that was often observed experimentally. While it might be possible to explain such an optimum with the help of an electrical conduction model, one can also consider another model that concentrates on the thermodynamics of TiH₂ itself. This is discussed next.

2.2.2. Thermodynamic considerations

One effect that was neglected so far is the decomposition of TiH₂ in the cathode from the collision cascades in the active layer. For this, consider that approximately half the projectile energy might be used to heat TiH₂ (with the other half heating the Silver). The exact value depends on the composition of the surface layer and can be extracted from tab. 2.1 on page 29. TiH₂ has an atomic density of about $0.14 \frac{\text{atoms}}{\text{\AA}^3}$ and when approximating the volume of the collision cascade as l^3 with l as the (active) surface layer thickness, an approximation for the energy deposited per atom can be calculated. This is shown in fig. 2.3 on the next page. This assumes no heat conduction can take place.

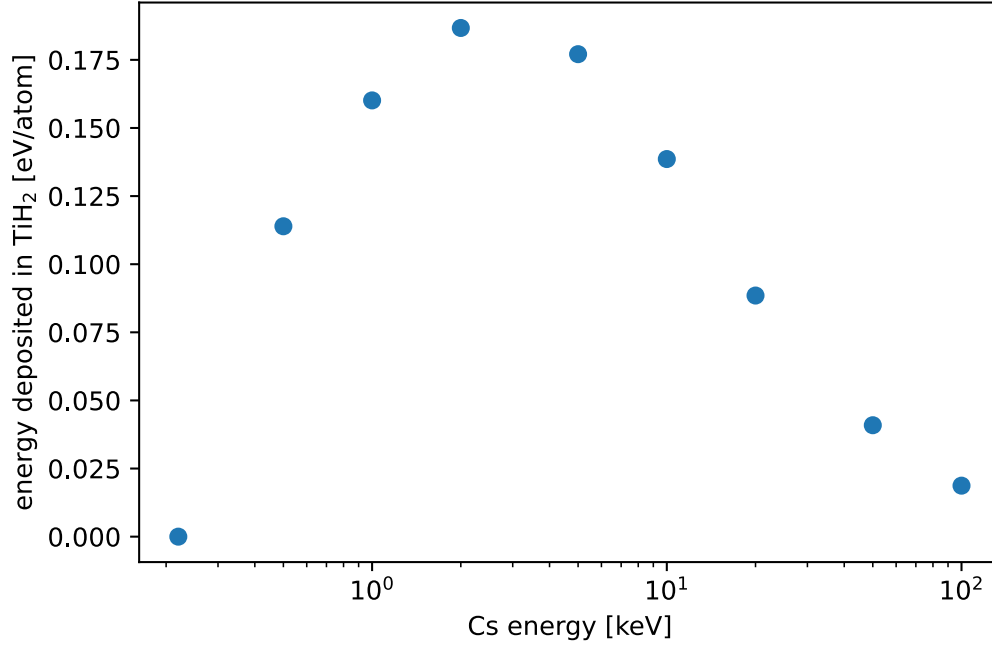


Figure 2.3.: Energy deposited per atom in TiH₂ in collision cascades of Cs of varying kinetic energy in the cathode of a SNICS.

The energy deposited per atom in TiH₂ likely leads to an outgasing of Hydrogen, an effect that starts in TiH₂ at 350°C in atmospheric pressure and that is virtually complete at the melting point of Titanium at about 1668°C [301]. In the binary collision simulations carried out, the energy transferred to each atom is about in this range of temperatures. It would thereby follow that by this model the primary mechanism of Hydrogen anion generation is the outgasing of Hydrogen from the cathode material due to localized heating. It follows that a clear optimum between 1 and 10 keV Cs energy should exist, which is also observed experimentally (in case of MaRPel this it at about 6.6 keV). The negative charge of some of the hydrogen atoms would in this case be explainable by both the negative charge of the cathode itself and the relatively high electronegativity of Hydrogen in comparison to its former bond partner Titanium.

Left behind from a collision cascade would be a Hydrogen poor region, which requires sputtering by Cs. Both Ag and Ti are, according to the SRIM simulation, easier (this is: more efficient) to sputter by a factor of more than two than Hydrogen. In this model, the role of Silver in the cathode might however be more subtle than in the previous considerations. While conduction might play a role, the Silver power might also support the sputtering of the source and enable the faster creation of new surfaces that contain more Hydrogen rich material.

In comparison it is likely that both processes, the direct creation of sputtered Hydrogen

and the indirect creation via thermodynamic decomposition of the cathode surface, play a role in the function of the cathode. However the latter process seems to be dominant at the typical operation energies as both the number of Hydrogen atoms involved is by far greater and the predicted Cs energy optimum roughly corresponds to the experimentally observed one as well.

2.3. Tandem accelerator

After the SNICS, the negatively charged ions are further accelerated by a 10 to 50 keV extractor, focused slightly by an Einzel lens and injected into the high energy part of the accelerator [144]. This happens via the source switching magnet. The ions are then accelerated in the high voltage tank of MaRPel. The high voltage is created by transporting charge from a voltage supply to the center of the high pressure tank via a chain of metal pellets that are alternatively interrupted by insulator links. These pellets are the origin of the name “pelletron”. To control the voltage of the accelerator a corona discharge probe mounted in the wall of the tank is used. In the middle of the tank, the ions hit a low pressure stripper gas in a small tube that is used to reversly charge the ions by removing several Electrons in collisions, thereby creating positively charged ions. This stripping process can be up to 90% efficient [48]. The ions are then accelerated with the same, positive voltage again. As such, a voltage of 1 MV is enough to generate 2 MeV Protons, for example. This MV potential difference, however, is so large that it would violently discharge towards the walls and floor, if the high voltage assembly were exposed to ambient conditions. To prevent this, a gas with a much greater breakdown voltage than air is used: pressurized SF₆. This gas is circulated and filtered and also acts as cooling for some of the components inside the high pressure tank. The gas itself is cooled via a water-cooling system. Inside and behind the high pressure tank several electrostatic lenses are mounted to both focus and displace the high energy beam. Behind the lenses a 90° mass separation magnet is placed. This magnet acts as both a mass and an energy filter for the projectiles. Mounted directly in front of and behind the 90° magnet is a pair of slits with a differential current measurement. This device, called an Amsel steerer [238], allows for precision control and stabilisation of the particle beam energy. Behind the 90° mass separation magnet, a quadrupole magnet was installed. The 90° magnet acts like a defocusing lens in one direction and this quadrupole magnet allows to effectively compensate for this.

This point can be supported with a set of simulations. For this Monte Carlo ray tracing simulations are carried out. The Protons are emitted from the center of the high voltage tank, normally distributed in 3D with a standard deviation of 1 mm. They are given a velocity that corresponds to 2 MeV energy per Proton with a standard deviation of 0.1%, which resembles the energy distribution of the particles resonably well [238]. The equations of motion of the Protons in the beam-line are integrated via Boris integration [32] which is a second order accurate integrator and one of the most common methods for the motion of charged particles in electromagnetic fields when phase space properties and conservation of energies are important [210]. This integrator allows to integrate the

2. PBW facilities in Göttingen

relativistic equations of motion:

$$\frac{d\vec{r}(t)}{dt} = \vec{v}(t)$$

$$\frac{d\gamma\vec{v}(t)}{dt} = \frac{q}{m} \left(\vec{v}(t) \times \vec{B}(\vec{r}) \right)$$

where $\vec{r}(t)$ is the position, $\vec{v}(t)$ the velocity, $\gamma = \frac{1}{\sqrt{1-\frac{v^2}{c^2}}}$, q the charge and m the mass of the Proton. $\vec{B}(\vec{r})$ is the magnetic field at position \vec{r} . It should be noted that $\gamma = \text{const.}$ and $|\vec{v}(t)| = \text{const.}$ for a particle moving through time constant magnetic fields (as they do not exert work). Boris integration of these equations with a time step Δt leads to an update scheme [218] which is transformed here for the special case of a lack of an electric field to:

1. $\vec{r}(t + \frac{\Delta t}{2}) = \vec{r}(t) + \frac{1}{2}\vec{v}(t) \Delta t$
2. $\vec{t} = \frac{q\vec{B}(\vec{r}(t + \frac{\Delta t}{2}))}{2m\gamma} \Delta t$
3. $\vec{s} = \frac{2\vec{t}}{1+t^2}$
4. $\vec{v}(t + \Delta t) = \vec{v}(t) + [\vec{v}(t) + (\vec{v}(t) \times \vec{t})] \times \vec{s}$
5. $\vec{r}(t + \Delta t) = \vec{r}(t + \frac{\Delta t}{2}) + \frac{1}{2}\vec{v}(t + \Delta t) \Delta t$

Fig. 2.4 on the following page shows some of the results of these simulations. With the quadrupole magnet turned off, the standard deviation of the beam on target is about twice as large in the horizontal direction than in the vertical direction, while the optimal value for the field strength of the magnet makes them roughly equal in size. It was found that experimentally, approximately a doubling of the maximum beam current in the target chamber could be achieved. This confirms the general results of the simulations when considering that collimation slits are used in the micro-beam-line.

2. PBW facilities in Göttingen

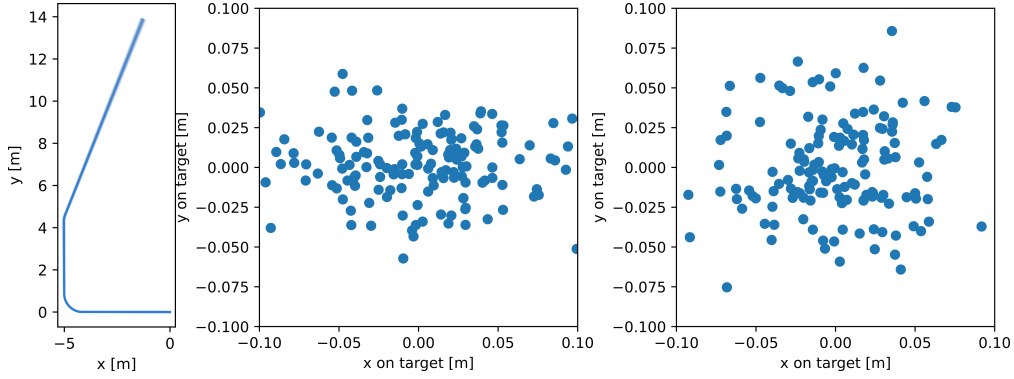


Figure 2.4.: Results of the Proton ray tracing simulations of the MaRPel accelerator with the micro-beam-line. On the left a top down view of the particle paths through the accelerator. In the center the distribution of Particles on the target with the quadrupole magnet after the 90 degree mass selection magnet at 0 strength and on the right at optimal strength.

While the overall layout of the high energy part of the tandem accelerator remained largely unchanged since the beginning of this work, many repairs and modifications were carried out in and around the high pressure tank. A source of vibrations inside the high energy, high pressure tank was identified and removed and some of the beam-line components were realigned during maintenance. This lead to slightly increased beam currents in the micro-beam-line, as well as a noticable reduction in beam jitter. The water cooling system of the SF_6 was found to be faulty and repaired and improved. The SF_6 warning system of the accelerator hall that detects leakage and alerts the users was also faulty and replaced. The energies of many projectiles accelerated in the high voltage tank are great enough to cause nuclear reactions when the beam pipe or other components of the accelerator are hit. Because of this, a set of radiation detectors are mounted around the high voltage area. These detectors had degraded over the years and were replaced by new ones. Due to damage the magnetic field sensor in the 90° magnet and a power supply had to be exchanged, with no noticable decrease in accelerator performance. The Amsel steerer [238] was repaired and is now the preferred method of energy stabilisation of the ion beam, once the approximate energy of the beam is tuned with the help of the corona discharge probe in the high voltage tank at the start of the accelerator.

2.4. Micro-beam-line

2.4.1. General layout

As mentioned previously, the micro-beam-line is one of three currently installed beam-lines at the MaRPel facility, with the other being the high energy implantation / low-level RNRA beam-line and the combined in-air PIXE / RBS / Proton coincidence spectroscopy beam-line. The primary purpose of the micro-beam-line is the production of a Proton micro-beam that is used in PBW, however the design of the large target chamber allows

2. PBW facilities in Göttingen

for other experiments as well, among them micro-beam PIXE, RBS and pixel detector tests. The current layout of the micro-beam-line is shown in fig. 2.5 on the next page.

2. PBW facilities in Göttingen

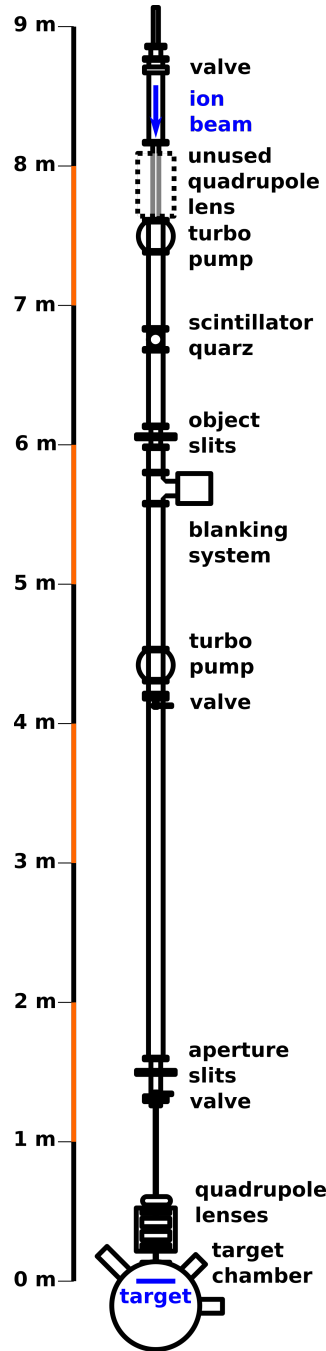


Figure 2.5.: Overview of the micro-beam-line at MaRPel. The Proton beam enters from the top and passes through two sets of slits and the focusing quadrupole lenses into the target chamber, where the irradiation target is located.

As the beam is guided into the beam-line towards the target, it passes a remotely controllable scintillator / camera system that aids in adjusting the beam, followed by the

2. PBW facilities in Göttingen

object slits which cut the beam into a small size. Following this the beam passes the new electrostatic blanking system, aperture slits, quadrupole lenses and finally it is guided into the target chamber. The object and aperture slits use the same remotely operated system that has been described previously [88], but the system went through an extensive overhaul in which all electrical connectors were exchanged for new, more reliable ones. The accuracy of slit controllers is roughly $10\text{ }\mu\text{m}$ [88]. An annotated photograph of the micro-beam-line can be found in fig. 2.6.

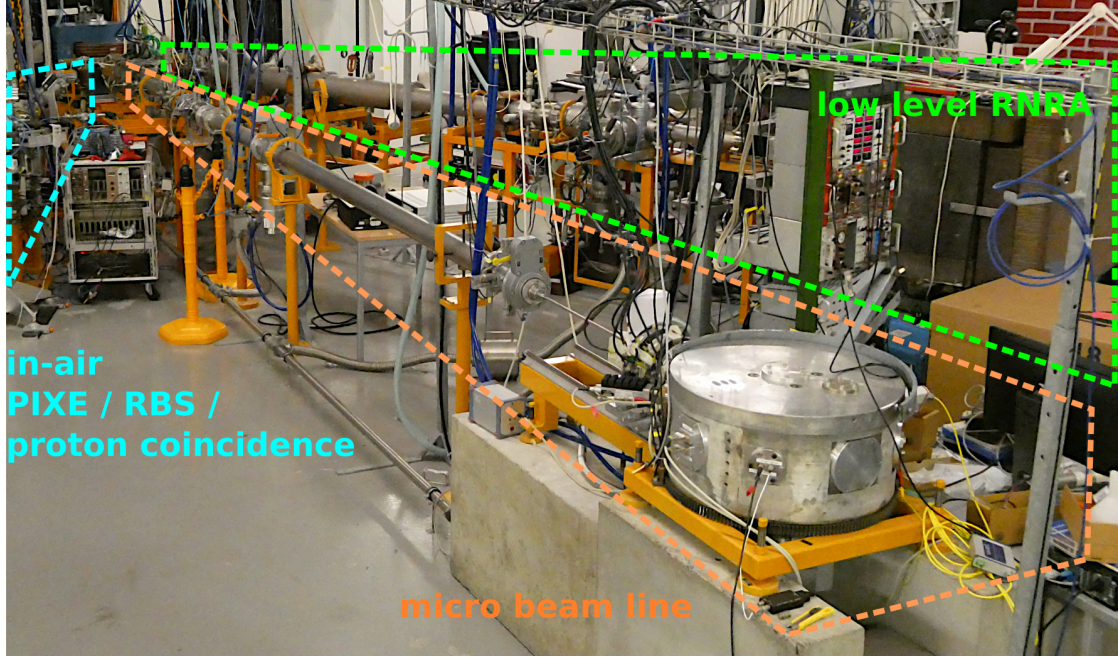


Figure 2.6.: Photo of the micro-beam-line at the MaRPel. Left and right of the micro-beam-line are two other beam-lines. The target chamber is located in the bottom right and the Proton beam enters the beam-line on the top left corner of the picture.

The micro-beam-line at the MaRPel accelerator has been redesigned and received several upgrades in the past years in an effort to increase overall performance. The goals of the upgrades of the beam-line were to improve the easily achievable beam spot size on the target, increase target current and develop new methods and tools to improve usability. These topics have been identified as critical for improving the PBW process, as mentioned in the introduction. In the following a short overview of the upgrades is provided.

A previously installed, unused RBS chamber was removed from the beam-line, improving the effective volume that needs to be evacuated, thereby accelerating the evacuation time after maintenance. The size of the easily achievable beam spot was reduced by moving the objects slits from their original distance of about 4 m from the target to about 6 m. At the same time a quadrupole magnet was installed after the 90° magnet in the high

2. PBW facilities in Göttingen

energy part of the accelerator to compensate for the focusing/defocusing effect of the 90° magnet. The last change also had the effect of slightly increasing the beam current on the target at a constant object slit opening. This is discussed further in the section on the high energy part of the accelerator. The old beam blanking system was replaced by a new one that could be remotely controlled over USB from the newly developed software.

The old turbo pumps on the beam-line were exchanged for new ones that are low enough in vibrations that long time irradiations with running pumps and at constant pressure of 10^{-6} mbar are possible. The reduced vibrations were confirmed by measurements. Fig 2.7 shows the frequency spectrum of different turbo-pumps as measured with a microphone on their housing. For this the background of the accelerator hall noise was subtracted and a Fourier transformation of the 192 kHz recordings was performed with a Hann Harris [87] window.

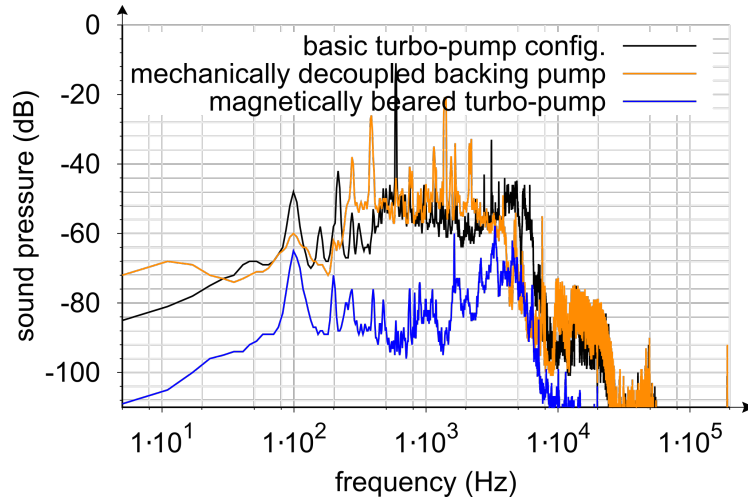


Figure 2.7.: Frequency spectrum of the vibrations of turbo-pumps as measured by a microphone positioned at the surface of the pumps with different measures to dampen vibrations.

2.4.2. Lens System

The magnetic lenses installed at the end of the beam-line are a magnetic russian quadruplet with a maximum demagnification of 16 [36] in a similar setup in Freiburg, and between 19.2 [237] to 29 [88] in Göttingen. It was reported that beam sizes of about 20 μm [36] were achievable with these lenses. Fig. 2.8 on the following page shows the experimentally achievable demagnification for beam diameters on the order of 5 mm in diameter on the target as a function of the lens distance from the target surface. Note that the maximum measured value agrees well with the latest theoretical estimate of 19.2 [237]. The smallest measured beam sizes with the lenses before they were modified were achieved when the lenses were tuned by the author of this work for a Bachelor's thesis with a beam diameter of slightly below $10 \times 8 \mu\text{m}$ [124]. At these beam diameters the collimation slits had

2. PBW facilities in Göttingen

to be closed to such an extent that the achievable currents were typically too small for practical PBW.

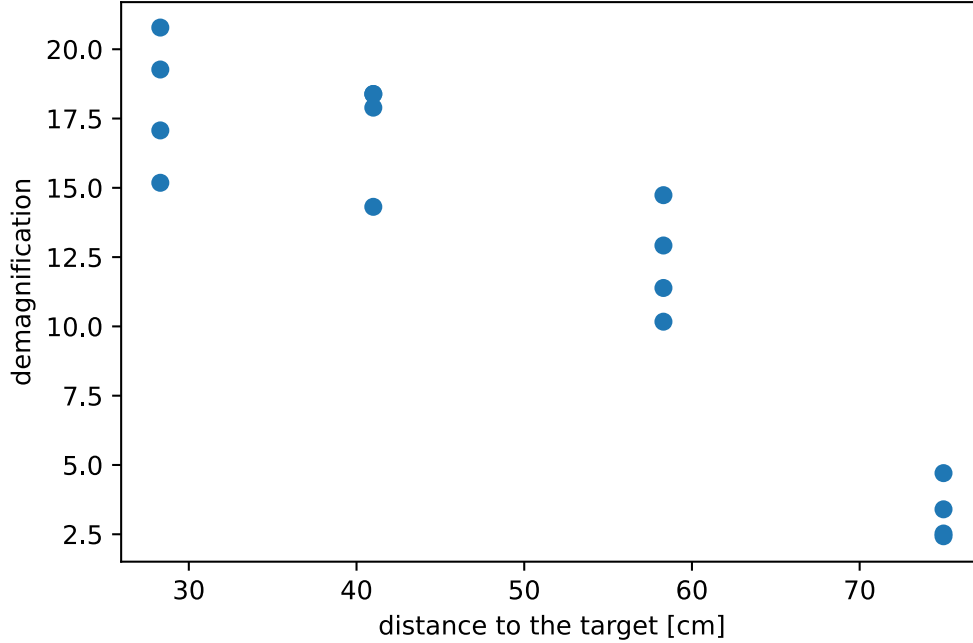


Figure 2.8.: Experimental demagnification for the quadruplet lens system at the micro-beam-line in Göttingen as a function of the mean distance of the lenses to the target surface. The beam sizes for these measurements on the target were between 2 and 5 mm in diameter.

Because of this, several modifications were performed on the lenses. The lenses were improved with new electric insulations, removing a source for occasionally observed electrical shorts. Additionally, a new air cooling system, a new micrometer positioning system and spring assisted mounting instead of the screw mounts were installed. These changes make it much easier to position (and adjust for optimal performance) the lenses correctly. The control electronics for the currents of the lenses were also improved with a new additional fine tuning dial and by overhauling the connections and exchanging current switches. These changes to the quadruplet lenses reduce the time to calibrate the lenses for optimal spot size and make them much more reliable. The plate on which the lenses are mounted was separated and equipped with a micrometer-screw to allow for fine-tuning of the distance between the first and the second lens pair. In practice this additional degree of freedom turned out unsatisfactory and did not improve the performance noticeably. Fig. 2.9 on the next page shows a picture of the modified lens system. With the new lens system it is regularly possible to achieve beam sizes of about

2. PBW facilities in Göttingen

$15 \times 15 \mu\text{m}$ at currents that remain practical for PBW.

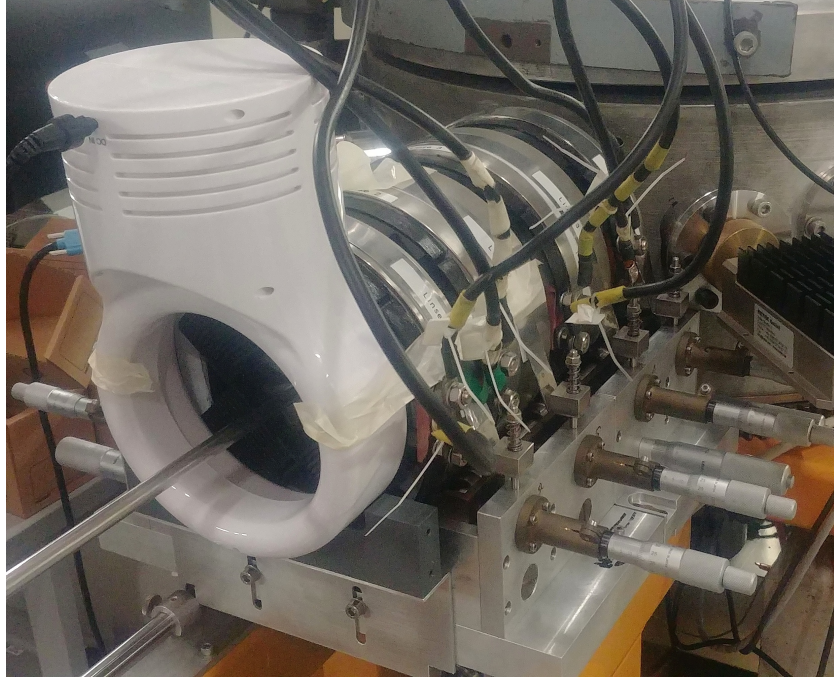


Figure 2.9.: Picture of the quadruplet lens system at the micro-beam-line after the upgrades. In the front the cooling system is mounted. The lenses are pressed against several fittings by a spring mounting. The lenses can be adjusted with a set of micro-screws.

A problem of the beam-line that was previously unnoticed due to the imprecise nature of the old lens system was the incorrect wiring of the beam-line selector magnet power supply. As a result, the current of the magnet tended to drift as the current of the quadruplet lenses was adjusted. A better grounding of the beam-line selector magnet power supply fixed this problem.

With other options ruled out, deemed impractical or too expensive, further improvements in the spot size of the micro-beam-line are likely only possible with a different set of demagnification lenses and large changes to the MaRPel accelerator.

2.5. Irradiation chamber

The target chamber of the micro-beam-line was entirely overhauled and received an internal redesign. It now houses a next generation sample holder that is mounted on a set of high precision linear stages, which in turn are mounted on a turnable plate. Furthermore a high definition microscope, an adjustable LED mount, an RBS sensor and a PIXE detector are pointed at the target surface. The target is surrounded by a cage that can be put on a potential of up to 1.5 kV with respect to the target to allow for

precise measurements of the beam current on the target by suppressing ejected secondary Electrons. Fig. 2.10 shows an overview of the new target chamber.

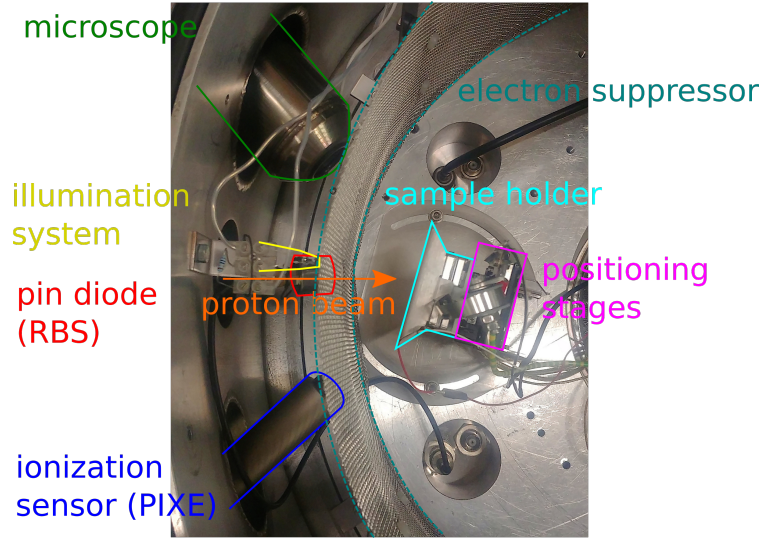


Figure 2.10.: Overview of the target chamber of the micro-beam-line. Visible is the sample holder, where the target is located. The sample holder is mounted on positioning stages. Several instruments are pointed towards the target surface and an Electron suppressor grid is mounted. The Proton beam enters from the left.

The new positioning system is based on closed loop linear stages with a positioning accuracy of 50 nm (repositioning accuracy of 4 nm) and maximum travel of 28 mm of type Q-522.230 from PI. These allow for the removal of the previous beam scanning magnets and allow for irradiations of much larger patterns on target samples without any stitching problems that could occur previously when irradiating a structure that was larger than the area that could be scanned by the scanning magnets. The stages can also be controlled through a newly developed software that was developed together within the scope of final theses of several students [181, 15, 104].

2.6. Sample holder

A common sample holder design for ion beam applications consists of a metal plate onto which a sample can be mounted with screws and metal strips. This design has many advantages, among them simplicity, good heat and electrical conduction for the target sample and support for a large variety of different sample sizes and thicknesses. This simple design, however, brings with it also several disadvantages that are specific to Proton beam writing. Since the focusing of the Protons happens relatively narrowly in front of the target, the focus of the beam is rather shallow, meaning the sample surface at all places of the target sample needs to be held at a very constant distance from the focusing

2. PBW facilities in Göttingen

lenses. Additionally, mounting small samples can be quite difficult and occasionally the sample can even break in the mounting process.

In the setup at CIBA, the first problem is solved by measuring the height of the samples (and scintillator) with a microscope and moving the entire sample holder towards or away from the focusing lenses as required to keep the sample surface in focus. This way, samples of different thicknesses can be mounted and irradiated together one after another on the same sample holder. Two sources of error still remain, even for ideally smooth samples: one from the measurement of the surface height and another one from mounting samples with an uneven front- or backside (resulting in a slightly angled sample surface with respect to the sample holder). As the samples that are regularly irradiated at MaRPel often have back contacts, a slight tilt of the samples would always be unavoidable with a plate type sample holder.

To avoid the aforementioned disadvantage, an entirely new sample holder was designed. The guiding idea of the design is to hold the surfaces of the samples in the same plane. For this a metal frame is used with a small lip against which the samples are held from the back side. This also allows to hold the samples in place with almost no mechanical strain. This design also avoids the problem of having to position small screws in the mounting process. This approach has a drawback though: samples that do not have standard measurements $((10.0 \pm 0.5) \times (10.0 \pm 0.5)$ mm with thicknesses up to 7 mm) require insets to be mounted securely. For the samples irradiated at MaRPel, this was not found to be a problem, as sample sizes within the mentioned size constraints were required for the etching chamber as well. Fig. 2.11 on the next page shows a schematic representation of the essential parts of the three types of sample holders mentioned here.



Figure 2.11.: Schematic representation of three sample holder designs. On the left a common design used in ion beam irradiation, in the middle a design similar to the one used in the CIBA Singapur and on the right the new design used at MaRPel.

The details of the new design can be understood better from a cut away view. This is done in fig. 2.12 on the following page. The spacer plates and the optional spacing frames are only used when several samples are mounted with thicknesses that differ by more than a few Millimeters.

2. PBW facilities in Göttingen

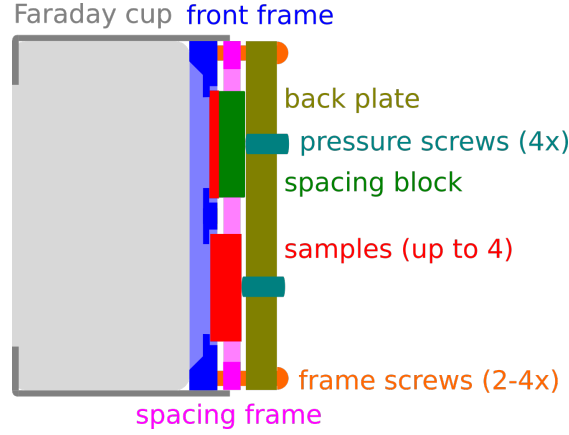


Figure 2.12.: Cut away drawing of the newly designed sample holder. The samples (in red) are held against the lips of the front frame (blue) by the pressure screws (blue green). For samples of very different thicknesses (as shown here) spacing plates (dark green) and spacing frames (fuchsia) can be used. The assembly is held together by the frame screws (orange). At the front a Faraday cup (grey) is mounted that doubles as a stand for inserting the samples when the sample holder is set on a table.

The design of the sample holder was optimized for light weight to reduce the mechanical work that has to be performed when moving the samples. The total weight amounts to about 26g. This low weight design reduces heat production in the positioning stages and allows for longer run times in vacuum without overheating. Additionally a hook is mounted to the top of the sample holder that hooks into a constant force spring that can be selected to balance the weight of the sample holder almost entirely, allowing for the irradiation of relatively heavy samples that would exceed the limits of the positioning stages by a large margin. It was found that the heat production even for a sample holder and sample weight below the design limitations of the positioning stages lead to stuck (overheated) stages after 3 to 6 h of regular operation in vacuum, requiring a cooling break and ventilation of the target chamber to continue operations. So even for light samples it is recommended to use an appropriate constant force spring.

The sample holder is held in place on the positioning stages via four pins and a magnet. Additionally, the PTFE holding the pins in place on the positioning stages doubles as secondary mechanical stabilisation when the Faraday cup is mounted to the sample holder. This fit is so tight, that even after years of operation, no screws are required to mount the sample holder and it instead simply snaps into place, making the mounting process a lot more comfortable than any of the other discussed designs.

The material used for the sample holder is Aluminium. It was chosen since in contrast to stainless steel [208] or copper [132], Aluminium atoms do not noticeably diffuse through their native oxide barrier into Gallium Arsenide (or Silicon) samples and alter the doping [314]. A disadvantage of the material choice is the relatively low threshold for nuclear reactions with Protons. Several reactions above 3 MeV are documented [159, 117]. To

2. PBW facilities in Göttingen

rule out safety concerns, the frame was irradiated with a 3 MeV Proton beam (the largest Proton beam energy typically employed in Proton beam writing at MaRPel) with large current and the radiation dose escaping the chamber was measured. On the roof of the target chamber (closest to the target) a slight increase of radiation was noticeable (around twice the background) while everywhere else no relevant increase in radiation was observed.

A design requirement is to not deform permanently under forces of 40 N in any direction. Forces like that are estimated to occur in case the holder was accidentally dropped or bent by hand. This design requirement was achieved by iterative refinement and repeated FEM simulations of the design with Adobe Inventor [231] until the goal was achieved with a safety factor of 1.2. This safety factor should guarantee the mechanical stability of the sample holder even with material defects and with the tolerances typically encountered in production.

To make the sample holder easy to use in practice, the part of the Faraday cup mounted to it doubles as a stand, on which the sample holder can be safely set while the samples are inserted. The screws holding the sample holder together are all the same type and only 2 to 4 screws are required to be loosened to change all samples. 6 screws need to be removed at most to entirely disassemble the sample holder. Fig. 2.13 on the next page shows pictures of the sample holder as it is currently used at MaRPel.

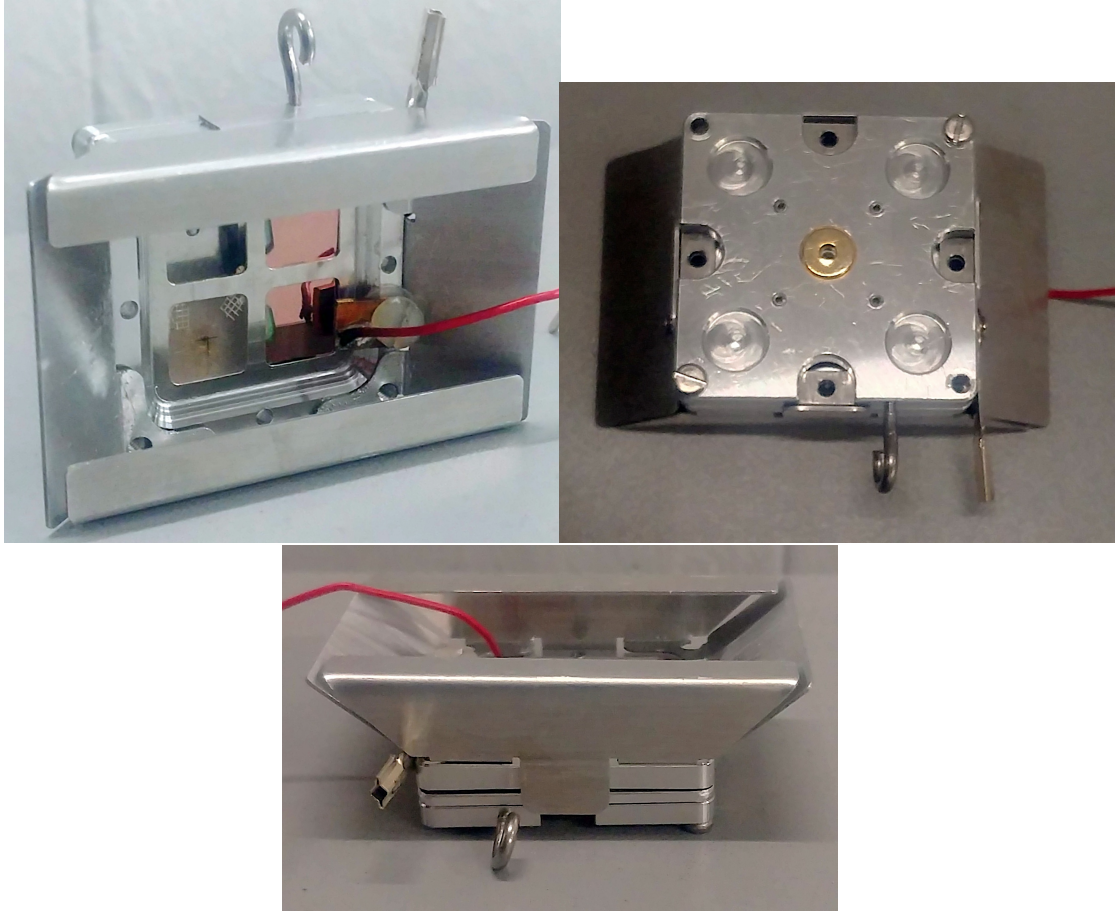


Figure 2.13.: Photographs of the sample holder at MaRPel, here shown with a scintillator (modified with painted on cross hairs and two mounted Nickel grids), two samples and an isolated Copper plate mounted above the sample surface. Note the hook on the top for attaching a constant force spring, the plug for attaching a cable for current measurements and a single mounted spacer frame.

2.7. Irradiation process

2.7.1. Beam size optimization

A first step in the irradiation process is the optimization of the Proton beam size on the target. The result of the optimization is a beam spot that is of roughly correct size and is measured more precisely afterwards (see sec. 2.7.2 on the following page). For this, three optimization steps are carried out one after another.

The first step is a rough optimization, where the lenses are individually aligned such that the beam passes them centrally and they are rotated to the same orientation. This is done by focusing the beam in the x - and y -direction with each lens individually and

2. PBW facilities in Göttingen

moving the lenses such that all of them focus on exactly the same point and their focusing planes are rotationally aligned. It should be noted that this focusing point should be as close to the center of the beam-line as possible, to ensure that the beam does not only pass through the center of the lenses, but also as close as possible orthogonally to the lens planes. A method of finding the beam-line center, if it is not known beforehand, is by the use of a very defocused beam that draws a shadow of the narrow beam pipe on the scintillator. In this first alignment step the lenses are often moved up to a fraction of a millimeter if they are not well aligned and only micrometers in the opposite case.

The rough optimization in Göttingen is performed with a new high definition microscope (described in sec. 2.5 on page 41) while observing the light emission of the Proton beam on a scintillator quartz. During this procedure the individual lens positions, rotations and the lens currents are adjusted as optimizable parameters.

Several optimizations to the lens system and current controls in Göttingen were carried out to make the procedure easier, faster and more precise (details in sec. 2.4 on page 35). Additionally to this, different tests were performed with different distances of the lenses to the target and an adjustable gap in the middle of the lenses. Fig. 2.8 on page 40 shows the achievable demagnification as a function of the distance of the lenses to the targets as an example.

It should be noted that below a spot size of about 50-200 μm the procedure described here becomes difficult and manually found settings have to be interpolated, requiring some skill. In Singapore the currents of the lens system are computer controllable and a least squares optimization of the beam size as measured with a different method (see sec. 2.7.2) is possible below this beam size. In particular, the Göttingen optimization scheme was also employed by the author of this work together with an automated lens current optimization scheme developed in Singapore to obtain the excellent beam spot size of $13 \times 32 \text{ nm}^2$ at the accelerator in Singapore [212].

2.7.2. Beam size measurement

In a second step the beam size is measured more precisely and if the shape and size of the beam spot on the target is found to be insufficient, optimization steps are repeated. While with the new microscope system it is possible to gauge the microscope image and measure the beam size directly from a single image, as discussed in sec. 2.7.1 on the previous page this only allows for precise measurements of the beam size down to 50-200 μm . As such, different alternative strategies for beam size measurements were investigated and compared. All of them involve scanning the Proton beam over an edge of some sort (one in the x -direction and one in the y -direction) and measuring the change of some emission or current. The following possibilities were investigated:

- measurement of the electrical current on an electrically isolated copper plate slightly above the target surface while moving the plate edge through the beam
- integration of the PIXE or RBS spectrum of Al while moving the Al frame of the target holder through the beam

2. PBW facilities in Göttingen

- integration of the PIXE or RBS spectrum of Ag while moving a dot of electrically conductive adhesive paint on the scintillator through the beam
- integration of the PIXE or RBS spectrum of Ni or Au while moving a surface mounted thin Ni or TEM Au grid through the beam
- counting of either back scattered or small angle scattered Protons or secondary Electrons while moving a thin, free standing Ni grid through the beam, using a PIN diode in the setup in Singapore [212]

Among the different measurement methods the microscopy measurements were the fastest and most reliable for beam spot sizes above $200\ \mu\text{m}$ while below $100\ \mu\text{m}$ PIXE and direct counting measurements on the nickel micro grid were most reliable. At low beam spot sizes an edge enhancement effect in the PIXE measurements and the direct counting measurements was observed occasionally. This is shown in fig. 2.14.

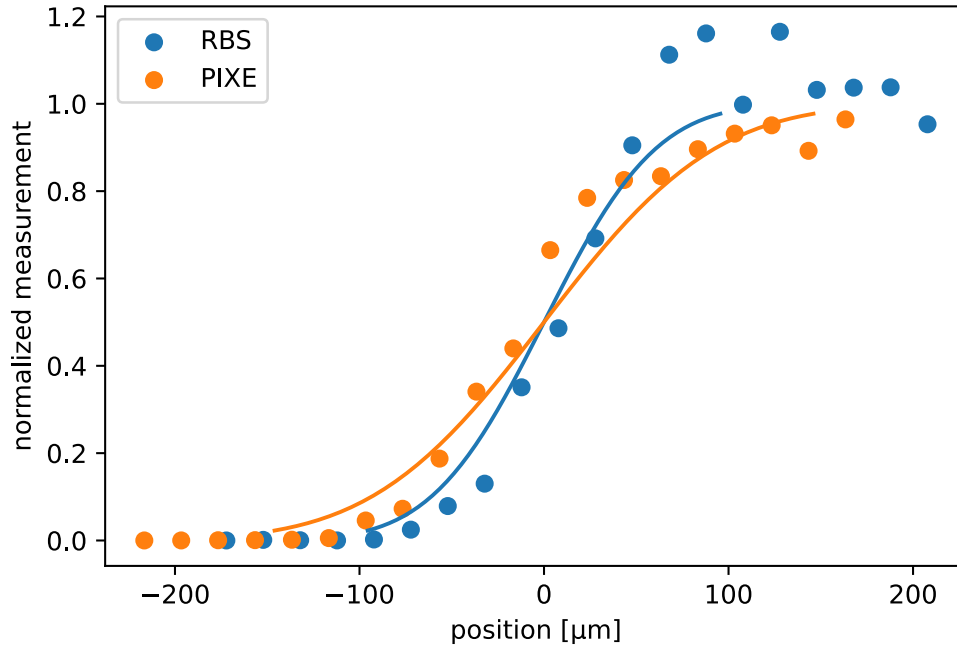


Figure 2.14.: Integrated x-ray intensity of the Nickel grid lines and the RBS spectrum of a Nickel edge on a GaAs sample as well a fit to these lines. Notable is the enhancement of the spectrum at the edge of the RBS signal.

Some of the measurements were partially automatized in the control software of the Göttingen or Singapore micro-beam-line. It should be noted that as these beam size measurements can take some time, changes in the beam current need to be accounted

2. PBW facilities in Göttingen

for. This is done by measuring the beam current in regular intervals and dividing the measured quantities by the interpolated beam current.

This experimental measurement is then followed by a fit. For small beam sizes it is found that assuming the beam intensity to be gaussian is a good approximation. As such the fit function is a convolution of the assumed gaussian beam profile with a step function (representing the edge). The beam size is then determined for the x - and y -direction independently as 2σ (where σ is the standard deviation of the least squares fitted gaussian).

This size measurement determined through this fit represents an upper bound (although a tight one) on the actual beam size. The main sources of error are small imperfections in the material edges the beam is scanned over, slight deviations from orthogonality of the beam incidence direction in comparison to the target surface and due to the positioning of the detectors slightly off the beam axis.

2.7.3. Irradiation plan

With the beam size on the target determined, an irradiation plan can be calculated. For this an irradiation pattern, that is to be irradiated on the target, is given and a plan to irradiate it as closely as possible to the pattern is determined. While the pattern determines by how much each point on the sample should be irradiated, the irradiation plan takes into account the beam shape and determines where the beam should irradiate the sample and for how long such that the root mean square discrepancy between plan and requested pattern is minimized, as well as the order in which these points should be irradiated such that the total required accelerator run time is minimized. The input of an algorithm for the calculation of an irradiation plan are therefore the requested 2D pattern and beam shape, in this case as an array of numbers. In a first step, the planned irradiation points and doses are determined and in a second step the path between them is optimized.

The simplest approach for generating an irradiation plan are points set on fixed patterns (rastering) or line scanning methods, however the overall performance of these approaches is often relatively poor. Several methods for improved beam scanning have been described in the literature [232], but for every fixed plan, there are always structures that cannot be efficiently irradiated by it. So in contrast to the system in Singapore, here a more flexible approach is developed that allows for the optimization of the irradiation plan.

In the following different deconvolution approaches for the two steps will be discussed and benchmarked in their performance on a set of test patterns, shown in fig. 2.15 on the next page. A small gaussian shaped beam spot (with $\sigma = 4$ pixels) will be considered for the irradiation.

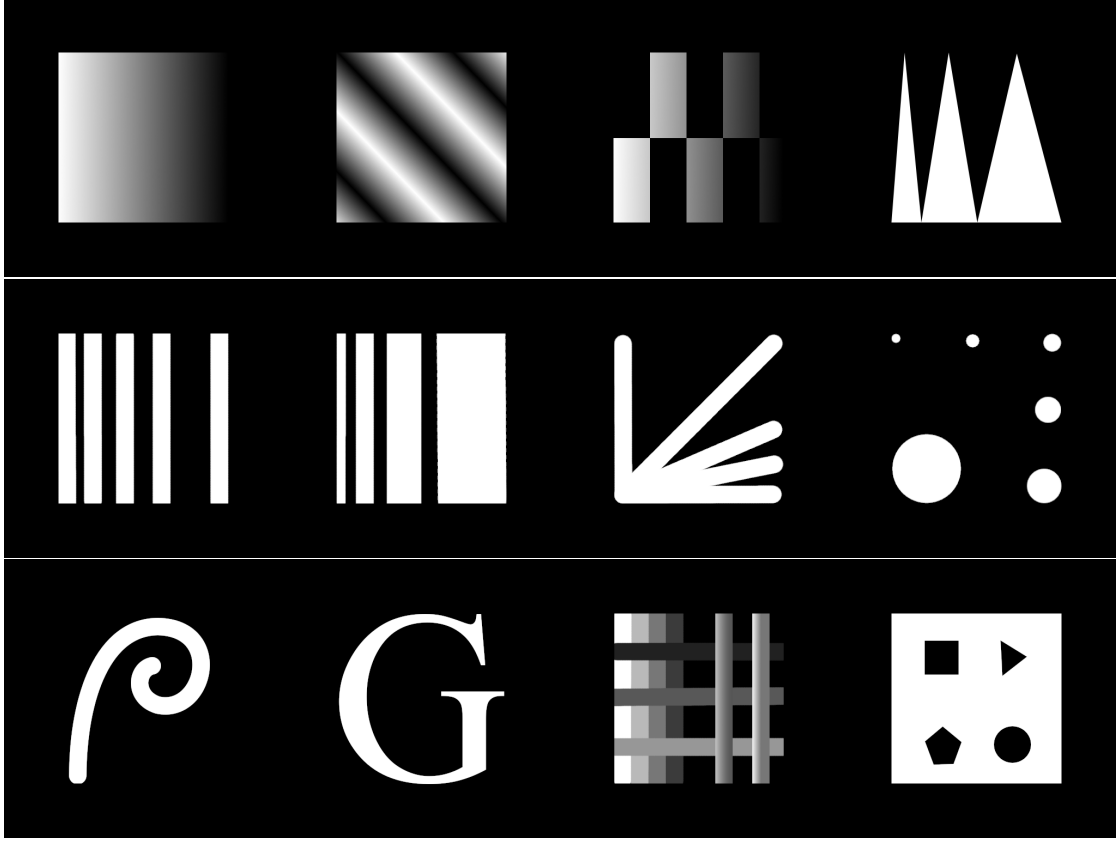


Figure 2.15.: Test patterns considered here for benchmarking irradiation planning algorithm performance. All patterns have a resolution of 512×512 with the brightness determining the local irradiation amount (white being maximal and black being no irradiation).

2.7.3.1. Optimization of irradiation points

If the beam spot were a point, the optimal irradiation plan would be given by a simple division of the input pattern by the beam current. The approximation is still relatively good for extended beams and used here as a starting guess. From then on, different iterative refinement strategies can be performed. Here the following deconvolution algorithms (deconvolution of the beam shape with the irradiation pattern) are considered:

- Van-Cittert deconvolution [50]
- Landweber deconvolution [129]
- Richardson-Lucy deconvolution [217]
- Poisson maximum a posteriori estimation deconvolution [306]

2. PBW facilities in Göttingen

After each iteration step, negative values in the irradiation plan are set to 0 (except for the Poisson maximum a posteriori estimate, where negative values are not possible by construction). By default, none of these algorithms converge, but under relaxation allows them to converge. The update procedures are therefore modified as follows:

$$\text{Plan}_{new} = (1 - \omega) \text{Plan}_{old} + \omega \text{Plan}_{predicted}$$

Optimal values of $\omega \approx 0.00025$ are found for this test, but in general, all these methods converge relatively slowly (with the best being less than 4% improvement per iteration for Landweber deconvolution) if they converge at all. As such, deconvolution methods are considered too slow for the optimization of the irradiation plan.

As an alternative, irradiation points are scattered over the target image and both their positions and fluences are optimized. The most successful approaches were found by local optimizations, where the optimal, local fluence and gradient of the positions are calculated and the points are updated iteratively. The optimizations based on this principle are described elsewhere [181, 104].

2.7.3.2. Beam time optimization

Given a list of points from sec. 2.7.3.1 on the preceding page, they need to be ordered such that beam time on the accelerator is minimized. This can be achieved by minimizing the path through all points such, that the total path length is minimized allowing the beam to spend as little time switched off / blanked as possible. Often the paths can even be so short that no blanking between some pairs of points is required at all.

As a side effect of this optimization, on systems where the sample is moved (like in Göttingen), the movement of the stages is minimized, thereby also reducing heat production in the movement stages, allowing them to run more reliably and for longer in the vacuum. On systems where the beam is steered with magnetic fields (like in Singapore, or in the old setup in Göttingen) the change in magnetic fields is minimized, thereby reducing the time required to change the magnetic fields to their target values.

The total path length is a simple sum of the distances of the irradiation points as they appear in the plan. The distance function is either the Manhattan distance (for the system in Göttingen) or the euclidean distance (for the system in Singapore). Optimization can be performed by reordering the points and with this the problem reduces to the classical “traveling salesman” problem with either arbitrary start and end points (for the system in Göttingen) or with the start and end points being the same (for the system in Singapore). Because of this, optimization strategies that work well for the traveling salesman problem are used here as well.

3. The irradiation process

The irradiation process describes the evolution of the target material under Proton irradiation. Generally it can be characterized by three separate processes:

- the slowing down (stopping) of the Protons and knock on target atoms and energy transfer from the projectile to the target atoms and Electrons
- the production of primary defects in the target material
- the evolution of these defects in the target material

In the following three sections these processes will be discussed and models for their simulation will be developed and compared to experimental data (where available) and literature models.

3.1. Stopping

3.1.1. General considerations

Stopping is the process of slowing down of projectiles in matter. It has been studied ever since the discovery of cathode rays by the end of the 19th century with some of the earliest theoretical models dating back to the beginning of the 20th century [226, 29]. In the case of Proton beam writing, the projectiles are fast Protons as well as target atoms and Electrons that were accelerated through collisions. As the projectiles pass through the target material, they can accelerate target atoms or transfer energy to the Electrons by excitation and ionization processes. These two processes usually occur simultaneously and approximately independently of each other. The nuclear stopping process (acceleration of target nuclei) can be described as the scattering of projectiles on effective target atomic potentials (for example the electronically screened Coulomb potentials of the target nuclei) while several approximations for the electronic stopping process (excitation and ionization of target nuclei) exist that can depend on the projectile velocity, charge and different target properties like the Electron density or mean excitation potential. At the projectile energies that are typically encountered in Proton beam writing, other stopping processes (like nuclear reactions or production of Bremsstrahlung in the target) can typically be neglected.

The stopping process is a statistical process where the mean energy loss of a projectile per length travelled (or stopping force) $-\langle \frac{dE}{dx} \rangle$ (with commonly used units eV/Å) is roughly proportional to the target mass density ρ_{target} . This allows for the definition of a mass stopping force $-\frac{1}{\rho_{target}} \langle \frac{dE}{dx} \rangle$ with the commonly used units $\frac{\text{MeV}\cdot\text{cm}^2}{\text{mg}}$. Often,

3. The irradiation process

alternatively the stopping cross section $-1.6605 \cdot A_{target} \cdot \frac{1}{\rho_{target}} \left\langle \frac{dE}{dx} \right\rangle$ is also used with units $10^{-15} \frac{\text{eVcm}^2}{\text{atom}}$ and target nucleon number A_{target} . As a symbol for the stopping related quantities S is commonly used in the literature for either the stopping force, mass stopping force or stopping cross section [247]. Here the same notation is used but special care is taken to denote which quantity is presented.

Fig. 3.1 shows the stopping force for Silicon atoms in Silicon as predicted by the empirical SRIM 2013 model [318] as a function of projectile speed and in comparison to the sound [155] and electronic orbital velocities (from the eigenvalues of an atomic Dirac-Hartree-Fock-Coulomb-Gaunt-Breit calculation with `pyscf` [267]). As visible, electronic stopping is most important when the projectile speeds are on the same order of magnitude as the electronic orbital velocities. Below this, nuclear stopping is important, while at the speeds of the sound velocities, stopping approaches zero. This allows for the definition of several energy regimes for stopping.

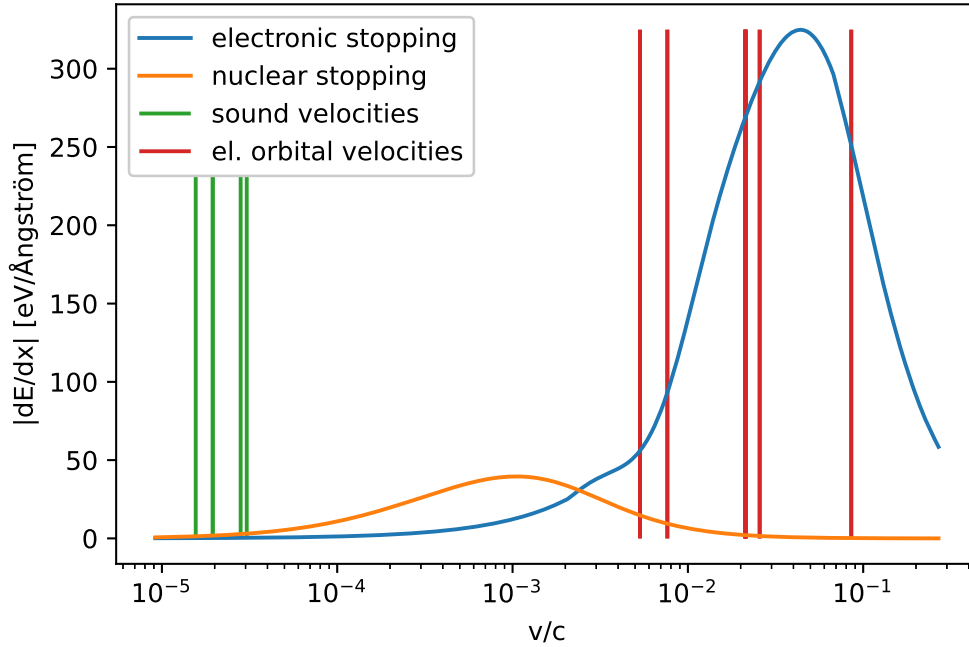


Figure 3.1.: Stopping force for Silicon atoms in solid Silicon as predicted by SRIM 2013 [318]. Also shown are the sound velocities [155] and electronic orbital velocities of Silicon.

The regime up to the slowest electronic orbital velocities is often called the low energy regime. Here often nuclear stopping is more important than electronic stopping. Electronic stopping often is roughly proportional to the projectile velocity in this regime, and behaves like a friction force [244, 169]. Some materials also show a threshold, below which likely no

3. The irradiation process

electronic stopping happens at all [149]. At the low end of this regime, multi-body effects become important in nuclear stopping while at the high energy end, nuclear stopping is well describable by the binary collision approximation. Projectiles tend to have little or no charge in this regime [311].

In the intermediate energy regime electronic stopping becomes most important. The maximum of the electronic stopping is in this regime due to the efficient excitation of target atoms as the projectile has similar velocities to the orbital velocities and the Fermi velocity of the target Electrons. The precise shape of the curve in this regime is difficult to predict theoretically and depends (among other things) on the orbital structure of the target [248]. Projectiles tends to be multiply ionized in this regime.

In the high energy regime the electronic stopping goes through a minimum and slowly rises again for very high projectile energies. In most targets the stopping power can be approximately described by only a few quantities in this regime. Among these are the mean excitation potential and the plasma frequency of the target Electrons [139]. At the high energy end of this regime relativistic effects and nuclear reactions become important.

The mass stopping force for different, relatively light projectiles in Silicon is shown in fig. 3.2 on the following page together with the predictions from SRIM 2013 [318]. As visible, for most projectiles and projectile energies in Silicon (and many other materials), electronic stopping is the dominant process, particularly at larger projectile kinetic energies. As the projectiles become heavier, nuclear stopping increases disproportionately to electronic stopping. Also shown is the experimental stopping of anti-Protons which continue the general trend.

3. The irradiation process

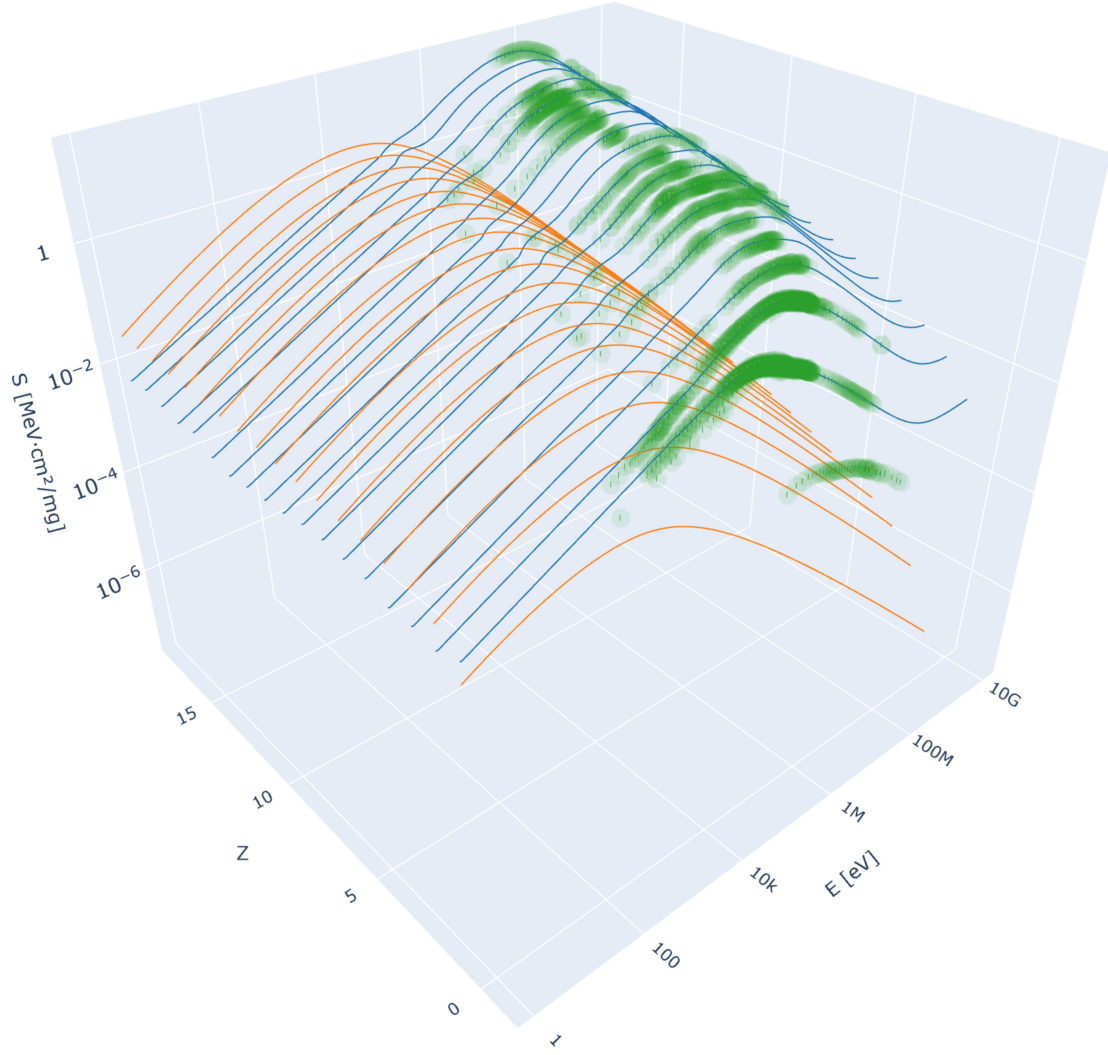


Figure 3.2.: Electronic stopping power (blue) and nuclear stopping power (orange) for different projectiles in Silicon as predicted by SRIM 2013 [318] in comparison to a compilation of experimental measurements (together with the reported uncertainties) [171] as a function of the projectile nuclear charge Z and kinetic energy E . Also shown are experimental data from anti-Proton stopping ($Z = -1$) [6, 168, 157, 170].

Concentrating on Protons, the mass stopping power for Protons for different materials is shown in fig. 3.3 on the next page. As visible, except for stopping in very low Z materials and at very low energies, the electronic stopping process is overall dominant. Everywhere else electronic stopping is several orders of magnitude larger in magnitude than nuclear stopping.

3. The irradiation process

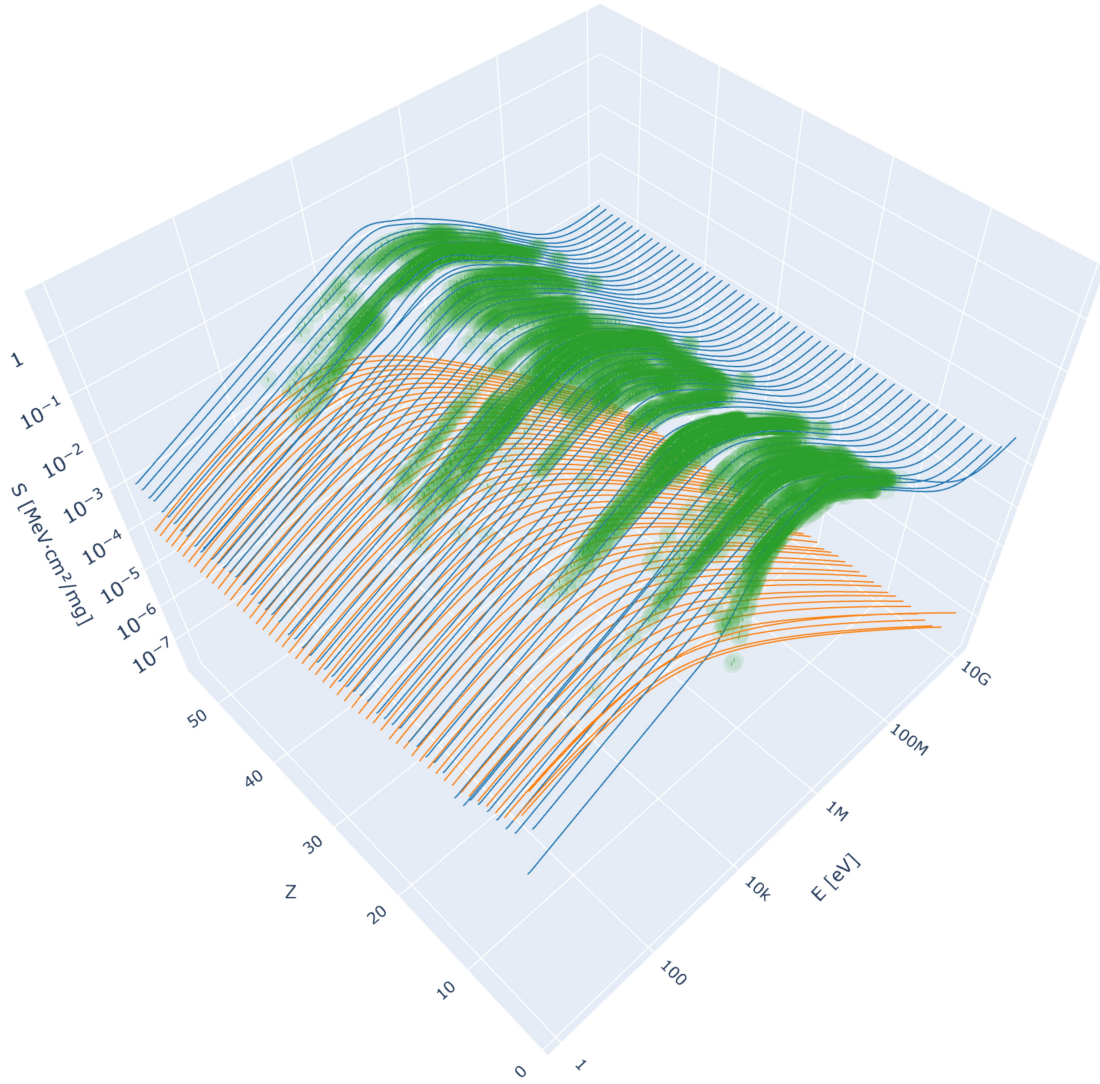


Figure 3.3.: Electronic stopping power (blue) and nuclear stopping power (orange) for Protons in different elemental materials as predicted by SRIM [318] in comparison to a compilation of experimental measurements (together with the reported uncertainties) [171] as a function of the target nuclear charge $Z \leq 54$ and projectile kinetic energy E .

It follows that the stopping process of keV to MeV energy Protons can often be understood as the electronic stopping of the projectile until the kinetic energy passes the electronic stopping maximum and the projectile deposits most of its remaining energy in a relatively small volume at the end of its range. Here most of the nuclear stopping occurs as well. Fig. 3.4 on page 59 shows the results of a stopping power calculation with SRIM 2013 [318] of 1 MeV Protons in Gallium Arsenide as an example of this behaviour. For non-elemental targets, like Gallium Arsenide, Bragg's rule can be applied where the

3. The irradiation process

total stopping power is estimated reasonably accurately from the atomic fractions ς_i of the components and their stopping powers $\langle \frac{dE}{dx} \rangle_i$ as $\langle \frac{dE}{dx} \rangle_{total} \approx \sum_i \varsigma_i \langle \frac{dE}{dx} \rangle_i$ [275]. Tab. 3.1 on page 60 shows how the energy of 1 MeV Protons, 42 MeV Silicon and 73 MeV Krypton (all with approximately the same maximum penetration depth) is distributed. The trends towards less electronic and more nuclear stopping for heavier projectiles is visible, as well as the production of more numerous but even more less energetic recoils (visible from the higher fraction of energy loss due to phonon generation of the recoils). Besides stopping, SRIM predicts that about 0.02 % of Protons are backscattered from the target, whereas none of the other projectiles out of 5000 were backscattered.

3. The irradiation process

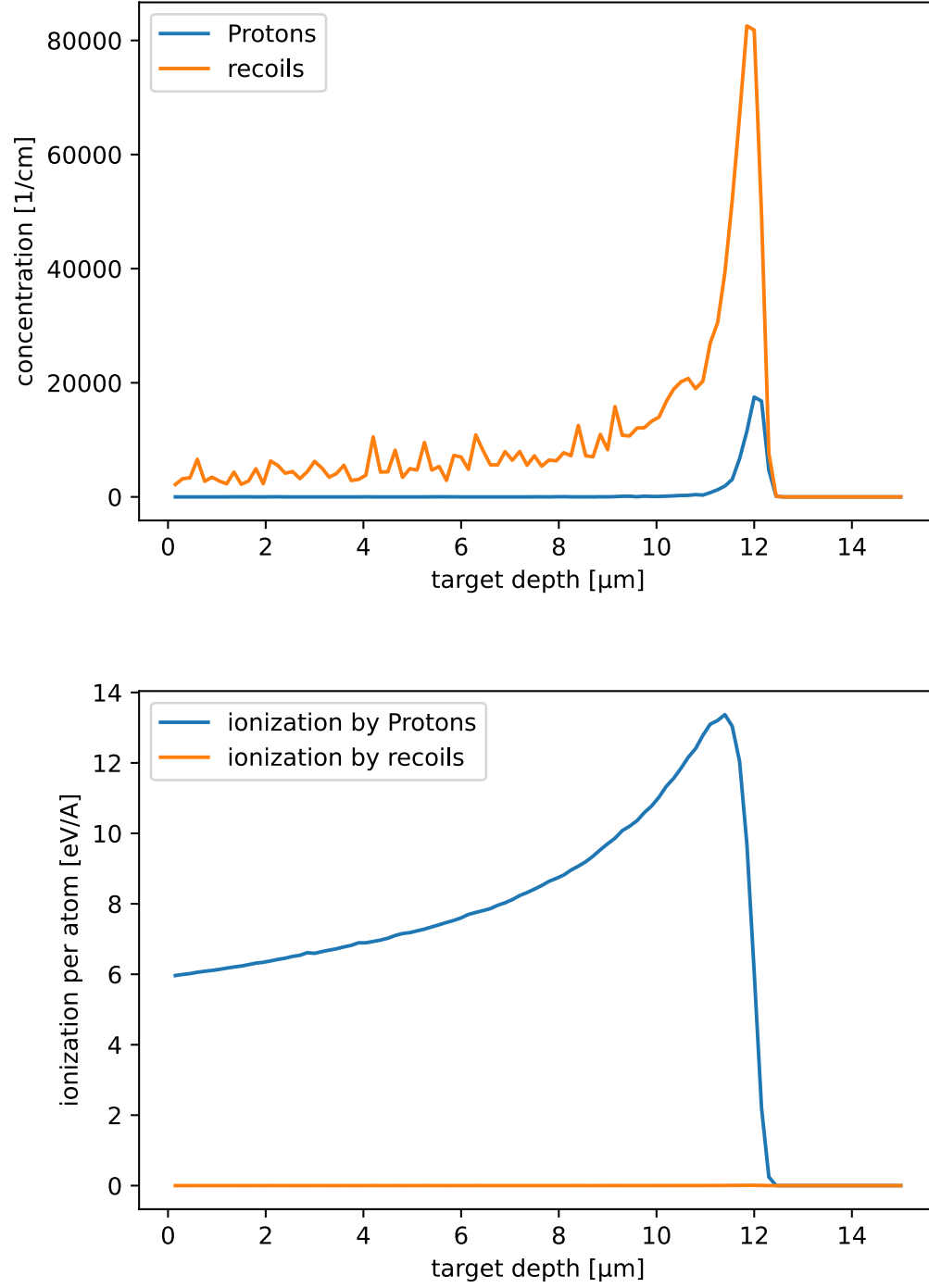


Figure 3.4.: Projectile and recoil distributions as well as distribution of ionization energy loss of 1 MeV Protons in Gallium Arsenide as a function of depth as simulated with SRIM 2013[318].

3. The irradiation process

energy loss process		projectile		
		1 MeV H	42 MeV Si	73 MeV Kr
projectiles	ionization	99.76 %	98.77 %	95.00 %
	vacancy generation	< 0.01 %	< 0.01 %	0.01 %
	phonon generation	0.07 %	0.03 %	0.04 %
recoils	ionization	0.02 %	0.30 %	1.64 %
	vacancy generation	0.01 %	0.07 %	0.26 %
	phonon generation	0.14 %	0.83 %	3.05 %

Table 3.1.: Distribution of energy losses for different projectiles at 0° impact angle in Gallium Arsenide as simulated with SRIM [318].

Sputtering is a side effect of ion beam irradiation and always occurs to some extent. It describes the phenomenon that some recoil atoms of the collision cascades in the target leave the target material. This effect is most pronounced for heavy projectiles in comparison to the target atoms and shallow irradiation angles. In Proton beam writing both of these conditions are usually not fulfilled and sputtering is negligible. In an irradiation run at the CIBA, I was nevertheless able to observe sputtering in Gallium Arsenide with a molecular Hydrogen beam at more than 1000 times the regular irradiation dose and likely aided by embrittlement and swelling of the affected target regions by Hydrogen implantation.

Besides backscattering of projectiles and sputtering, nuclear reactions can occur at high projectile energies. The kinetic energy at which nuclear reactions reach about 4% of the total Coulomb nuclear scattering (Rutherford) cross section can be estimated within 500 keV accuracy to about [34]:

$$E \approx \frac{M_1 + M_2}{M_2} \cdot \begin{cases} \frac{Z_2}{10} \text{ MeV} & Z_1 = 1 \\ \frac{Z_1 Z_2}{8} \text{ MeV} & Z_1 > 1 \end{cases}$$

This imposes a rough upper limit on the energy at which nuclear reactions can be neglected. For Proton beam writing this limit is plotted in fig. 3.5 on the following page.

3. The irradiation process

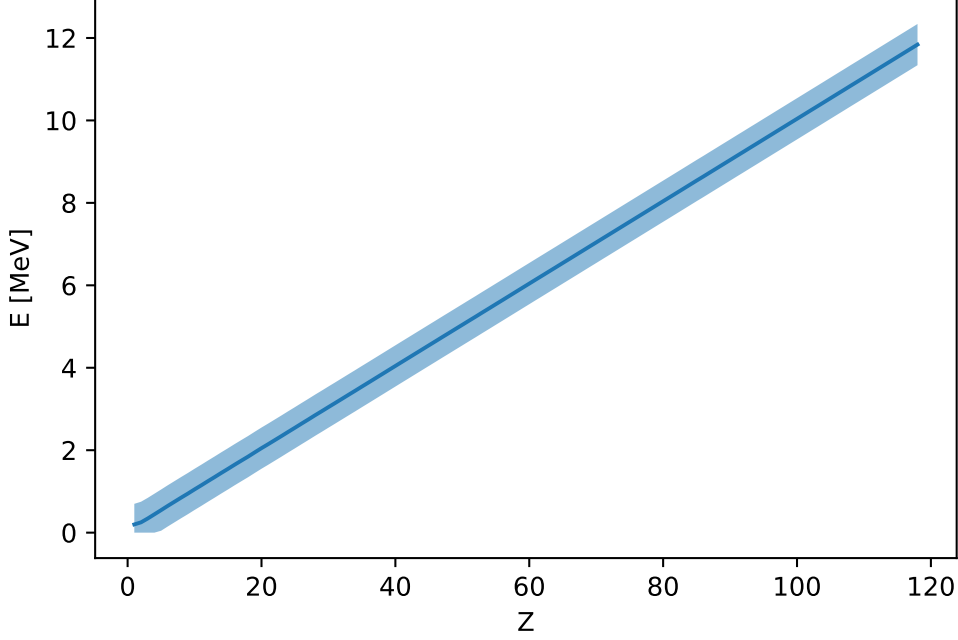


Figure 3.5.: Limiting energy at which nuclear reactions are expected to reach 4% of the Rutherford cross-section for Protons as a function of the nuclear charge of the target material Z .

From the mean stopping power $\langle \frac{dE}{dx} \rangle$ the range of a projectile with kinetic energy E can be calculated as:

$$R = - \int_0^E \frac{d\epsilon}{\langle \frac{dE}{dx} \rangle_\epsilon}$$

It should be noted, however, that scattering causes the projectiles to have non-straight paths. The longitudinally projected range (or penetration depth) of Protons for the typical energies used in Proton beam writing (between 100 keV and 5 MeV) can be well approximated by:

$$R \approx R_0 \cdot \left[\frac{E}{4.42 \text{ MeV}} + 4.52 \cdot \left(\frac{E}{4.42 \text{ MeV}} \right)^2 \right] \quad (3.1)$$

where R_0 is a target material dependent parameter with a value between 10^{-5} m and $2.5 \cdot 10^{-4}$ m. Fig. 3.6 on the next page shows the ranges of Protons in solids as simulated by SRIM [318] with 1000 projectiles per simulation and as fitted by eq. 3.1. For elements that are gaseous at room temperature (like Hydrogen or Nitrogen), solid state densities

3. The irradiation process

as estimated by SRIM were used to make them better comparable. In a gaseous state of the target the Proton ranges are several orders of magnitude larger (approximately $\frac{R_{gas}}{R_{solid}} \approx \frac{\rho_{solid}}{\rho_{gas}}$).

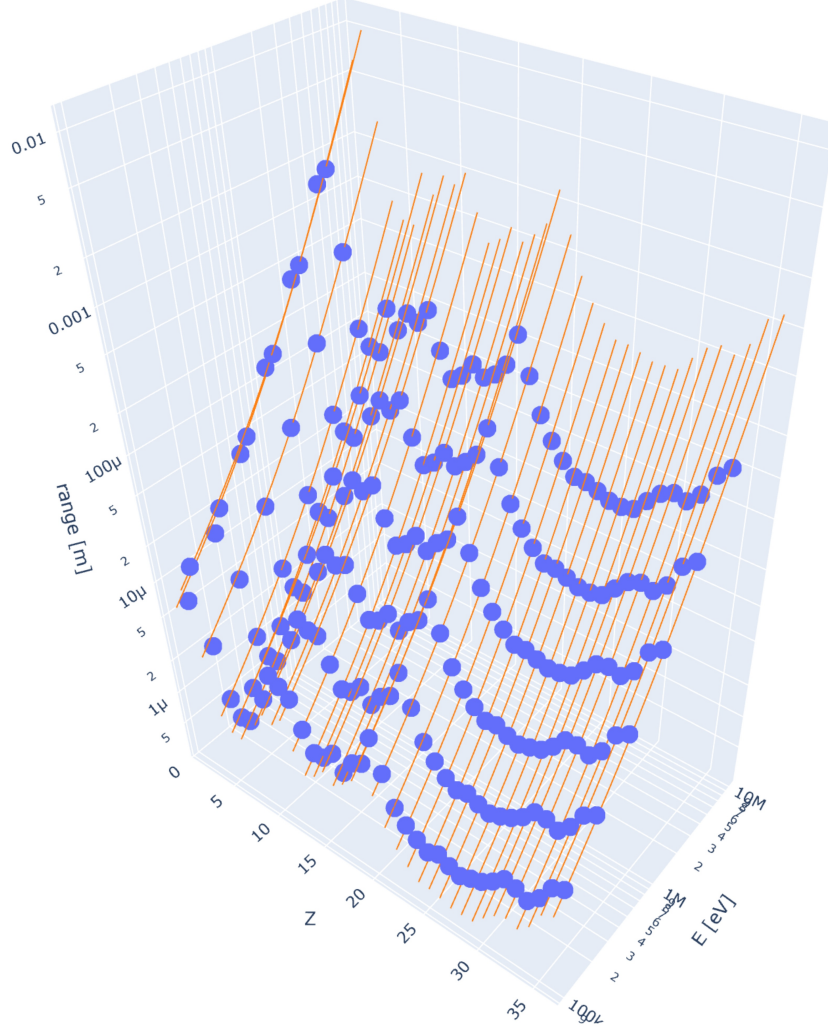


Figure 3.6.: Ranges of Protons in different solid targets as a function of the projectile energy for typical energies encountered in Proton beam writing as calculated with SRIM [318] and fit according to eq. 3.1 on the preceding page.

Since stopping is a statistical process, the spread of the depth at which Protons come to rest (called straggling and described by the standard deviation) is another important property. Fig. 3.7 on the next page shows the straggling of the penetration depth as a function of the penetration depth itself. The strong correlation between the two quantities shows that within a factor of two or so, straggling of Protons in a wide variety of materials can be estimated by $\sigma_R \approx 0.0135 (10) \cdot R + \sqrt{(4.20 (2) \cdot 10^{-9} \text{ m}) \cdot R}$.

3. The irradiation process

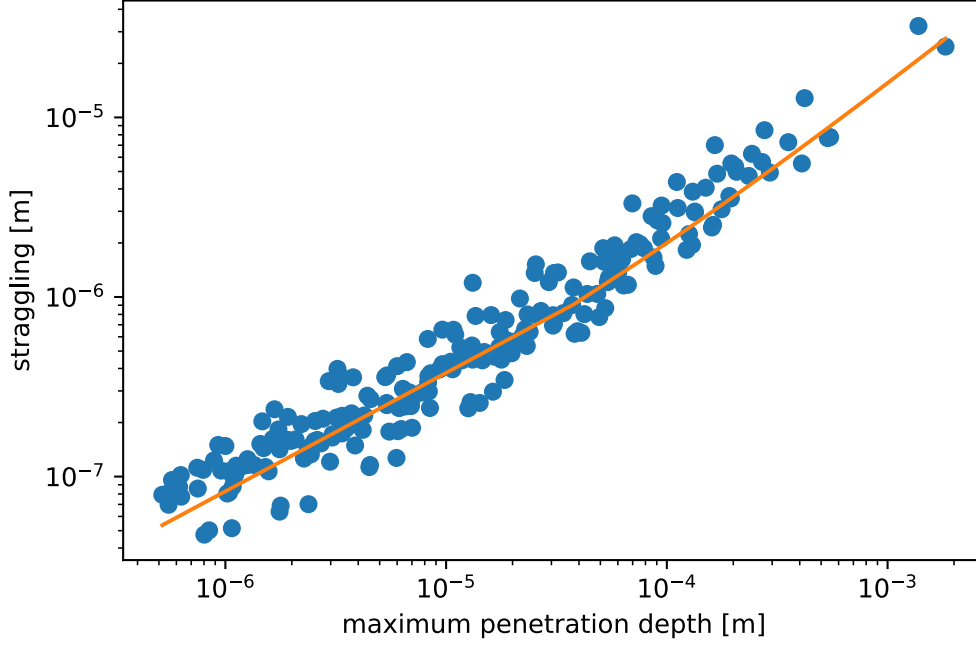


Figure 3.7.: Longitudinal straggling of Protons in different targets as simulated with SRIM [318] as a function of the laterally projected range (or penetration depth) and fit to this quantity.

Another interesting aspect of stopping is the impact of the target microstructure. It is known that materials show different mass stopping powers when they change phases, even though the mass stopping power is expected to be independent of the target density [276]. Additionally, even solid materials show different mass stopping behaviour depending on their crystal structure. For Proton beam writing, the most important effect among these is channelling. This describes an effect where the projectiles are channelled on their path through the target by the lattice structure of a crystalline material and show unexpectedly long ranges in the target material. Channeling requires an alignment of the beam with a crystal axis and a reasonably defect free material (as defects dechannel Protons quite easily) even though for most semiconductor crystals channeling always occurs to some small extent [242, 106]. Fig. 3.8 on the following page shows the final positions of a stopping simulation of 1 MeV Protons in Silicon for an $\langle 100 \rangle$ oriented perfect crystal (without defects but with estimated thermal vibrations at room temperature) and an amorphous target of the same density. A line of Protons that were channelled is visible.

3. The irradiation process

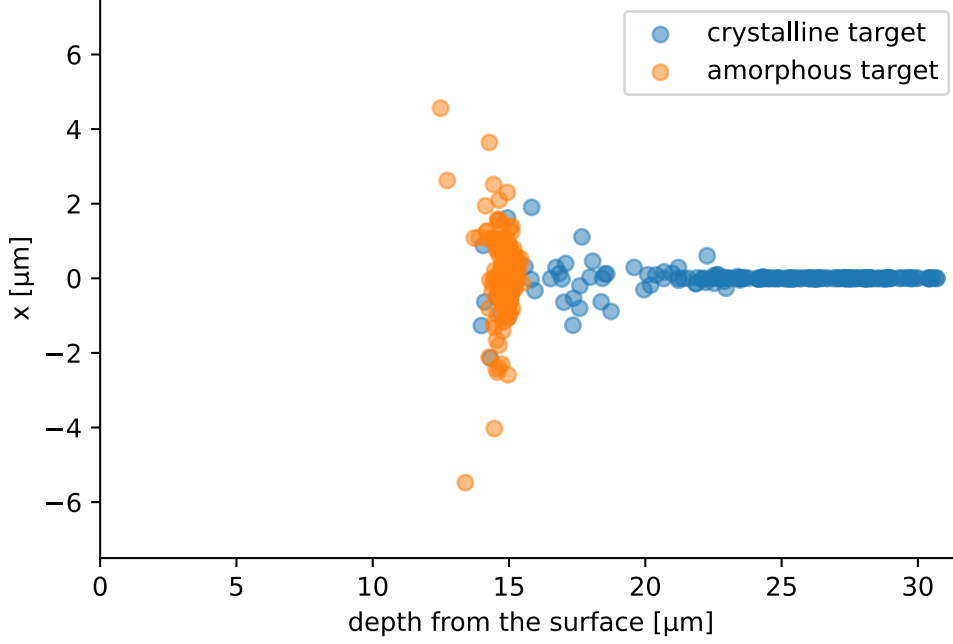


Figure 3.8.: Distribution of final positions of 200, 1 MeV Protons in Silicon for a $\langle 100 \rangle$ oriented perfect crystal and an amorphous target of the same density. In the crystalline target channeling of the projectiles is visible.

3.1.2. Nuclear stopping

Nuclear stopping can, over a wide projectile energy range, be described well in the binary collision approximation, where the interaction between the target nuclei and the projectile is described by an effective pair potential. Based on this and earlier approximations, Ziegler proposed a simple approximation for the total nuclear stopping cross section in $10^{-15} \frac{\text{eVcm}^2}{\text{atom}}$ [316]:

$$S_{nucl.} \approx \sqrt{\frac{8.462 \cdot Z_1 Z_2 M_2}{(M_1 + M_2) (Z_1^{2/3} + Z_2^{2/3})}} \cdot \begin{cases} 1.593 \epsilon^{1/2} & \epsilon < 0.01 \\ 1.7 \epsilon^{1/2} \frac{\log[\epsilon + \exp(1)]}{1 + 6.8\epsilon + 3.4\epsilon^{3/2}} & 0.01 \leq \epsilon \leq 10 \\ \frac{1}{2\epsilon} \log(0.47\epsilon) & \epsilon > 10 \end{cases}$$

with the reduced projectile kinetic energy

$$\epsilon = \frac{\frac{32.53}{\text{keV}} M_2 E}{Z_1 Z_2 (M_1 + M_2) \sqrt{Z_1^{2/3} + Z_2^{2/3}}}$$

3. The irradiation process

where Z_1 (Z_2) are the nuclear charges of the projectile (target atom) and M_1 (M_2) their masses. A slightly more accurate expression was recently determined through fits of direct simulations of pair potential scattering [320]:

$$S_{nucl.} \approx \sqrt{\frac{8.462 \cdot Z_1 Z_2 M_2}{(M_2 + M_2) \left(Z_1^{2/3} + Z_2^{2/3} \right)}} \cdot \frac{\log(1 + 1.1383\epsilon)}{2(\epsilon + 0.01321\epsilon^{0.21226} + 0.19593\epsilon^{0.5})}$$

More precise calculations are possible when solving the equations of motion of the projectiles explicitly with approximate pair potentials [320]. Many potentials exist, that are calculated through either Thomas-Fermi theory, Kohn-Sham density functional theory with local density approximations or Hartree-Fock theory simulations [61]. Though these potentials commonly assume that the Electrons are in their lowest energy state, which may not always be accurate. It should also be noted that while the binary collision approximation is very accurate at high collision energies, at low collision energies multibody effects become important [219].

When considering the shapes of the potentials, one can consider the two extreme cases:

- the high velocity limit, where the projectile is entirely ionized and the target Electrons are essentially static with respect to the projectile
- the low velocity limit, where the projectile is almost neutral and the collision happens so slowly that all Electrons can relax into the ground state

In the following both cases are discussed separately and compared.

3.1.2.1. High velocity limit

In the high velocity limit, the effective binary potential should be the total Coulomb potential of the electronically screened target atoms in their ground state and the entirely ionized projectile. These potentials are calculated here using the decontracted HGBS-9 basis set in *Orca* with density functional theory (r2SCAN functional and for $Z > 36$) and relaxed MP2 densities (for $Z \leq 36$). The resulting radial screening functions $\phi(R)$ that screen the nuclear potential to the total electrostatic potential $V(R) = \frac{Z}{R}\phi(R)$ for all atoms that converged well are shown in fig. 3.9 on the next page.

3. The irradiation process

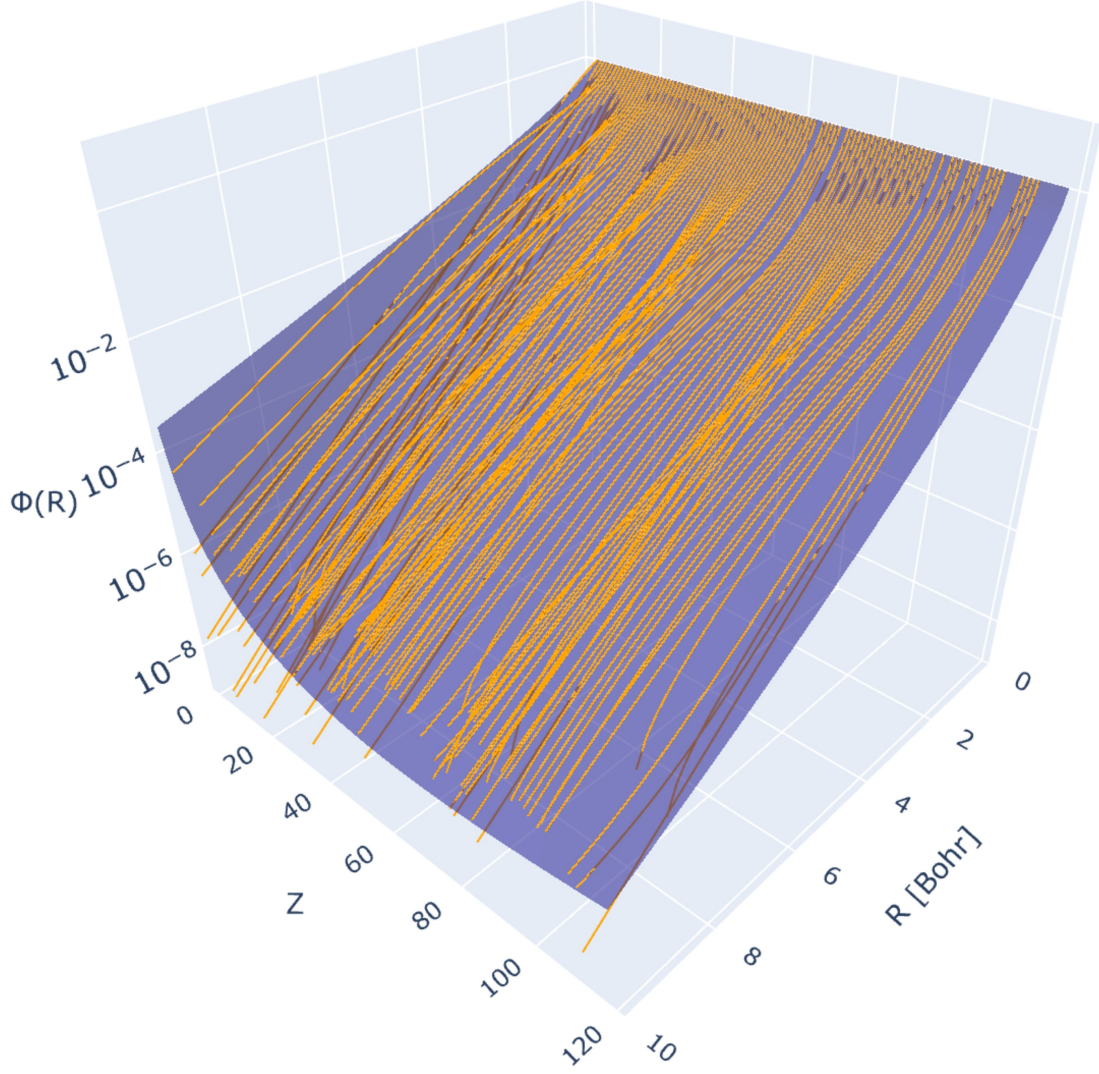


Figure 3.9.: Radial screening functions for the Coulomb potentials of the neutral atoms of the periodic table as a function of the distance R to the nucleus as predicted from density functional theory and relaxed MP2 theory calculations. Also shown is a fit of shape $\exp\left(-\left(\frac{R}{a_0 Z^{n_Z}}\right)^{n_{R,0}+Z \cdot n_{R,1}}\right)$.

As visible, the screening functions show an approximately exponential decay with R . Besides the shell effects, a trend of decreased screening lengths (the length scale on which the nuclear charge is screened) with Z can be observed. This trend is already predicted by simple atomic models, like the Thomas-Fermi model, where it scales like $Z^{-1/3}$ [272, 66]. Here a fit of a screening function $\exp\left(-\left(\frac{R}{a(Z)}\right)^{n_{R,0}+Z \cdot n_{R,1}}\right)$ with $a(Z) = a_0 Z^{n_Z}$ is performed. For this the potentials were sampled on an exponential grid. The best fit

3. The irradiation process

is observed for $a_0 = 0.85$ Bohr and $n_Z = -0.28$. Similar values for n_Z are assumed by Ziegler [317] with $n_Z = -0.23$ and Nakagawa [175] with $n_Z \approx -0.205$. An approximate screening length for each atom can also be extracted. This is shown in fig. 3.10 together with some of the other predictions.

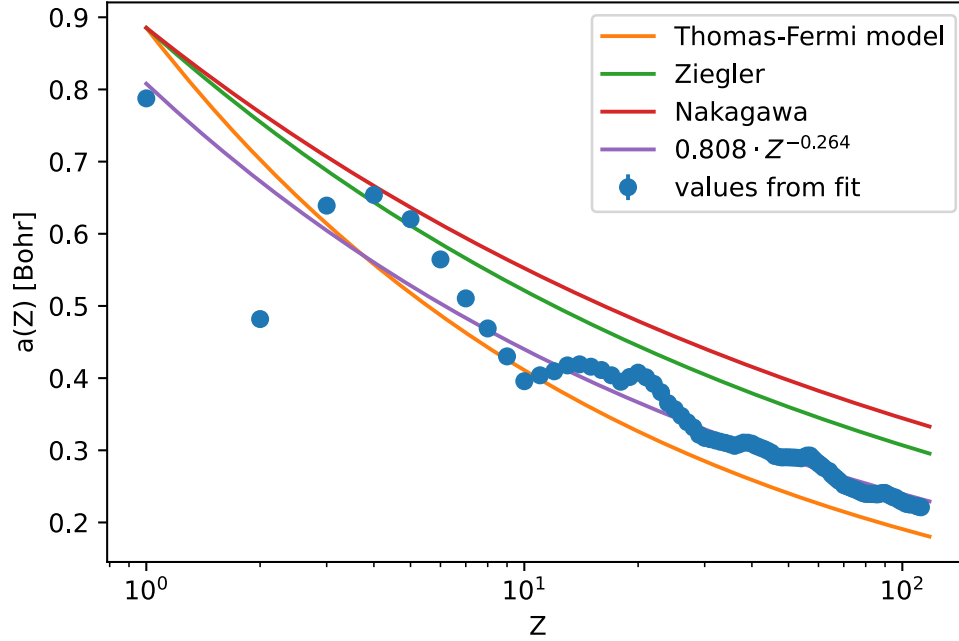


Figure 3.10.: Screening lengths of the nuclear potentials by the Electrons as a function of the nuclear charge Z and as predicted from a fit of the function $\exp\left(-\left(\frac{R}{a(Z)}\right)^{n_R(Z)}\right)$, by Thomas-Fermi theory and as assumed by Ziegler's and Nakagawa's models.

Tab. 3.2 on the next page shows the best fits for screening functions of type $\phi(R) = \exp\left(-\left(\frac{R}{a(Z)}\right)^{n_R(Z)}\right)$ to the atomic potentials.

3. The irradiation process

Z	a [Bohr]	n_R	Z	a [Bohr]	n_R	Z	a [Bohr]	n_R
1	0.7876	1.1158	39	0.3105	0.7766	79	0.2403	0.7841
2	0.4818	1.0891	40	0.3092	0.7748	80	0.2398	0.7823
3	0.6390	0.7797	41	0.3061	0.7770	81	0.2397	0.7789
4	0.6538	0.7683	42	0.3040	0.7772	82	0.2396	0.7759
5	0.6203	0.7908	43	0.3019	0.7773	83	0.2394	0.7731
6	0.5645	0.8233	44	0.2994	0.7783	84	0.2393	0.7702
7	0.5105	0.8538	45	0.2968	0.7799	85	0.2392	0.7677
8	0.4688	0.8753	46	0.2921	0.7859	86	0.2390	0.7654
9	0.4301	0.8959	47	0.2910	0.7839	87	0.2397	0.7602
10	0.3958	0.9144	48	0.2902	0.7816	88	0.2405	0.7553
11	0.4039	0.8657	49	0.2903	0.7769	89	0.2409	0.7516
12	0.4095	0.8326	50	0.2902	0.7731	90	0.2409	0.7490
13	0.4176	0.8030	51	0.2900	0.7700	91	0.2395	0.7503
14	0.4191	0.7896	52	0.2898	0.7669	92	0.2382	0.7516
15	0.4158	0.7856	53	0.2895	0.7646	93	0.2370	0.7523
16	0.4112	0.7845	54	0.2889	0.7627	94	0.2358	0.7530
17	0.4039	0.7877	55	0.2909	0.7552	95	0.2347	0.7536
18	0.3950	0.7934	56	0.2927	0.7483	96	0.2344	0.7519
19	0.4016	0.7752	57	0.2927	0.7459	97	0.2328	0.7538
20	0.4076	0.7607	58	0.2887	0.7504	98	0.2313	0.7556
21	0.4011	0.7643	59	0.2848	0.7551	99	0.2300	0.7566
22	0.3920	0.7710	60	0.2817	0.7580	100	0.2288	0.7575
23	0.3805	0.7811	61	0.2788	0.7606	101	0.2275	0.7586
24	0.3653	0.7975	62	0.2756	0.7640	102	0.2262	0.7597
25	0.3569	0.8031	63	0.2734	0.7651	103	0.2258	0.7582
26	0.3477	0.8104	64	0.2713	0.7663	104	0.2253	0.7570
27	0.3389	0.8170	65	0.2666	0.7727	105	0.2248	0.7560
28	0.3316	0.8211	66	0.2636	0.7757	106	0.2243	0.7551
29	0.3216	0.8307	67	0.2606	0.7786	107	0.2238	0.7543
30	0.3172	0.8295	68	0.2577	0.7816	108	0.2233	0.7534
31	0.3155	0.8228	69	0.2548	0.7844	109	0.2228	0.7525
32	0.3137	0.8174	70	0.2519	0.7873	110	0.2222	0.7519
33	0.3119	0.8130	71	0.2506	0.7862	111	0.2216	0.7514
34	0.3103	0.8087	72	0.2494	0.7852	112	0.2210	0.7509
35	0.3084	0.8058	73	0.2482	0.7845	113	0.2210	0.7500
36	0.3062	0.8040	74	0.2468	0.7844	114	0.2205	0.7500
37	0.3082	0.7926	75	0.2458	0.7833	115	0.2200	0.7500
38	0.3107	0.7813	76	0.2445	0.7831	116	0.2195	0.7500
			77	0.2431	0.7836	117	0.2190	0.7500
			78	0.2416	0.7841	118	0.2185	0.7500

Table 3.2.: Best fit values for screening functions $\phi(R) = \exp\left(-\left(\frac{R}{a(Z)}\right)^{n_R(Z)}\right)$ for the elements. Values in blue were inter- or extrapolated. The relative fit accuracy of the values is approximately 1/1000.

3. The irradiation process

It should be noted, that the effective screening functions should also depend on (in descending order of effect magnitude at room temperature):

- the (partial) atomic charge of the atom
- chemical bonds to neighbor atoms
- polarization effects due to electric fields at the position of the atom
- Electron temperature and degree of excitation

Heavier atoms are expected to show less changes in their screening functions as mostly the valence Electrons are affected and these contribute less to the total screening function in them. Of the discussed effects for light atoms, the partial atomic charge is the most important effect, as it alters the long range behaviour of the screened nuclear potential. Experimentally, the influence of the charge state of the target atoms is most easily visible in rainbow scattering experiments (a type of low energy scattering at shallow angles to the target surface) [247]. A simple approximation for the charge dependent screening function is proposed here:

$$\phi(R, q) = (1 - q/Z) \cdot \exp \left(- \left(\frac{R}{(1 - q/Z) \cdot a(Z)} \right)^{n_R(Z)} \right) + q/Z$$

A similar scaling of the screening length $a(Z)$ with the charge state of the atom q was proposed by Sigmund [245] and found here to be reasonably accurate. As simple example of this charge dependence of the screening function is shown in fig. 3.11 on the following page for the case of a Carbon atom in various charge states where it is presented together with the proposed screening function.

3. The irradiation process

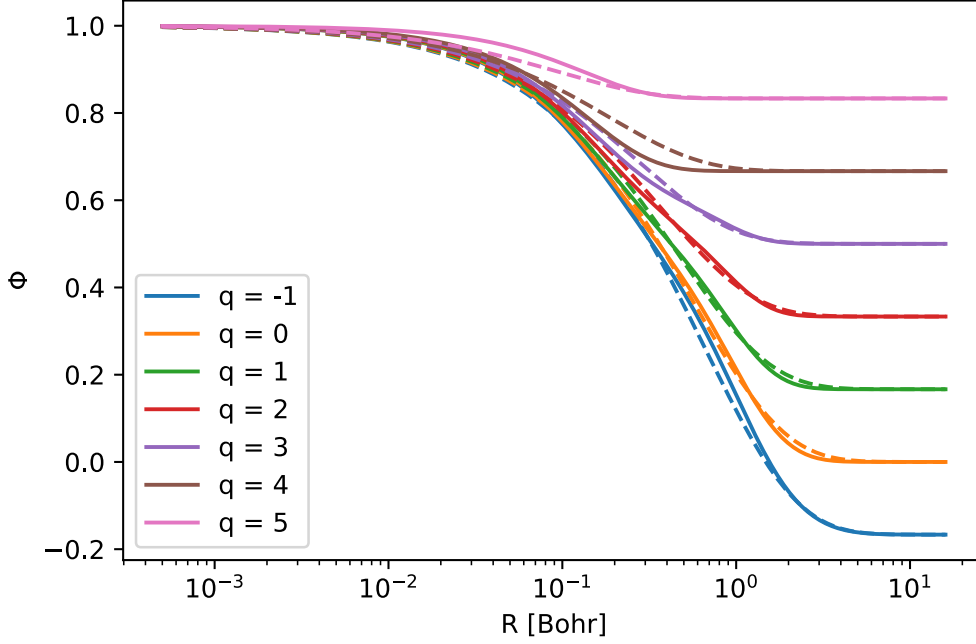


Figure 3.11.: Effective screening function ϕ to the Coulomb potential of the nucleus of Carbon as a function of distance from the nucleus for different charge states q of the atom as determined from relaxed MP2 densities (solid lines) as well as the approximation proposed here (dashed lines).

If a charge dependent screening function is to be used in a simulation, approximations to atomic charges need to be determined. These can be calculated from charge equilibration schemes [215], though in this work Hishfeld charges [97, 230] from DFT simulations of the target materials were used where applicable.

3.1.2.2. Low velocity limit

In the low velocity limit, the potential should be the Born-Oppenheimer potential of the (almost) neutral projectile and target. To approximate the low energy limit, the potentials of the atoms of the periodic table up to $Z_{\text{projectile}} + Z_{\text{target}} = 55$ are considered at nuclear distances between 0.1 and 2.0 Bohr with both atoms in a neutral ground state with `pyscf` using the decontracted ANO-R [321] basis set and the long range corrected VV10 exchange-correlation functional [289].

At these relatively short distances, multi-body effects should be negligible and as discussed in sec. 3.1.3.2 on page 77 at very low velocities, projectiles tend to be neutral. The multiplicities of the pseudo-molecules are determined from comparative calculations (the alternative would be spin relaxation, however in the calculations here it was found that the implementation in `pyscf` does not always relax to the correct ground state).

3. The irradiation process

For the longer range part of the potentials, the potentials of all projectiles $Z_{projectile} = 1...10, 18, 36, 86$ with the noble gases $Z_{target} = 2, 10, 18, 36, 86$ between 2.1 and 8.0 Bohr are added.

A special case is the collision of atoms with Hydrogen. Hydrogen forms relatively short bonds (1.4 Bohr in H_2 [100], noticeably shorter than the 2.0 Bohr cutoff used here) and the sole 1s Electron is involved in bonding, causing Hydrogen atoms bound in a compound in a collision to behave likely very differently than collisions with atomic Hydrogen. Because of this, the interatomic potentials of a projectile with Hydrogen are calculated by taking the average potential of a collision of the projectile with a Hydrogen molecule and a collision of an Hydrogen atom with the projectile. The geometry of the collision of a projectile with Hydrogen is shown in fig. 3.12.

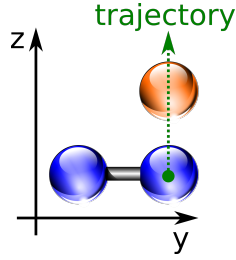


Figure 3.12.: Collision geometry of a projectile with an Hydrogen molecule used in this work. Hydrogen atoms are shown in blue, the projectile in orange and the trajectory for the potential calculation is shown in green.

A common approximation to the interatomic potentials is:

$$V(Z_1, Z_2, R) \approx \frac{Z_1 Z_2}{R} \phi\left(\frac{R}{a(Z_1, Z_2)}\right)$$

where $\phi(x)$ is a screening function with the limits 1 for $x \rightarrow 0$ and 0 for $x \rightarrow \infty$. This causes the nuclei to scatter according to their almost unscreened nuclear Coulomb potentials for short range (high energy) collisions while accounting for electronic screening at long ranges. Tab. 3.3 on the next page shows some common approximations for the screening function $\phi(x)$. Many different approximations have been used in the past to determine this function. Bohr used a simplified atomic model, Moliere used an analytical approximation to the Thomas Fermi atomic potential, Wilson et al. [302] and Ziegler et al. [317] used a free Electron gas interaction model with non-relativistic Hartree Fock Slater Electron densities. Some more recent approaches are mentioned in a publication by Nordlund et al. [184].

3. The irradiation process

name	$\phi(x)$
Bohr [30]	$\exp(-x)$
Moliere [166]	$0.35 \exp(-0.3x) + 0.55 \exp(-1.2x) + 0.10 \exp(-6.0x)$
Wilson, Haggmark, and Biersack [302]	$0.190945 \exp(-0.278544x) + 0.473674 \exp(-0.637174x)$ $+ 0.335381 \exp(-1.919249x)$
Ziegler, Littmark, and Biersack [317]	$0.02817 \exp(-0.20162x) + 0.28022 \exp(-0.4029x)$ $+ 0.50986 \exp(-0.94229x) + 0.18175 \exp(-3.19980x)$

Table 3.3.: Common approximations for the screening function $\phi(x)$ used in nuclear stopping.

3. The irradiation process

$a(Z_1, Z_2)$ is the effective screening length of the collision, typically with one of the forms shown in tab. 3.4. The early screening length models are based on the scale of the Thomas-Fermi atom that has the effective length scale $a(Z) = \left(\frac{9\pi^2}{128Z}\right)^{1/3}$ Bohr, while more modern models are based on fits to experimental data or ab initio theoretical calculations.

name	$a(Z_1, Z_2)$ [Bohr]
Firsov [71]	$\frac{a_0}{(Z_1^{1/2} + Z_2^{1/2})^{2/3}}$
Lindhard [137]	$\frac{a_0}{(Z_1^{2/3} + Z_2^{2/3})^{1/2}}$
Ziegler [317]	$\frac{a_0}{Z_1^{0.23} + Z_2^{0.23}}$
Nakagawa [175]	$\frac{a_0}{(Z_1^{0.307} + Z_2^{0.307})^{2/3}}$
O'Connor, Biersack [186]	$a_0 \frac{0.045(\sqrt{Z_1} + \sqrt{Z_2}) + 0.54}{(Z_1^{1/2} + Z_2^{1/2})^{2/3}}$
Zinoviev [319]	$0.0215 \frac{(Z_1 + Z_2)^{2.432} - Z_1^{2.432} - Z_2^{2.432}}{Z_1 Z_2}$

Table 3.4.: Effective screening lengths of interatomic collisions for nuclear stopping potentials with $a_0 = \left(\frac{9\pi^2}{128}\right)^{1/3}$.

The combinations of the different screening functions with the calculated screening functions are shown in tab. 3.5 on the next page. The combination with the overall lowest root mean square deviation is found to be the Ziegler, Littmark, and Biersack [317] potential and screening length. This combination also performs well for interatomic distances of less than 2 Bohr. For distances of greater than 2 Bohr the Wilson, Haggmark, and Biersack [302] potential with the O'Connor, Biersack [186] screening length performs slightly better.

3. The irradiation process

	Firsov [71]	Lindhard [137]	Ziegler [317]
Bohr [30]	0.0637	0.0504	0.0553
	0.0041	0.0039	0.0043
	0.0567	0.0448	0.0493
Moliere [166]	0.0202	0.0299	0.0254
	0.0072	0.0101	0.0059
	0.0183	0.0270	0.0227
Wilson et al. [302]	0.0142	0.0282	0.0219
	0.0048	0.0072	0.0035
	0.0129	0.0253	0.0195
Ziegler et al. [317]	0.0170	0.0132	0.0114
	0.0030	0.0046	0.0019
	0.0151	0.0119	0.0102
	Nakagawa [175]	O'Connor [186]	Zinoviev [319]
Bohr [30]	0.0319	0.0795	0.0750
	0.0038	0.0045	0.0044
	0.0284	0.0708	0.0668
Moliere [166]	0.0725	0.0253	0.0664
	0.0148	0.0019	0.0131
	0.0649	0.0225	0.0593
Wilson et al. [302]	0.0760	0.0194	0.0675
	0.0106	0.0016	0.0101
	0.0677	0.0173	0.0602
Ziegler et al. [317]	0.0541	0.0338	0.0604
	0.0069	0.0021	0.0076
	0.0482	0.0301	0.0538

Table 3.5.: Root mean square deviations of the different combinations of screening functions and screening lengths from the calculated DFT screening functions of this work. For each combination of screening function and screening length, the root mean square deviation for all distances $R \leq 2$ Bohr, $R > 2$ Bohr and overall are shown from top to bottom. The lowest value in each category is shown in **bold**.

A comparison of the resulting potentials with one of the best approximations is shown in fig. 3.13 on the following page. As visible, for very short ranges, the screening function is relatively well approximated. At longer distances (and thereby lower energies) however, individual pair potentials or low energy / long range corrections should be used to describe the scattering. In general, the interatomic potential also is too repulsive at distances beyond about 5 Bohr.

3. The irradiation process

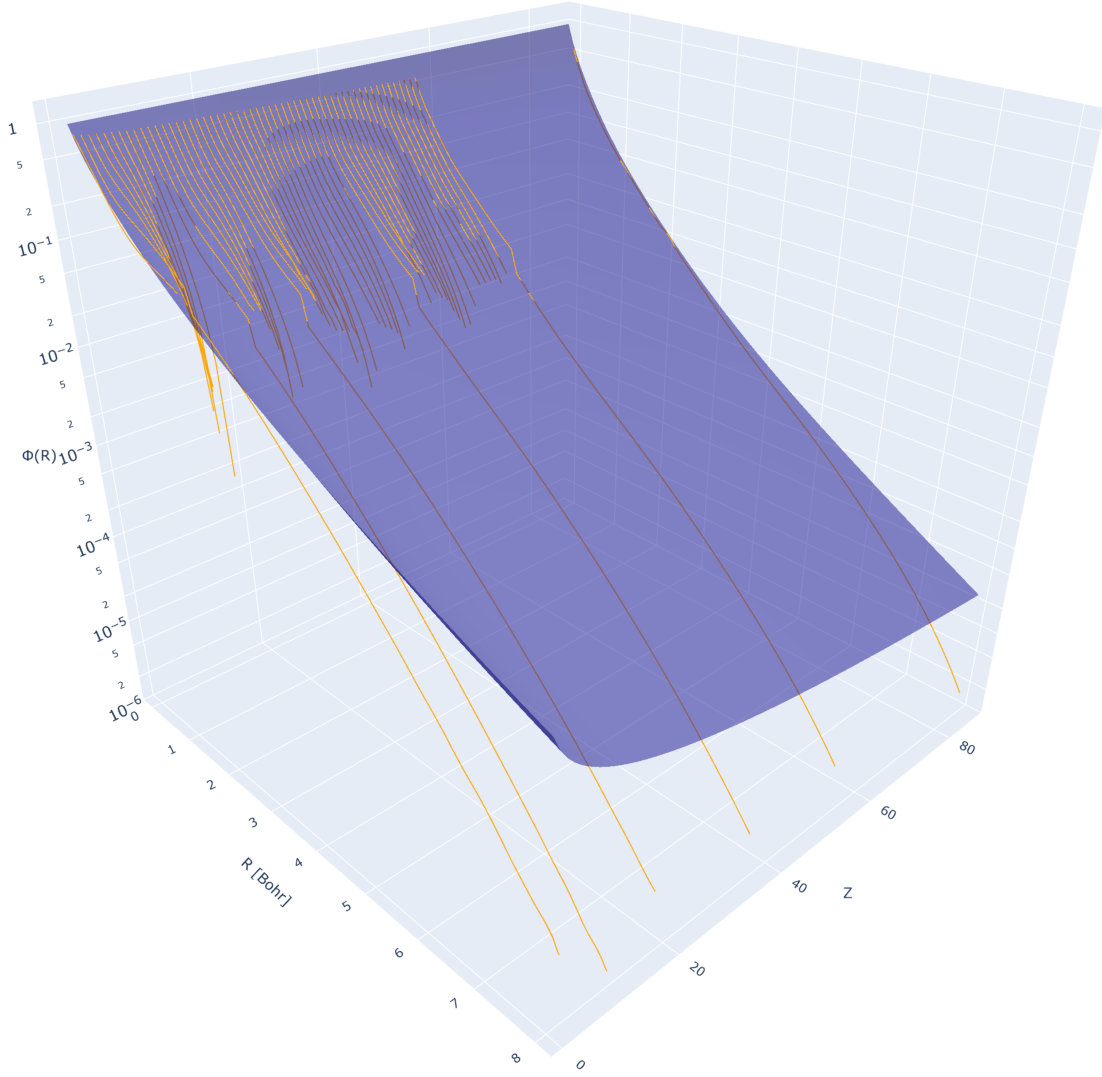


Figure 3.13.: Screening functions to the bare nuclear potentials for the Born Oppenheimer potentials for Protons as calculated with `pyscf` and comparison with the Ziegler, Littmark, and Biersack [317] potential.

3.1.3. Electronic stopping

3.1.3.1. Stopping of point charges

As discussed in sec. 3.1.1 on page 53, over a wide range of energies for many projectile-target combinations electronic stopping (energy loss of the projectile due to excitation of target Electrons) is the dominant process. Many models exist in the literature that describe different aspects of this stopping process approximately. The most important theories are the ones of Bohr and Bethe, which describe the energy transfer to classical,

3. The irradiation process

harmonically bound Electrons [29] and the energy transfer to quantum mechanical, free Electrons [17], respectively. As a simple model, here the approximation of Ferraris and Arista [68] is used that interpolates between Bohr's and Bethe's approaches:

$$S_{el.} = - \left\langle \frac{dE}{dx} \right\rangle_{el.} = \frac{4\pi Z_1^2 \rho(r)}{m_e v^2} \cdot \left(\frac{e^2}{4\pi\epsilon_0} \right)^2 \cdot L \quad (3.2)$$

$$L \approx \ln \left(\frac{C m_e v^3}{|Z_1| v_0 \hbar \omega} \cdot \frac{1}{\sqrt{1 + (C v / 2 Z_1 v_0)^2}} \right)$$

with the Bohr velocity v_0 , the projectile charge Z_1 and velocity v , the Electron density $\rho(r)$ and the constant $C = 1.1229$. $\hbar\omega$ is the mean excitation potential of the target. A local Electron gas approximation $\omega \approx \chi \sqrt{\frac{4\pi\rho(r)e^2}{m_e}}$ with a small constant $\chi > 1$ (often set to about $\sqrt{2}$) [136] or experimentally determined mean excitation potentials [263] are often used for the calculation of mean electronic stopping powers, though corrections are often necessary to describe compound targets with different chemical bonds, phases or oxidation states than their elemental counterparts [110, 229, 243].

At low velocity, eq. 3.2 diverges. A possible correction, that also approximates the Barkas-Anderson effect, follows from perturbation theory [11, 249]. A simplified version is used here:

$$L \approx \frac{1}{n} \ln \left(1 + \left(\frac{C m_e v^3}{|Z_1| v_0 \hbar \omega} \right)^n \cdot \frac{1}{\sqrt{1 + (C v / 2 Z_1 v_0)^2}^n} \right) \quad (3.3)$$

Note that often $n = 2$ is used, which follows from perturbation theory [11, 249], however $n = 1$ provides a much better fit to experimental data and is used here. Sigmund and Schinner also used a similar expression with $n = 1$ in their paper as a fit to the stopping due to a single, harmonically bound Electron but noted that the expression should not be “adequate to evaluate stopping cross sections” [248]. Fig. 3.14 on the next page shows a comparison of anti-Protons in different target materials and the description of the stopping process with $n = 1$ and $n = 2$. As visible, the experimental data is better represented by $n = 1$.

3. The irradiation process

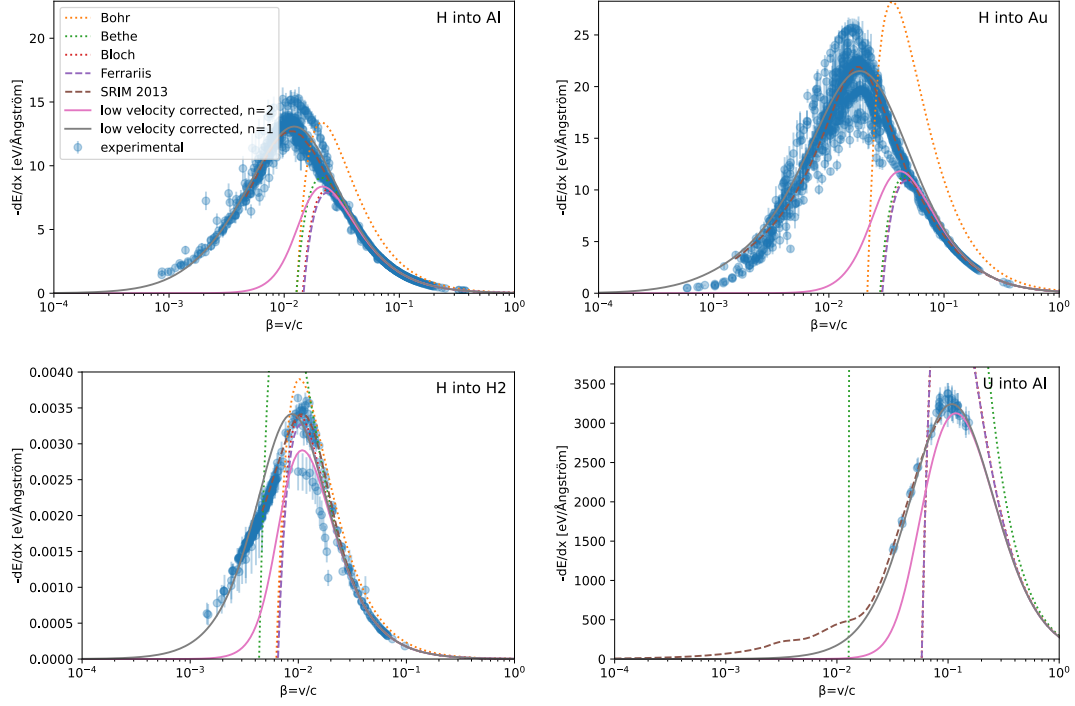


Figure 3.14.: Electronic stopping power of Hydrogen and Uranium in different target materials with nuclear charge Z and the prediction by eq. 3.3 on the previous page with $n = 1$ and $n = 2$.

At low velocity the electronic stopping for $n = 1$ is:

$$S_{el.} = \frac{4\pi |Z_1| \rho(r)}{m_e} \cdot \left(\frac{e^2}{4\pi\epsilon_0} \right)^2 \frac{C m_e}{v_0 \hbar \omega} v + \mathcal{O}(v^3) \quad (3.4)$$

reproducing the experimentally observed (see for example [244, 169]) and theoretically predicted [138, 70, 135, 278] stopping power that is proportional to projectile velocity. Note that $n = 2$ creates a stopping power that is proportional to v^4 and with approximate shell corrections [246] to v^2 . As such $n = 1$ is determined to be a more realistic model in the low velocity case.

3.1.3.2. Effective charge

As discussed in sec. 3.1.3.1 on page 75 as a projectile travels through matter, it can get (partially) ionized or pick up Electrons in collisions. Several models exist to treat this phenomenon and describe the mean charge state of the projectile as a function of the projectile velocity. Among them are approaches that consider Electrons removed from the projectile when [150]:

- their mean orbital velocities are smaller than the velocity of the projectile (called the velocity criterium) [28]

3. The irradiation process

- it is energetically favourable to slow the projectile Electrons down instead of keeping them bound to the projectile (called the energy criterium) [128]

For simplicity these models are often based on either the Thomas-Fermi atomic model [200, 311] or tabulated orbital binding energies [28, 128]. Beyond that, several empirical models exist as well [241, 317, 235].

An alternative point of view is to treat the projectile and its Electrons as a thermodynamic ensemble that can interact with the target through the exchange of Electrons. Imposing an effective temperature based on the kinetic energy of the projectile with respect to the target and enforcing Boltzmann statistics, the weight w_i of a state i with a charge Q_i and internal (electronic) energy U_i , a mass M_i at a velocity v_i can be written as:

$$w_i \approx \frac{1}{\sum_j w_j} \cdot \exp \left(- \frac{(Z - Q_i) m_{el.} (\gamma - 1) c^2 + U_i - Q_i \cdot W}{k_B T} \right) \quad (3.5)$$

with $\gamma = \frac{1}{\sqrt{1 - \frac{v^2}{c^2}}}$, the work function of the target material W and the relativistic temperature $k_B T$:

$$k_B T = \frac{1}{3} \frac{m_{el.} v^2}{\gamma}$$

which among the models proposed in the literature (see for example [121, 63]) fits the experimental data best. The internal energy could include excitations, that is, be temperature (or velocity) dependent, though this was ignored here. Fig. 3.15 on the next page shows the charge states of Carbon atoms as a function of projectile velocities from this model for different materials. Where either the experimental energies after passing through the targets were used or, where possible, the initial energies were corrected with energy loss simulations from SRIM [318]. The experimental probabilities for Carbon targets do not add up to 1, as knock on atoms from the target may exit it as well, as such a perfect fit is impossible without also describing this effect. An effective work function $W \approx 3$ eV was assumed and the internal energies U_i determined by fit are given and compared to ground state total electronic binding energies in tab 3.6 on the following page.

3. The irradiation process

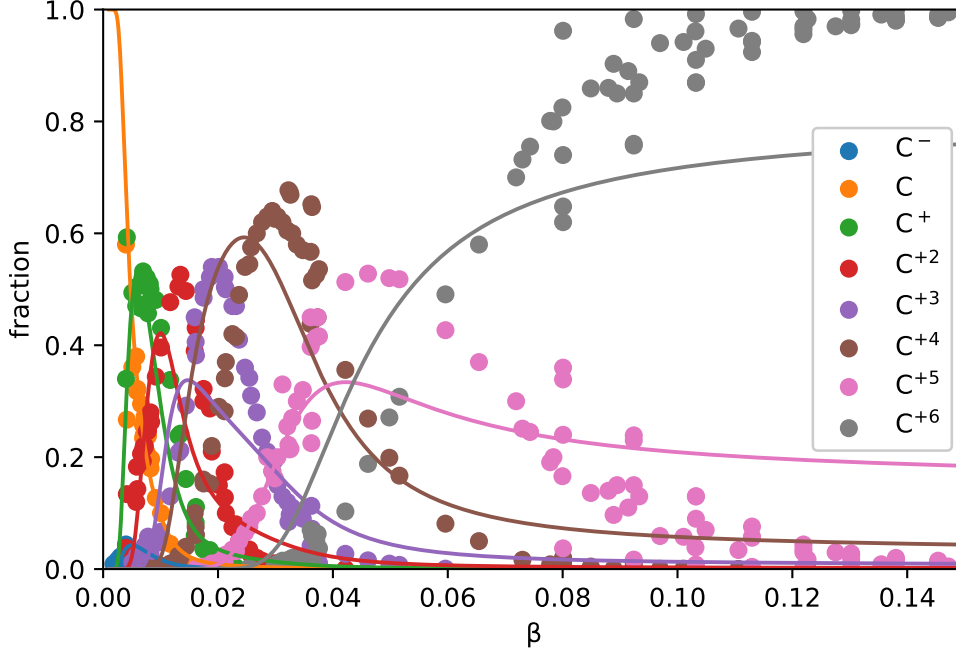


Figure 3.15.: Charge states of Carbon as a function of projectile velocity $\beta = \frac{v}{c}$ for different targets [303, 241] and as described from eq. 3.5 on the preceding page.

charge state	binding energy [eV]	best model fit [eV]
-1	-1.26	-1.3
0	0	0
+1	11.3	6.3
+2	35.6	24
+3	83.5	68
+4	148	153
+5	540	440
+6	1030	1124

Table 3.6.: Comparison of ground state Electron binding energies of carbon atoms [125, 90] with the best fit parameters from eq. 3.5 on the preceding page.

The mean charge of the projectile is then:

$$\langle Q \rangle = \sum_i w_i Q_i$$

whereas the mean charge square that is relevant in stopping can be expressed as:

3. The irradiation process

$$\langle Q^2 \rangle = \sum_i w_i Q_i^2$$

In comparison to some of the previously discussed theories, this approach also allows to predict the occurrence of negative ions and can be used for predicting charge states of molecular projectiles. In the limit of low velocities the mean charge square reduces to:

$$\begin{aligned} \langle Q^2 \rangle &\approx \frac{w_1 1^2 + w_0 \cdot 0^2}{w_1 + w_0} \\ &= \frac{\exp\left(-\frac{2U_1}{Mv^2} + \frac{m_{el.}}{M} + \frac{2EA_{target}}{Mv^2}\right)}{\exp\left(-\frac{2U_1}{Mv^2} + \frac{m_{el.}}{M} + \frac{2EA_{target}}{Mv^2}\right) + \exp\left(-\frac{2U_0}{Mv^2}\right)} \\ &= \frac{1}{1 + \exp\left(-\frac{2(U_0 - U_1)}{Mv^2} - \frac{m_{el.}}{M} - \frac{2EA_{target}}{Mv^2}\right)} \\ &\approx \frac{1}{1 + \exp\left(-\frac{2(U_0 - U_1)}{Mv^2} - \frac{2EA_{target}}{Mv^2}\right)} \\ &\rightarrow \begin{cases} 0 & \text{for } EA_{target} > U_1 - U_0 \\ 1 & \text{for } EA_{target} < U_1 - U_0 \end{cases} \end{aligned}$$

if we assume that at low velocities only the neutral ground state and the single positively charged states are relevant. Note that the limit in the last line essentially compares the ionization potential of the projectile with the Electron affinity of the target. In reality Electron affinities are usually lower (for noble gases even 0) than the always positive atomic ionization potential.

While this simple thermodynamic model may not predict the charge states of projectiles at high energy particularly accurately, the situation is reversed entirely at very low energies. In contrast to the otherwise accurate empirical models for the charge states, the model proposed here can also be used to understand stopping of low energy ions in complicated materials where no experimental data is available. This makes this model a substitute for some of the empirical models at low energy stopping, meaning either PBW at nano-dimensions or the end of range cascades of fast projectiles in a target material.

3.1.3.3. Bond relaxation

An interesting aspect that is usually ignored in the binary collision approximation to stopping, is the formation, excitation and breaking of chemical bonds between projectiles and target atoms. Usually, the energetics of a collision cascade within the binary collision approximation is considered as entirely elastic scattering on the (screened) nuclear potentials, a friction like force to simulate electronic stopping and an energy penalty for target atoms to leave their lattice sites. Fig. 3.16 on the next page shows an example of the excited and ground states of Hydrogen collisions with Gallium.

3. The irradiation process

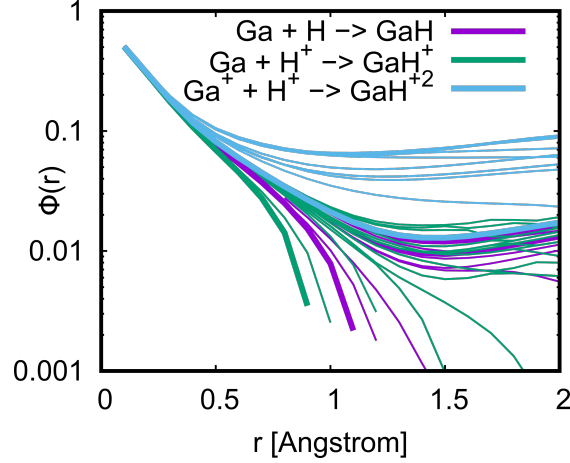


Figure 3.16.: Effective screening function of Hydrogen collisions with Gallium. The ground state is shown with thick lines and the first 10 excited states with thin lines. The simulation was performed in `Orca` with a X3LYP potential.

An approach for this phenomenon follows naturally with the introduction of velocity dependent interatomic potentials. More specifically: potentials that interpolate between the high velocity and low velocity approximations of the interaction potentials based on the projectile velocity with respect to the target atoms. Such a potential is here parameterized as:

$$V(R, v) = \frac{Z_1 Z_2}{R} \phi(Z_1, Z_2, R) + \zeta(v) \phi_{relax.}(Z_1, Z_2, R)$$

where $\zeta(v)$ is a function of the relative velocity of the projectile to the target v . ϕ the screening function due to Coulomb screening of the target Electrons alone in their ground state (Hartree potential) and $\phi_{relax.}$ is an approximation for the difference to the Born-Oppenheimer limit of the collision with target and projectile being (almost) uncharged. A rough approximation for $\zeta(v)$ can be constructed by comparing the ion velocity to the typical velocity of valence Electrons in the target (the Fermi-velocity). It is then:

$$\zeta(v) \approx \exp\left(-\frac{v}{v_R}\right)$$

with a reference velocity v_R that is a function of the Fermi-velocity of the target. Such a formalism guarantees agreement between ground state molecular dynamics simulations and scattering experiments at high energy. It also introduces a simple mechanism for Electron-phonon coupling that is often difficult to treat in stopping simulations without knowledge of additional target material parameters [312]. With the Lagrange formalism, it leads to the following equations of motion of the target and projectile when neglecting small terms due to the large mass of the nuclei:

3. The irradiation process

$$m_i \frac{d\vec{v}_i}{dt} \approx -\frac{dV(R, v)}{dR} \frac{\vec{R}_i}{R} + \frac{d^2V(R, v)}{dv dR} \frac{\vec{v}_i \cdot \vec{R}_i}{vR} \vec{v}_i$$

where the index i stands for the collision partner i . Fig. 3.17 shows an application of this model for Helium stopping in Helium. Here the effective charge of the Helium projectile is used to interpolate between the velocity dependent potential and the stopping with the previously discussed electronic stopping model. For this the equations of motion of the collision pair were explicitly integrated at different collision energies and impact parameters. As visible, the theoretical stopping cross-section introduced here is able to reproduce the experimental data relatively accurately over the entire range.

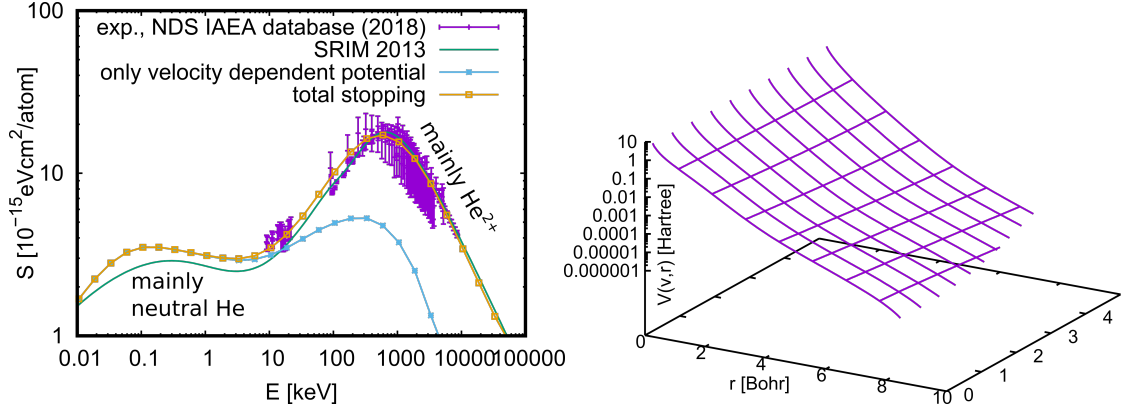


Figure 3.17.: Stopping cross section for He stopping in He as calculated with the stopping model including the approximation for bond breaking in comparison to experimental measurements [171] on the left. On the right a plot of the used potential.

Similarly, the velocity dependent potential also works well for other projectile target combinations. This is shown in fig. 3.18 on the next page for the example of Silicon stopping in Gallium Arsenide.

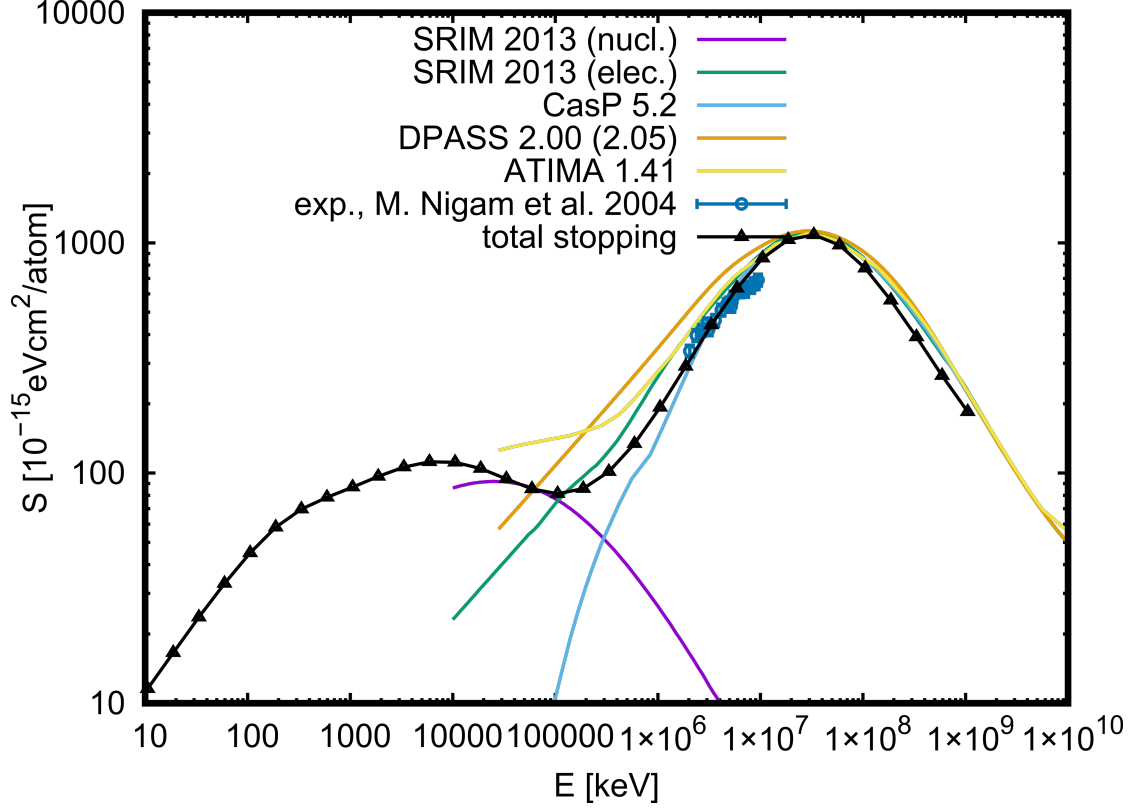


Figure 3.18.: Stopping cross section for Silicon stopping in Gallium Arsenide as calculated with the stopping model including the approximation for bond breaking in comparison to several simulations as well as experimental measurements.

3.1.3.4. Delta-Electrons and spatial extend

As fast Protons pass the target material, some of the Electrons created though ionization of the target atoms might have enough energy to travel some distance in the target and ionize atoms themselves. These Electrons are called δ -Electrons. The spatial energy deposition $D(r)$ around a Proton track due to δ -Electrons can be expressed as [49, 291]:

$$D(r) = \frac{\rho_{el}.e^4 Z_{eff.}^2(v)}{\alpha m_{el}.v^2 r} \left[\frac{\left(1 - \frac{r+\theta}{R+\theta}\right)^{\frac{1}{\alpha}}}{r + \theta} \right]$$

where $\rho_{el.}$ is the Electron density of the resist, $Z_{eff.}(v)$ the effective charge of the projectile, R the maximum range for δ -Electrons and θ the range of an Electron with a specific energy. $\alpha \approx 1.667$ is a constant. This leads to a small smearing out of the electronic energy deposition around the path of a fast projectile. Electrons are relatively light, however, so the energy transferred to target nuclei directly is not affected by this. Fast Electrons can however still create reactive in resists [285].

3.2. Defect production

Defects can be produced in the target material by displacing target atoms from their lattice sites or changing the bond structure of the target. Displacement of target atoms can happen directly, as a result of nuclear stopping, or indirectly, as a result of delta Electron creation which in turn can displace target atoms. Changes in the bond structure on the other hand are primarily caused by excitation or ionization of the target Electron system, and thereby a result of electronic stopping.

A description of the direct defect production within the binary collision approximation is possible with the help of a lattice binding energy and a threshold displacement energy [61]. When a collision with a target atoms takes place and a kinetic energy larger than the threshold displacement energy is transfered to it, it can permanently leave the lattice site with a kinetic energy that is reduced by the lattice binding energy, leaving behind a potential target vacancy site. Alltogether, radiation damage production in the target material can be divided into two categories:

- the primary damage that is produced directly in the collision cascade, within picoseconds after the projectile impact and in collision processes far from thermal equilibrium
- the damage evolution that happens nanoseconds to years afterwards, caused by thermally activated processes

Both processes happen after and during the irradiation process, but are very different in their physical description and time scales. Here the primary damage is treated while sec. 3.3 on the following page focuses on the evolution of the primary defects.

A common measure for radiation damage is the number of displacements per projectile $N_{disp.}$. However, a microscopically precise model of damage formation requires a large amount of information, such as the damage cluster size, thermal mobility and recombination, nonlinear damage buildup at high doses and more. As an approximation, a rough model exists that relates the number of displacements created in a cascade in the primary damage production to the energy transfered to the recoil atom E_{recoil} [185]:

$$N_{disp.}(E_{recoil}) \approx \begin{cases} 0 & E_{recoil} < E_{thres.displ.} \\ 1 & E_{thres.displ.} < E_{recoil} < 2.5 \cdot E_{thres.displ.} \\ \frac{E_{recoil}}{2.5 \cdot E_{thres.displ.}} \xi(E_{recoil}) & 2.5 \cdot E_{thres.displ.} < E_{recoil} \end{cases}$$

where $\xi(E_{recoil})$ is a target dependent efficiency function with values between about 0.3 and 1 and $E_{thres.displ.}$ is the threshold displacement energy, the crystal direction averaged minimum energy required to produce a stable Frenkel pair (vacancy - interstitial atom - pair) in a collision. The threshold displacement energy is an empirical parameter that fits the effects of many complicated processes in the target and is difficult to define rigorously but often has values between 12 and 90 eV [61, 122]. It also describes damage evolution to an extend.

3. The irradiation process

A more accurate description of primary damage is possible with binary collision approximation simulations. Simulations of this type require additionally to the threshold displacement energy a bulk binding energy and a cutoff energy. The bulk binding energy is the energy required to overcome the local bond forces of a target atom and allow it to move through the lattice. An atom displaced from its lattice site thus leaves it with a kinetic energy that is reduced by the bulk binding energy. The cutoff energy in turn defines a limit at which the tracking of moving atoms is stopped. This last parameter is necessary to reduce the computational burden in binary collision simulations [61].

From energy conservation it follows that removing an atom from a solid would require at least the sublimation enthalpy. The sum of the bulk binding energy and a surface binding energy (the energy to move an unspecifically bonded atom from the surface to the vacuum) should therefore yield the sublimation energy (when neglecting dissipative processes like electronic and nuclear stopping). Often the bulk binding energy is set to a small value (3 eV, 0.25 eV or 0 eV [61, 318]) with the surface binding energy adding up to the remainder. But it has also been shown that simulations without a surface binding energy can yield realistic distributions of the particles involved in stopping and sputtering processes near surfaces [99].

3.3. Defect evolution

The primary damage produced in ion irradiation quickly thermalizes after it was created. Left behind are Electrons in excited states, broken chemical bonds, vacancies, interstitial atoms, a heated up target and in very dense collision cascades also amorphized regions. These defects and affected target regions can then also follow a complex evolution on timescales on the order of nanoseconds up to many years, depending on the target temperature, the activation energy of the processes and the availability of the reaction partners [295].

For Proton beam writing in crystalline inorganic materials, the diffusion of the recoils or implanted Protons, recombination with vacancies (occasionally also forming anti-sites in binary- or multi-component semiconductors, that is atoms of the wrong species on the lattice sites), creation of complex defect structures, amorphization of the target, local phase changes of the target and mixing of the target atoms can occur [295]. For the commonly used semiconductors Silicon and many binary semiconductors, the creation of vacancies, interstitial atoms, Frenkel-pairs (vacancy-interstitial pairs), anti-sites and doping through the implanted Hydrogen-atoms are the most important effects [73, 300]. At very high local defect densities the semiconductor target can also locally amorphize or form metastable phases. Excited Electrons and broken chemical bonds, though commonly more numerous than displaced atoms (as discussed in sec. 3.1.1 on page 53), can often recombine to the ground state again, mainly causing the target semiconductor material to heat up and reanneal some of the damage [115, 206]. Some simple models exist that can treat the evolution of radiation damage in these materials approximately [299, 261].

In case of Proton beam writing in organic materials, the changes in the bond structure are often more important than the displacement of single atoms. A key value for defect

3. The irradiation process

evolution in resists is the G -value. It is defined as the number of events, either chain scission or cross linking, per absorbed energy of 100 eV in the resist. This value can be measured by irradiating thin layers of a resist (thin enough so that the energy loss of the particles in the material does not vary much over the thickness of the film) and then exposure of the film to a developer. The film thickness after partial dissolution in the developer is then an indicator for the G -value of the resist [227, 9]. In general, materials with a higher G -value at the chosen irradiation energy require a lower effective Proton dose and are preferred for creating 3D structures. PMMA, for example, was found to have G -values of about 1.31 for γ -radiation, 0.75 for 25 keV Electron irradiation (1 μm thin film on Si, 1.65 for bulk material) and 0.70 for 100 keV Proton irradiation (1 μm thin film on Si) [2].

3.3.1. Resists and polymers

As mentioned in the introduction of this work, in resists and polymers the two most important reactions for PBW after irradiation are chain scission and cross-linking. A simple model that mimics this behaviour can be constructed from a Monte Carlo simulation. Here N_{molecule} molecules with an effective length L_{molecule} are used. For each reactive site generated during irradiation, a random molecule is chosen which either splits into two molecules that add up in length to the initial molecule with a probability p_{scission} or cross-links with another molecule with an effective length that is the sum of its constituents with a probability $p_{\text{cross-linking}}$. Alternatively, none of the previous reactions may take place with a probability of $p = 1 - p_{\text{scission}} - p_{\text{cross-linking}}$. For the defect evolution of the resists, only the effective number of reactive sites generated per molecule $R = \frac{N_{\text{reactive}}}{N_{\text{molecule}}} (p_{\text{scission}} + p_{\text{cross-linking}})$ that lead to either scission or cross-linking need to be considered in this simple model. Fig. 3.19 on the following page shows the evolution of the probability distribution of chain lengths in a resist or polymer under Proton irradiation with $p_{\text{scission}} + p_{\text{cross-linking}} = 1$ and an initial length distribution with a standard deviation of $\sigma_{\text{initial}} = \frac{1}{4}L_{\text{molecule}}$. As visible, in every case the standard deviation of lengths in the target increases, while the mean length approaches $\frac{1}{2}L_{\text{molecule}}$, L_{molecule} or ∞ as R approaches 1 for the cases $p_{\text{scission}} = 1$, $p_{\text{scission}} = \frac{1}{2}$ and $p_{\text{scission}} = 0$, respectively. It is also visible that, except in the extreme case of $p_{\text{cross-linking}} = 1$, there is an accumulation of molecules with very small lengths.

3. The irradiation process

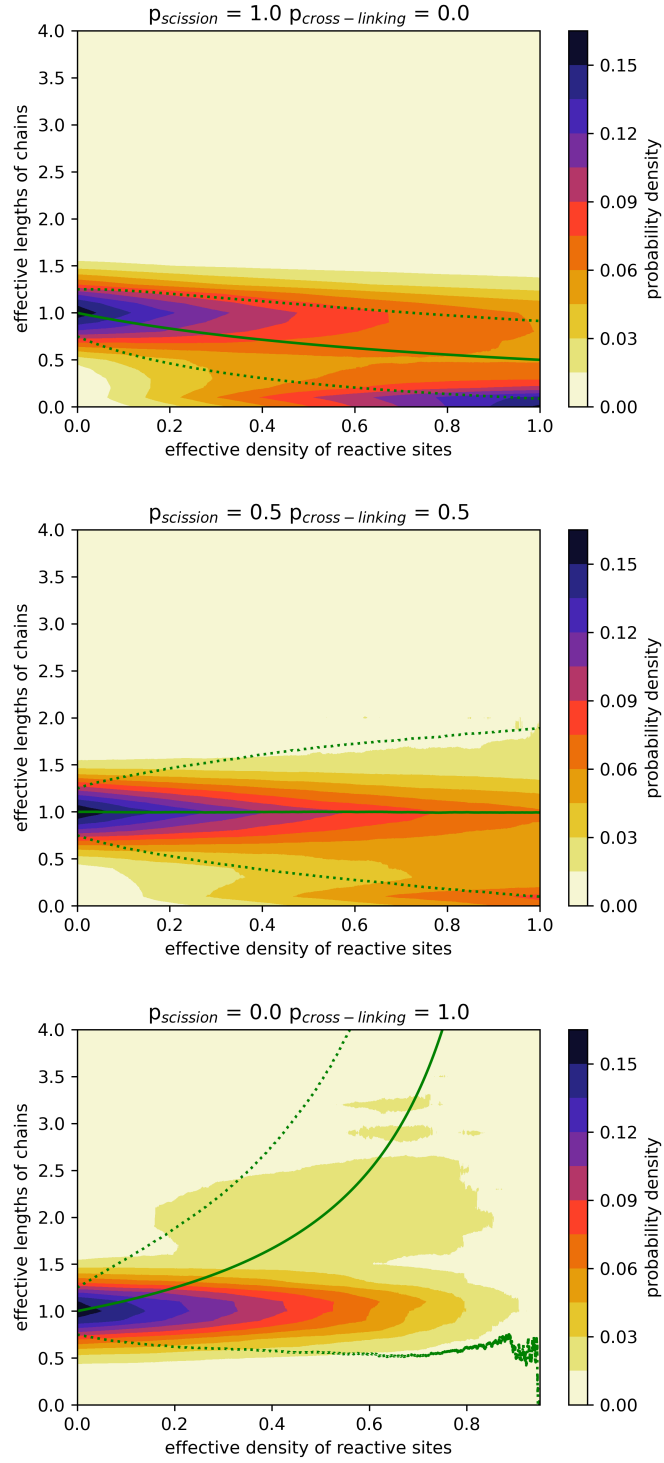


Figure 3.19.: Evolution of the distribution of chain lengths relative to the initial mean chain length as a function of the effective density of reactive sites created due to irradiation with fast ions. Also shown is the mean chain length and the standard deviation in green.

4. Etching

Etching in Proton beam writing is the process of removing material from the solid that was irradiated in such a way that a 3D structure is generated. For this the etching process needs to be able to selectively remove material depending on the local Proton beam irradiation induced defect concentration. This leads to two methods that are commonly employed:

- chemical etching for resist materials where the different solubility of longer and shorter chains of the polymers making up the resist after irradiation is used.
- electrochemical etching for semiconductor materials (and to a lesser extend insulators) where the change of doping in the irradiated regions is used.

Tab. 4.1 on the next page provides an overview of some materials commonly used in PBW as well as the etching process and the electrolyte or solvent used during etching.

material	type	electrolyte/solvent	process
PMMA	positive	2-(2-Ethoxyethoxy)ethan-1-ol and water [256, 233]	chemical
PMGI	positive	4-Methylpentan-2-one and Propan-2-ol [35]	chemical
SU-8	negative	2-(2-Ethoxyethoxy)ethan-1-ol and water [113]	chemical
Si	positive	1-Methoxy-2-propanyl acetate [80, 271]	chemical
GaAs	positive / negative	HF in water and Ethanol followed by KOH solution [203]	electrochemical + chemical
InP	positive / negative	KOH solution [237] KOH solution [237]	electrochemical electrochemical

Table 4.1.: Overview of etching recipies of different resists used in Proton beam writing. The type determines if the target material behaves like a positive or negative resist.

4. Etching

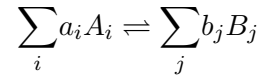
In general, inorganic semiconductors are etched electrochemically, whereas organic semiconductors and resists are etched chemically with organic solvents. In inorganic semiconductors mainly the change in doping and electrical conduction is responsible for the selective removal of the target material, whereas in resists the solubility of the target is altered by radiation damage. Selection of proper etching solutions can be difficult in some cases as they need to be highly selective for the radiation damage in the target such that no large fluences are required for PBW.

While in principle organic semiconductors could also be etched electrochemically, no such experiments were reported so far and the comparatively in-homogeneous conduction in many organic semiconductors in comparison to their inorganic counter parts, combined with the problem of graphitization upon irradiation make it unlikely that such experiments can be conducted soon.

To understand the etching process, chemical equilibria will be discussed and with that the conditions under which etching can occur, followed by rate equations for etching and solvation, that allow to describe the chemical etching / solvation process. Finally, reaction drift diffusion models for etching are described for semiconductors.

4.1. Chemical equilibrium

Etching of a solid occurs when the chemical equilibrium of it in contact with an electrolyte (and under an applied potential) favors the dissolution of the solid. To determine when etching occurs, one can consider the chemical equilibrium of the solid surface under the external conditions (e.g. solvent, applied potential, pH value). For this consider a general chemical reaction:



with educts A_i , products B_j and their respective stoichiometric factors a_i and b_j . This way of writing a chemical reaction means that for every a_i molecules of type A_i that react, b_j molecules of type B_j are produced. This means a rate equation can be formulated that describes the changes in the respective concentrations (where $[X]$ marks the concentration of species X) [262, 16]:

$$-\frac{1}{a_i} \frac{d[A_i]}{dt} = \frac{1}{b_j} \frac{d[B_j]}{dt} = R \approx k_{forward} \prod_i [A_i]^{\alpha_i} - k_{backward} \prod_j [B_j]^{\beta_j}$$

where R is the reaction rate (with units concentration per time) and $k_{forward}$ and $k_{backward}$ are the reaction rate coefficients. The right hand side of the equation is called the law of mass action [83, 84, 290, 82]. The law of mass action can be explained by considering that collisions between the participating molecules need to occur. The frequency of these collisions, and thereby also approximately the reaction rate, depends on the concentration of the participating molecules. The units of the reaction rate coefficients are typically concentrations raised to some negative power per time, so that the overall units of the mass action law turn out to be concentrations per time. α_i and

4. Etching

β_j are constants (often, but not necessarily integers) and are not necessarily related to the stoichiometric coefficients for the total chemical reaction. α_i and β_j can even have negative values. Further more, in some reactions other substances may appear in the rate equations that may not show up in the stoichiometric equation, for example transient intermediates or catalysts). For some reactions even more complicated expressions for the reaction rate are necessary [262, 16].

With the mass action law, it is possible to calculate the change in concentration of molecules in a chemical reaction, as long as the reaction occurs slowly enough that quasi-equilibrium conditions occur throughout the reaction [262]. In turn it is also possible to define conditions where the macroscopic concentrations of the reactants not change over time. This is called the equilibrium or steady state approximation. A reaction is in equilibrium when the forward and backward reaction rates are in equilibrium [152, 262, 16]:

$$\frac{k_{forward}}{k_{backward}} = \frac{\prod_i [A_i^{eq.}]^{\alpha_i}}{\prod_j [B_j^{eq.}]^{\beta_j}} \approx \frac{\prod_i \{A_i^{eq.}\}^{\alpha_i}}{\prod_j \{B_j^{eq.}\}^{\beta_j}} = K = e^{-\frac{\Delta_r G^0}{RT}}$$

where the equilibrium activities $\{A_i^{eq.}\}$ and $\{B_j^{eq.}\}$, equilibrium concentrations $[A_i^{eq.}]$ and $[B_j^{eq.}]$ are introduced, along with the equilibrium constant K and the Gibbs free energy change of the reaction $\Delta_r G^0$. If $K > 1$ the equilibrium favors the educts and the reaction will happen in reverse, whereas for $K < 1$ the products are favored and the reaction happens in the forward direction [152].

The approximation in the middle of the equation comes from the fact that K is usually expressed in terms of thermodynamics activities instead of concentrations. K can, however be expressed with the concentrations as well when ideal behavior of the reactants is assumed [16].

It is also possible to derive similar expressions for a half-cell in electrode reactions. For this the Gibbs free energy change of the reaction $\Delta_r G$ needs to be expressed as a function of the concentrations of the reactants [152]:

$$\Delta_r G = \Delta_r G^0 + RT \ln \left(\frac{\prod_i \{A_i\}^{\alpha_i}}{\prod_j \{B_j\}^{\beta_j}} \right) \approx \Delta_r G^0 + RT \ln \left(\frac{\prod_i [A_i]^{\alpha_i}}{\prod_j [B_j]^{\beta_j}} \right) \quad (4.1)$$

To relate this to parameters that can easily be measured for an electrochemical cell the standard potential of a half-cell can be introduced [64]:

$$E^0 = -\frac{\Delta_r G^0}{nF} \quad (4.2)$$

where n is the number of Electrons that is transferred in the stoichiometric equation. With this, an open cell potential E_{oc} can be defined [64]:

4. Etching

$$E_{oc} = E^0 - \frac{RT}{nF} \ln \left(\frac{\prod_i [A_i]^{\alpha_i}}{\prod_j [B_j]^{\beta_j}} \right) \approx E^0 - \frac{RT}{nF} \ln \left(\frac{\prod_i [A_i]^{a_i}}{\prod_j [B_j]^{b_j}} \right) \quad (4.3)$$

The last estimate uses an approximation of the constants α_i and β_j by the stoichiometric factors a_i and b_j . This equation is known as the Nernst equation [64]. Assuming that one of the products is an hydronium ion and using the pH value for dilute solutions with the stoichiometric factor m , one finds:

$$E_{oc} = E^0 - \frac{RT}{nF} \ln \left(\frac{\prod_i [A_i]^{a_i}}{[\text{H}_3\text{O}^+]^m \prod_j [B_j]^{b_j}} \right) = E^0 - \frac{RT}{nF} \ln \left(\frac{\prod_i [A_i]^{a_i}}{\prod_j [B_j]^{b_j}} \right) + \frac{RT}{nF} m \cdot \text{pH} \cdot \ln(10) \quad (4.4)$$

$$\frac{dE_{oc}}{dpH} = \frac{RT}{nF} m \cdot \ln(10) \quad (4.5)$$

Much of the etching of photo resists can be understood from the standpoint of chemical equilibrium. During PBW the chain length and solubility of these materials is modified, shifting the chemical equilibrium between solvated and unsolvated target material in a controlled manner [298].

4.2. Rate equations

The current due to reactions of this type can be expressed as:

$$I_{BV} = -nFAk^0 \left\{ \prod_j [B_j]^{b_j} \exp \left[\frac{-\vec{\alpha} nF (E - E_0)}{RT} \right] - \prod_i [A_i]^{a_i} \exp \left[\frac{\overleftarrow{\alpha} nF (E - E_0)}{RT} \right] \right\} \quad (4.6)$$

with the electrode area A , the standard rate constant $k^0 = k_{forward}(E_0) = k_{backward}(E_0)$, the charge transfer coefficients $\vec{\alpha}$ and $\overleftarrow{\alpha}$ that are linked through $\vec{\alpha} + \overleftarrow{\alpha} = 1$ for simple reactions where only a single Electron is transferred [81]. Often the (activation) over potential η is used rather than E [26]. This means it can be written as [26]:

$$I_{BV} = -nFAk^0 \left\{ \prod_j [B_j]^{b_j} \exp \left[\frac{-\vec{\alpha} nF (\eta + E_0)}{RT} \right] - \prod_i [A_i]^{a_i} \exp \left[\frac{(1 - \vec{\alpha}) nF (\eta + E_0)}{RT} \right] \right\} \quad (4.7)$$

Eq. 4.3 can be written as [26]:

4. Etching

$$E_0 = \frac{RT}{nF} \ln \left(\frac{\prod_i [A_i]^{a_i}}{\prod_j [B_j]^{b_j}} \right) \quad (4.8)$$

in the equilibrium case. Replacing E_0 in equation 4.7 on the previous page by this expression and simplification leads to [26]:

$$I_{BV} = I_0 \left\{ \exp \left[\frac{-\vec{\alpha} n F \eta}{RT} \right] - \exp \left[\frac{(1 - \vec{\alpha}) n F \eta}{RT} \right] \right\} = I_0 \left\{ \exp \left[\frac{-\vec{\alpha} n F \eta}{RT} \right] - \exp \left[\frac{\overleftarrow{\alpha} n F \eta}{RT} \right] \right\} \quad (4.9)$$

with:

$$I_0 = -nFAk^0 \left(\prod_j [B_j]^{b_j} \right)^{1-\vec{\alpha}} \left(\prod_i [A_i]^{a_i} \right)^{\vec{\alpha}} \quad (4.10)$$

Eq. 4.9 is also known as the Butler-Volmer equation [16, 26]. In the general case, more complicated reactions are possible with rate determining steps. Then the charge transfer coefficients $\vec{\alpha}$ and $\overleftarrow{\alpha}$ are linked through $\vec{\alpha} + \overleftarrow{\alpha} = \frac{n}{v}$ with v as the number of times the rate determining step has to occur at the electrode for one full reaction to take place and n as the number of elementary charges that are transferred for each reaction [26, 81]. In this case equation 4.9 can be written as:

$$I_{BV} = I_0 \left\{ \exp \left[\frac{\left(\frac{n}{v} - \vec{\alpha} \right) n F \eta}{RT} \right] - \exp \left[\frac{-\vec{\alpha} n F \eta}{RT} \right] \right\} \quad (4.11)$$

However, there is a mass transport limit, that describes the situation that the current is limited by the diffusion of the products to the surface of the material. The mass transport limited current can be written as [69]:

$$I_{limit} = \frac{nFD_{AB}}{\delta} C^* = \frac{nFD_{AB}}{\sqrt{\pi D_{AB} t}} C^* \quad (4.12)$$

with the diffusion coefficient D_{AB} of the dilute species A in the solvent B , the Nernst diffusion layer thickness δ and the concentration of the dilute species A in the bulk C^* . With equation 4.6 on the preceding page and equation 4.12 the total current can be expressed as:

$$\frac{1}{I} = \frac{1}{I_{BV}} + \frac{1}{I_{limit}} \quad (4.13)$$

In the etching cell used for this work, the electrolyte is stirred and this limits the maximum thickness of the diffusion layer. In the equilibrium case the limiting current due to diffusion is proportional to $\sqrt{\eta}$ while the supply of free charge carriers to the surface of the material may cause a limiting current that is proportional to the over potential itself [81].

4.3. Reaction drift diffusion models

A simple set of equations that can capture much of the dynamics of the etching process in inorganic semiconductors is available with the reaction drift diffusion equations [189]. In the following a short review of these equations is provided along with the particularities when using them to describe PBW.

4.3.1. Poisson's equation

The first main ingredient of The electrostatic potential V is determined by Poisson's equation and the boundary conditions [53]:

$$-\vec{\nabla} \cdot (\epsilon_0 \epsilon_r \vec{\nabla} V) = -q_{el} (p - n + N_d - N_a) \quad V(d\Omega) = V_0$$

where ϵ_0 is the vacuum permittivity, ϵ_r the relative permittivity of the medium, q_{el} the elemental charge, p, n, N_d, N_a the charge densities of holes, Electrons, donators and acceptors (respectively) and V_0 the value of the potential on the boundary $d\Omega$. In general, the permittivity is a material dependent parameter that can also be a function of the temperature, local field strength, frequency of the applied field and other properties. Since the etching happens mostly around room temperature and with static external potentials, the temperature and frequency dependence will be ignored here, whereas the local field strength dependence may become important at the solid-liquid interface, but the simulations carried out here do not have a high enough resolution to resolve this phenomenon. The relative static permittivities used in this work are summarized in tab. 4.2 on the following page.

4. Etching

material	relative permittivity
Water	78.4 [10]
Metals	1
KOH	14 [199], 35 [fig. 4.1]
HCl	2.76 [199], 1 [fig. 4.1]
Diamond	5.7 [191]
Si	11.9 [191]
Ge	16.0 [191]
3C-SiC	9.72 [118]
4H-SiC	10 [118]
6H-SiC	9.8 [118]
AlN	8.5 [191]
GaN	9.7 [191]
InN	13.52 [191]
AlP	10.41 [199]
GaP	11.1 [191]
InP	12.4 [191]
AlAs	10.1 [191]
GaAs	13.1 [191]
InAs	14.6 [191]
AlSb	12.04 [191]
GaSb	15.7 [191]
InSb	16.8 [191]

Table 4.2.: Relative static permittivities of different materials.

In case of a mixture (for example KOH- or HCl-solution), the permittivities are linearly interpolated. Fig. 4.1 on the next page shows that this approach is a good approximation.

4. Etching

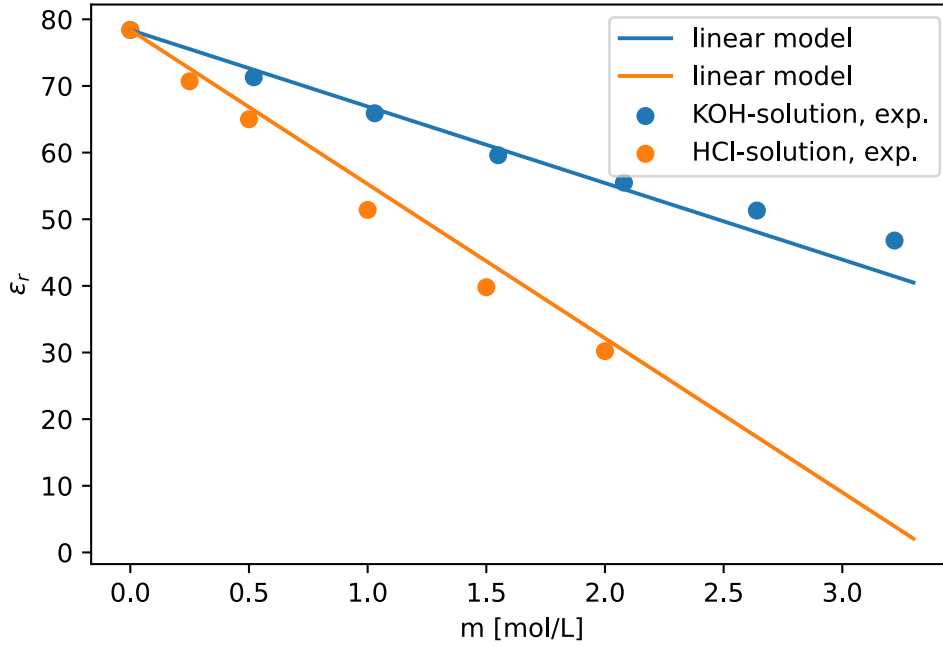


Figure 4.1.: Experimental [134, 133] and linearly interpolated relative permittivities of KOH- and HCl-solutions with water at room temperature for different concentrations.

4.3.2. Defects

Radiation damage can form many complex defects in crystalline semiconductor material. For PBW, the most important types of radiation induced point defects in semiconductors are:

vacancies denoted V_A where an atom of species A is missing from a lattice site

interstitial denoted I_A where an atom of species A is on an interstitial site

substitutions denoted C_A where an atom of species C has replaced an atom of type A at its usual lattice site

anti-sites denoted A_B where in a binary (or ternary) semiconductor an atom of species A is substituting an atom of species B at its usual lattice site

Frenkle-pairs denoted $V_A - I_A$ where an atom of species A is displaced from its usual lattice site to a nearby interstitial site

Depending on the semiconductor material, the effects of the different types of defects can be very different. However in general, the different defect types can introduce scattering

4. Etching

centers for the motion of free charge carriers into the semiconductor material, act as dopants or create charge traps for the free charge carriers.

The effect of charge traps can be a reduction of the effective doping of the semiconductor material. This effect can be supported by the observation of new shallow and deep defects in the band gap of Gallium Arsenide by Positron lifetime spectroscopy experiments. It was observed that the majority charge carrier density was reduced with a rising defect density and a simultaneous movement of the Fermi-energy level towards the center of the band gap [204]. This behavior can be explained when considering that charge traps will mostly trap the majority charge carriers, thereby reducing the effective doping of the semiconductor material. This interpretation is also supported by simulations [52] and by the observation that the radiation dose required to make some materials highly resistive is proportional to the amount of doping before the irradiation [255]. This means that in general, doped semiconductor material will initially increase in resistivity as it is irradiated.

At a certain irradiation dose the doping due to the introduced defects may become dominant in the target material. This phenomenon is well known in Silicon, which, with high radiation defect densities, will behave like p-type material [201].

At very high radiation defect densities the conduction mechanism of the semiconducting material may also change entirely towards a thermally activated hopping process [115]. In materials that do not show net doping due to radiation damage, like Gallium Arsenide or Indium Phosphide, this means the material may become more conductive again [115, 255, 33, 52]. It has been shown previously [261] though that the electrical conductivity in this regime can also be described by the mobility models of the shape used here, if band gap narrowing is taken into account and the material is described as highly doped, but intrinsic, material.

From a certain defect density on, the target material should be largely amorphized and further irradiation cannot change the conductivity any more [115].

4.3.3. Mobility model

One important part of drift diffusion models is the mobility model. Those are models that describe the mobility of free charge carriers in the semiconductor lattice as a function of the temperature, electric fields and the impurity concentration. Since the drift-diffusion model is a rather simple model for the simulation of semiconductor material in comparison to solutions of the BOLTZMANN transport equations or other, more accurate models, relatively complex mobility models have to be employed to correct for all the simplifications that are used in the drift-diffusion models [53].

If no strong electric fields exist, the average drift velocity $\vec{v}_{n/p}$ of the free charge carriers can be related to the mobility $\mu_{n/p}$ of the free charge carriers and the electric field \vec{E} through [269]:

$$\vec{v}_{n/p} \approx \mu_{n/p} \vec{E} \quad (4.14)$$

The mobility $\mu_{n/p}$ at low field strengths is influenced by three important, temperature

4. Etching

dependent, effects [211, 269, 164]:

- degradation of mobility due to phonon scattering,
- degradation due to Coulomb scattering on ionized impurities,
- and degradation due to polar-optical-phonon scattering.

The mobility due to the different effects μ_i can then be combined into an approximate overall mobility using Matthiessen's rule[151, 270, 269]:

$$\frac{1}{\mu_{total}} = \sum_i \frac{1}{\mu_i} \quad (4.15)$$

The mobility of the charge carriers here is based on the Caughey and Thomas model at room temperature [43]:

$$\mu_{n/p}(N_{def.}) = \mu_{min,n/p} + \frac{\mu_{max,n/p} - \mu_{min,n/p}}{1 + \left(\frac{N_{def.}}{N_{ref.,n/p}}\right)^{\lambda_{n/p}}}$$

which relates the mobilities for Electrons / holes ($\mu_{n/p}$) with the total defect or impurity concentration $N_{def.}$ in the material. Fig. 4.2 on the following page shows a fit of the Caughey and Thomas model for Gallium Arsenide at room temperature, showing the typical behavior of lowered mobilities with increasing impurity concentration as well as the lower mobility of holes in comparison to Electron mobilities which is quite common in IV-IV and III-V semiconductors. Tab. 4.3 on page 100 shows the room temperature parameters for some of the group IV and binary group III-V semiconductors that are interesting for Proton beam writing.

4. Etching

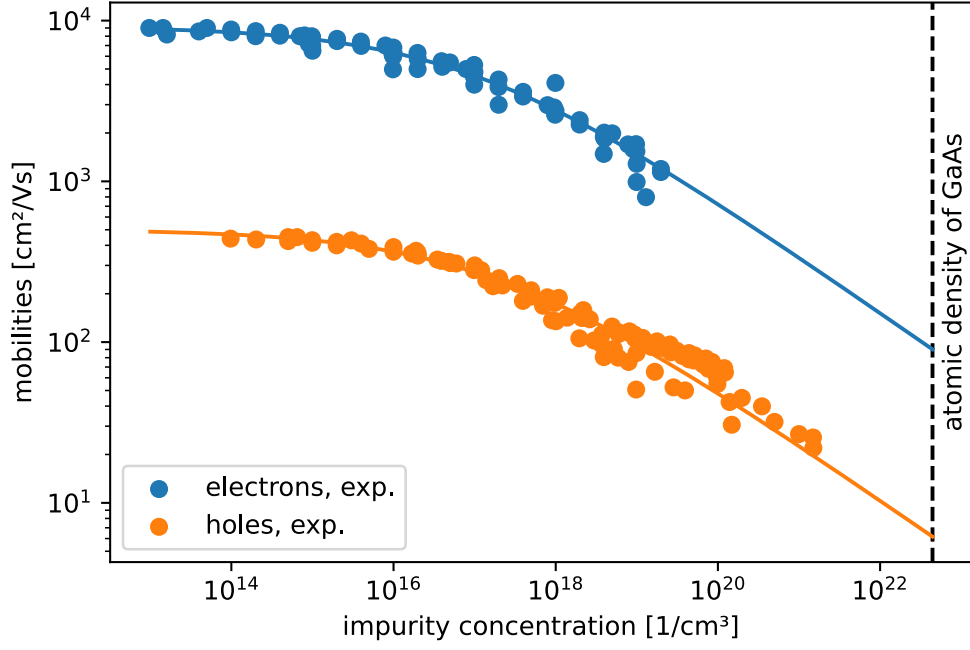


Figure 4.2.: Room temperature mobilities of Electrons and holes in Gallium Arsenide as a function of impurity concentrations and fit of the Caughey and Thomas model. Experimental data were taken from [253] and references therein.

4. Etching

material		$\mu_{max} \left[\frac{\text{cm}^2}{\text{Vs}} \right]$	$\mu_{min} \left[\frac{\text{cm}^2}{\text{Vs}} \right]$	$N_{ref.} \left[\frac{1}{\text{cm}^3} \right]$	λ	reference
Diamond	<i>n</i>	4500	0	5×10^{16}	1	[216]
	<i>p</i>	3443	55	1.12×10^{14}	0.589	
Si	<i>n</i>	1412	66	9.7×10^{16}	0.725	[147]
	<i>p</i>	469	44	2.4×10^{17}	0.70	
Ge	<i>n</i>	3800	850	2.6×10^{17}	0.56	[191]
	<i>p</i>	1800	300	1.0×10^{17}	1.0	
3C-SiC	<i>n</i>	1000	0	2×10^{17}	0.6	[118]
	<i>p</i>	100	0	2×10^{18}	0.7	
4H-SiC	<i>n</i>	1100	0	1.8×10^{17}	0.6	[118]
	<i>p</i>	120	0	2.2×10^{18}	0.7	
6H-SiC	<i>n</i>	275	0	2.5×10^{17}	0.6	[118]
	<i>p</i>	100	0	2.4×10^{18}	0.7	
AlN	<i>n</i>	683	297	1.0×10^{17}	0.86	[191]
	<i>p</i>	14	0	1×10^{17}	1	
GaN	<i>n</i>	1478	295	1×10^{17}	0.81	[191]
	<i>p</i>	170	3	3.0×10^{17}	1	
InN	<i>n</i>	3800	834	2.88×10^{17}	0.76	[191]
	<i>p</i>	200	0	1×10^{17}	1	
AlP	<i>n</i>	50	10	1×10^{18}	1	
	<i>p</i>	120	10	1×10^{18}	1	
GaP	<i>n</i>	150	10	4.4×10^{18}	0.80	[191]
	<i>p</i>	160	10	5×10^{17}	1.0	
InP	<i>n</i>	5300	1120	4×10^{16}	0.6	[191]
	<i>p</i>	200	10	4×10^{16}	1.0	
AlAs	<i>n</i>	410	10	5.0×10^{17}	0.5	[191]
	<i>p</i>	130	5	2.9×10^{17}	1.0	
GaAs	<i>n</i>	9222 ± 235	0	$(9 \pm 2) \times 10^{16}$	0.35 ± 0.02	[fig. 4.2]
	<i>p</i>	503 ± 14	0	$(16 \pm 4) \times 10^{16}$	0.35 ± 0.02	
InAs	<i>n</i>	32500	11700	4.4×10^{16}	0.5	[191]
	<i>p</i>	510	48	2.55×10^{17}	1.0	
AlSb	<i>n</i>	202	5	6×10^{18}	1.21	[191]
	<i>p</i>	450	50	1×10^{17}	1	
GaSb	<i>n</i>	5500	680	3.2×10^{17}	1.08	[191]
	<i>p</i>	1231	154	4×10^{17}	0.67	
InSb	<i>n</i>	77000	200	2×10^{17}	0.57	[191]
	<i>p</i>	774	48	2.36×10^{18}	0.39	

Table 4.3.: Parameters for the Caughey and Thomas mobility model. Values marked in blue were estimated by comparison to similar materials and rough interpolation.

4.3.4. Band structure and Fermi-Dirac statistics

Together with the mobility model, an accurate model for the density of free holes and Electrons needs to be used. The Electron and hole densities can be very well described by Fermi-Dirac statistics [269]. That means the density of free charge carriers as a function of the Fermi-energy level E_F is [269]:

$$n = 2 \left(\frac{m_n^* k_B T}{2\pi\hbar^2} \right)^{\frac{3}{2}} F_{1/2} \left(\frac{E_F - E_{c,eff.}}{k_B T} \right) \quad (4.16)$$

$$p = 2 \left(\frac{m_p^* k_B T}{2\pi\hbar^2} \right)^{\frac{3}{2}} F_{1/2} \left(\frac{E_{v,eff.} - E_F}{k_B T} \right) \quad (4.17)$$

with the effective upper edge of the valence band $E_{v,eff.}$, the effective lower edge of the conduction band $E_{c,eff.}$ and with the $1/2$ order Fermi integral $F_{1/2}(x)$ [53]:

$$F_{1/2}(x) = \frac{2}{\sqrt{\pi}} \int_0^{+\infty} \frac{\sqrt{y}}{1 + \exp(y - x)} dy \quad (4.18)$$

It is clear that the band gap is given by $E_g \approx E_{v,eff.} - E_{c,eff.}$. Tab. 4.4 shows the band gaps and effective masses m_n and m_p (for Electrons and holes) of many currently used materials in PBW as well as a few future candidates.

material	band gap [eV]	m_n [$m_{el.}$]	m_p [$m_{el.}$]
Diamond	5.47	0.2	0.25
Si	1.124	0.98	0.49
Ge	0.663	1.64	0.28
3C-SiC	2.36	0.247	1.32
4H-SiC	3.26	0.42	0.66
6H-SiC	3.02	0.48	0.66
AlN	6.22		
GaN	3.434	0.20	0.80
InN	1.894	0.12	
AlP	3.57	0.22	0.145
GaP	2.261	0.13	0.60
InP	1.350	0.0795	0.64
AlAs	2.163	0.15	0.22
GaAs	1.424	0.0635	0.56
InAs	0.360	0.026	0.40
AlSb	1.60	0.14	0.98
GaSb	0.73	0.039	0.40
InSb	0.176	0.0135	0.40

Table 4.4.: Band gaps [51, 191, 118] and density of states effective masses [288, 269, 118] of some semiconductors.

4. Etching

Due to the very high defect densities that can be reached in semiconductor material, band gap narrowing has to be taken into account. This describes the decrease in the effective band gap with increasing defect density. This is expected as when the doping density is at $10^{18} \frac{1}{\text{cm}^3}$, the average distance between impurities is about 10 nm and the energy levels of the impurities start to form energy bands instead of discrete energy levels [261]. The effective band gap in the new model is given by:

$$E_{gap,eff.} \approx E_{gap,0} + (E_{gap,atomic} - E_{gap,0}) \cdot \left(\frac{N_a + N_d}{\rho_0} \right)^{\frac{1}{3}}$$

with N_a as the density of acceptors and N_d the number of donators. In case of Gallium Arsenide, the atomic band gap is given by $E_{gap,atomic} = \frac{0.30120+0.8048}{2}$ eV, the mean of the band gaps of Gallium and Arsenic atoms. The exponent of $\frac{1}{3}$ follows from the screening of a free Electron gas and while not directly applicable to amorphous semiconductor material, it has been calculated that at high enough defect densities, Thomas-Fermi screening (which has this characteristic exponent) would dominate at low temperatures [273, 274]. Fig. 4.3 shows a comparison between the newly proposed model and the experimentally measured band gaps.

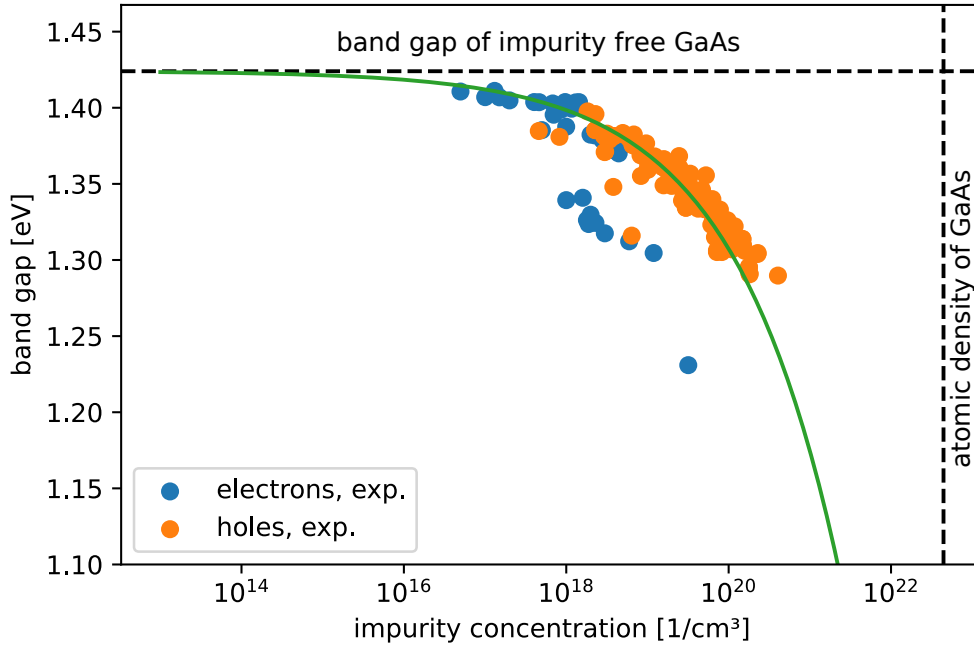


Figure 4.3.: Comparison between the experimentally [31, 308, 86, 146, 307, 126, 27] determined band gap of Gallium Arsenide as a function of the doping density and the newly proposed model.

4. Etching

4.3.5. Current densities

There are several processes by which the concentration of free charge carriers can change at a certain point in space. Due to charge conservation they can only move away, causing a net current at the point, they could recombine with free charge carriers of the opposite sign or new charge carriers can be created in pairs of opposite signs. Using the current densities \vec{J}_n and \vec{J}_p and the carrier recombination rate R this can be written as [53, 109]:

$$\frac{\partial n}{\partial t} = \frac{1}{q} \vec{\nabla} \cdot \vec{J}_n + R_n \quad (4.19)$$

$$\frac{\partial p}{\partial t} = -\frac{1}{q} \vec{\nabla} \cdot \vec{J}_p + R_p \quad (4.20)$$

The current densities in a drift diffusion model can be written as [53, 109]:

$$\vec{J}_n = q\mu_n n \vec{\nabla} V \quad (4.21)$$

$$\vec{J}_p = -q\mu_p p \vec{\nabla} V \quad (4.22)$$

The reaction rates R can include charge carrier generation or recombination as well as the surface reactions that belong to the corrosion processes. An approximate surface reaction rate can be reconstructed from the Butler-Volmer equation for example [16]. For the interior of the semiconductor material, many different charge carrier generation and recombination models exist [269] and an appropriate selection needs to be made based on the material. For simplicity, for Gallium Arsenide, in this work only a direct recombination model is used [269]:

$$R \approx c \cdot (n \cdot p - n_i^2)$$

with $c \approx 10^{-10} \frac{\text{cm}^3}{\text{s}}$ and the intrinsic charge carrier density [269]:

$$n_i = 2 \sqrt{\left(\frac{m_n^* k_B T}{2\pi \hbar^2} \right)^{\frac{3}{2}} \left(\frac{m_p^* k_B T}{2\pi \hbar^2} \right)^{\frac{3}{2}}} \exp \left(\frac{-E_g}{2k_B T} \right) \underset{T=300 \text{ K}}{\approx} 2.0 \times 10^6 \text{ cm}^{-3}$$

4.4. Deformation

One aspect of the PBW that was largely ignored as of yet, is the deformation of the defect rich material during the etching process. Commonly, the irradiated (defect rich) material has slightly different mechanical properties than the surrounding material. Both the density and the elastic moduli are expected to differ slightly, while at the same time the material may also become more brittle. Amorphous Silicon, as an example of a defect rich material, was found to be about 1.8% less dense than its mono-crystalline counterpart [54], in case of $\alpha - \text{Al}_2\text{O}_3$ the difference can even exceed 4% while the similar material MgAl_2O_4 does not show any signs of radiation induced swelling [119]. This means, that the radiation damage of Protons as well as interstitial Hydrogen in the target material

4. Etching

will usually create some strain. While structures on the micrometer scale are usually not deformed very much as they are freed from the surrounding material during etching, under certain conditions, particularly at the nanometer scale or in complicated structures, the final 3D structures might deform noticeably or even break. The impact on negative resists (or p-doped semiconductors) is expected to be by far greater than on positive resists (or n-doped semiconductors) as the defect rich and modified material is left behind in the former case, whereas it is removed in the later case.

To model these effects, a model for the mechanical properties of the target material needs to be used. The simplest models for this consider only linear elasticity. Fig. 4.4 on the following page shows the deformation during the etching process of a 2D cut through an irradiated negative resist modeled by assuming only isotropic, harmonic interactions in the material. For this the impact of Proton beam induced defects on the material properties were assumed to be as simple as possible, that is a linear change of the density as well as an exponentially decreased solubility with no change in elastic moduli. The simulation uses a coarse-graining technique where the material is approximated by representative particles that interact harmonically with 6 surrounding other particles. Structural relaxation is performed by a simplified Newtonian method.

4. Etching

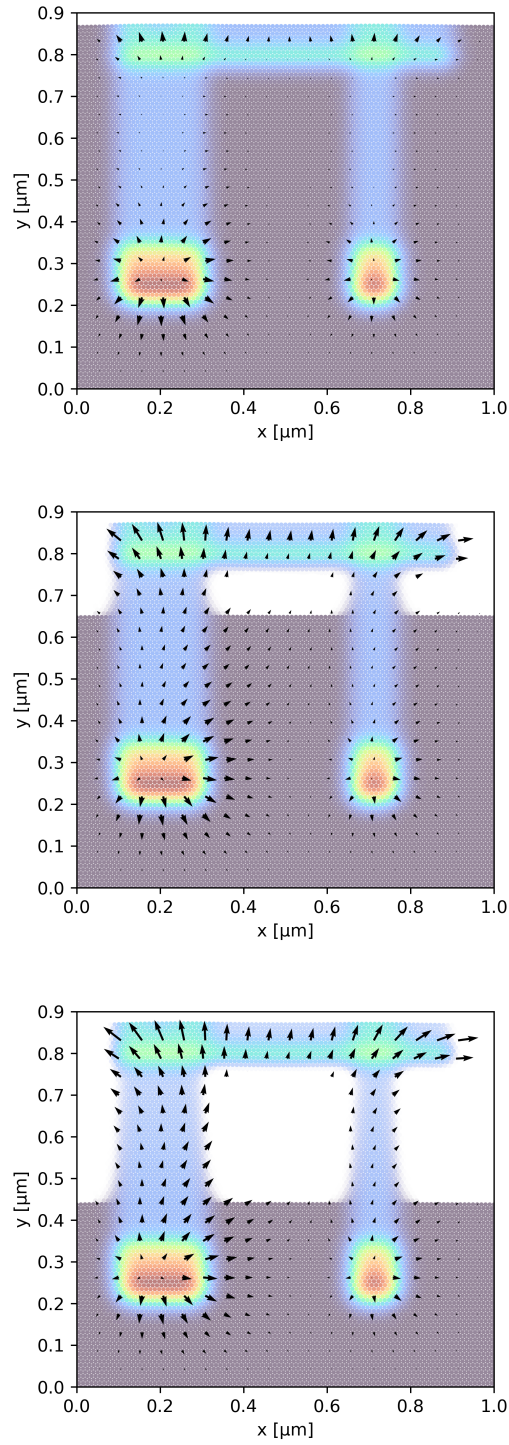


Figure 4.4.: Slice through a 3D structure in a negative resist during etching. The arrows indicate the deformation due to radiation damage caused swelling of the material. The colors indicate the local defect density.

4. Etching

For these type of elastic simulations the mechanical properties of the target need to be known, including an estimate for the swelling due to radiation damage and Hydrogen incorporation. While for the latter case the density of the amorphous target may be used as an estimate, the former case requires knowledge of several elastic constants of the target. While for resists experimental or values from molecular dynamics simulations may have to be used, for a large fraction of the technologically important inorganic semiconductors, several empirical relations are available. In fig. 4.5 on the next page the relation between the elastic constants of various group IV and III-V compound semiconductors in the Zincblende or Diamond phase with the equilibrium volume per atom is shown. These materials cover a large fraction the technologically important semiconductors. It is visible, that the constants follow an approximate exponential dependence of the elastic constants with the equilibrium volume per atom that is most pronounced for the bulk modulus $B_0 = \frac{c_{11}+2c_{12}}{3}$. c_{ij} are the commonly used elastic constants [313]. More specifically:

$$B_0(V_0) \approx 4.7 \cdot 10^5 \cdot \exp \left[- \left(\frac{V_0}{3.8 \cdot 10^{-4} [\text{Bohr}^3/\text{atom}]} \right)^{0.159} \right] [\text{GPa}]$$

Relations like this can be used to approximate elastic properties of new materials without having to perform ab initio simulations [305] and are ideally suited for the type of deformation simulations considered here. It should be noted that the stable phase under standard conditions for the Nitrides is the Wurtzite crystal structure phase instead of the Zincblende structure phase considered here.

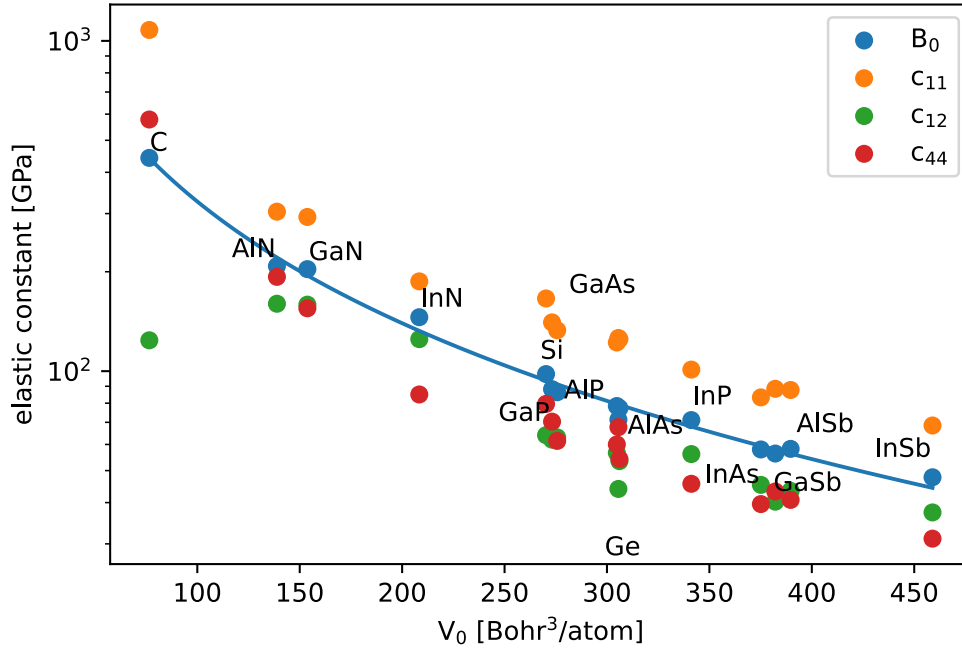


Figure 4.5.: Elastic constants of Diamond crystal structure group IV and Zincblende crystal structure III-V compound semiconductors as a function of the equilibrium volume per atom [153, 154, 182, 288] as well as an approximate exponential fit. Some of the values in a comprehensive review [288] were also found to have a unit conversion error and were corrected for this plot.

In many applications, more complicated compounds with the sum formula A_xB_{1-x} or $A_xB_{1-x}C$ (for example SiC, $\text{In}_x\text{Ga}_{1-x}\text{As}$ or $\text{Al}_x\text{Ga}_{1-x}\text{P}$) are used. Such ternary compounds can also be created in the target through ion induced mixing when irradiating layered materials. In case there is no phase change, the mechanical properties of these compounds can be interpolated linearly from the properties of the simpler compounds that constitute them. This mixing rule of properties is known as Vergard's law [287]. Though it was found that the experimental lattice constants usually are slightly smaller than predicted by Vergard's law, with some notable exceptions (for example $\text{Al}_x\text{Ga}_{1-x}\text{As}$) [174].

As indicated in fig. 4.4 on page 105, in some cases reasonably large deformations could be present in some volumes of the target material. This means an accurate theory of describing materials under large strains beyond the harmonic approximation employed here may be necessary to predict the correct final shapes of the resulting 3D structures. In particular equations of state and elasticity constants are required that cover the experimentally achievable conditions. As an initial work towards such a theory, the equations of state at room temperature for group IV and III-V compound semiconductors

4. Etching

in the Zincblende or Diamond structural phase are investigated. Fig. 4.6 shows the energy per atom of some of these compounds as simulated with `Elk 8` with the `r2SCAN` functional and a k -point density of $10 \times 10 \times 10$. The energy per atom relative to the equilibrium state is shown as a function of the volume per atom divided by the equilibrium volume. As visible, the curves are very similar, hinting at similar elastic behavior even up to $\frac{V}{V_0} = 1.5$. It should be noted that Indium and Antimony containing compounds were also simulated but showed unphysical energy-volume curves, hinting at some problems with the atom setup configurations of the two elements in `Elk 8`.

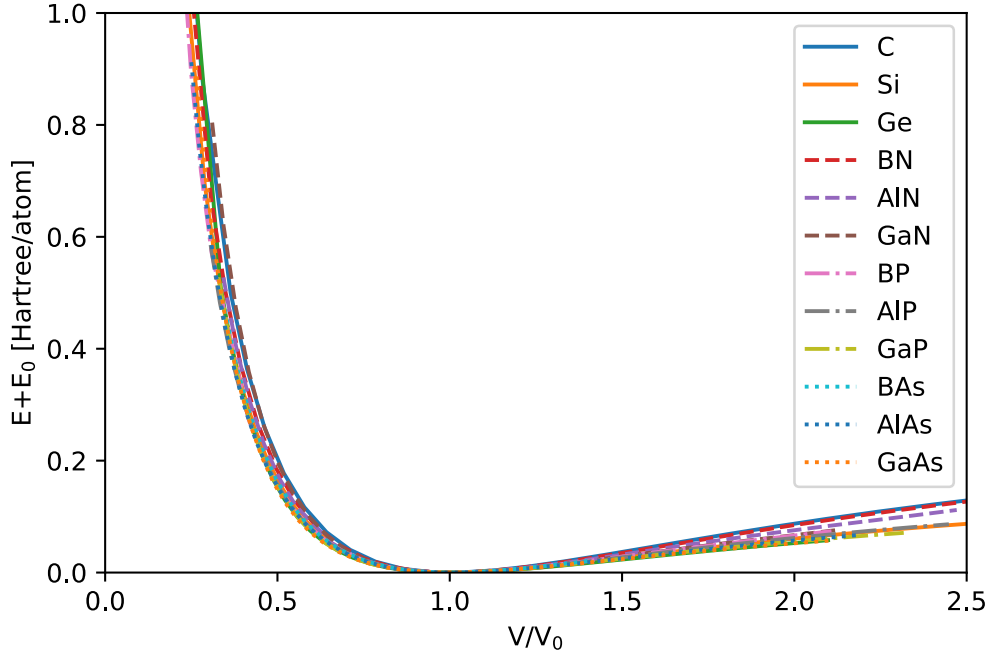


Figure 4.6.: Energy per atom relative to the equilibrium value as a function of the reduced volume per atom for different semiconductors in the Diamond or Zincblende structure phase.

At low volumes the pressure necessarily approaches infinity. The ratio between pressure and bulk modulus likely does not and instead it approaches a finite, positive value [259]. This is shown in fig. 4.7 on the following page for the semiconductors simulated here. The calculation of the pressures and bulk moduli were performed with `Gibbs2` [224, 223, 225] using a quasi-harmonic Deybe model for thermal corrections at room temperature [22]. This thermal model requires the Poisson ratio of the materials. For some materials, experimental Poisson ratios were used [252, 277], otherwise they were estimated as $\frac{c_{12}}{c_{11}+c_{12}}$ [153, 154, 182, 288] or left at 0.25.

4. Etching

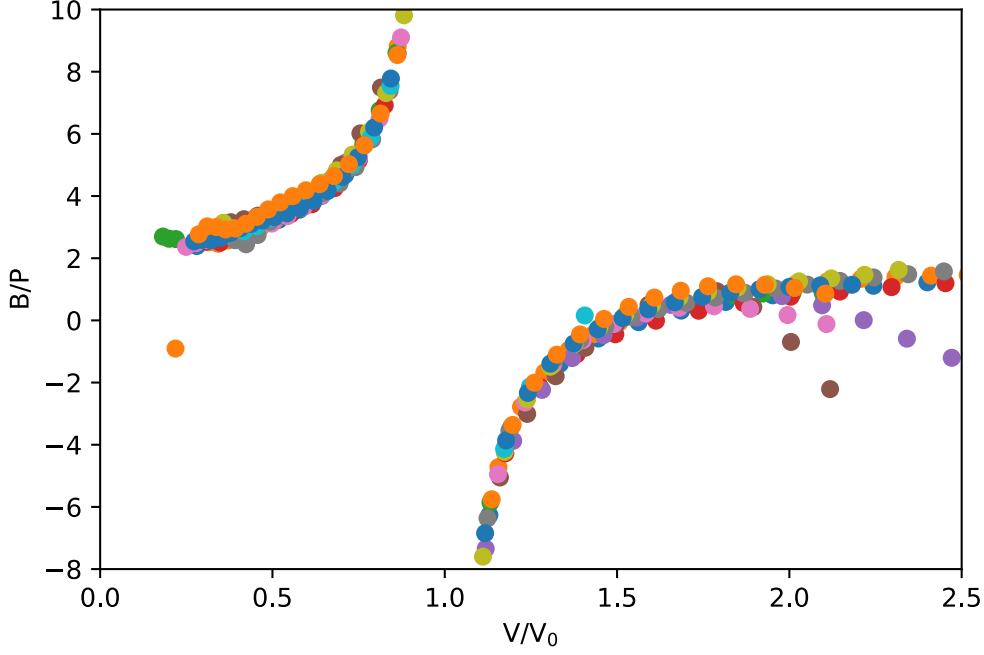


Figure 4.7.: The ratio of bulk modulus and pressure $\frac{B}{P}$ as a function of the atomic volume relative to the ground state $\frac{V}{V_0}$ for the semiconductors considered here.

The visible relationship implies equations of state of the form [259]:

$$\left. \frac{\left(\frac{V}{V_0}\right)^{-B'_\infty}}{P} \right|_{\frac{V}{V_0} \rightarrow 0 \text{ or } \frac{V}{V_0} \rightarrow \infty} = B'_\infty$$

where $B'_\infty = 2.910(3)$ is found by least squares fitting. It has been argued that this value should be greater than $\frac{5}{3}$ [259], which is also supported by the simulations carried out here. It is notable that for $\frac{V}{V_0} \rightarrow \infty$ the same value is approached. Based on the simulations, a new equation of state can be proposed:

$$P = \frac{B_0}{2B'_\infty - B'_0} \left[1 - \left(\frac{V}{V_0}\right)^{2B'_\infty - B'_0} \right] \left(\frac{V}{V_0}\right)^{-B'_\infty}$$

In this equation, $B'_0 = 3.6558(2)$ was found by least squares fitting and seems to describe the materials considered here fairly accurately. This equation of state can also be compared to experimental data and existing equations of state. A large variety of equations of state exist that are commonly used to describe materials over a wide range of pressures. Some of the most popular ones are the Vinet, generalized Rydberg and

4. Etching

Birch-Murnaghan equations of state. The Birch-Murnaghan equation of state can be written as [173, 21]:

$$P = \frac{3B_0}{2} \left[\left(\frac{V}{V_0} \right)^{\frac{7}{3}} - \left(\frac{V}{V_0} \right)^{\frac{5}{3}} \right] \cdot \left\{ 1 - \frac{3}{4} (4 - B'_0) \cdot \left[\left(\frac{V}{V_0} \right)^{\frac{2}{3}} - 1 \right] \right\}$$

where, in addition to V_0 , B_0 and B'_0 are fitting parameters. B_0 is the bulk modulus at equilibrium volume and $B'_0 = \frac{dB}{dP}|_{P=0}$ its pressure derivative. The generalized Rydberg equation of state is given by [12, 258]:

$$P = 3B_0 \left(\frac{V}{V_0} \right)^{-B'_\infty} \left[1 - \left(\frac{V}{V_0} \right)^{\frac{1}{3}} \right] \exp \left\{ \left(\frac{3}{2}B'_0 - 3B'_\infty + \frac{1}{2} \right) \left[1 - \left(\frac{V}{V_0} \right)^{\frac{1}{3}} \right] \right\}$$

where V_0 , B_0 , B'_0 and B'_∞ are fitting parameters. Setting $B'_\infty = \frac{2}{3}$ the equation reduces to the original Rydberg equation of state [12]. The original Rydberg equation of state and the Vinet equation of state are identical [257]. Fig . 4.8 on the next page shows a fit of the different equations of state to the experimental data [156] of Gallium Arsenide in comparison to the ab-initio DFT results. As visible, in comparison to the experimental data, the simulations with the r2SCAN functional create a slightly too attractive interaction between the atoms in the solid but are otherwise fairly accurate. The Birch-Murnaghan equation of state is unfortunately only accurate over a relatively narrow range of volumes (about $0.8 < \frac{V}{V_0} < 1.05$) whereas the generalized Rydberg equation of state is not easily invertible but relatively accurate over the entire range of data. The newly proposed equation of state is both accurate and easier to invert than the generalized Rydberg equation of state. It also can be integrated to an energy-volume form that is similar to the Birch-Murnaghan equation and can be interpreted in a similar manner.

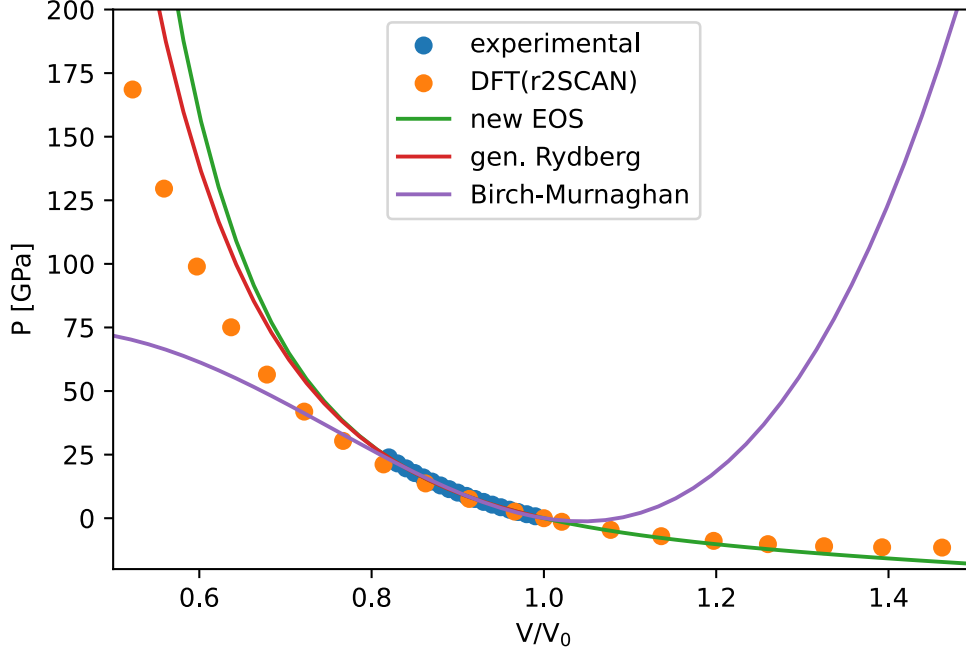


Figure 4.8.: Comparison between experimental [156] pressure versus volume data of Gallium Arsenide with fits to them by the different equations of state as well as the ab-initio DFT simulations with the r2SCAN functional.

Besides the bulk modulus, the other elastic constants also need to be estimated under pressure. As a very rough estimate, the change of the other elastic constants can be approximated to be identical to the change of the bulk modulus from the equilibrium value. This works well for c_{11} and c_{12} , as their pressure derivatives are about the same as the one of the bulk modulus for Gallium Arsenide, for example. For c_{44} about $\frac{1}{4}$ of this change fits rather well when compared with experimental data [156].

As presented in this section, it is possible to construct very simple models that describe the deformation of irradiated and etched structures. These models can also be extended to non-linear elastic models in case of large deformations of the target structures. These types of simulations can serve as a powerful tool to investigate deformations of target structures. It should be noted though that most of the structures created for this work and found in the literature do not show very significant deformation, which is not surprising, considering that the density changes of amorphous materials is only in the order of a few percent and the target defect densities are often orders of magnitude below the defect densities required to fully amorphize the target material locally, as previously discussed.

5. PBW in Gallium Arsenide

5.1. Radiation damage

Gallium Arsenide has been the primary target material for PBW research in Göttingen for a relatively long time [237, 236, 222, 261]. The reasons for this were the early successes in the creation of 3D structures with this material, the excellent quality of readily available wafers and the (by comparison) relatively safe etchant. Before the beginning of this work, an approximate Proton fluence threshold for PBW in Gallium Arsenide had been experimentally established and with it simple structures were created [237, 222], the electrochemistry of the unirradiated material was investigated [261] and the first generation of mostly ohmic models for the description of the etching process were developed [236, 261]. This work expands upon this previous work and investigates some aspects in more detail.

A first step in the description of PBW in Gallium Arsenide is the description of the changes in the material due to the radiation damage. For this a detailed model was previously developed [261] that describes how the effective doping of the target changes locally due to radiation damage. This model already surpassed the previously published models in both the range of validity and accuracy [52]. Based on a larger set of experimental data and more precise simulations, this model is revised.

For this, irradiation experiments [33] were considered, where semi-insulating samples of Gallium Arsenide were implanted with 900 keV Mg^+ ions up to a dose of $2.5 \cdot 10^{13} \frac{1}{\text{cm}^2}$ or C^+ ions up to a dose of $5 \cdot 10^{13} \frac{1}{\text{cm}^2}$ at room temperature. This was followed by cap-less rapid thermal annealing to 950 °C for 10 s to activate the dopants and perform defect defect annealing. While diffusion at these elevated temperatures may also cause a broadening of the implantation distribution in the sample, it was shown [261] that in this case this is negligible, which is also one of the aims of the chosen annealing method [281]. The chosen, cap-less (Gallium Arsenide proximity) annealing has the advantage that surface degradation due to Arsenic loss is largely avoided [116]. This procedure creates conductive, p-type layers inside the target material. The sheet hole concentrations and sheet resistances were measured and the material was then irradiated with 400 keV Protons with doses ranging between $5 \cdot 10^{10} \frac{1}{\text{cm}^2}$ to $2 \cdot 10^{16} \frac{1}{\text{cm}^2}$ under a tilt angle of 7°. The tilt angle was introduced to suppress channeling effects [293]. The depth of the previously created conductive layer was chosen in such a way that the radiation damage of the 400 keV Protons would be relatively homogeneous over the entire conductive layer. As such, the effects of radiation damage on the conduction of the sample could be studied by measuring the sheet resistance of the sample to a good approximation. This is shown in fig. 5.1 on the following page, where the concentration of Mg and C after implantation is shown, based on a simulation with SRIM, together with the predicted free charge carrier

5. PBW in Gallium Arsenide

densities of Electrons and holes based on Fermi-Dirac charge carrier statistics and the mobility and band gap models proposed in this work, as well as the sheet resistance and sheet hole concentration measured [33]. Also shown is the concentration of Hydrogen and defects created during irradiation with a Proton dose of $10^{14} \frac{1}{\text{cm}^2}$. Note how the defect density does not vary very much over the thin conductive layer produced by implantation.

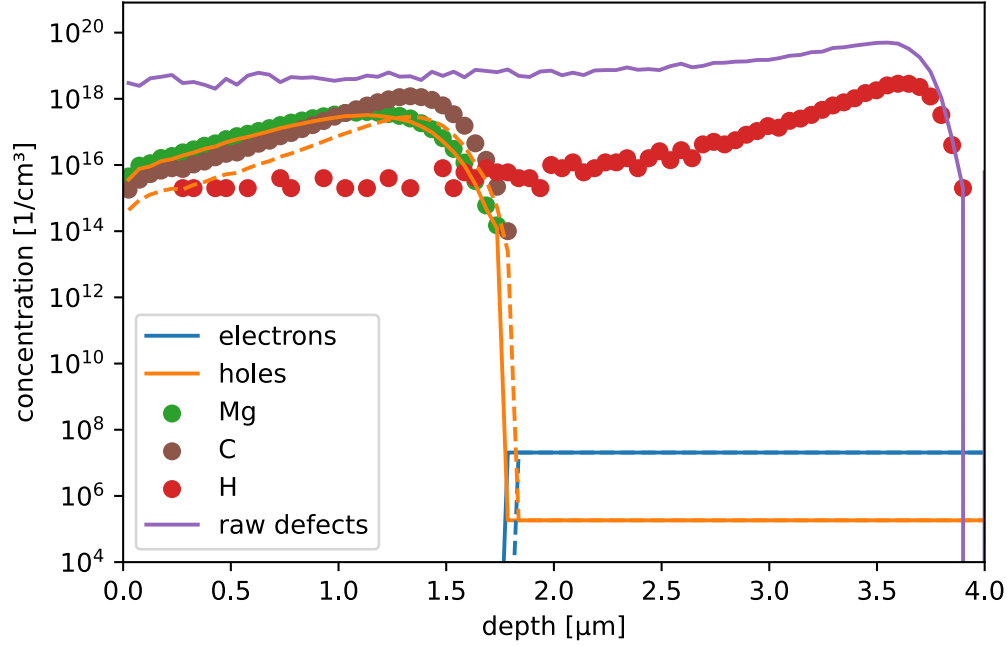


Figure 5.1.: Concentration of Mg and C in GaAs according to a simulation with SRIM and a semiconductor simulation of the experimental conditions described in the text. Also shown is the resulting free charge carrier density of holes and Electrons in the sample, as well as the defect and Hydrogen density introduced by irradiation with 400 keV Protons under a tilt angle of 7° with a dose of $10^{14} \frac{1}{\text{cm}^2}$. The continuous lines correspond to the Magnesium implantation, the dashed lines to Carbon.

Fig. 5.2 on the next page shows the resulting sheet resistance as a function of the Proton dose. In this plot it is visible that for low doses the sheet resistance rises up to the point of the bulk sheet resistance of the semi-insulating wafer this experiment is carried out in. At a certain dose the sheet resistance falls off again due to hopping conductivity in the irradiated material. As discussed previously, this behavior can be explained best if it is assumed that the introduced defects by radiation damage partially act as charge traps and counter the previous doping of the target material. Based in this and previous work [261], a new effective doping model is proposed:

5. PBW in Gallium Arsenide

$$N_{a/d,eff.}(\vec{r}) \approx N_{a/d}(\vec{r}) \cdot \exp \left[-2.097 \cdot 10^7 \cdot \left(\frac{\rho_{Defects}(\vec{r})}{\rho_{GaAs}} \right)^{1.368} \right] \\ + 0.8 \cdot \rho_{GaAs} \cdot \left[1 - \exp \left(-25.0 \cdot \frac{\rho_{Defects}(\vec{r})}{\rho_{GaAs}} \right) \right]$$

where $N_{a/d,eff.}(\vec{r})$ is the effective doping (for acceptors a or donators d) at position (\vec{r}) based on the doping before irradiation $N_{a/d}(\vec{r})$ and the dose of radiation induced defects $\rho_{Defects}(\vec{r})$. The dimensionless fitting constants have relative uncertainties on the order of 0.1. In contrast to the previous model [261], the new model is slightly more accurate and altogether simpler. The interpretation of the general behavior of the target materials remains the same, though. That is: the first term describes the removal of the doping of the target material due to the introduction of defects deep in the band gap that can trap charges. The second term describes the introduction of new doping levels near the band edges due to radiation damage. In the limit of large radiation defect densities, the doping reaches a value of about $2 \times 0.8 \cdot \rho_{GaAs} \approx 7 \cdot 10^{22} \frac{1}{\text{cm}^3}$ which compares rather well with the density of hopping centers observed experimentally ($5 \cdot 10^{22} \frac{1}{\text{cm}^3}$ [115]).

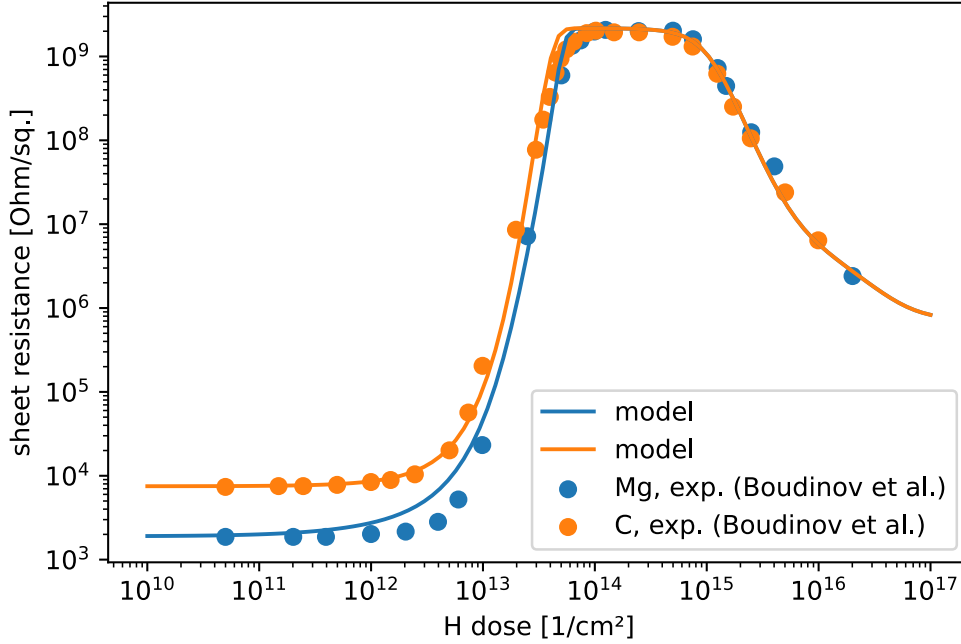


Figure 5.2.: Sheet resistance as measured [33] for a semi-insulating Gallium Arsenide sample with a conductive layer created though ion implantation. Measurements were performed at varying degrees of irradiation with Protons. Shown are the experimental values and the model fit proposed here in comparison.

The fit of the new model to the experimental data is shown in fig. 5.2 on the preceding page. It should be noted that in contrast to previously published models [115, 52], a description of the conductivity over the entire fluence range is possible.

5.2. Etching

With the effects of radiation damage of the target well described, the etching step needs to be considered next. Fig. 5.3 shows the Pourbaix diagram of Gallium Arsenide as calculated with SPANA/MEDUSA [209] using the simplified Helgeson-Krikham-Flowers activity model [92, 209]. This diagram can also be compared to similar, albeit less complete, diagrams in the literature [194, 44, 140, 207, 180].

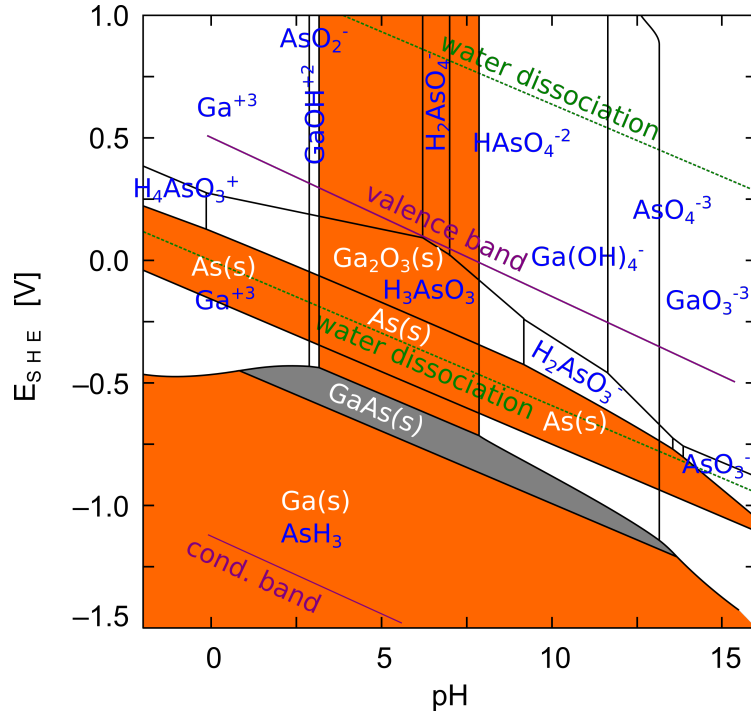


Figure 5.3.: Pourbaix diagram (phase diagram as a function of pH value and applied voltage with respect to a standard hydrogen electrode) of Gallium Arsenide as calculated with SPANA/MEDUSA [209]. Also shown is the region of stability of water (marked by the dissociation limit) and the position of the valence and conduction bands of Gallium Arsenide.

From the Pourbaix-diagram of Gallium Arsenide alone it is difficult to decide on an optimal pH value for the electrolyte for etching. Regions of interest are the regions at very low pH and medium to high pH as here voltages exist where Gallium Arsenide dissociates into solvated ions. A limitation on the possible potentials is given by the region of stability of water. Among these regions the high pH region is particularly suited

5. PBW in Gallium Arsenide

for etching. This is due to the fact, that Gallium and Arsenide atoms on the surface tend to behave more similar electrochemically for these high pH values [3]. This means that different surfaces with differing Gallium and Arsenide surface atomic fractions will be etched with similar rates, thus reducing anisotropy in the final structures due to etching. As discussed previously, the corrosion process also involves electrical conduction. Fig. 5.4 shows the conductivity of KOH electrolytes as a function of pH. As visible, an optimum exists around pH 14.8. Experimentally, structures etched around pH 14 to 15 in this work tended to have the least washed out appearance. From a conductivity standpoint, this appears reasonable, as a highly conductive electrolyte will hinder the corrosion process less than a low conductivity one, thus preserving more of the detail and sharp corners of the structures.

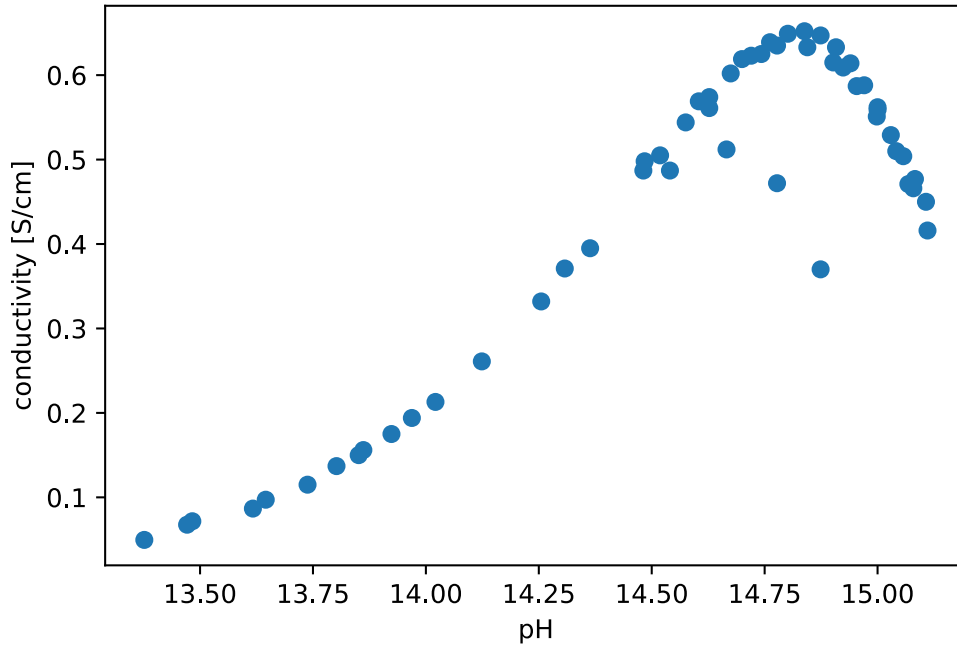
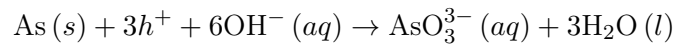
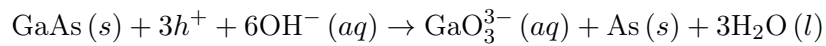


Figure 5.4.: Experimental conductivity (from the sources of [75]) of KOH solutions with water at 25°C as a function of the pH value of the solution.

At pH 13.3 and up, the sum reaction of the corrosion process of a Gallium Arsenide electrode can be written as (corrected from [3]):



5. PBW in Gallium Arsenide

Since the chemical reactions happen with holes h^+ from the valence band of Gallium Arsenide, the expected equilibrium voltage of the reaction with respect to the standard Hydrogen electrode potential should be in the range of -0.2 ... -0.5 V, which is also what is observed experimentally. The (etching-) current through a p-type (Zn doped) Gallium Arsenide $\langle 100 \rangle$ was investigated in an etch cell. For this ohmic back contacts made from Indium were applied and the voltage and current were recorded in a PTFE etching cell with a KOH electrolyte with a 3 point measurement and a reversible Hydrogen electrode. These back contacts were previously characterized and due to their almost ideal ohmic behavior [261] they replaced the conductive Silver contacts of previous measurements that had a more rectifying behavior [237, 222].

5. PBW in Gallium Arsenide

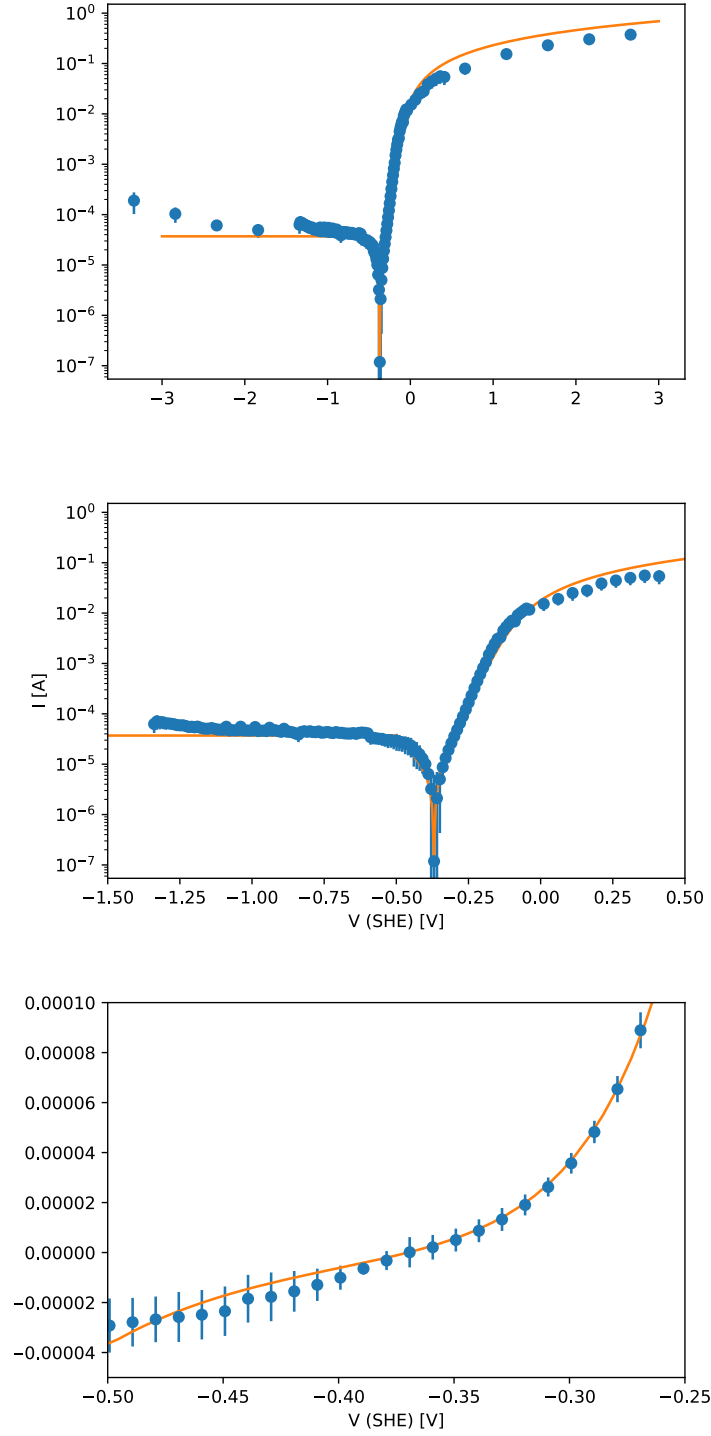


Figure 5.5.: Current in the dark as a function of applied voltage across a p-doped Gallium Arsenide $\langle 100 \rangle$ surface in a KOH solution with a pH of 14.2 as measured with a standard Hydrogen electrode at room temperature.

5. PBW in Gallium Arsenide

As discussed previously and also in more detail in previous work [261], the current in an etching process can be described approximately using the Butler-Volmer equation. Fig. 5.5 on the previous page shows an example of a current measurement across a Gallium Arsenide surface. In the area around the equilibrium potential E_0 , the current can be described well with the Butler-Volmer equation:

$$I(V, T) = I_0 \cdot \left[\exp \left(\alpha_1 z \frac{q_{el.}}{k_B T} (V - E_0) \right) - \exp \left(-\alpha_2 z \frac{q_{el.}}{k_B T} (V - E_0) \right) \right]$$

where V is the applied potential and T is the temperature. In the direct vicinity of the equilibrium potential, the Butler-Volmer equation can also be linearized to read:

$$I(V, T) \approx I_0 (\alpha_1 + \alpha_2) z \frac{q_{el.}}{k_B T} (V - E_0) + \mathcal{O}((V - E_0)^2)$$

this allows to extract the equilibrium potential easily by fit. In the high over-potential regions, the current though the surface is limited by the rate at which the reaction partners can be supplied to it. Several models exist to describe this behavior[261], however, here the following implicit equation is used:

$$I(V, T) \approx I_0 \cdot \left[\exp \left(\alpha_1 z \frac{q_{el.}}{k_B T} (V - E_0 - R \cdot I) \right) - \exp \left(-\alpha_2 z \frac{q_{el.}}{k_B T} (V - E_0 - R \cdot I) \right) \right] \quad (5.1)$$

where the over-potential $V - E_0$ is reduced by the potential drop $R \cdot I$ in the bulk of the material at large currents. In tab. 5.1 the fit values to the experimental data for this equation are shown.

quantity	value
I_0	$5.6 (12) \cdot 10^{-6} \text{ A}$
$\alpha_1 z$	$0.71 (6)$
$\alpha_2 z$	$0.38 (6)$
E_0	$-0.370 (4) \text{ V}$
R	$4.25 (7) \Omega$

Table 5.1.: Fit values for the parameters for the modified Butler-Volmer current eq. 5.1 for p-type Gallium Arsenide at pH 14.2.

Upon Hydrogen irradiation, the current-voltage relation across the surface necessarily changes. The largest effect, which is also the primary mechanism for PBW in p-type GaAs, is the change in resistance of the bulk material. This leads to a lowering of the current limit. A more subtle effect happens due to the shifting of the Fermi level in the band gap towards the center. This means the equilibrium potential of the corrosion reaction is shifted towards the center of the band gap of Gallium Arsenide. A similar effect has also been discussed in the literature for doped material [4]. Another change in the electrochemical behavior of the surface happens when Hydrogen is near the surface.

5. PBW in Gallium Arsenide

In this case the surface will act more like a Hydrogen electrode as the Hydrogen partakes in the surface reactions. That is: the equilibrium potential is shifted towards the potential of a reversible hydrogen electrode and the reverse current is suppressed.

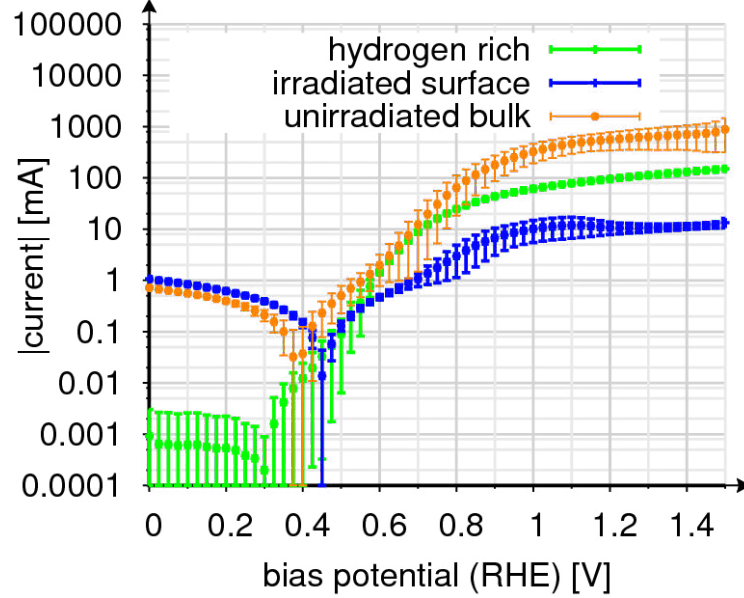


Figure 5.6.: Experimental current through a $\langle 100 \rangle$ p-type Gallium Arsenide surface at pH 14.3 in the dark as a function of the applied potential (measured with a reversible Hydrogen electrode). See the text for an explanation of the three samples.

As visible in fig. 5.6, these effects were investigated separately. For this, three samples were prepared from a single p-type (Zn doped) Gallium Arsenide $\langle 100 \rangle$ wafer and, except for the irradiation step, were treated identically. For the influence of near surface defects, one sample was irradiated with Protons at an energy of 400 keV at the IONAS accelerator up to a dose of $50 \frac{\mu\text{As}}{\text{cm}^2}$. Fig. 5.7 on the following page shows the estimated defect density in the target as simulated with IIS [95]. This simulation takes the crystal structure of the target into account and can account for channeling to some extent. Additionally, a one lattice constant thin, amorphous layer was added in the simulation to take into account the degradation of the crystal structure at the surface of the sample. As visible, almost no Hydrogen is present at the surface of the sample. For investigation of near surface Hydrogen, the second sample was irradiated up to $500 \frac{\mu\text{As}}{\text{cm}^2}$ with 100 eV Protons at the ADONIS accelerator. At these energies, very little damage is generated in the target, while the Hydrogen is implanted to a depth of about 20 Angstrom, as estimated by SRIM 2013. This creates a very high Hydrogen concentration near the target surface. The third sample acts as a control.

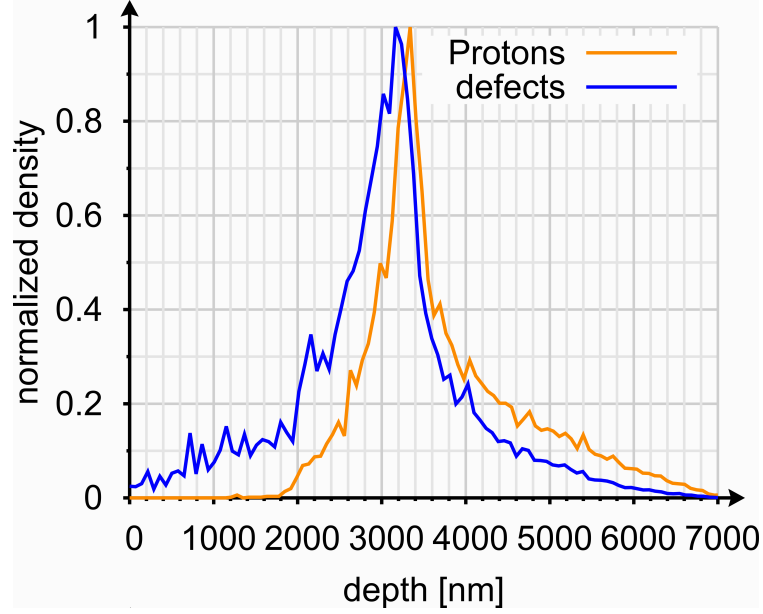


Figure 5.7.: IIS [95] simulated, normalized defect density of 400 keV Proton irradiated $\langle 100 \rangle$ Gallium Arsenide as a function of depth from the surface of the sample.

This information on the effects on radiation defects near the surface as well as the influence of Hydrogen at the surface of the target can be used to reconstruct the material that is etched away and to control the etching process. Fig. 5.8 on the next page shows the etching of the sample that was irradiated with 400 keV Protons up to a dose of $50 \frac{\mu\text{As}}{\text{cm}^2}$. These Protons had a range of about $6 \mu\text{m}$ in Gallium Arsenide, estimated by simulations. This range is also visible in the current voltage curves, as they change gradually up to a depth of about $6 \mu\text{m}$ when they assume the shape of unirradiated material rather abruptly and etch away much quicker. The etching depth was reconstructed by integration of the total etching current (current in the forward direction). Since the chemical reaction at the surface it known to use $6h^+$ in total for each pair of atoms removed from the sample, the etch rate and depth can be reconstructed easily, as was also shown previously [237, 261].

5. PBW in Gallium Arsenide

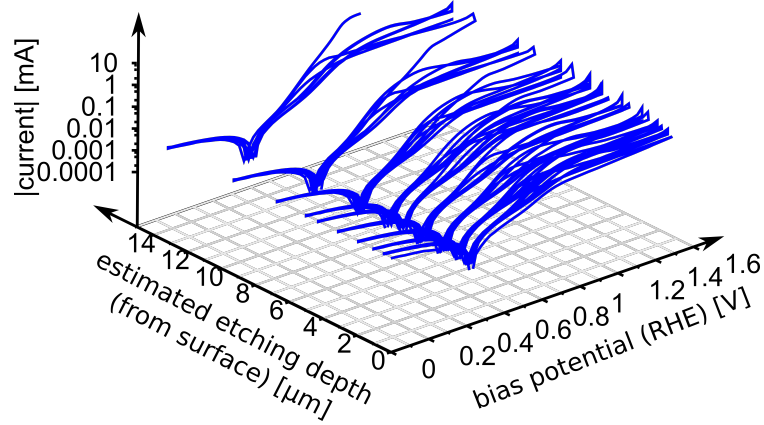


Figure 5.8.: Absolute value of the current as a function of the applied potential (measured here with a reversible Hydrogen electrode) and a reconstruction of the etching depth of the target as a Gallium Arsenide irradiated with 400 keV Protons is etched.

The results so far raise the question on how the microscopic conditions change at the interface between the semiconductor and the electrolyte due to the radiation damage. The primary changes discussed so far point to a change of the equilibrium potential of the corrosion reaction that can be associated primarily with a shift in the Fermi-energy level in the band gap of the Gallium Arsenide. However, the effective voltage across the interface (and thereby the charged carrier densities at the interface) may also change as well as the microscopic structure of the electrolyte near the surface. To investigate the effects further, several options for measurements exist. The simplest measurements for this would be cyclic voltammetry measurements, where the voltage across the semiconductor and electrolyte is continuously swept between two extreme values. Fig. 5.9 on the following page shows such a measurement for a Platinum electrode mounted in the etching cell. The peaks visible in the current of the electrode are associated with adsorption, desorption and charge transfer reactions at the electrode surface. In case of Gallium Arsenide surfaces, however, very little new information was gained by these measurements.

5. PBW in Gallium Arsenide

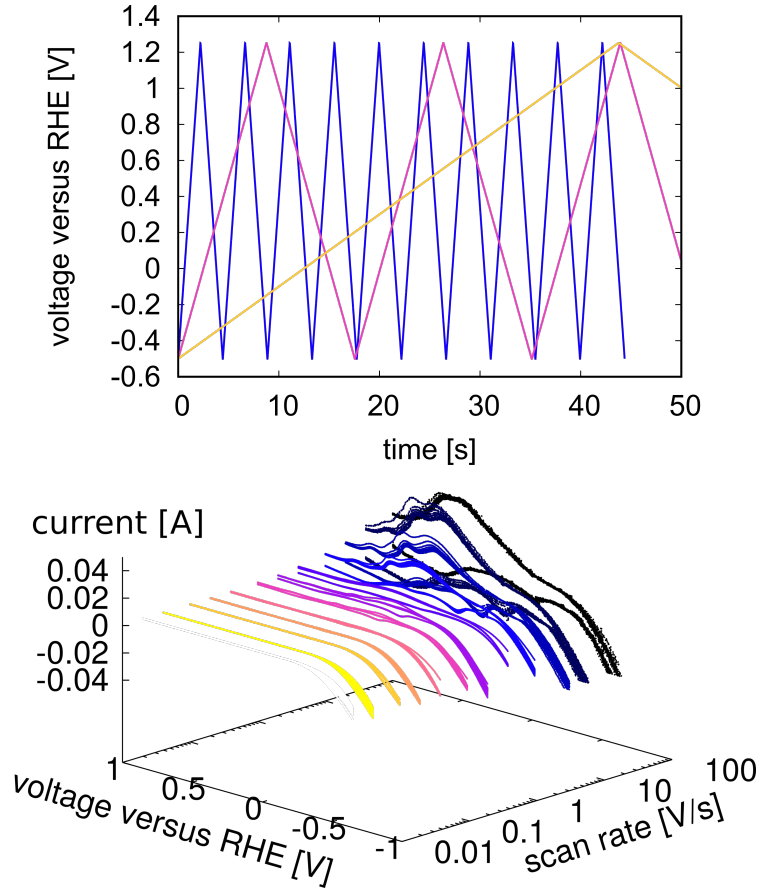


Figure 5.9.: Cyclic voltammetry measurements for a Platinum electrode mounted in the etching cell.

Instead impedance spectroscopy measurements were performed. Impedance spectroscopy in this context means that, in addition to a DC voltage, a small AC perturbation is applied across the semiconductor-electrolyte interface and the resulting current is recorded. From the amplitude and phase of the measured AC current in relation to the voltage perturbation, the impedance can be reconstructed. These impedance measurements are then usually repeated across a wide variety of perturbation frequencies and DC voltages. The resulting impedance spectra can then be compared with physically motivated models to gain insight into the electrical behavior of the interface of the semiconductor-electrolyte interface [77, 280].

Impedance measurements were performed on unirradiated, p-type Gallium Arsenide samples with frequencies ranging between 20 Hz and 1 MHz with DC voltages between 0.2 and 1.2 V as measured with a reversible Hydrogen electrode. The electrolyte was a 26% (by weight) KOH solution. Fig. 5.10 on the next page show a double logarithmic plot of the real and imaginary impedances. A plot like this is called a Nyquist plot. The physical properties of the interface can be extracted by fitting a model to the measurements. In

this case a good fit was achieved by this equivalent circuit:

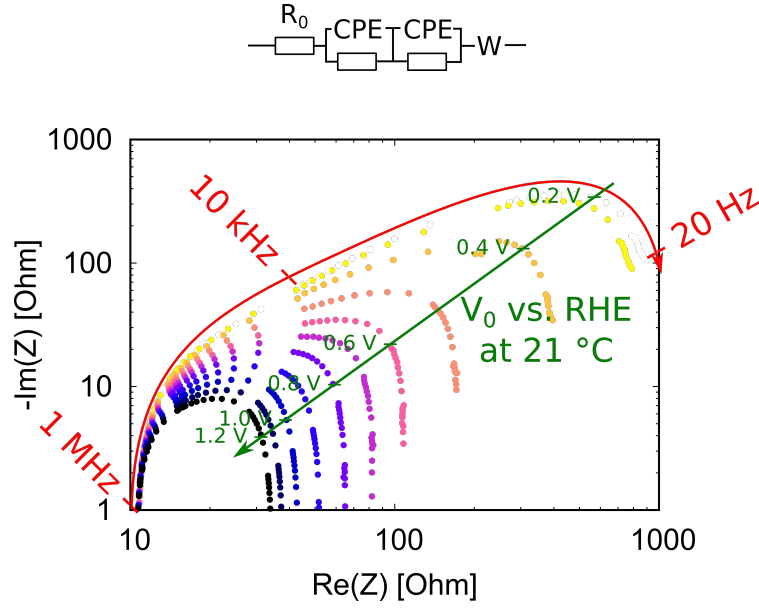


Figure 5.10.: Double logarithmic plot of the real and imaginary parts of the measured impedance Z of $\langle 100 \rangle$ p-type Gallium Arsenide in 26% KOH solution.

This model is based on the assumption that the entire setup can be characterized largely by the bulk resistance R_0 , two elements consisting of a parallel circuit of a constant phase element CPE and a resistor representing the surface of the semiconductor and the Helmholtz layer (the layer of the first few molecules of the electrolyte at the interface) of the electrolyte and a Warburg impedance W , representing the diffusive (Debye) layer in the electrolyte. R_0 is a usual resistance with a fit value of about $10.68(3) \Omega$. CPE are a generalization of capacitances with impedance [37]:

$$Z_{CPE}(\omega) = \frac{1}{Q(i\omega)^n}$$

where by fit, a value of $n = 0.8 \dots 1.0$ is found. A value of $n = 1$ would represent an ideal capacitance. ω is the frequency of the perturbation. The Warburg element W has an impedance of [294]:

$$Z_W = \frac{A_W}{\sqrt{\omega}} + \frac{A_W}{i\sqrt{\omega}}$$

The coefficient A_W of the Warburg element can be related to the diffusion process in the electrolyte towards or away from the semiconductor surface as [172]:

$$A_W = \frac{RT}{n^2 F^2 A \sqrt{2}} \left(\frac{1}{\sqrt{D_1 \rho_1}} + \frac{1}{\sqrt{D_2 \rho_2}} \right)$$

5. PBW in Gallium Arsenide

where n is the number of Electrons, F Faraday's constant, A the surface area and D_1 (D_2) the diffusion coefficients of the oxidized (reduced) species and ρ_1 (ρ_2) their concentrations. Fig. 5.11 shows the Warburg coefficient as a function of the applied DC potential. Assuming all other properties remain the same, this shows mostly the trend of changing concentrations at the active species at the interface between semiconductor and electrolyte.

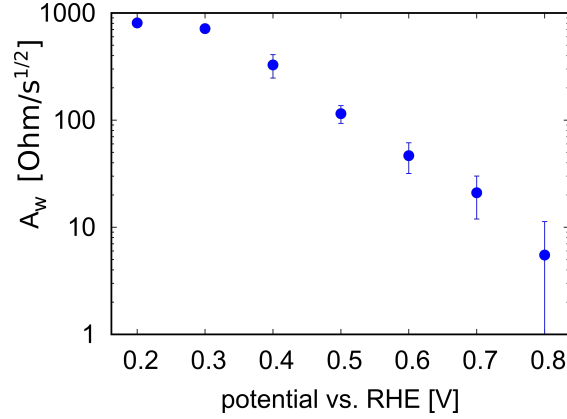


Figure 5.11.: Warburg coefficient (representing the formation of a diffusive layer) of the p-type Gallium Arsenide - KOH solution interface as a function of the applied potential.

Very interesting are the changes that occur upon irradiation of the semiconductor. For this, samples from the same wafer as the previously measured material were irradiated by 3 MeV Protons to $2.02 \frac{\text{pC}}{\mu\text{m}^2}$ and $4.44 \frac{\text{pC}}{\mu\text{m}^2}$. Fig. 5.12 on the next page shows the Nyquist plots of these samples. While the Warburg impedance was not significantly changed by the irradiation, the CPE surface capacitances showed a splitting. This can be interpreted as an observation of changes in the structure of the Helmholtz layer and the Electronic band structure (and surface charge density) of the Gallium Arsenide. This can partially be attributed to the previously discussed shift in the Fermi-level, resulting in an altered, effective electrostatic potential difference across the interface and altogether a difference in free charge carrier concentrations near the interface. A comparison to fig. 5.10 on the preceding page shows that this picture is incomplete, as no applied voltage exactly reproduces the measured impedances.

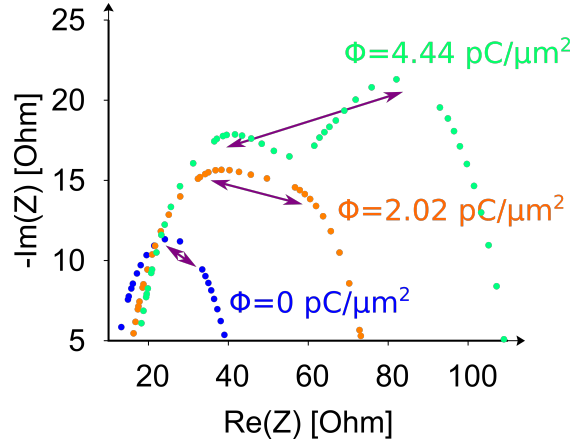


Figure 5.12.: Double logarithmic plot of the real and imaginary parts of the measured impedance Z of $\langle 100 \rangle$ p-type Gallium Arsenide in 26% KOH solution with an applied DC potential of 1 V (RHE) for three samples irradiated to three different fluences by 3 MeV Protons.

Based on these findings, similar measurements were conducted on $\langle 100 \rangle$ p-type Indium Antimonide surfaces. The samples were selected to match the doping of the Gallium Arsenide as closely as possible and treated the same. Again, irradiation with 3 MeV Protons was performed and the impedance spectra were recorded. It should be noted, that the equilibrium potential of the p-type Indium Antimonide was at 0.218(2) V (RHE) in contrast to the 0.413(6) V of Gallium Arsenide. As such, an offset of 0.2 V was used to make the measurements comparable. Fig. 5.13 on the next page shows the Nyquist plot without irradiation and with different levels of irradiation. As visible, the effects observed with Gallium Arsenide are repeated, but generally weaker. This means that the trends of shifts in the capacitances and surface properties are largely mirrored, but weaker.

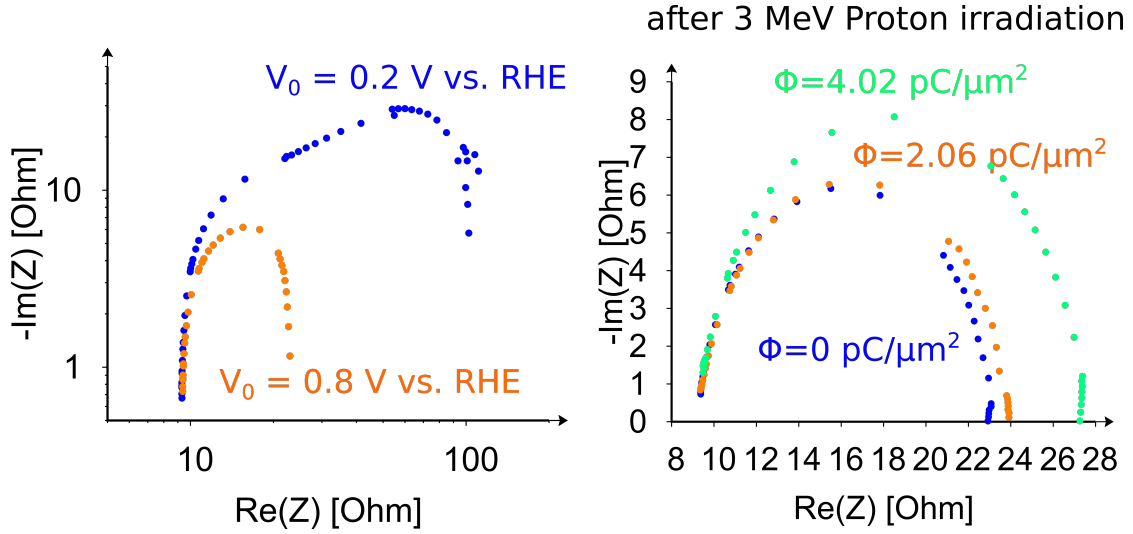


Figure 5.13.: Nyquist plot of p-type Indium Antimonide. On the left: unirradiated material for two different DC voltages. On the right: values after 3 MeV Proton irradiation to two different fluences at a potential of 0.8 V (RHE).

As the etching process requires holes to break the bonds of the surface atoms of the Gallium Arsenide, these holes in turn largely determine the etching rate. To understand the effect of defects and the electrolyte on the surface charge states, and thereby also the hole concentrations, ab-initio molecular dynamics simulations with CP2K were performed to understand and test the different surface conditions. For this a $2 \times 2 \times 2$ super cell of Gallium Arsenide, consisting of 32 Gallium and 32 Arsenide atoms, was used and placed in such a way as to simulate a $\langle 100 \rangle$ Gallium and Arsenide rich surface (respectively). For a second run, 82 water molecules were added on top of the surfaces, simulating the interface between the semiconductor to water. To simulate the KOH electrolyte, 6 water molecules were replaced by K^+ ions and 6 further water molecules were replaced by OH^- ions. This last simulation run was repeated twice with either an Arsenic or a Gallium cavity near the surface. Since here only the charge distributions are considered, the evaluated molecular dynamics runs were quite short (2000 steps of 0.5 fs at most). A canonical sampling through velocity rescaling thermostat and barostat with a time constant of 100 fs was used, which is ideally suited to these type of simulations [38]. A temperature of 330 K was set, approximating a temperature of 300 K for the electrolyte without having to explicitly include quantum effects for the motion of the atoms [46]. The simulations used the r2SCAN functional that was observed to describe both solids and water with good accuracy [72]. The atomic charges were calculated based on Hirshfeld partition [97, 230]. Further details on the simulations can be found in chap. 6 on page 134.

Fig. 5.14 on page 129 shows the charge of the atoms, sampled in 10 fs steps at the surface. In comparison to the Arsenic rich surface, the Gallium rich surface tends to have little changes of the charge states of the atoms at the surface, except for a scattering of Gallium charged states that is increased by the presence of defects. On the Arsenic rich

5. PBW in Gallium Arsenide

surface the Arsenic tends to be more neutral than in the bulk. This effect is amplified by the presence of water and decreased by the presence of the KOH electrolyte. For the KOH electrolyte, the Gallium and Arsenic atomic charges tend to be very comparable to the bulk charges. Defects also tend to create more scattering in the Arsenic charge for the Arsenic rich surface. Additionally, no matter the electrolyte or presence of defects, about 5 Angstrom from the surface, the charge states of the atoms tend to be the same as in bulk material.

From these simulations several conclusions can be drawn:

1. The largest changes to surface charge states occur on the chemical more active Arsenic rich surface.
2. Defects lead to a scattering of surface charge states that is more pronounced for Gallium atoms at a Gallium rich surface.
3. The KOH electrolyte leads to surface charge states that are similar to charge states in the bulk.
4. Defects likely only affect surface states if they are within 5 Angstrom or so to the surface.

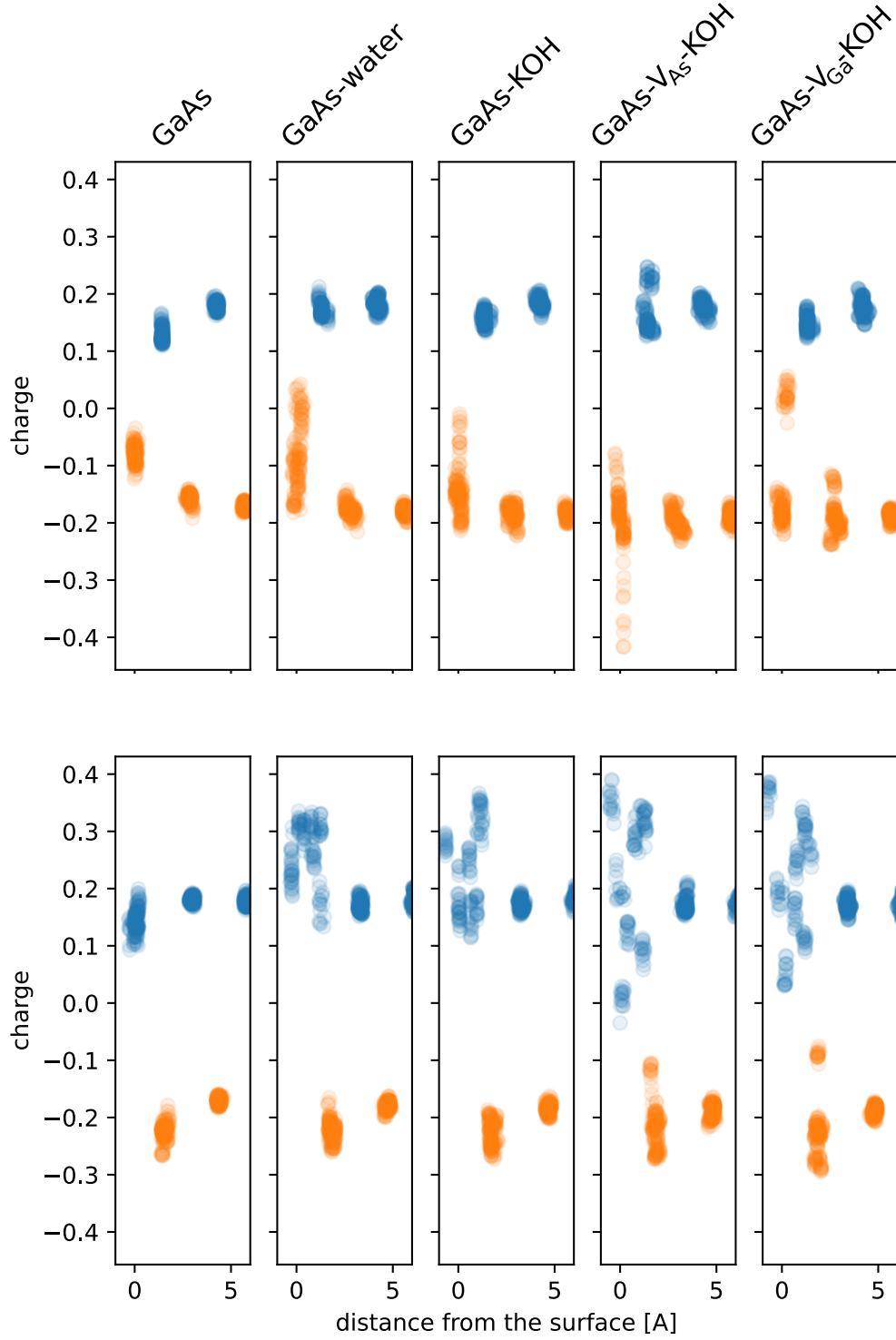


Figure 5.14.: Charge distributions at the Gallium and Arsenic rich $\langle 100 \rangle$ surface in water and KOH solution. Arsenic is shown in orange and Gallium in blue. The top row shows the Arsenic rich surface and the bottom row the Gallium rich surface. For a discussion of the changes see the text.

In light of these simulations it seems plausible that the effective capacitance and also reactivity of the surface would change significantly due to the presence of defects near the surface. Furthermore, the simulations give a hint at the microscopic origins of the experimentally observed changes to the impedance and conductivity of irradiated Gallium Arsenide.

5.3. Simulations in comparison to experiments

With many aspects of PBW in Gallium Arsenide well understood, it is interesting to determine to what extent the structures that can be created experimentally, can be reproduced in simulations. Simulations with entirely ohmic models were previously used for this and showed generally good agreement between experimental and simulated structures [123, 261]. However, these models are limited to p-type material. Here, drift diffusion models are used for the semiconductor, allowing to describe etching in n-type material (and other semiconductors) as well. These models solve Poisson's equation by multi-grid methods, as previously published [261], while using a predictor-corrector method for the simulation of charge transport. The electrolyte is modeled as an entirely ohmic material. In contrast to previously published simulations, the resolution was also increased thanks to a more efficient implementation from slightly better than $10\text{ }\mu\text{m}$ [123] and $1\text{-}2\text{ }\mu\text{m}$ [261] to $0.1\text{ }\mu\text{m}$ here. At the same time the convergence time of the simulations reduced from about 6h [123] to less than 4h here.

Fig. 5.15 on the following page shows an application of the new models for etching by showing a cut through two, homogeneously developed, long, $10\text{ }\mu\text{m}$ wide lines in p-type Gallium Arsenide. In this simulation the beam shape was assumed to be ideally sharp, that is: the beam is homogeneous and has a sharp boundary. As visible, the line irradiated to about $10^{12}\frac{\text{Protons}}{\text{cm}^2}$ largely remains standing after etching, except for the top of the line, where some the corners appear slightly rounded. Of the line irradiated with $2\cdot 10^{11}\frac{\text{Protons}}{\text{cm}^2}$ only the region with the largest defect densities at the end of the Proton range remains. Very typically for these simulations, the unirradiated material around very defect rich material etches faster, creating slight "trenches" around irradiated volumes that disappear again after the structure is freed entirely from the surrounding material. This is an artifact of the type of simulations performed here that do not take the fluid dynamics of the electrolyte into account. Very characteristic is also the slightly peaked surface below free standing structures, which was also reported in simulations and experiments with Silicon [214, 65].

5. PBW in Gallium Arsenide

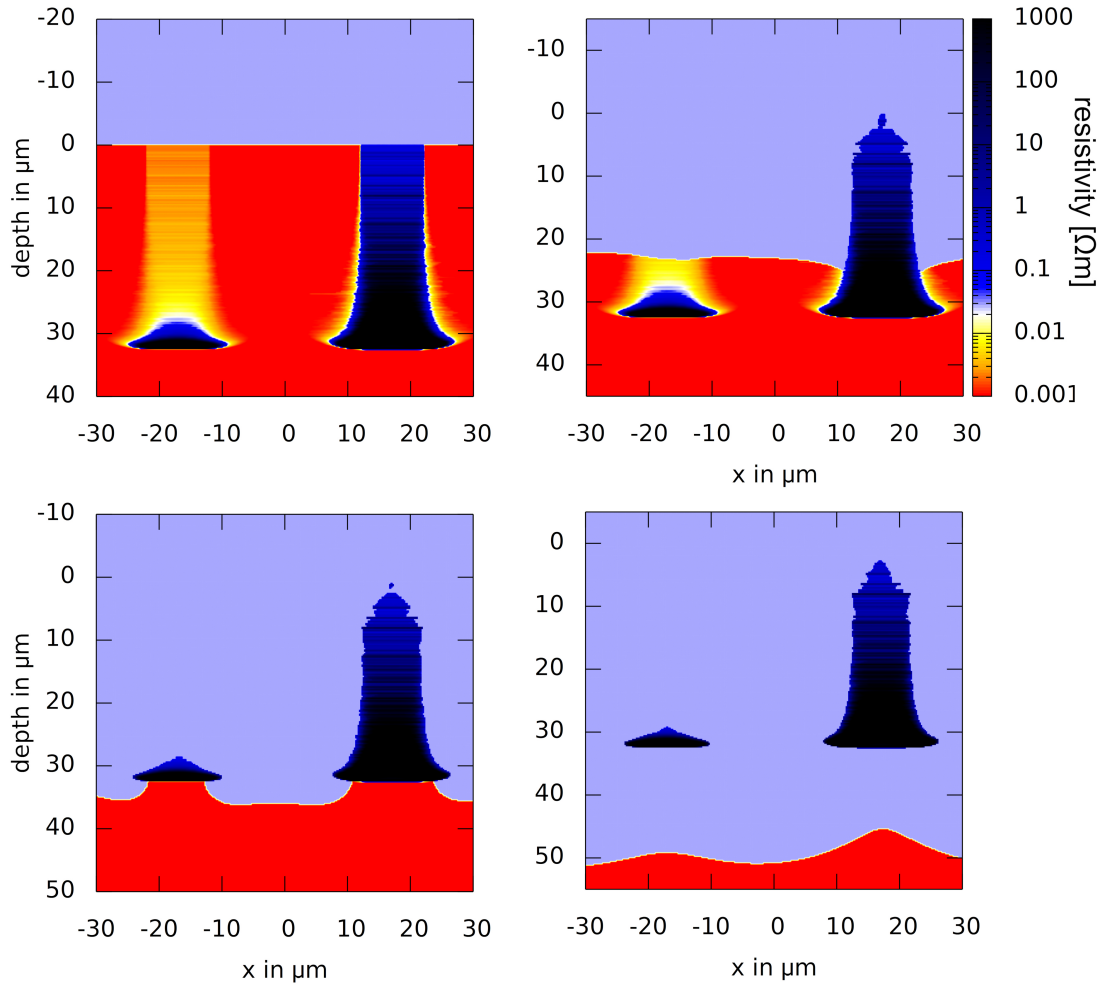


Figure 5.15.: Cut through two long, $10 \mu\text{m}$ wide lines, irradiated by 2 MeV Protons to $2 \cdot 10^{11} \frac{\text{Protons}}{\text{cm}^2}$ (left) and $10^{12} \frac{\text{Protons}}{\text{cm}^2}$ (right) during etching in 10% KOH solution.

In many real settings, the Proton beam does not show such a homogeneous current density over its diameter. Instead it more closely resembles a convolution between a Gaussian and a window function. At the smallest beam sizes the beam profile can be measured to be almost entirely gaussian [212]. Fig. 5.16 on the next page therefore shows a simulation of a cut through a long lines, irradiated by 2 MeV Protons to $10^{12} \frac{\text{Protons}}{\text{cm}^2}$ during etching in 10% KOH solution. Instead of the homogeneous beam of the previous simulation, the beam profile is here described by a $10 \mu\text{m}$ wide window function convoluted with a $5 \mu\text{m}$ wide Gaussian. Two interesting aspects become visible in this simulation. The first is that the resulting, wider structure requires deeper (longer) etching to be completely under-etched. The second aspect is a reduction of the steepness of the side-walls of the structure from almost vertical to an approximate 60° tilt.

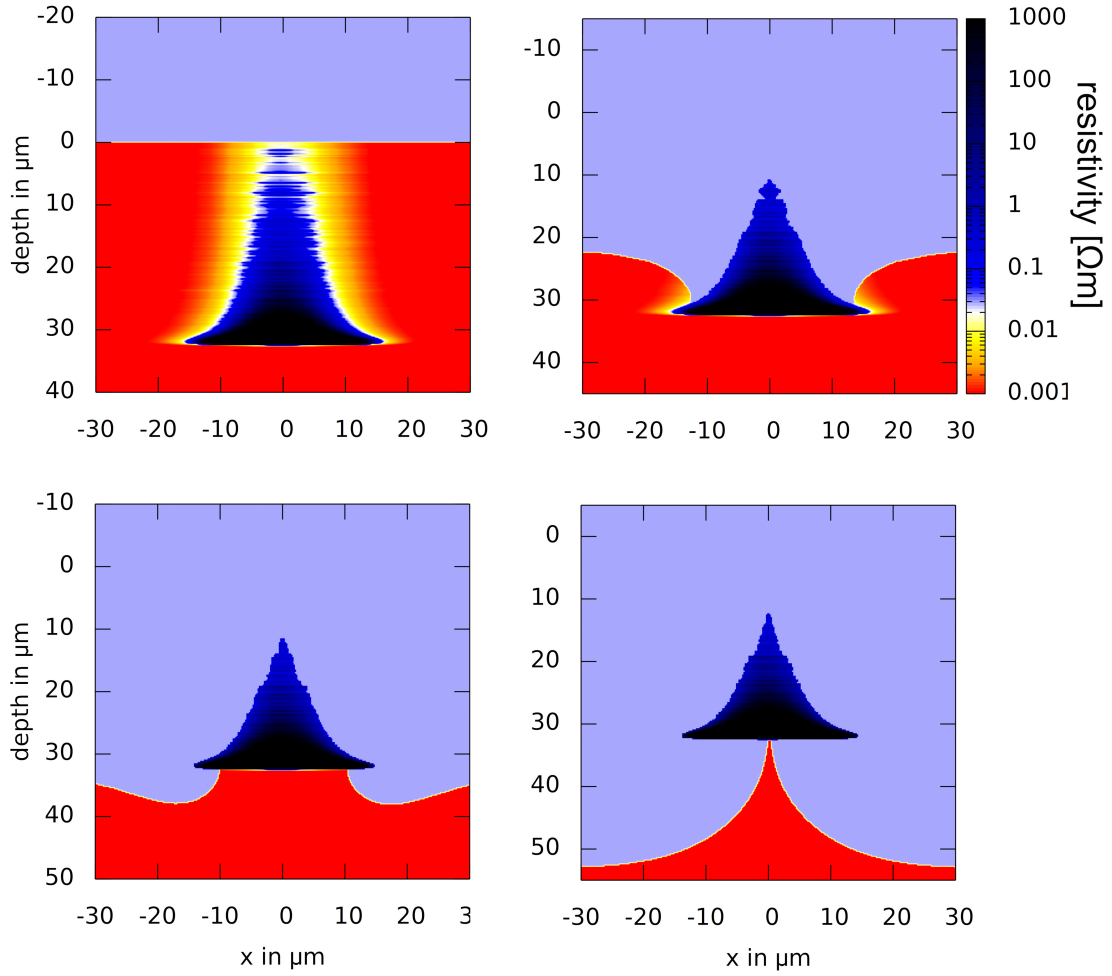


Figure 5.16.: Cut through a long line, irradiated by 2 MeV Protons to $10^{12} \frac{\text{Protons}}{\text{cm}^2}$ during etching in 10% KOH solution. The beam profile of this beam was modeled by the convolution of a $5\mu\text{m}$ wide Gaussian with a $10\mu\text{m}$ windows function.

This can be compared to some of the experimental results. Fig. 5.17 on the following page shows several SEM pictures of short lines that were written into p-type Gallium Arsenide with a 4 MeV H_2^+ beam. The pictures were taken from 2 identically lines in staggered $8\mu\text{m}$ etching steps, thus creating a progression of the etching process in $4\mu\text{m}$ steps. As visible, the general trends observed in the etching model are well reproduced. That is the appearance of a non-vertical side of the structure and a rounded top of the irradiated material. However, the flanks of the structure are more washed out than predicted by the simulation with the homogeneous beam. In this case this was caused by a beam that was less uniform and more gaussian than expected. Also visible is the electrical charging of the high resistance / irradiated material that is visible by the brighter appearance of the irradiated line. The surface of the etched bulk semiconductor material

5. PBW in Gallium Arsenide

looks rough in these pictures. This is a results of the rapid rinsing and drying of the sample after each etching step that left behind small amounts of oxides and KOH on the surface, that formed the snow like patterns.

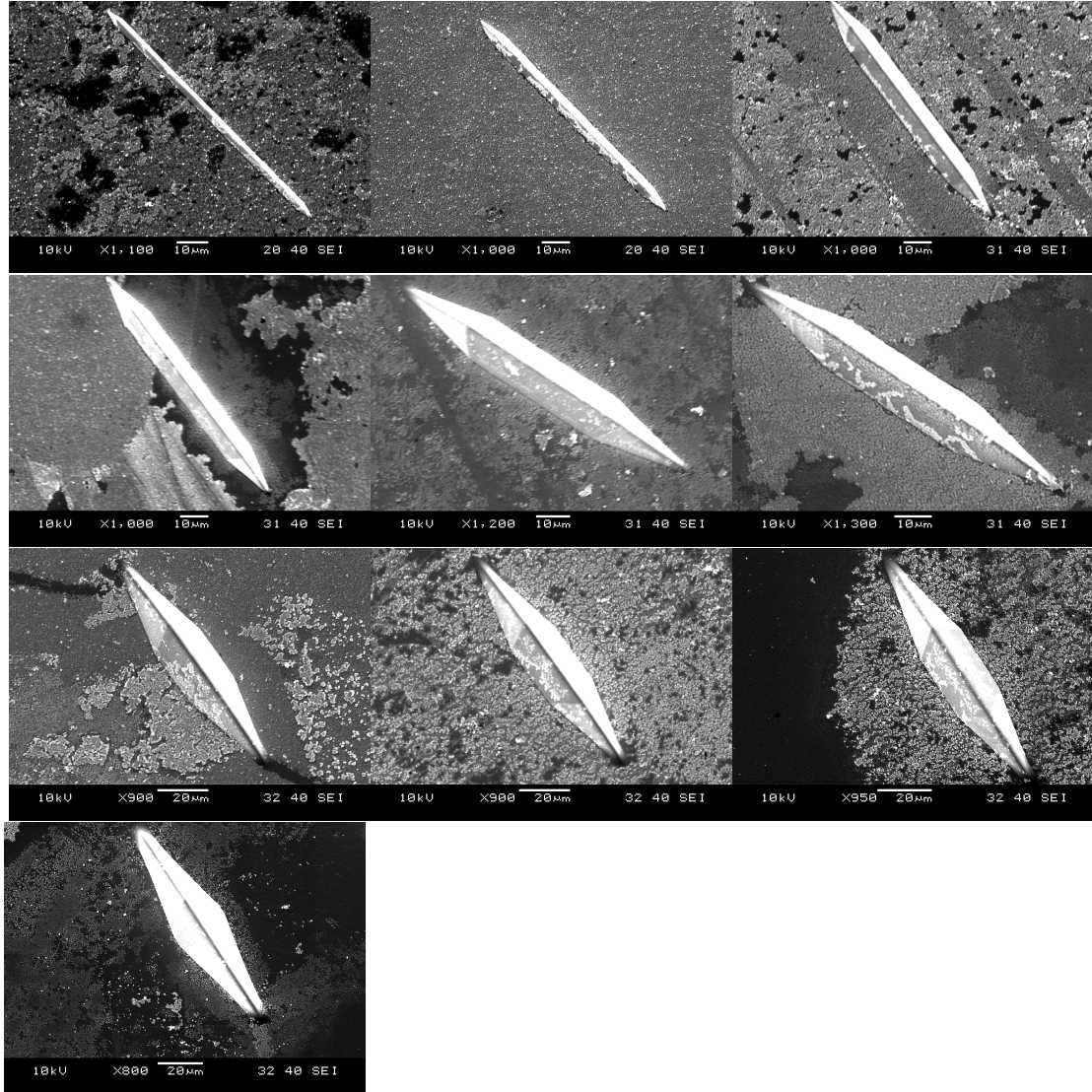


Figure 5.17.: SEM pictures of several lines written into p-type Gallium Arsenide in 4 μm steps. See the text for details.

6. Computational Quantum Chemistry

Many of the results of this work direct or indirectly rely on results of computational quantum chemistry. Because of this a review of the chosen methods and their implementations as well as an estimation of the accuracy of the necessary approximations is included here.

The basis for some of the calculations here are the wave-functions and energies calculated in the unrestricted Hartree Fock approximation. The unrestricted Hartree Fock equation is based on the formulation of a products of Slater determinants for the single particle orbitals for each spin with an interaction between them. In the simplest case considered here the Hamiltonian is the multi Electron Schrödinger equation in the external field of different nuclei and the interaction the Coulomb repulsion between Electrons. The “unrestricted” part of the name points to the fact that different spin up and spin down Electrons are allowed to have different orbital shapes and energy eigenvalues. The Hartree-Fock Hamiltonian (here for the spin up \uparrow Electrons) can be written as [190, 60]:

$$\hat{F}^\uparrow |\phi_m^\uparrow\rangle = \epsilon_m^\uparrow |\phi_m^\uparrow\rangle$$

with the single particle wave-functions ϕ_m^\uparrow , their corresponding eigenvalues ϵ_m^\uparrow and the Fock operator:

$$\hat{F}^\uparrow = \hat{h} + \sum_n \left(\langle \phi_n^\uparrow | \hat{w} | \phi_n^\uparrow \rangle - |\phi_n^\uparrow\rangle \langle \phi_n^\uparrow| \hat{w} + \langle \phi_n^\downarrow | \hat{w} | \phi_n^\downarrow \rangle \right)$$

where \hat{h} is the single particle Hamiltonian [234, 143]:

$$\hat{h} = \begin{cases} \frac{\vec{p}^2}{2m_{el.}} + V_{ext.} & \text{non relativistic} \\ c\vec{\alpha} \cdot \vec{p} + \beta m_{el.} c^2 + V_{ext.} & \text{Dirac} \end{cases}$$

with the momentum operator $\vec{p} = -i\hbar\vec{\nabla}$, $\vec{\alpha} = \begin{pmatrix} \alpha_x \\ \alpha_y \\ \alpha_z \end{pmatrix}$, $\alpha_i = \begin{bmatrix} 0_{2 \times 2} & \sigma_i \\ \sigma_i & 0_{2 \times 2} \end{bmatrix}$, the

Pauli spin 2×2 matrices $\vec{\sigma} = \begin{pmatrix} \sigma_x \\ \sigma_y \\ \sigma_z \end{pmatrix}$, $\beta = \begin{bmatrix} 1_{2 \times 2} & 0_{2 \times 2} \\ 0_{2 \times 2} & -1_{2 \times 2} \end{bmatrix}$, the Electron rest mass $m_{el.}$, speed of light c , the external potential (for example the Coulomb potential of the nuclei) $V_{ext.}$ and \hat{w} is the Electron interaction operator [5, 234]:

$$\hat{w} = \begin{cases} \frac{e^2}{4\pi\epsilon_0} \frac{1}{|\vec{r}_1 - \vec{r}_2|} & \text{Coulomb} \\ \frac{e^2}{4\pi\epsilon_0} \frac{1}{|\vec{r}_1 - \vec{r}_2|} \left\{ 1 - \frac{1}{2} \left[\vec{\alpha}_1 \cdot \vec{\alpha}_2 + \frac{[\vec{\alpha}_1(\vec{r}_1 - \vec{r}_2)] \cdot [\vec{\alpha}_2(\vec{r}_1 - \vec{r}_2)]}{|\vec{r}_1 - \vec{r}_2|^2} \right] \right\} & \text{Breit-Gaunt} \end{cases}$$

6. Computational Quantum Chemistry

where the Breit-Gaunt potential is a relativistic expansion of the Electron-Electron interaction up to second order in $\frac{1}{c}$. The indices 1 and 2 are used here to mark the two different Electrons. It should be noted that in the non-relativistic case each Electron wave-function has only a single component, whereas in the fully relativistic (Dirac) case, it has four. Besides these Hamiltonians, many other approximate forms exist, that are often not presentable in such a compact form. Among them the Pauli-Hamiltonian and the scalar relativistic ZORA (zero order regular approximation), scalar relativistic IORA (infinite order regular approximation), X2C (Dirac exact 2 component) and DKH (Douglas-Kroll-Hess) Hamiltonians [234]. All of these offer computational benefits in comparison to the often difficult to converge Dirac Hamiltonian while neglecting or approximating some of the relativistic aspects of it [142].

An aspect that is not well represented by the Hartree Fock approximation is Electron correlation. In the Hartree Fock approach the wave-function of two opposite spin Electrons $\phi_a^\uparrow, \phi_b^\downarrow$ for example is approximated by a Hartree product between them $\phi_{ab} = \phi_a^\uparrow \cdot \phi_b^\downarrow$. However, Coulomb repulsion between them leads, among other things, to the formation of a cusp in the product wave-function $\left. \frac{d\phi_{ab}}{dr_{ab}} \right|_{r_{ab}=0} = \frac{1}{2}\phi_{ab}|_{r_{ab}=0}$ (when spherically averaged) that increases the mean distance between the Electrons and lowers their energy, which is not well captured in the Hartree product [58]. A simple correction to the total energy is possible through perturbation theory. Among the various approaches for a perturbative treatment of Electron correlation, the Møller–Plesset perturbation theory of second order (abbreviated as MP2) [167] gives a rough approximation of this effect as [79]:

$$E_{MP2}^\uparrow = \frac{1}{2} \sum_{i,j}^{\text{occ.}} \sum_{a,b}^{\text{virt.}} \left(\frac{\langle \phi_i^\uparrow \phi_a^\uparrow | \hat{w} | \phi_j^\uparrow \phi_b^\uparrow \rangle}{\epsilon_i^\uparrow + \epsilon_j^\uparrow - \epsilon_a^\uparrow - \epsilon_b^\uparrow} - \frac{\langle \phi_j^\uparrow \phi_b^\uparrow | \hat{w} | \phi_i^\uparrow \phi_a^\uparrow \rangle}{\epsilon_i^\uparrow + \epsilon_j^\uparrow - \epsilon_a^\uparrow - \epsilon_b^\uparrow} \right) \langle \phi_i^\uparrow \phi_a^\uparrow | \hat{w} | \phi_j^\uparrow \phi_b^\uparrow \rangle$$

$$E_{MP2}^{\uparrow\downarrow} = \sum_{i,j}^{\text{occ.}} \sum_{a,b}^{\text{virt.}} \frac{\langle \phi_i^\uparrow \phi_a^\uparrow | \hat{w} | \phi_j^\downarrow \phi_b^\downarrow \rangle}{\epsilon_i^\uparrow + \epsilon_j^\downarrow - \epsilon_a^\uparrow - \epsilon_b^\downarrow} \langle \phi_i^\uparrow \phi_a^\uparrow | \hat{w} | \phi_j^\downarrow \phi_b^\downarrow \rangle$$

where $\sum_{i,j}^{\text{occ.}}$ represents the sum over the occupied orbitals i, j with energy eigenvalues ϵ_i, ϵ_j and $\sum_{a,b}^{\text{virt.}}$ the same sum over the virtual (unoccupied) orbitals. An analogue term exists for the other component of the correlation energy E_{MP2}^\downarrow .

Among the many different methods to treat Electron correlation, the coupled cluster methods is often considered the “gold standard” of computational quantum chemistry as it allows to approximate correlation in a relatively reliable, accurate, systematic and computationally reasonably expensive way [14]. In coupled cluster theory the Hartree Fock Hamiltonian is augmented by the coupled cluster operator $\exp(\hat{T})$ [141]:

$$\hat{F}^\uparrow \exp(\hat{T}) |\phi_m^\uparrow\rangle = \epsilon_m^\uparrow \exp(\hat{T}) |\phi_m^\uparrow\rangle$$

6. Computational Quantum Chemistry

where $\hat{T} = \hat{T}_S + \hat{T}_D + \hat{T}_T \dots$ is the excitation operator, given as a sum of all single excitations \hat{T}_S , double excitations \hat{T}_D , triple excitations \hat{T}_T and higher. The exponential operator $\exp(\hat{T})$ can be expanded as a Taylor series $\exp(\hat{T}) = 1 + \hat{T}_S + \hat{T}_D + \frac{1}{2}(\hat{T}_S^2 + \hat{T}_S\hat{T}_D + \hat{T}_D\hat{T}_S + \hat{T}_D^2) + \dots$ when for example using only single and double excitations. Application of the coupled cluster operator then leads to a set of coupled equations that are typically solved iteratively [14]:

$$\langle \phi_m^\uparrow | \exp(-\hat{T}) \hat{F}^\uparrow \exp(\hat{T}) | \phi_m^\uparrow \rangle = E_{cc} \langle \phi_m^\uparrow | \phi_m^\uparrow \rangle = E_{cc}$$

$$\langle \phi_m^{\uparrow*} | \exp(-\hat{T}) \hat{F}^\uparrow \exp(\hat{T}) | \phi_m^\uparrow \rangle = E_{cc} \langle \phi_m^{\uparrow*} | \phi_m^\uparrow \rangle = 0$$

where $\phi_m^{\uparrow*}$ stands for the excited wave-function, which can be generated from the ground state wave-function ϕ_m^\uparrow by single excitations \hat{T}_S or double excitations \hat{T}_D for example. Each of these excitations comes with an excitation amplitude (t_i^a for example for single excitations from the i th occupied orbital into the a th unoccupied orbital or t_{ij}^{ab} for double excitations) that needs to be determined through solution of the corresponding equation. Due to the large computational effort involved in solving the coupled cluster equations, typically only single and double excitations are considered. The method is then called CCSD (coupled cluster method with single and double excitations). From these excitations it is also possible to calculate a perturbative estimate for the inclusion of triple excitations, marked a (T) as CCSD(T) [14]. Through orbital rotations it is also possible to make the single excitation amplitudes 0. This leads to Brückner orbitals [260] and the orbital optimized coupled cluster method [240].

Another important method to describe multi-Electron systems is Kohn Sham density functional theory [120]. Here the system is transformed into a system of independent single Electron systems that interact through a mean field potential. The Hamiltonian is then:

$$\hat{F}_{DFT}^\uparrow | \phi_m^\uparrow \rangle = \epsilon_m^\uparrow | \phi_m^\uparrow \rangle$$

with:

$$\hat{F}_{DFT}^\uparrow = \hat{h} + \sum_i^{\text{occ.}} \left(\langle \phi_i^\uparrow | \hat{w} | \phi_i^\uparrow \rangle + \langle \phi_i^\downarrow | \hat{w} | \phi_i^\downarrow \rangle \right) + V_{XC}$$

where the individual orbitals are required to be orthogonal with respect to all other ones of the same spin. The last term V_{XC} is the exchange correlation potential. It should be noted that this method is exact for the density and total energy of the ground state of any multi-Electron system, however, the form of the exchange-correlation functional for arbitrary systems is not known, only approximations to it and solutions in special cases. The basis for the construction of the exchange-correlation functional is the homogeneous Electron gas, which is entirely described in its ground state by the Electron densities $\rho^\uparrow, \rho^\downarrow$. This leads to the following approximation:

6. Computational Quantum Chemistry

$$V_{XC}^{\uparrow}(\rho^{\uparrow}, \rho^{\downarrow}) \approx \varepsilon_{xc}(\rho^{\uparrow}, \rho^{\downarrow}) + \rho^{\uparrow} \frac{\partial \varepsilon_{xc}(\rho^{\uparrow}, \rho^{\downarrow})}{\partial \rho^{\uparrow}}$$

where $\varepsilon_{xc}(\rho^{\uparrow}, \rho^{\downarrow})$ is the exchange-correlation energy per particle (also called the homogeneous Electron gas exchange-correlation functional). The exchange component of this energy is known exactly as $\varepsilon_x(\rho^{\uparrow}, \rho^{\downarrow}) = -\frac{3}{8} \left(\frac{3}{\pi}\right)^{1/3} \left[(2\rho^{\uparrow})^{4/3} + (2\rho^{\downarrow})^{4/3}\right]$ [57, 23]. In the description of in-homogeneous Electron systems (for example molecules) the description of the exchange-correlation energy can be improved by a prefactor f_{xc} called the enhancement factor that can depend on the gradient or the Laplacian of the Electron density or similar quantities. It has recently been determined that the most appropriate quantities for the exchange part of f_{xc} to depend on are $p = \frac{|\vec{\nabla}\rho|}{4(3\pi^2)^{2/3}\rho^{8/3}}$ and $\alpha = \frac{\sum_i \tau_i - \frac{1}{8}|\vec{\nabla}\rho|^2/\rho}{\frac{3}{10}(3\pi^2)^{2/3}\rho^{5/3}}$ where $\tau_i = \frac{1}{2}|\vec{\nabla}\phi_i|^2$ is the kinetic energy density of the i th Kohn Sham orbital (given here for the unpolarized Electron gas case $\rho = 2\rho^{\uparrow} = 2\rho^{\downarrow}$ for simplicity) [266]. For example, the exchange enhancement factor of the PBE functional, one of the most popular functionals, is given by [198]:

$$f_x^{PBE} = 1 + \kappa \left(1 - \frac{1}{1 + \frac{\mu p}{\kappa}}\right)$$

with $\mu = 0.2195$ and $\kappa = 0.804$ chosen in such a way that several constraints on the shape of f_{xc} are satisfied. Many functional forms exist for this enhancement factor. They can generally be classified according to the quantities that form the ingredients of the functional. Functionals that depend only on the densities are called local (spin) density approximations or L(S)DA, whereas functionals that also depend on the gradient of the density, like the PBE functional, are called GGAs or generalized gradient approximations. Functionals that also include second derivatives of the density as well as the orbital kinetic energy densities are called MGGA's or meta generalized gradient approximations. Functionals can also be mixed (or hybridized) with an amount of Hartree Fock exchange (that is the part of the Hartree Fock Hamiltonian that acts like an Electron exchange interaction). These hybrid functionals are marked with an "h", for example hGGAs are functionals that include a certain amount of Hartree Fock exchange with a GGA functional. It should be noted that functionals that include more components have the potential to be more accurate for a broader range of systems (for example different isolated or interacting molecules or solids with different bond types) but more complex functionals are also more difficult to implement and often require finer integration grids for the potential calculations. Among the large zoo of more than 600 published functionals [131] the ones that perform well for the prediction of the properties of diverse systems but are constructed from theoretical considerations (as opposed to fitting the functionals to a set of experimental properties) are particularly interesting. Of these functionals, besides the PBE functional and many modifications of it, in this work the SCAN functional and the version modified for numerical performance r2SCAN [72] are used. The SCAN functional

is notable as it is the first functional to satisfy all known constraints on the functional shape [265].

Often the functionals used in simulations of non-covalent bonded systems underestimate the van-der-Waals attractions between atoms. To alleviate this problem, several methods were developed, among which the Grimme D3 and D4 method [39, 40, 41] and the rVV10 non-local functional [289, 228] are some of the most accurate ones. In both cases, an additional contribution to the correlation energy is added to the system. In the D3/D4 methods it is based on a coordination and charge dependent force field, whereas the rVV10 calculates the energy through a non-local functional that can be calculated efficiently from the Electron density.

No matter which quantum chemical method is used, the Electron wave-functions need to be represented in some way. For computational efficiency, this happens mostly by using (here for example spherical as opposed to cartesian) gaussian basis functions:

$$\phi_n^\uparrow(\vec{r}) \approx \sum_i c_{i,n} N_{n_i,l_i,m_i} Y_{l_i,m_i}(\theta, \vartheta) \left| \vec{r} - \vec{R}_i \right|^{l_i} \exp\left(-\zeta_i \left| \vec{r} - \vec{R}_i \right|\right)$$

or in case of periodic systems also plane waves. $c_{i,n}$ are the expansion coefficients, N a normalization factor, l is the angular quantum number, m the magnetic quantum number and $Y_{l,m}$ the Laplace spherical harmonic. Both of the presented basis functions do in practice not represent the single particle wave-functions of density functional and Hartree-Fock theory in atoms exactly (for example the cusp of the s -orbitals at the nucleus that follows from the non-relativistic Schrödinger equation at the point-nucleus is not exactly resolvable) but can be constructed in such a way that they can systematically approach them. To improve computational efficiency, several gaussians may be combined onto a single basis with fixed coefficients. If this is reversed, the basis set is called decontracted. A common nomenclature for the gaussian basis functions is to specify the number of different wave-functions in the basis set per valence Electron shell as for example double, triple or quadruple zeta (for two, three and four), to note of additional polarization functions are present (that is: high angular momentum functions) that aid in describing polarization and if the basis set was augmented (has additional very low exponent functions) that aid in describing excited states and negative charge states. A basis set with name **x2c-TZVP** is therefore a non augmented, triple zeta valence basis set with one set of additional polarization functions that was constructed with a X2C Hamiltonian.

Tab. 6.1 on page 140 shows the contributions to the total energy of some of the atoms used in the simulations here. For the simulations **pyscf** 1.7.6[267, 268] and **Orca** 5 [178, 179] are used with the decontracted **x2c-TZVP**[205] basis set. The calculations are carried out with the spin unrestricted Schrödinger / spin free X2C and the Dirac Hartree Fock Hamiltonian with the atoms in their ground state multiplicities. The differences between the Schrödinger and spin free X2C (sfX2C) Hamiltonians give an estimate for the scalar relativistic effects, whereas the differences between the sfX2C and Dirac Hamiltonian allow for an estimation of non-scalar relativistic effects. For the estimation of correlation effects, CCSD(T) calculations with the orbitals from the sfX2C Hamiltonian calculation

6. Computational Quantum Chemistry

are used. QED corrections, the largest being the one-Electron self energy and vacuum polarization, are not included here [220]. As visible, for the elements considered here the scalar relativistic corrections are most important when considering total Electron binding energies, followed by correlation effects. Non-scalar relativistic effects are often partially canceled by the Breit-Gaunt interaction and more than an order smaller than their scalar relativistic counter parts. The total energies are also comparable to predictions from DFT and MP2 (and the spin component scaled variant SCS-MP2 [79]) simulations, based on the sfX2C and the second order DKH Hamiltonian with AMFI approximation [96]. The table shows a selection of DFT simulations with exchange-correlation functionals of low empiricism. For completeness the values predicted by the Thomas-Fermi atomic model [272, 66] are also shown.

	element					
	H	O	Si	K	Ga	As
non-relativistic Hartree-Fock	-0.4998	-74.8164	-288.8520	-599.1547	-1923.2261	-2234.1982
correction	finite nucleus	$4.32 \cdot 10^{-10}$	$1.32 \cdot 10^{-5}$	$7.92 \cdot 10^{-4}$	$9.35 \cdot 10^{-3}$	$1.31 \cdot 10^{-2}$
	scalar relativistic	$-6.54 \cdot 10^{-6}$	$-5.23 \cdot 10^{-2}$	$-6.03 \cdot 10^{-1}$	-2.2972	-24.8393
	non-scalar relativistic	$-8.83 \cdot 10^{-12}$	$-3.40 \cdot 10^{-3}$	$1.39 \cdot 10^{-2}$	$-6.15 \cdot 10^{-2}$	$-3.62 \cdot 10^{-1}$
	Breit-Gaunt interaction	0	$7.50 \cdot 10^{-3}$	$5.49 \cdot 10^{-2}$	$1.60 \cdot 10^{-1}$	1.0560
	Electron correlation	0	$-2.16 \cdot 10^{-1}$	$-3.52 \cdot 10^{-1}$	$-8.82 \cdot 10^{-1}$	$-8.87 \cdot 10^{-1}$
total binding energy	-0.4998	-75.0810	-289.6932	-601.7044	-1942.5429	-2259.2180
other estimates	Thomas-Fermi	-98.4	-363	-740	-2321	-2685
	sfX2C PW (LDA)	-0.4784	-288.8084	-600.4739	-1940.6968	-2257.2881
	sfX2C PBE (GGA)	-0.4996	-289.8372	-602.0146	-1943.5724	-2260.4190
	sfX2C SG4 (GGA)	-0.5001	-289.7280	-601.8984	-1943.5036	-2260.3667
	sfX2C LC-VV10 (hGGA)	-0.5067	-289.8689	-602.0674	-1943.6102	-2260.4808
	sfX2C TPSS (MGGA)	-0.4999	-290.0002	-602.2383	-1943.8249	-2260.6768
	sfX2C SCAN (MGGA)	-0.4999	-289.9976	-602.2712	-1943.9762	-2260.9074
	sfX2C PW6B95 (hMGGA)	-0.5013	-290.2430	-602.6570	-1944.8145	-2261.7976
	sfX2C MP2	-	-289.7397	-601.7900	-1943.1091	-2259.9481
	DKH2(AMFI) UHF	-0.4998	-289.4542	-601.4450	-1942.0725	-2258.8769
other estimates	DKH2(AMFI) MP2	-	-289.7389	-601.7838	-1943.0058	-2259.8008
	DKH2(AMFI) SCS-MP2	-	-289.7352	-601.7728	-1942.9357	-2259.7264
	DKH2(AMFI) CCSD(T)	-	-289.7611	-601.7966	-1942.9546	-2259.7644

Table 6.1.: Contributions to the Electronic total binding energies in Hartree of different atoms and estimates from DFT and MP2 for the decontracted **x2c-TZVP** basis set as calculated with **pyscf** and **Orca**. For an explanation of the different effects see the text.

Besides the total Electronic binding energy, another important property in atomic simulations is the accuracy of the predicted Electron density. Fig. 6.1 shows the radial density of Carbon (and fig. 6.2 on the next page of Silicon) as predicted with different methods as calculated with `Orca 5` [178, 179] using the large `AHGBSP1-9` basis set [130] and a second order Douglas-Kroll-Hess Hamiltonian (plus AMFI correction). The Thomas-Fermi model density and the density implied by the ZBL inter-atomic potential (used in nuclear stopping) are shown for reference as well. The densities produced in coupled cluster calculations have been found to be quite accurate [25, 158] and are considered as the reference here. It is visible that the DFT methods, as well as Hartree Fock and MP2 relaxed densities agree very well with the orbital optimized coupled cluster densities in the regions close to the nucleus, while at large radii the accuracy from best to worst is relaxed MP2, Hartree-Fock, DFT (SCAN, MGGA), DFT (PW, LDA) and DFT (PBE, GGA). This agrees with the assessment that MP2 calculations produce on average more accurate densities than DFT methods and that the SCAN functional is the most accurate for densities among the three considered functionals in this test [158]. For these light elements the effects of the individual shells in the density are well visible, but heavier atoms tend to approach the Thomas-Fermi model densities more and more.

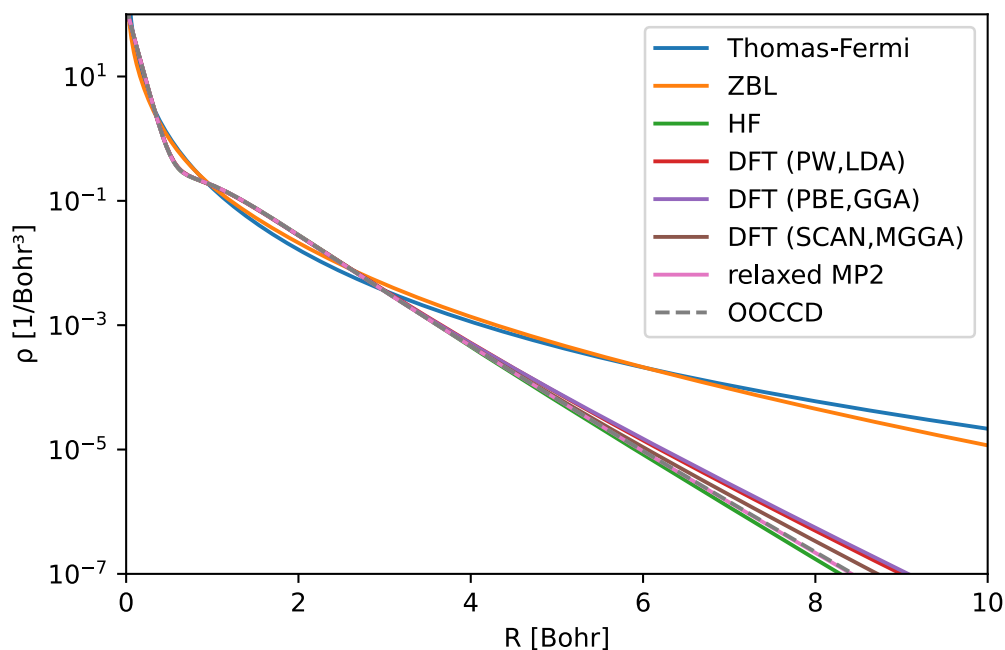


Figure 6.1.: Radial Electron density of Carbon as predicted by different methods.

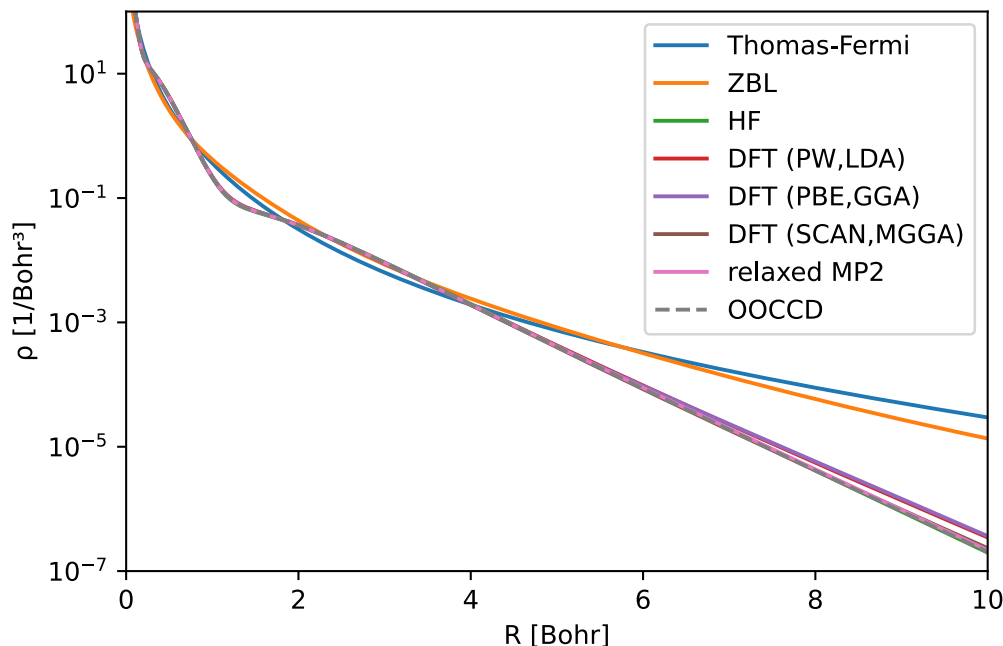


Figure 6.2.: Radial Electron density of Silicon as predicted by different methods.

For calculations of the properties of solids as well as very large scale simulations, among other approximations, pseudo-potentials are used to make the simulations computationally feasible. Here the nuclear Coulomb potential of all-Electron simulations is replaced by an effective core potential that does include the contributions from tightly bound (core) Electrons in such a way that the calculated properties (energies, forces, partial atomic charges ...) are still predicted accurate enough. Several methods for pseudo-potential construction (and subsequent simulations) were developed in the past, including empirical [67, 93], norm-conserving [85], ultra-soft [286] pseudo-potentials and as a generalization projector augmented wave function methods [24]. All of them allow to treat only some of the Electrons from the valence space of the atoms explicitly and often with wave-functions with a reduced number of radial nodes and softer cusps at the nucleus, allowing for the use of less complex basis sets (lower cutoff plane waves or less components in gaussian wave-functions) than the same valence Electrons would require in all Electron simulations. As a downside, pseudo-potential construction and validation is a very long and complicated process. Here HGH pseudo-potentials [89] that were optimized against all Electron calculations with the SCAN functional by Jürg Hutter are used in CP2K 9 [127] and compared against all-Electron simulations.

Fig. 6.3 on page 144 shows the dissociation curve (energy as a function of the bond length) of O₂ as computed with different methods. While pseudo-potentials can only reproduce the results of all-Electron calculations to an extend, in this case the different

6. Computational Quantum Chemistry

methods (except the Hartree-Fock calculations) agree very well around the minimum of the bond length, while the computational savings of the pseudo-potentials are already noticeable. It is possible to improve computing times with all-Electron simulations, however for very large scale system simulations (even up to millions of atoms), pseudo-potentials are commonly used [18].

The reference is here the basis set superposition error corrected [59] orbital optimized coupled cluster theory with perturbative triple excitations (OOCCD(T) [240]) with the decontracted **x2c-TZVP** basis set in **Orca 5**. Additionally, NEVPT2 [7] results are shown (based on a CASSCF calculation of 12 Electrons in 8 at most doubly occupied orbitals) that may offer a more balanced and multi-determinant treatment of the bond-breaking process. As a rough comparison, on a four core **Intel Core i7** processor and without any of the typically employed additional performance improving techniques (like RIJK approximations, frozen core approach) the run time of the OOCCD(T) method in **Orca** was about 85 min for 19 data points, NEVPT2 11.5 min, SCAN-D4 [62] 13.5 min, while the r2SCAN calculation in **CP2k** ran about 2.5 min for the 18 points where it converged easily to the minimum of the correct symmetry.

The pseudo-potential used for Oxygen approximates the 1s Electrons as core Electrons. The corresponding basis set is given in the appendix and includes orbitals with $l = 0, 1, 2$. It is found during testing that the orbitals with $l = 2$ are important in modeling the polarization of the $l = 1$ orbitals and help to describe the bond between the Oxygen atoms around the equilibrium bond length correctly as well as describing the shorter range repulsion between the atoms.

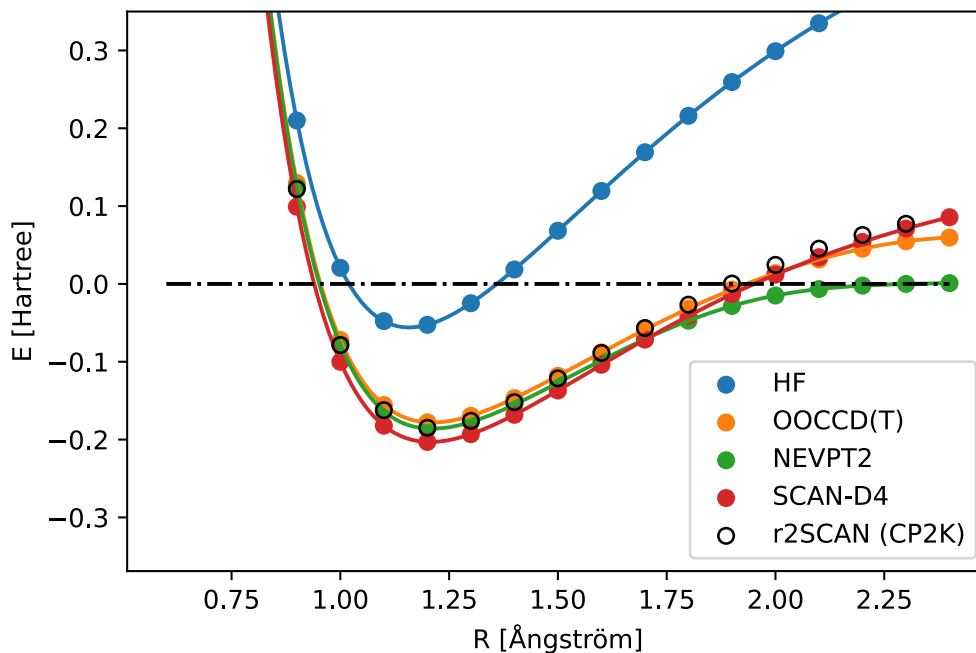


Figure 6.3.: Dissociation curve of triplet O_2 as computed with different all-Electron methods with the decontracted $x2c$ -TZVP basis set in `Orca` and as computed with a pseudo-potential method and `r2SCAN` in `cp2k`. Lines are a guide to the eye and the horizontal line marks the energy of the Oxygen atoms at infinite separation.

A similar set of simulations are performed for singlet H_2 . Fig. 6.4 on the next page shows the result of these calculations. The calculations were performed with the same $x2c$ -TZVP basis set in `Orca 5` and include the MP2 method and the orbital optimized coupled cluster method as well as the SCAN functional with the D4 dispersion correction. The calculations were again basis set superposition error corrected. These calculations, with the exception of the Hartree Fock calculation, agree very well, similar to the previous calculation of Oxygen. The basis set used in `CP2k` is given in the appendix and includes orbitals with $l = 0, 1$.

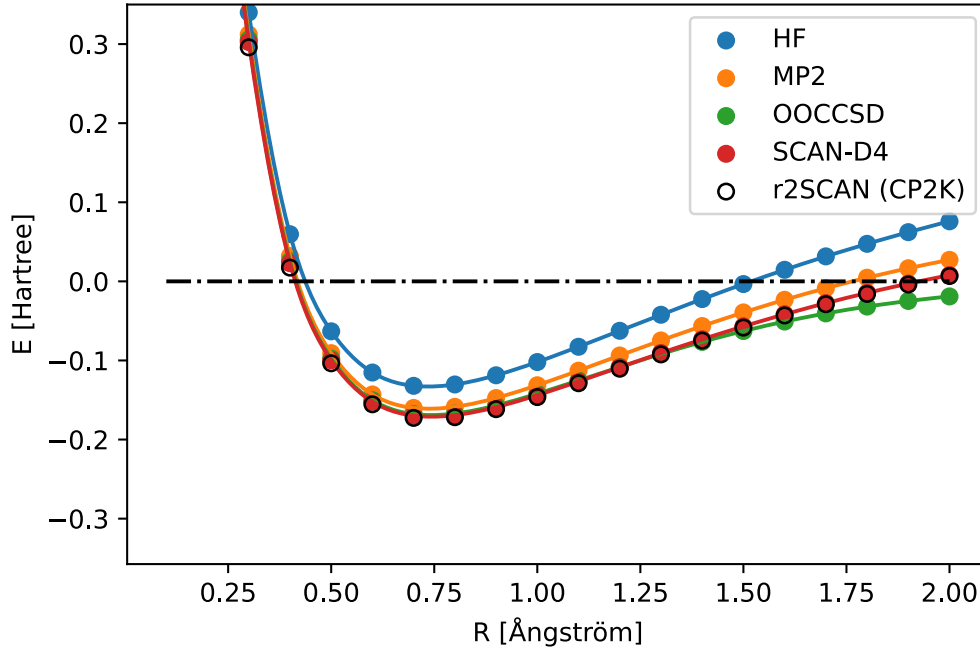


Figure 6.4.: Dissociation curve of singlet H_2 as computed with different all-Electron methods with the decontracted `x2c-TZVP` basis set in `Orca` and as computed with a pseudo-potential method and `r2SCAN` in `cp2k`. Lines are a guide to the eye and the horizontal line marks the energy of the Hydrogen atoms at infinite separation.

Fig. 6.5 on the following page shows an application of the pseudo-potential method for Gallium Arsenide in the Zincblende (ground state) structure. Here the energies computed with an all-Electron method (`E1k 8` in linearized augmented plane waves muffin tin mode and $16 \times 16 \times 16$ k-points per unit cell) and the `r2SCAN` functional are compared to a pseudo-potential calculation in `CP2K` 9. The pseudo-potentials do include the valence *s* and *p* states of Gallium and Arsenic as well as the *d* Electrons that can become important for the bond structure of the atoms under compression or ionization, but otherwise do not form any strong bonds themselves. The `SCAN` and `r2SCAN` functionals with `CP2K` could not be brought to agree with the all-Electron calculations in `E1k 8` with any provided basis sets, despite careful testing. As such, a new basis set was developed for this purpose and is given in the appendix. This hints at numerical problems with the implementation of MGGA functionals with periodic boundary conditions within `CP2K`. It is also notable that the predicted lattice constant in `E1k 8` with the `r2SCAN` functional is larger than usual for this functional and material.

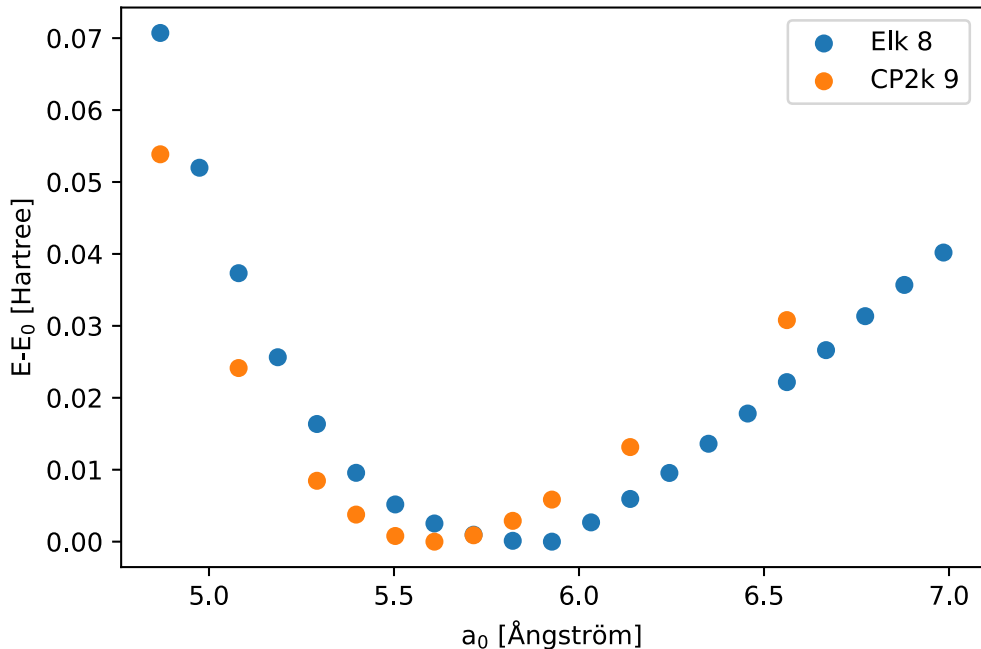


Figure 6.5.: Energy per atom of Gallium Arsenide relative to the ground state as a function of the lattice constant a_0 as computed with an all-Electron method in Elk and a pseudo-potential method in CP2K.

The basis sets used in this work with CP2K were optimized to reproduce all Electron calculations closely while providing reasonable convergence properties without having ghost states in the tested configurations. A ghost state here is a bound Electronic state in a system that is simulated with pseudo-potentials that does not exist in reality or all Electron calculations but is rather an artifact of the chosen pseudo-potential and/or basis set. Usually ghost states are tested for and avoided during pseudo-potential construction, this does however not guarantee the absence of ghost states. Instead studies with many reference systems need to be performed. For the pseudo-potentials used in this work, these studies were performed by the authors of the pseudo-potentials, showing no ghost states. During molecular dynamics simulations, however, a few systems, for example Gallium Arsenide in the Zincblende phase, showed unreasonably slow convergence as well as unphysical ground state geometries and energies. Careful simulations then showed that the basis sets provided by the authors for the pseudo-potentials, while offering good properties for the tested systems, created ghost states under slight compression of the bonds. As such a series of calculations with different pseudo-potentials as well as basis sets and exchange-correlation functionals were performed to find the source of the problem. Many combinations also showed the same problem to some extent. As such, there was a choice to either use a less accurate combination of pseudo-potential, basis set and

exchange correlation functional in this work than initially aimed for or create and test a new set of basis functions. After several attempts, a new basis set was constructed from the orbital exponent range of the CRENL basis set [102] that was optimized for the use in solids in CP2K. For this a geometric progression was used for all the exponents, here $\zeta_i = \alpha \cdot \beta^i$ where $\alpha = 0.15$ Bohr and $\beta = 2.3$. The choice of α was constrained by the numerics of the Cholesky decomposition step of the overlap matrix under strong compression of the solid in CP2K to $\alpha \gtrsim 0.12$ as well as poor convergence of the calculation for large bond lengths to $\alpha \lesssim 0.4$. A larger freedom of choice exists for β . Many basis sets use a value around 3, with larger values offering slightly smaller basis sets and faster convergence and smaller values offering more accuracy. The value used here was found to perform well for the calculations carried out. The largest i included in the basis set was determined by reducing it until ghost states disappeared. This lead to a value of about $i_{max} = 6$. The final degree of freedom with the choice of the maximum orbital angular momentum l_{max} in the basis set. Here it was observed that for Oxygen, Gallium and Arsenic $l_{max} = 2$ was enough to provide realistic dissociation curves, while Hydrogen only required $l_{max} = 1$. In molecular dynamics simulations with the newly constructed basis sets, it was found that some diffuse (low exponent) basis functions with large l often could not be converged with sufficient accuracy in CP2K. Thus they were deleted. The explicit form of the basis sets in the CP2K format is given in appendix A on page 184.

Tab. 6.2 shows the multi-pole moments of H₂O as calculated with the same methods used previously and decontracted ANO-R Zobel, Widmark, and Veryazov [321] basis set (in Orca, TZVP basis set in CP2K). NEVPT2 used an unrelaxed density and was based on a CASSCF calculation with 8 Electrons in 6 at most doubly occupied orbitals. The prediction of accurate multi-pole moments and polarizabilities can be seen, besides correct prediction of charge states, as an indication of the accuracy of long ranged inter-molecular interactions (as opposed to short range bond forces or repulsive interactions). It is visible, that the methods mostly agree well on the electrostatic moments and polarizabilities and the pseudo-potential method is a reasonable approximation.

method	dipole moment	trace-less quadrupole moment	polarizability
experimental	0.730 [107]	-1.859, 1.955, -0.097 [94]	10.13 [188]
HF	0.782	-1.192, 1.263, -0.071	8.27
OOCCD	0.723	-1.194, 1.267, -0.073	8.97*
NEVPT2	0.722	-1.141, 1.228, -0.087	7.95*
SG4	0.721	-1.193, 1.269, -0.076	13.1
SCAN	0.729	-1.184, 1.265, -0.081	9.51
r2SCAN (CP2K)	0.719	-1.579, 1.668, -0.089	-

Table 6.2.: Multi-pole moments and polarizability of H₂O at the experimental ground state geometry in atomic units as computed with different methods in a comparison to the experimental values. Values marked with “*” were calculated from numeric differentiation of dipole moments at finite fields.

7. Summary

Proton beam writing is a complex topic. This is due to complicated physical and chemical processes involved that happen over timescales spanning many orders of magnitude in a large variety of possible target materials. This work provides a detailed review of the state of the art and theoretical understanding of the whole process. This understanding is expanded in several key areas by careful simulations and experiments. In particular, the description of the physical processes in the SNICS (the ion source used in Göttingen at the MaRPeL accelerator) is revised and a new model is proposed that allows for a more realistic description of the behavior of the ion source. Further more, the stopping process of fast projectiles in matter has been described by a new approach that allows a description of this complicated process down to much lower energies in the binary collision approximation than typically possible. At the same time new parametrizations of commonly used approximations for fast ion stopping were explored. The etching process of inorganic semiconductors is investigated more closely and the influence of defects and Hydrogen at the surface is investigated separately for the first time. Progress was also made to understand the electric changes at the surface of Gallium Arsenide due to the presence of defects. A new generation of PBW simulations was also developed that, for the first time, allow to model the entire process for p-type and n-type inorganic semiconductors on the same theoretical foundation with high resolution. Further more, a first model is provided for the simulation of the deformation of radiation damaged structures created in PBW.

Beyond that, the accelerator facilities in Göttingen are modified and several routes for improving the micro-beam-line are investigated. These upgrades and their impacts are reported here. They include changes to the layout, magnetic focusing lens system, target chamber, a newly designed sample holder and sample positioning stage system, as well as an entirely new control software for the writing process.

8. Discussion and Outlook

Many of the upgrades to the accelerator facilities carried out in the scope of this work in Göttingen have improved the reliability and practicality of the PBW process in Göttingen greatly. This includes the redesigned micro-beam-line, PBW target chamber and the replacement and modification of many unreliable components along the entire beam-line. However, some hardware limitations have also been found that would require large redesigns to mitigate. As such, valuable experience on the layout and functionality of future PBW beam-lines can be drawn from this work. Overall many aspects of the MaRPel accelerator are now also better understood through this work. Ray-tracing simulations have also been developed for the MaRPel accelerator that can help with future upgrades to the experimental beam-lines as well as the electrostatic and magnetic lens systems along the accelerator.

The software for the micro-beam target chamber stage positioning control developed with this work showed excellent performance and a great route for future developments. The approach to find an optimal target irradiation plan is entirely new to PBW and was found to be very successful. Future research could expand on the initial work done with this thesis.

In the scope of this work, an entirely new design for a sample holder was explored. This newly developed sample holder showed overall great performance and the design shows an interesting route for the development of future sample holders.

The simulation of the stopping process of fast ions in matter was enriched by new simulations and novel points of view. This includes the development of new inter-atomic potentials, simplified approaches to Electronic stopping and approximate models for bond breaking that could benefit many other applications of ion solid interactions in research and industry. In particular the extension of the classical binary collision approximation simulations down to lower interactions energies and complicated target structures is an area of active research that can benefit from this work.

The simulations and experiments on structure formation during PBW have uncovered some interesting aspects of radiation damage during corrosion processes that warrant further investigation. These observations have enhanced the theoretical understanding of the PBW process and can help to extend PBW to even smaller length scales than currently possible. The simulations developed for this thesis might also be used as a basis for future PBW software tools that might be able to generate recipes for irradiation and etching given a target material and final 3D structure, taking into account defect production, defect evolution, the etching chemistry and defect induced swelling of the target. Such tools could be an important corner stone for the use of PBW as a rapid prototyping technique but were outside the scope of this thesis.

Further more, initial research was carried out on deformation of irradiated 3D structures

8. *Discussion and Outlook*

during the etching process. While the typical amount of deformation encountered in the current generation of PBW-produced structures is low, the research here can help investigate the internal strains of irradiated structures in future applications, particularly for applications at the nanometer scale.

Bibliography

- [1] R. Abdolvand and F. Ayazi. “An advanced reactive ion etching process for very high aspect-ratio sub-micron wide trenches in silicon”. In: *Sensors and Actuators A: Physical* 144.1 (May 2008), pp. 109–116.
- [2] Ilesanmi Adesida. “Ion bombardment of resists”. In: *Nuclear Instruments and Methods in Physics Research* 209-210 (1983), pp. 79–86. DOI: 10.1016/0167-5087(83)90785-8.
- [3] P. Allongue and S. Blonkowski. “Corrosion of III-V compounds; a comparative study of GaAs and InP”. In: *Journal of Electroanalytical Chemistry and Interfacial Electrochemistry* 317.1-2 (1991), pp. 77–99. DOI: 10.1016/0022-0728(91)85004-9.
- [4] P. Allongue and S. Blonkowski. “Influence of the doping concentration on the electrochemical etching of semiconductors”. In: *Electrochimica Acta* 38.7 (1993), pp. 889–895. DOI: 10.1016/0013-4686(93)87006-y.
- [5] Peter Van Alstine and Horace W. Crater. “A tale of three equations: Breit, Eddington-Gaunt, and two-body Dirac”. In: *Foundations of Physics* 27.1 (Jan. 1997), pp. 67–79. DOI: 10.1007/bf02550156.
- [6] L. H. Andersen et al. “Measurement of the Z13 contribution to the stopping power using MeV protons and antiprotons: The Barkas effect”. In: *Physical Review Letters* 62.15 (1989), pp. 1731–1734. DOI: 10.1103/physrevlett.62.1731.
- [7] C. Angeli et al. “Introduction of n-electron valence states for multireference perturbation theory”. In: *The Journal of Chemical Physics* 114.23 (June 2001), pp. 10252–10264. DOI: 10.1063/1.1361246.
- [8] K. Ansari et al. “Fabrication of high aspect ratio 100nm metallic stamps for nanoimprint lithography using proton beam writing”. In: *Applied Physics Letters* 85.3 (2004), pp. 476–478. DOI: 10.1063/1.1773933.
- [9] Yasushi Aoki et al. “Radiation effects of ion beams on polystyrene resist films”. In: *Nuclear Instruments and Methods in Physics Research Section B: Beam Interactions with Materials and Atoms* 33.1-4 (1988), pp. 799–802. DOI: 10.1016/0168-583x(88)90686-6.
- [10] Donald G. Archer and Peiming Wang. “The dielectric constant of water and Debye-Hückel limiting law slopes”. In: *Journal of Physical and Chemical Reference Data* 19.2 (1990), pp. 371–411. DOI: 10.1063/1.555853.
- [11] Néstor R. Arista. “Z3 corrections to the scattering of electrons and positrons in atoms and to the energy loss of fast particles in solids”. In: *Physical Review A* 26.1 (July 1982), pp. 209–216. DOI: 10.1103/physreva.26.209.

Bibliography

- [12] K. Arunesh and K. Dharmendra. “Analysis of the generalised Rydberg equation of state”. In: *Physica B: Condensed Matter* 364.1-4 (2005), pp. 130–132. DOI: 10.1016/j.physb.2005.04.004.
- [13] M. Bacal, M. Sasao, and M. Wada. “Negative ion sources”. In: *Journal of Applied Physics* 129.22 (2021), p. 221101. DOI: 10.1063/5.0049289.
- [14] Rodney J. Bartlett. “How and why coupled-cluster theory became the pre-eminent method in an ab initio quantum chemistry”. In: *Theory and Applications of Computational Chemistry*. Elsevier, 2005, pp. 1191–1221. DOI: 10.1016/b978-044451719-7/50085-8.
- [15] Clemens Martin Beckmann. “Protonenstrahlschreiben in dünnen Schichten der organischen Halbleiter Alq3 und MEH-PPV”. MA thesis. Universität Göttingen, 2017.
- [16] R. S. Berry, S. A. Rice, and J. Ross. *Physical Chemistry*. 2nd. New York: Oxford University Press, 2000. Chap. 27-31.
- [17] H. Bethe. “Zur Theorie des Durchgangs schneller Korpuskularstrahlen durch Materie”. In: *Annalen der Physik* 397.3 (1930), pp. 325–400. DOI: 10.1002/andp.19303970303.
- [18] Iain Bethune et al. *Million atom KS-DFT with CP2K*. Tech. rep. Partnership for advanced computing in europe, 2011.
- [19] A. A. Bettiol et al. “Fabrication of buried channel waveguides in photosensitive glass using proton beam writing”. In: *Applied Physics Letters* 88.17 (2006), p. 171106. DOI: 10.1063/1.2198798.
- [20] J. H. Billen and H. T. Richards. “SNICS: a Source of Negative Ions by Cesium Sputtering”. In: *SNEAP 78: symposium of Northeastern accelerator personnel*. 1979.
- [21] Francis Birch. “Finite elastic strain of cubic crystals”. In: *Physical Review* 71.11 (1947), pp. 809–824. DOI: 10.1103/physrev.71.809.
- [22] M. A. Blanco, E. Francisco, and V. Luaña. “GIBBS: isothermal-isobaric thermodynamics of solids from energy curves using a quasi-harmonic Debye model”. In: *Computer Physics Communications* 158.1 (2004), pp. 57–72. DOI: 10.1016/j.comphy.2003.12.001.
- [23] F. Bloch. “Bemerkung zur elektronentheorie des ferromagnetismus und der elektrischen leitfähigkeit”. In: *Zeitschrift für Physik* 57.7-8 (1929), pp. 545–555. DOI: 10.1007/bf01340281.
- [24] P. E. Blöchl. “Projector augmented-wave method”. In: *Physical Review B* 50.24 (1994), pp. 17953–17979. DOI: 10.1103/physrevb.50.17953.
- [25] Artem D. Bochevarov and Richard A. Friesner. “The densities produced by the density functional theory: Comparison to full configuration interaction”. In: *The Journal of Chemical Physics* 128.3 (2008), p. 034102. DOI: 10.1063/1.2821123.

Bibliography

- [26] J. O'M. Bockris and A. K. N. Reddy. *Modern Electrochemistry*. New York: Kluwer Academic/Plenum Publishers, 2000.
- [27] V. A. Bogdanova et al. "Effective electron mass in heavily doped GaAs in the ordering of impurity complexes". In: *Semiconductors* 36.4 (2002), pp. 385–389. DOI: 10.1134/1.1469184.
- [28] N. Bohr. "Scattering and stopping of fission fragments". In: *Physical Review* 58.7 (1940), pp. 654–655. DOI: 10.1103/physrev.58.654.
- [29] Niels Bohr. "On the Theory of the Decrease of Velocity of Moving Electrified Particles on Passing Through Matter". In: *Phil. Mag.* 25 (Jan. 1913), pp. 10–31.
- [30] Niels Bohr. "The Penetration of Atomic Particles Through Matter". In: *Mat.-Fys. Medd. Dan. Vidensk. Selsk.* 18.4 (1948), pp. 423–568. DOI: 10.1016/s1876-0503(08)70172-5.
- [31] G. Borghs et al. "Band-gap narrowing in highly doped n- and p-type GaAs studied by photoluminescence spectroscopy". In: *Journal of Applied Physics* 66.9 (1989), pp. 4381–4386. DOI: 10.1063/1.343958.
- [32] Jay P. Boris. "Relativistic plasma simulation-optimization of a hybrid code". In: *Proc. Fourth Conf. Num. Sim. Plasmas*. 1970, pp. 3–67.
- [33] H. Boudinov, A. V. P. Coelho, and J. P. de Souza. "Electrical isolation of p-type GaAs layers by ion irradiation". In: *Journal of Applied Physics* 91.10 (2002), p. 6585. DOI: 10.1063/1.1469693.
- [34] Michael Bozoian. "A useful formula for departures from Rutherford backscattering". In: *Nuclear Instruments and Methods in Physics Research Section B: Beam Interactions with Materials and Atoms* 82.4 (1993), pp. 602–603. DOI: 10.1016/0168-583x(93)96017-7.
- [35] M. B. H. Breese et al. "MeV ion beam lithography of PMMA". In: *Nuclear Instruments and Methods in Physics Research Section B: Beam Interactions with Materials and Atoms* 77.1-4 (1993), pp. 169–174. DOI: 10.1016/0168-583x(93)95540-1.
- [36] R. Brenn et al. "Post-mortem intake of lead in 11th century human bones and teeth studied by milli- and microbeam PIXE and RBS". In: *Nuclear Instruments and Methods in Physics Research Section B: Beam Interactions with Materials and Atoms* 158.1-4 (1999), pp. 270–274. DOI: 10.1016/s0168-583x(99)00305-5.
- [37] G. J. Brug et al. "The analysis of electrode impedances complicated by the presence of a constant phase element". In: *Journal of Electroanalytical Chemistry and Interfacial Electrochemistry* 176.1-2 (1984), pp. 275–295. DOI: 10.1016/s0022-0728(84)80324-1.
- [38] Giovanni Bussi, Davide Donadio, and Michele Parrinello. "Canonical sampling through velocity rescaling". In: *The Journal of Chemical Physics* 126.1 (2007), p. 014101. DOI: 10.1063/1.2408420.

Bibliography

- [39] Eike Caldeweyher, Christoph Bannwarth, and Stefan Grimme. “Extension of the D3 dispersion coefficient model”. In: *The Journal of Chemical Physics* 147.3 (2017), p. 034112. DOI: 10.1063/1.4993215.
- [40] Eike Caldeweyher et al. “A generally applicable atomic-charge dependent London dispersion correction”. In: *The Journal of Chemical Physics* 150.15 (2019), p. 154122. DOI: 10.1063/1.5090222.
- [41] Eike Caldeweyher et al. “Extension and evaluation of the D4 London-dispersion model for periodic systems”. In: *Physical Chemistry Chemical Physics* 22.16 (2020), pp. 8499–8512. DOI: 10.1039/d0cp00502a.
- [42] G. T. Caskey et al. “A simple negative-ion sputter source”. In: *Nuclear Instruments and Methods* 157.1 (1978), pp. 1–7. DOI: 10.1016/0029-554x(78)90581-5.
- [43] D. M. Caughey and R. E. Thomas. “Carrier mobilities in silicon empirically related to doping and field”. In: *Proceedings of the IEEE* 55.12 (1967), pp. 2192–2193. DOI: 10.1109/proc.1967.6123.
- [44] S. Chandra and N. Khare. “Electro-deposited gallium arsenide film: I. Preparation, structural, optical and electrical studies”. In: *Semiconductor Science and Technology* 2.4 (1987), pp. 214–219. DOI: 10.1088/0268-1242/2/4/003.
- [45] M. Chatzichristidi et al. “Aqueous base developable: easy stripping, high aspect ratio negative photoresist for optical and proton beam lithography”. In: *Microsystem Technologies* 14.9-11 (2008), pp. 1423–1428. DOI: 10.1007/s00542-008-0571-x.
- [46] Mohan Chen et al. “Ab initio theory and modeling of water”. In: *Proceedings of the National Academy of Sciences* 114.41 (2017), pp. 10846–10851. DOI: 10.1073/pnas.1712499114.
- [47] Xiongyeu Chew et al. “Dynamic tuning of an optical resonator through MEMS-driven coupled photonic crystal nanocavities”. In: *Optics Letters* 35.15 (2010), p. 2517. DOI: 10.1364/ol.35.002517.
- [48] Yong-Sub Cho, Bum-Sik Park, and In-Seok Hong. “Simulation of charge exchange interactions in a tandem accelerator for proton irradiations”. In: *Journal of the Korean Physical Society* 54.5(2) (2009), pp. 1970–1974. DOI: 10.3938/jkps.54.1970.
- [49] Z. Chunxiang, D. E. Dunn, and R. Katz. “Radial distribution of dose and cross-sections for the inactivation of dry enzymes and viruses”. In: *Radiation Protection Dosimetry* 13.1-4 (1985), pp. 215–218. DOI: 10.1093/rpd/13.1-4.215.
- [50] P. H. van Cittert. “Zum Einfluß der Spaltbreite auf die Intensitätsverteilung in Spektrallinien. II”. In: *Zeitschrift für Physik* 69.5-6 (1931), pp. 298–308. DOI: 10.1007/bf01391351.
- [51] C. D. Clark, P. J. Dean, and P. V. Harris. “Intrinsic edge absorption in diamond”. In: *Proceedings of the Royal Society of London. Series A. Mathematical and Physical Sciences* 277.1370 (1964), pp. 312–329. DOI: 10.1098/rspa.1964.0025.

Bibliography

- [52] A. V. P. Coelho and H. Boudinov. “Sheet resistance of GaAs conductive layers isolated by proton irradiation”. In: *Nuclear Instruments and Methods in Physics Research Section B: Beam Interactions with Materials and Atoms* 245.2 (2006), pp. 435–439. DOI: 10.1016/j.nimb.2005.11.149.
- [53] E. A. B. Cole. *Mathematical and numerical modelling of heterostructure semiconductor devices: from theory to programming*. Springer-Verlag GmbH, Nov. 2009. 406 pp. ISBN: 9781848829374. URL: https://www.ebook.de/de/product/19205416/e_a_b_cole_mathematical_and_numerical_modelling_of_heterostructure_semiconductor_devices_from_theory_to_programming.html.
- [54] J. S. Custer et al. “Density of amorphous Si”. In: *Applied Physics Letters* 64.4 (1994), pp. 437–439. DOI: 10.1063/1.111121.
- [55] Dimitrios Damianos, Jérôme Mouly, and Pierre Delbos. *Status of the MEMS industry*. Tech. rep. Yole Développement, June 2021.
- [56] Hendrix Demers et al. “Three-dimensional electron microscopy simulation with the CASINO Monte Carlo software”. In: *Scanning* 33.3 (2011), pp. 135–146. DOI: 10.1002/sca.20262.
- [57] P. A. M. Dirac. “Note on exchange phenomena in the thomas atom”. In: *Mathematical Proceedings of the Cambridge Philosophical Society* 26.3 (1930), pp. 376–385. DOI: 10.1017/s0305004100016108.
- [58] N. D. Drummond, M. D. Towler, and R. J. Needs. “Jastrow correlation factor for atoms, molecules, and solids”. In: *Physical Review B* 70.23 (Dec. 2004). DOI: 10.1103/physrevb.70.235119.
- [59] Frans B. van Duijneveldt, Jeanne G. C. M. van Duijneveldt-van de Rijdt, and Joop H. van Lenthe. “State of the art in counterpoise theory”. In: *Chemical Reviews* 94.7 (1994), pp. 1873–1885. DOI: 10.1021/cr00031a007.
- [60] Pablo Echenique and J. L. Alonso. “A mathematical and computational review of Hartree-Fock SCF methods in quantum chemistry”. In: *Molecular Physics* 105.23-24 (2007), pp. 3057–3098. DOI: 10.1080/00268970701757875.
- [61] Wolfgang Eckstein. *Computer Simulation of Ion-Solid Interactions*. Berlin, Heidelberg: Springer Berlin Heidelberg, 1991. ISBN: 9783642735134.
- [62] Sebastian Ehlert et al. “r2SCAN-D4: dispersion corrected meta-generalized gradient approximation for general chemical applications”. In: *The Journal of Chemical Physics* 154.6 (2021), p. 061101. DOI: 10.1063/5.0041008.
- [63] Cristian Farías, Victor A. Pinto, and Pablo S. Moya. “What is the temperature of a moving body?” In: *Scientific Reports* 7.1 (2017). DOI: 10.1038/s41598-017-17526-4.
- [64] A. S. Feiner and A. J. McEvoy. “The Nernst Equation”. In: *J. Chem. Educ.* 71.6 (June 1994), pp. 493–494.

Bibliography

- [65] Z. Fekete et al. “Characterization of the end-of-range geometric effects in complex 3D silicon micro-components formed by proton beam writing”. In: *Journal of Micromechanics and Microengineering* 20.6 (2010), p. 064015. DOI: 10.1088/0960-1317/20/6/064015.
- [66] E. Fermi. “Eine statistische Methode zur Bestimmung einiger Eigenschaften des Atoms und ihre Anwendung auf die Theorie des periodischen Systems der Elemente”. In: *Zeitschrift für Physik* 48.1-2 (1928), pp. 73–79. DOI: 10.1007/bf01351576.
- [67] Enrico Fermi. “Sopra lo spostamento per pressione delle righe elevate delle serie spettrali”. In: *Nuovo Cimento* 11 (1934), p. 157.
- [68] Leonardo de Ferrariis and Néstor R. Arista. “Classical and quantum-mechanical treatments of the energy loss of charged particles in dilute plasmas”. In: *Physical Review A* 29.4 (Apr. 1984), pp. 2145–2159. DOI: 10.1103/physreva.29.2145.
- [69] H. O. Finklea. *Studies in physical and theoretical chemistry: Semiconductor electrodes*. Amsterdam: Elsevier, 1988.
- [70] O. B. Firsov. “A qualitative interpretation of the mean electron excitation energy in atomic collisions”. In: *J. Exptl. Theoret. Phys. (U.S.S.R.)* 36 (May 1959), pp. 1517–1523.
- [71] O. B. Firsov. “Calculation of the interaction potential of atoms”. In: *Soviet Physics JETP* 6.33 (1958).
- [72] James W. Furness et al. “Accurate and numerically efficient r2SCAN meta-generalized gradient approximation”. In: *The Journal of Physical Chemistry Letters* 11.19 (2020), pp. 8208–8215. DOI: 10.1021/acs.jpclett.0c02405.
- [73] J. F. Gibbons. “Ion implantation in semiconductors—part II: damage production and annealing”. In: *Proceedings of the IEEE* 60.9 (1972), pp. 1062–1096. DOI: 10.1109/proc.1972.8854.
- [74] M. D. Giles. “Ultimate resolution and contrast in ion-beam lithography”. In: *Journal of Vacuum Science & Technology B: Microelectronics and Nanometer Structures* 5.6 (1987), p. 1588. DOI: 10.1116/1.583677.
- [75] R. Gilliam et al. “A review of specific conductivities of potassium hydroxide solutions for various concentrations and temperatures”. In: *International Journal of Hydrogen Energy* 32.3 (2007), pp. 359–364. DOI: 10.1016/j.ijhydene.2006.10.062.
- [76] J. Goettert et al. “LiGA Research and Service at CAMD”. In: *Journal of Physics: Conference Series* 34 (May 2006), pp. 912–918.
- [77] W. P. Gomes and D. Vanmaekelbergh. “Impedance spectroscopy at semiconductor electrodes: Review and recent developments”. In: *Electrochimica Acta* 41.7-8 (1996), pp. 967–973. DOI: 10.1016/0013-4686(95)00427-0.

Bibliography

- [78] I. Gomez-Morilla et al. “Rapid deep micromachining of polytetrafluoroethylene by MeV ion bombardment in oxygen-rich atmospheres”. In: *Journal of Micromechanics and Microengineering* 15.4 (2005), pp. 698–701. DOI: 10.1088/0960-1317/15/4/004.
- [79] Stefan Grimme. “Improved second-order Møller-Plesset perturbation theory by separate scaling of parallel- and antiparallel-spin pair correlation energies”. In: *The Journal of Chemical Physics* 118.20 (2003), pp. 9095–9102. DOI: 10.1063/1.1569242.
- [80] L. J. Guerin et al. “Simple and low cost fabrication of embedded micro-channels by using a new thick-film photoplastic”. In: *Proceedings of International Solid State Sensors and Actuators Conference (Transducers '97)*. IEEE, 1997. DOI: 10.1109/sensor.1997.635730.
- [81] R. Guidelli et al. “Defining the transfer coefficient in electrochemistry: An assessment (IUPAC Technical Report)”. In: *Pure Appl. Chem.* 86.2 (Feb. 2014), pp. 245–258.
- [82] C. M. Guldberg. “Concerning the Laws of Chemical Affinity”. In: *C. M. Forhandlinger: Videnskabs-Selskabet i Christiania* 111 (1864).
- [83] C. M. Guldberg and P. Waage. “Concerning Chemical Affinity”. In: *Erdmann’s Journal für Practische Chemie* 127 (1879), pp. 69–114.
- [84] C. M. Guldberg and P. Waage. “Studies Concerning Affinity”. In: *C. M. Forhandlinger: Videnskabs-Selskabet i Christiania* 35 (1864).
- [85] D. R. Hamann, M. Schlüter, and C. Chiang. “Norm-conserving pseudopotentials”. In: *Physical Review Letters* 43.20 (1979), pp. 1494–1497. DOI: 10.1103/physrevlett.43.1494.
- [86] E. S. Harmon, M. R. Melloch, and M. S. Lundstrom. “Effective band-gap shrinkage in GaAs”. In: *Applied Physics Letters* 64.4 (1994), pp. 502–504. DOI: 10.1063/1.111110.
- [87] F. J. Harris. “On the use of windows for harmonic analysis with the discrete Fourier transform”. In: *Proceedings of the IEEE* 66.1 (1978), pp. 51–83. DOI: 10.1109/proc.1978.10837.
- [88] Jonas Martin Hartwig. “Aufbau eines MeV Protonen Mikrostrahls”. MA thesis. Georg-August-Universität Göttingen, 2008.
- [89] C. Hartwigsen, S. Goedecker, and J. Hutter. “Relativistic separable dual-space Gaussian pseudopotentials from H to Rn”. In: *Physical Review B* 58.7 (1998), pp. 3641–3662. DOI: 10.1103/physrevb.58.3641.
- [90] William Haynes. *CRC handbook of chemistry and physics : a ready-reference book of chemical and physical data*. Boca Raton, Florida: CRC Press, 2017. ISBN: 9781498754293.

Bibliography

- [91] H. van Heeren and P. Salomon. *MEMS - recent developments, future directions*. Tech. rep. Electronics Enabled Products Knowledge Transfer Network, Wolfson School of Mechanical and Manufacturing Engineering, Loughborough University, 2007.
- [92] H. C. Helgeson, D. H. Kirkham, and G. C. Flowers. “Theoretical prediction of the thermodynamic behavior of aqueous electrolytes by high pressures and temperatures IV, calculation of activity coefficients, osmotic coefficients, and apparent molal and standard and relative partial molal properties to 600 degrees c and 5kb”. In: *American Journal of Science* 281.10 (1981), pp. 1249–1516. DOI: 10.2475/ajs.281.10.1249.
- [93] H. Hellmann. “A new approximation method in the problem of many electrons”. In: *The Journal of Chemical Physics* 3.1 (1935), pp. 61–61. DOI: 10.1063/1.1749559.
- [94] K.-H. Hellwege and A. M. Hellwege, eds. *Molecular constants from microwave, molecular beam, and electron spin resonance spectroscopy*. Springer-Verlag, 1974. DOI: 10.1007/b19951.
- [95] J. M. Hernández-Mangas et al. “Enhanced modelization of ion implant simulation in compound semiconductors”. In: *Solid-State Electronics* 46.9 (2002), pp. 1315–1324. DOI: 10.1016/s0038-1101(02)00072-2.
- [96] Bernd A. Heß et al. “A mean-field spin-orbit method applicable to correlated wavefunctions”. In: *Chemical Physics Letters* 251.5-6 (1996), pp. 365–371. DOI: 10.1016/0009-2614(96)00119-4.
- [97] F. L. Hirshfeld. “Bonded-atom fragments for describing molecular charge densities”. In: *Theoretica Chimica Acta* 44.2 (1977), pp. 129–138. DOI: 10.1007/bf00549096.
- [98] H. Hofsäss, K. Zhang, and A. Mutzke. “Simulation of ion beam sputtering with SDTrimSP, TRIDYN and SRIM”. In: *Applied Surface Science* 310 (2014), pp. 134–141. DOI: 10.1016/j.apsusc.2014.03.152.
- [99] Hans Hofsäss and Alrik Stegmaier. “Binary collision approximation simulations of ion solid interaction without the concept of surface binding energies”. In: *Nuclear Instruments and Methods in Physics Research Section B: Beam Interactions with Materials and Atoms* 517 (2022), pp. 49–62. DOI: 10.1016/j.nimb.2022.02.012.
- [100] K. P. Huber and G. Herzberg. *Molecular spectra and molecular structure*. Springer US, 1979. DOI: 10.1007/978-1-4757-0961-2.
- [101] Michael Huff. *Process variations in microsystems manufacturing*. Springer International Publishing, 2020. DOI: 10.1007/978-3-030-40560-1.
- [102] M. M. Hurley et al. “Ab initio relativistic effective potentials with spin-orbit operators. II. K through Kr”. In: *The Journal of Chemical Physics* 84.12 (1986), pp. 6840–6853. DOI: 10.1063/1.450689.
- [103] S. Jacobsen. *A Proposal for the Development of Micro Electro-Mechanical Systems (MEMS)*. submitted to Defense Advanced Research Projects Agency. The Center for Engineering Design, University of Utah, July 1986.

Bibliography

- [104] Lukas Raam Jäger. “Optimierung des Steuerungsprogramms für Protonenstrahlschreiben und Anwendung in Polycarbonat”. MA thesis. Universität Göttingen, 2019.
- [105] Fatin Syazana Jamaludin and Mohd Faizul Mohd Sabri. “Investigation on fabricating high aspect ratio microholes on silicon by FIB/SEM milling”. In: *Advanced Materials Research* 626 (2012), pp. 436–439. DOI: 10.4028/www.scientific.net/amr.626.436.
- [106] M. Jelinek et al. “MeV-proton channeling in crystalline silicon”. In: *2014 20th International Conference on Ion Implantation Technology (IIT)*. IEEE, 2014. DOI: 10.1109/iit.2014.6940059.
- [107] Russell Johnson. *NIST 101. Computational Chemistry Comparison and Benchmark Database*. en. Aug. 2020.
- [108] J. W. Judy. “Microelectromechanical systems (MEMS): fabrication, design and applications”. In: *Smart Mater. Struct.* 10 (Nov. 2001), pp. 1115–1134.
- [109] Ansgar Jüngel. *Transport equations for semiconductors*. Springer Berlin Heidelberg, 2009. DOI: 10.1007/978-3-540-89526-8.
- [110] Efsthios Kamaratos. “Developments regarding the Bragg rule for stopping power and critical examination of its application to water”. In: *Nuclear Instruments and Methods in Physics Research* 215.1-2 (Sept. 1983), pp. 337–344. DOI: 10.1016/0167-5087(83)91326-1.
- [111] J. A. van Kan, A. A. Bettiol, and F. Watt. “Three-dimensional nanolithography using proton beam writing”. In: *Applied Physics Letters* 83.8 (2003), pp. 1629–1631. DOI: 10.1063/1.1604468.
- [112] J. A. van Kan, P. Malar, and Armin Baysic de Vera. “The second generation Singapore high resolution proton beam writing facility”. In: *Review of Scientific Instruments* 83.2 (2012), 02B902. DOI: 10.1063/1.3662205.
- [113] J. A. van Kan et al. “Resist materials for proton micromachining”. In: *Nuclear Instruments and Methods in Physics Research Section B: Beam Interactions with Materials and Atoms* 158.1-4 (1999), pp. 179–184. DOI: 10.1016/s0168-583x(99)00392-4.
- [114] Jeroen A. van Kan, Andrew A. Bettiol, and Frank Watt. “Proton beam writing of three-dimensional nanostructures in hydrogen silsesquioxane”. In: *Nano Letters* 6.3 (2006), pp. 579–582. DOI: 10.1021/nl052478c.
- [115] Y. Kato et al. “Electrical conductivity of disordered layers in GaAs crystal produced by ion implantation”. In: *Journal of Applied Physics* 45.3 (1974), pp. 1044–1049. DOI: 10.1063/1.1663366.
- [116] T. E. Kazior, S. K. Brierley, and F. J. Piekarski. “Capless rapid thermal annealing of GaAs using a graphite susceptor”. In: *IEEE Transactions on Semiconductor Manufacturing* 4.1 (1991), pp. 21–25. DOI: 10.1109/66.75860.

Bibliography

- [117] Hyeon Il Kim and Young-Ouk Lee. “Nuclear Data Evaluation for Proton-Induced Reactions of Aluminum based on the Talys Code”. In: *Journal of the Korean Physical Society* 52.9(3) (2008), pp. 837–842. DOI: 10.3938/jkps.52.837.
- [118] Tsunenobu Kimoto and James A. Cooper. *Fundamentals of silicon carbide technology*. John Wiley & Sons Singapore Pte. Ltd, 2014. DOI: 10.1002/9781118313534.
- [119] Chiken Kinoshita and Steven J. Zinkle. “Potential and limitations of ceramics in terms of structural and electrical integrity in fusion environments”. In: *Journal of Nuclear Materials* 233-237 (1996), pp. 100–110. DOI: 10.1016/s0022-3115(96)00319-4.
- [120] W. Kohn and L. J. Sham. “Self-consistent equations including exchange and correlation effects”. In: *Physical Review* 140.4A (1965), A1133–A1138. DOI: 10.1103/physrev.140.a1133.
- [121] Arthur Komar. “Relativistic equipartition”. In: *General Relativity and Gravitation* 28.4 (1996), pp. 379–385. DOI: 10.1007/bf02105082.
- [122] A. Yu. Konobeyev et al. “Evaluation of effective threshold displacement energies and other data required for the calculation of advanced atomic displacement cross-sections”. In: *Nuclear Energy and Technology* 3.3 (2017), pp. 169–175. DOI: 10.1016/j.nucet.2017.08.007.
- [123] Tristan Koppe et al. “Modeling electrochemical etching of proton irradiated p-GaAs for the design of MEMS building blocks”. In: *Journal of Microelectromechanical Systems* 23.4 (2014), pp. 955–960. DOI: 10.1109/jmems.2014.2309178.
- [124] Steffen Korn. “Studium durch Ionenstrahlen hervorgerufener induzierter Ladung in Halbleiterpixeldetektoren”. Bachelor’s thesis. Universität Göttingen, July 2017.
- [125] Alexander Kramida and Yuri Ralchenko. *NIST Atomic Spectra Database, NIST Standard Reference Database* 78. en. www.nist.gov/pml/atomic-spectra-database. 1999. DOI: 10.18434/T4W30F.
- [126] R. E. Kroon et al. “Photoluminescence of Be implanted Si-doped GaAs”. In: *Journal of Electronic Materials* 28.12 (1999), pp. 1466–1470. DOI: 10.1007/s11664-999-0143-6.
- [127] Thomas D. Kühne et al. “CP2K: an electronic structure and molecular dynamics software package - quickstep: efficient and accurate electronic structure calculations”. In: *The Journal of Chemical Physics* 152.19 (2020), p. 194103. DOI: 10.1063/5.0007045.
- [128] Willis E. Lamb. “Passage of uranium fission fragments through matter”. In: *Physical Review* 58.8 (1940), pp. 696–702. DOI: 10.1103/physrev.58.696.
- [129] L. Landweber. “An iteration formula for fredholm integral equations of the first kind”. In: *American Journal of Mathematics* 73.3 (1951), p. 615. DOI: 10.2307/2372313.
- [130] Susi Lehtola. “Polarized gaussian basis sets from one-electron ions”. In: *The Journal of Chemical Physics* 152.13 (2020), p. 134108. DOI: 10.1063/1.5144964.

- [131] Susi Lehtola et al. “Recent developments in libxc - a comprehensive library of functionals for density functional theory”. In: *SoftwareX* 7 (2018), pp. 1–5. DOI: 10.1016/j.softx.2017.11.002.
- [132] H. S. Leipner et al. “Copper diffusion in dislocation-rich gallium arsenide”. In: *Philosophical Magazine A* 79.11 (1999), pp. 2785–2802. DOI: 10.1080/01418619908212024.
- [133] A. S. Lileev, D. V. Loginova, and A. K. Lyashchenko. “Microwave dielectric properties of potassium hydroxide aqueous solutions”. In: *Russian Journal of Inorganic Chemistry* 56.6 (2011), pp. 961–967. DOI: 10.1134/s0036023611060167.
- [134] Alexander S. Lileev, Dar’ya V. Loginova, and Andrey K. Lyashchenko. “Dielectric properties of aqueous hydrochloric acid solutions”. In: *Mendeleev Communications* 17.6 (2007), pp. 364–365. DOI: 10.1016/j.mencom.2007.11.024.
- [135] J. Lindhard and M. Scharff. “Energy Dissipation by Ions in the keV Region”. In: *Physical Review* 124.1 (1961), pp. 128–130. DOI: 10.1103/physrev.124.128.
- [136] J. Lindhard and M. Scharff. “Energy loss in matter by fast particles of low charge”. In: *Dan. Mat. Fys. Medd.* 27.15 (1953).
- [137] Jens Lindhard. *Influence of crystal lattice on motion of energetic charged particles*. Vol. 34. 16. Munksgaard Copenhagen, 1965.
- [138] Jens Lindhard. “On the properties of a gas of charged particles”. In: *Dan. Mat. Fys. Medd.* 28.8 (1954).
- [139] Jens Lindhard and Allan H. Sørensen. “Relativistic theory of stopping for heavy ions”. In: *Physical Review A* 53.4 (1996), pp. 2443–2456. DOI: 10.1103/physreva.53.2443.
- [140] Gordon Gan Liu. “Electrochemical behaviour of gallium arsenide”. MA thesis. University of british Columbia, 1991.
- [141] Junzi Liu and Lan Cheng. “Relativistic coupled-cluster and equation-of-motion coupled-cluster methods”. In: *WIREs Computational Molecular Science* 11.6 (2021). DOI: 10.1002/wcms.1536.
- [142] Wenjian Liu. “Essentials of relativistic quantum chemistry”. In: *The Journal of Chemical Physics* 152.18 (2020), p. 180901. DOI: 10.1063/5.0008432.
- [143] Wenjian Liu. *Handbook of relativistic quantum chemistry*. Berlin, Germany: Springer, 2016. ISBN: 9783642407666.
- [144] C. A. Valerio Lizarraga et al. “A study on the negative ion beam production in the ININ sputtering ion source”. In: *Revista Mexicana de Física* 65.3 May-Jun (2019), pp. 278–283. DOI: 10.31349/revmexfis.65.278.
- [145] Roger Loger et al. “Ion source workshop MC-SNICS areas of improvement”. In: *Ion source workshop MC-SNICS areas of improvement*. NEC. Middleton, Wisconsin, 2003.
- [146] Z. H. Lu, M. C. Hanna, and A. Majerfeld. “Determination of band gap narrowing and hole density for heavily C-doped GaAs by photoluminescence spectroscopy”. In: *Applied Physics Letters* 64.1 (1994), pp. 88–90. DOI: 10.1063/1.110877.

Bibliography

- [147] Josef Lutz et al. *Semiconductor power devices*. Springer Berlin Heidelberg, 2011. DOI: 10.1007/978-3-642-11125-9.
- [148] V. R. Mamilla and K. S. Chakradhar. “Micro machining for micro electro mechanical systems (MEMS)”. In: *Procedia Materials Science* 6 (2014), pp. 1170–1177.
- [149] S. N. Markin, D. Primetzhofer, and P. Bauer. “Vanishing electronic energy loss of very slow light ions in insulators with large band gaps”. In: *Physical Review Letters* 103.11 (2009), p. 113201. DOI: 10.1103/physrevlett.103.113201.
- [150] Richard J. Mathar and Matthias Posselt. “Effective-charge theory for the electronic stopping of heavy ions in solids: Stripping criteria and target-electron models”. In: *Physical Review B* 51.1 (1995), pp. 107–116. DOI: 10.1103/physrevb.51.107.
- [151] A. Matthiessen and C. Vogt. “On the Influence of Temperature on the Electric Conducting-Power of Alloys”. In: *Philosophical Transactions of the Royal Society of London* 154.167 (1864).
- [152] D. A. McQuarrie and J. D. Simon. *Physical Chemistry, a molecular approach*. Sausalito, California: University Science Books, 1997.
- [153] H. J. McSkimin. “Measurement of elastic constants at low temperatures by means of ultrasonic waves—data for silicon and germanium single crystals, and for fused silica”. In: *Journal of Applied Physics* 24.8 (1953), pp. 988–997. DOI: 10.1063/1.1721449.
- [154] H. J. McSkimin and P. Andreatch. “Elastic moduli of diamond as a function of pressure and temperature”. In: *Journal of Applied Physics* 43.7 (1972), pp. 2944–2948. DOI: 10.1063/1.1661636.
- [155] H. J. McSkimin and P. Andreatch. “Elastic moduli of Silicon vs hydrostatic pressure at 25.0°C and - 195.8°C”. In: *Journal of Applied Physics* 35.7 (July 1964), pp. 2161–2165. DOI: 10.1063/1.1702809.
- [156] H. J. McSkimin, A. Jayaraman, and P. Andreatch. “Elastic moduli of GaAs at moderate pressures and the evaluation of compression to 250 kbar”. In: *Journal of Applied Physics* 38.5 (1967), pp. 2362–2364. DOI: 10.1063/1.1709884.
- [157] R. Medenwaldt et al. “Measurement of the stopping power of silicon for antiprotons between 0.2 and 3 MeV”. In: *Nuclear Instruments and Methods in Physics Research Section B: Beam Interactions with Materials and Atoms* 58.1 (1991), pp. 1–5. DOI: 10.1016/0168-583x(91)95670-9.
- [158] Michael G. Medvedev et al. “Density functional theory is straying from the path toward the exact functional”. In: *Science* 355.6320 (2017), pp. 49–52. DOI: 10.1126/science.aah5975.
- [159] M. K. Mehta et al. “Reactions induced by proton bombardment of aluminium”. In: *Nuclear Physics* 89.1 (1966), pp. 22–32. DOI: 10.1016/0029-5582(66)90843-1.
- [160] F. Menzel et al. “Fabrication of microstructures in III-V semiconductors by proton beam writing”. In: *Nuclear Instruments and Methods in Physics Research Section B: Beam Interactions with Materials and Atoms* 267.12-13 (2009), pp. 2321–2326. DOI: 10.1016/j.nimb.2009.03.023.

Bibliography

- [161] R. Middleton. “A survey of negative ions from a cesium sputter source”. In: *Nuclear Instruments and Methods* 144.3 (1977), pp. 373–399. DOI: 10.1016/0029-554x(77)90001-5.
- [162] R. Middleton. “A versatile high intensity negative ion source”. In: *Nuclear Instruments and Methods in Physics Research* 214.2-3 (1983), pp. 139–150. DOI: 10.1016/0167-5087(83)90580-x.
- [163] R. Middleton and Charles T. Adams. “A close to universal negative ion source”. In: *Nuclear Instruments and Methods* 118.2 (1974), pp. 329–336. DOI: 10.1016/0029-554x(74)90634-x.
- [164] G. Milovanović. “Numerical Modeling of Quantum Cascade Lasers”. PhD thesis. Technische Universität Wien, Fakultät für Elektrotechnik und Informationstechnik, Mar. 2011.
- [165] P. Mistry et al. “New developments in the applications of proton beam writing”. In: *Nuclear Instruments and Methods in Physics Research Section B: Beam Interactions with Materials and Atoms* 237.1-2 (2005), pp. 188–192. DOI: 10.1016/j.nimb.2005.04.099.
- [166] Gert Moliere. “Theorie der Streuung schneller geladener Teilchen I. Einzelstreuung am abgeschirmten Coulomb-Feld”. In: *Zeitschrift für Naturforschung A* 2.3 (Mar. 1947), pp. 133–145. DOI: 10.1515/zna-1947-0302.
- [167] Chr. Møller and M. S. Plesset. “Note on an approximation treatment for many-electron systems”. In: *Physical Review* 46.7 (1934), pp. 618–622. DOI: 10.1103/physrev.46.618.
- [168] S. P. Møller. “Measurement of the barkas effect using MeV antiprotons and protons and an active silicon target”. In: *Nuclear Instruments and Methods in Physics Research Section B: Beam Interactions with Materials and Atoms* 48.1-4 (1990), pp. 1–7. DOI: 10.1016/0168-583x(90)90059-4.
- [169] S. P. Møller et al. “Antiproton Stopping at Low Energies: Confirmation of Velocity-Proportional Stopping Power”. In: *Physical Review Letters* 88.19 (2002). DOI: 10.1103/physrevlett.88.193201.
- [170] S. P. Møller et al. “Direct measurements of the stopping power for antiprotons of light and heavy targets”. In: *Physical Review A* 56.4 (1997), pp. 2930–2939. DOI: 10.1103/physreva.56.2930.
- [171] C. C. Montanari and P. Dimitriou. “The IAEA stopping power database, following the trends in stopping power of ions in matter”. In: *Nuclear Instruments and Methods in Physics Research Section B: Beam Interactions with Materials and Atoms* 408 (Oct. 2017), pp. 50–55. DOI: 10.1016/j.nimb.2017.03.138.
- [172] V. S. Muralidharan. “Warburg impedance - basics revisited”. In: *Anti-Corrosion Methods and Materials* 44.1 (1997), pp. 26–29. DOI: 10.1108/00035599710157387.

Bibliography

- [173] F. D. Murnaghan. “The compressibility of media under extreme pressures”. In: *Proceedings of the National Academy of Sciences* 30.9 (1944), pp. 244–247. DOI: 10.1073/pnas.30.9.244.
- [174] S. T. Murphy et al. “Deviations from Vegard’s law in ternary III-V alloys”. In: *Physical Review B* 82.7 (2010), p. 073201. DOI: 10.1103/physrevb.82.073201.
- [175] S. T. Nakagawa and Y. Yamamura. “Interatomic potential in solids and its applications to range calculations”. In: *Radiation Effects* 105.3-4 (1988), pp. 239–256. DOI: 10.1080/00337578808229950.
- [176] H. C. Nathanson et al. “The resonant gate transistor”. In: *IEEE Trans. Elec. Dev.* 14.3 (Mar. 1967), pp. 117–133.
- [177] Harvey C. Nathanson and Robert A. Wickstrom. “Microelectronic frequency selective apparatus with vibratory member and means responsive thereto”. U.S. pat. 3413573. 1965.
- [178] Frank Neese. “Software update: the ORCA program system, version 4.0”. In: *WIREs Computational Molecular Science* 8.1 (July 2017). DOI: 10.1002/wcms.1327.
- [179] Frank Neese et al. “The ORCA quantum chemistry program package”. In: *The Journal of Chemical Physics* 152.22 (2020), p. 224108. DOI: 10.1063/5.0004608.
- [180] Roland Neueder. “Conductivity of electrolytes”. In: *Encyclopedia of Applied Electrochemistry*. Springer New York, 2014, pp. 260–264. DOI: 10.1007/978-1-4419-6996-5_4.
- [181] Stefan Nießner. “Ansteuerung eines Systems von Linearverstärkern zum Protonenstrahlschreiben”. Bachelor’s thesis. Universität Göttingen, 2016.
- [182] S. P. Nikanorov and Bo K. Kardashev. “Elasticity and dislocation inelasticity of crystals”. In: *Moscow Izdatel Nauka* (1985).
- [183] Rattanaorn Norarat et al. “Why are hydrogen ions best for MeV ion beam lithography?” In: *Microelectronic Engineering* 102 (2013), pp. 22–24. DOI: 10.1016/j.mee.2012.02.012.
- [184] Kai Nordlund, N. Runeberg, and D. Sundholm. “Repulsive interatomic potentials calculated using Hartree-Fock and density-functional theory methods”. In: *Nuclear Instruments and Methods in Physics Research Section B: Beam Interactions with Materials and Atoms* 132.1 (1997), pp. 45–54.
- [185] Kai Nordlund et al. “Improving atomic displacement and replacement calculations with physically realistic damage models”. In: *Nature Communications* 9.1 (2018). DOI: 10.1038/s41467-018-03415-5.
- [186] D. J. O’Connor and J. P. Biersack. “Comparison of theoretical and empirical interatomic potentials”. In: *Nuclear Instruments and Methods in Physics Research Section B: Beam Interactions with Materials and Atoms* 15.1-6 (1986), pp. 14–19. DOI: 10.1016/0168-583x(86)90243-0.

Bibliography

- [187] Takeshi Ohshima et al. “Creation of silicon vacancy in silicon carbide by proton beam writing toward quantum sensing applications”. In: *Journal of Physics D: Applied Physics* 51.33 (2018), p. 333002. DOI: 10.1088/1361-6463/aad0ec.
- [188] Terry N. Olney et al. “Absolute scale determination for photoabsorption spectra and the calculation of molecular properties using dipole sum-rules”. In: *Chemical Physics* 223.1 (1997), pp. 59–98. DOI: 10.1016/s0301-0104(97)00145-6.
- [189] F. W. Ostermayer, P. A. Kohl, and R. M. Lum. “Hole transport equation analysis of photoelectrochemical etching resolution”. In: *Journal of Applied Physics* 58.11 (1985), pp. 4390–4396. DOI: 10.1063/1.335529.
- [190] Neil S. Ostlund and Attila Szabo. *Modern quantum chemistry*. Dover Publications Inc., Jan. 1, 1996. 480 pp. ISBN: 0486691861.
- [191] Vassil Palankovski and Rüdiger Quay. *Analysis and simulation of heterostructure devices*. Springer Vienna, 2004. DOI: 10.1007/978-3-7091-0560-3.
- [192] J. Parasuraman et al. “Deep reactive ion etching of sub-micrometer trenches with ultra high aspect ratio”. In: *Microelectronic Engineering* 113 (Jan. 2014), pp. 35–39.
- [193] S. Park et al. “Massive Replication of Polymeric High Aspect Ratio Microstructures Using PDMS Casting”. In: *Proc. SPIE, Smart Structures and Materials 2001: Smart Electronics and MEMS* 4334 (Mar. 2001).
- [194] Su-Moon Park and Matthew E. Barber. “Thermodynamic stabilities of semiconductor electrodes”. In: *Journal of Electroanalytical Chemistry and Interfacial Electrochemistry* 99.1 (1979), pp. 67–75. DOI: 10.1016/s0022-0728(79)80411-8.
- [195] S. J. Pearton. “Ion implantation for isolation of III-V semiconductors”. In: *Materials Science Reports* 4.6 (1990), pp. 313–363. DOI: 10.1016/s0920-2307(05)80001-5.
- [196] R. Fabian Pease. “Imprints offer Moore”. In: *Nature* 417.6891 (2002), pp. 802–803. DOI: 10.1038/417802a.
- [197] Linfa Peng et al. “Micro hot embossing of thermoplastic polymers: a review”. In: *Journal of Micromechanics and Microengineering* 24.1 (2013), p. 013001. DOI: 10.1088/0960-1317/24/1/013001.
- [198] John P. Perdew, Kieron Burke, and Matthias Ernzerhof. “Generalized gradient approximation made simple”. In: *Physical Review Letters* 77.18 (1996), pp. 3865–3868. DOI: 10.1103/physrevlett.77.3865.
- [199] Kristin Persson. *Materials Data on AlP (SG:216) by Materials Project*. An optional note. Nov. 2014. DOI: 10.17188/1191200.
- [200] T. E. Pierce and Marshall Blann. “Stopping Powers and Ranges of 5-90-MeV S32, Cl35, Br79 and I127 Ions in H2, He, N2, Ar and Kr: A Semiempirical Stopping Power Theory for Heavy Ions in Gases and Solids”. In: *Physical Review* 173.2 (1968), pp. 390–405. DOI: 10.1103/physrev.173.390.
- [201] I. Pintilie et al. “Second-order generation of point defects in gamma-irradiated float-zone silicon, an explanation for “type inversion””. In: *Applied Physics Letters* 82.13 (2003), pp. 2169–2171. DOI: 10.1063/1.1564869.

Bibliography

- [202] E. N. Plotnikov, S. I. Lopatin, and V. L. Stolyarova. “Application of the sanderson method to the calculation of bonding energies in oxide glass-forming systems”. In: *Glass Physics and Chemistry* 29.6 (2003), pp. 517–521. DOI: 10.1023/b:gpac.0000007924.65496.ea.
- [203] P. Polesello et al. “Micromachining of silicon with a proton microbeam”. In: *Nuclear Instruments and Methods in Physics Research Section B: Beam Interactions with Materials and Atoms* 158.1-4 (1999), pp. 173–178. DOI: 10.1016/s0168-583x(99)00382-1.
- [204] A. Polity et al. “Defects in electron-irradiated GaAs studied by positron lifetime spectroscopy”. In: *Physical Review B* 55.16 (1997), pp. 10467–10479. DOI: 10.1103/physrevb.55.10467.
- [205] Patrik Pollak and Florian Weigend. “Segmented contracted error-consistent basis sets of double- and triple- ζ valence quality for one- and two-component relativistic all-electron calculations”. In: *Journal of Chemical Theory and Computation* 13.8 (2017), pp. 3696–3705. DOI: 10.1021/acs.jctc.7b00593.
- [206] M. Posselt et al. “Competition between damage buildup and dynamic annealing in ion implantation into Ge”. In: *Applied Physics Letters* 89.15 (2006), p. 151918. DOI: 10.1063/1.2360238.
- [207] J. Price et al. “A study of the interaction of gallium arsenide with wet chemical formulations using thermodynamic calculations and spectroscopic ellipsometry”. In: *Microelectronic Engineering* 87.9 (2010), pp. 1661–1664. DOI: 10.1016/j.mee.2009.11.046.
- [208] I. A. Prudaev and S. S. Khludkov. “Diffusion and solubility of electrically active iron atoms in gallium arsenide”. In: *Russian Physics Journal* 51.11 (2008), pp. 1157–1160. DOI: 10.1007/s11182-009-9153-3.
- [209] I. Puigdomènech et al. “A tool to draw chemical equilibrium diagrams using SIT: Applications to geochemical systems and radionuclide solubility”. In: *MRS Proceedings* 1665 (2014), pp. 111–116. DOI: 10.1557/opl.2014.635.
- [210] Hong Qin et al. “Why is Boris algorithm so good?” In: *Physics of Plasmas* 20.8 (2013), p. 084503. DOI: 10.1063/1.4818428.
- [211] R. Quay. “Analysis and Simulation of High Electron Mobility Transistors”. PhD thesis. Technische Universität Wien, Fakultät für Elektrotechnik und Informationstechnik, July 2001.
- [212] Sarfraz Qureshi et al. “Quadrupole lens alignment with improved STIM and secondary electron imaging for proton beam writing”. In: *Nuclear Instruments and Methods in Physics Research Section B: Beam Interactions with Materials and Atoms* 404 (2017), pp. 74–80. DOI: 10.1016/j.nimb.2016.12.016.
- [213] I. Rajta et al. “Proton beam micromachining on PMMA, foturan and CR-39 materials”. In: *Nuclear Instruments and Methods in Physics Research Section B: Beam Interactions with Materials and Atoms* 210 (2003), pp. 260–265. DOI: 10.1016/s0168-583x(03)01025-5.

Bibliography

- [214] I. Rajta et al. “Si micro-turbine by proton beam writing and porous silicon micromachining”. In: *Nuclear Instruments and Methods in Physics Research Section B: Beam Interactions with Materials and Atoms* 267.12-13 (2009), pp. 2292–2295. DOI: 10.1016/j.nimb.2009.03.087.
- [215] Anthony K. Rappe and William A. Goddard. “Charge equilibration for molecular dynamics simulations”. In: *The Journal of Physical Chemistry* 95.8 (1991), pp. 3358–3363. DOI: 10.1021/j100161a070.
- [216] S. J. Rashid et al. “Numerical parameterization of chemical-vapor-deposited (CVD) single-crystal diamond for device simulation and analysis”. In: *IEEE Transactions on Electron Devices* 55.10 (2008), pp. 2744–2756. DOI: 10.1109/ted.2008.2003225.
- [217] William Hadley Richardson. “Bayesian-based iterative method of image restoration”. In: *Journal of the Optical Society of America* 62.1 (1972), p. 55. DOI: 10.1364/josa.62.000055.
- [218] B. Ripperda et al. “A comprehensive comparison of relativistic particle integrators”. In: *The Astrophysical Journal Supplement Series* 235.1 (2018), p. 21. DOI: 10.3847/1538-4365/aab114.
- [219] M. T. Robinson. “The binary collision approximation: Background and introduction”. In: *Radiation Effects and Defects in Solids* null.1 (1994), pp. 3–20. DOI: 10.1080/10420159408219767.
- [220] Héctor O. Di Rocco and Fernando Lanzini. “Breit and quantum electrodynamics energy contributions in multielectron atoms from the relativistic screened hydrogenic model”. In: *Brazilian Journal of Physics* 46.2 (2016), pp. 175–183. DOI: 10.1007/s13538-015-0397-9.
- [221] L. Romano et al. “High aspect ratio metal microcasting by hot embossing for X-ray optics fabrication”. In: *Microelectronic Engineering* 176 (2017), pp. 6–10. DOI: 10.1016/j.mee.2016.12.032.
- [222] Charlotte Rothfuchs. “Proton beam writing for the fabrication of three-dimensional microstructures in p-GaAs and p-InP”. MA thesis. Georg-August Universität Göttingen, Aug. 2014.
- [223] A. Otero-de la Roza, David Abbasi-Pérez, and Víctor Luaña. “Gibbs2: A new version of the quasiharmonic model code. II. Models for solid-state thermodynamics, features and implementation”. In: *Computer Physics Communications* 182.10 (2011), pp. 2232–2248. DOI: 10.1016/j.cpc.2011.05.009.
- [224] A. Otero-de la Roza and Víctor Luaña. “Gibbs2: A new version of the quasiharmonic model code. I. Robust treatment of the static data”. In: *Computer Physics Communications* 182.8 (2011), pp. 1708–1720. DOI: 10.1016/j.cpc.2011.04.016.
- [225] Alberto Otero-de la Roza and Víctor Luaña. “Equations of state in solids: Fitting theoretical data, possibly including noise and jumps”. In: *Computational and Theoretical Chemistry* 975.1-3 (2011), pp. 111–115. DOI: 10.1016/j.comptc.2011.03.050.

Bibliography

- [226] E. Rutherford. “The scattering of α and β particles by matter and the structure of the atom”. In: *The London, Edinburgh, and Dublin Philosophical Magazine and Journal of Science* 21.125 (1911), pp. 669–688. DOI: 10.1080/14786440508637080.
- [227] H. Ryssel, K. Habberger, and H. Kranz. “Ion-beam sensitivity of polymer resists”. In: *Journal of Vacuum Science and Technology* 19.4 (1981), pp. 1358–1362. DOI: 10.1116/1.571210.
- [228] Riccardo Sabatini, Tommaso Gorni, and Stefano de Gironcoli. “Nonlocal van der Waals density functional made simple and efficient”. In: *Physical Review B* 87.4 (2013). DOI: 10.1103/physrevb.87.041108.
- [229] John R. Sabin and Jens Oddershede. “Theoretical stopping cross sections of C-H, C-C and C=C bonds for swift protons”. In: *Nuclear Instruments and Methods in Physics Research Section B: Beam Interactions with Materials and Atoms* 27.2 (June 1987), pp. 280–286. DOI: 10.1016/0168-583x(87)90566-0.
- [230] Soumen Saha, Ram Kinkar Roy, and Paul W. Ayers. “Are the Hirshfeld and Mulliken population analysis schemes consistent with chemical intuition?” In: *International Journal of Quantum Chemistry* 109.9 (2008), pp. 1790–1806. DOI: 10.1002/qua.21901.
- [231] Jacob Sain et al. *Autodesk Inventor*. Tech. rep. San Rafael, CA: Autodesk, 2014.
- [232] J. L. Sanchez et al. “A high resolution beam scanning system for deep ion beam lithography”. In: *Nuclear Instruments and Methods in Physics Research Section B: Beam Interactions with Materials and Atoms* 136-138 (1998), pp. 385–389. DOI: 10.1016/s0168-583x(97)00878-1.
- [233] Jose Luis Sanchez et al. “Proton micromachining of substrate scaffolds for cellular and tissue engineering”. In: *Nuclear Instruments and Methods in Physics Research Section B: Beam Interactions with Materials and Atoms* 158.1-4 (1999), pp. 185–189. DOI: 10.1016/s0168-583x(99)00528-5.
- [234] Trond Saue. “Relativistic hamiltonians for chemistry: a primer”. In: *ChemPhysChem* 12.17 (2011), pp. 3077–3094. DOI: 10.1002/cphc.201100682.
- [235] G. Schiwietz and P. L. Grande. “Improved charge-state formulas”. In: *Nuclear Instruments and Methods in Physics Research Section B: Beam Interactions with Materials and Atoms* 175-177 (2001), pp. 125–131. DOI: 10.1016/s0168-583x(00)00583-8.
- [236] M. Schulte-Borchers et al. “3D microstructuring in p-GaAs with proton beam writing using multiple ion fluences”. In: *Journal of Micromechanics and Microengineering* 22.2 (2012), p. 025011. DOI: 10.1088/0960-1317/22/2/025011.
- [237] Martina Schulte-Borchers. “Microstructuring of semiconductors with proton beam writing”. MA thesis. Georg-August Universität Göttingen, Oct. 2011.
- [238] M. Schwickert et al. “Nitrogen and hydrogen depth profiling with MaRPel”. In: *Surface and Coatings Technology* 151-152 (2002), pp. 222–226. DOI: 10.1016/s0257-8972(01)01610-3.

Bibliography

- [239] R. L. Seliger et al. “High-resolution, ion-beam processes for microstructure fabrication”. In: *Journal of Vacuum Science and Technology* 16.6 (1979), pp. 1610–1612. DOI: 10.1116/1.570253.
- [240] C. David Sherrill et al. “Energies and analytic gradients for a coupled-cluster doubles model using variational Brueckner orbitals: application to symmetry breaking in $O4^+$ ”. In: *The Journal of Chemical Physics* 109.11 (1998), pp. 4171–4181. DOI: 10.1063/1.477023.
- [241] Kunihiro Shima, Toyoyuki Ishihara, and Takashi Mikumo. “Empirical formula for the average equilibrium charge-state of heavy ions behind various foils”. In: *Nuclear Instruments and Methods in Physics Research* 200.2-3 (1982), pp. 605–608. DOI: 10.1016/0167-5087(82)90493-8.
- [242] E. T. Shipatov and B. A. Kononov. “Proton channeling in ionic and semiconducting single crystals”. In: *Soviet Physics Journal* 11.9 (1968), pp. 46–49. DOI: 10.1007/bf00817942.
- [243] P. Sigmund and A. Schinner. “Electronic stopping in oxides beyond Bragg additivity”. In: *Nuclear Instruments and Methods in Physics Research Section B: Beam Interactions with Materials and Atoms* 415 (2018), pp. 110–116. DOI: 10.1016/j.nimb.2017.11.023.
- [244] P. Sigmund and A. Schinner. “Is electronic stopping of ions velocity-proportional in the velocity-proportional regime?” In: *Nuclear Instruments and Methods in Physics Research Section B: Beam Interactions with Materials and Atoms* 440 (Feb. 2019), pp. 41–47. DOI: 10.1016/j.nimb.2018.10.031.
- [245] Peter Sigmund. “Charge-dependent electronic stopping of swift nonrelativistic heavy ions”. In: *Physical Review A* 56.5 (1997), pp. 3781–3793. DOI: 10.1103/physreva.56.3781.
- [246] Peter Sigmund. “Kinetic theory of particle stopping in a medium with internal motion”. In: *Physical Review A* 26.5 (Nov. 1982), pp. 2497–2517. DOI: 10.1103/physreva.26.2497.
- [247] Peter Sigmund, ed. *Stopping of Heavy Ions*. Springer Berlin Heidelberg, 2004. DOI: 10.1007/b98483.
- [248] Peter Sigmund and Andreas Schinner. “Binary theory of electronic stopping”. In: *Nuclear Instruments and Methods in Physics Research Section B: Beam Interactions with Materials and Atoms* 195.1-2 (Oct. 2002), pp. 64–90. DOI: 10.1016/s0168-583x(01)01162-4.
- [249] Peter Sigmund and Andreas Schinner. “Notes on Barkas-Andersen effect”. In: *The European Physical Journal D* 68.10 (Oct. 2014). DOI: 10.1140/epjd/e2014-50461-3.
- [250] G. W. Simon, J. M. Denney, and R. G. Downing. “Energy dependence of proton damage in silicon”. In: *Physical Review* 129.6 (1963), pp. 2454–2459. DOI: 10.1103/physrev.129.2454.

Bibliography

- [251] H. Vernon Smith and H. T. Richards. “A sputter PIG source (SPIGS) for negative ions”. In: *Nuclear Instruments and Methods* 125.4 (1975), pp. 497–502. DOI: 10.1016/0029-554x(75)90464-4.
- [252] V. L. Solozhenko and V. Bushlya. “Mechanical properties of boron phosphides”. In: *Journal of Superhard Materials* 41.2 (2019), pp. 84–89. DOI: 10.3103/s1063457619020023.
- [253] M. Sotoodeh, A. H. Khalid, and A. A. Rezazadeh. “Empirical low-field mobility model for III-V compounds applicable in device simulation codes”. In: *Journal of Applied Physics* 87.6 (Mar. 2000), pp. 2890–2900. DOI: 10.1063/1.372274.
- [254] *Source of negative ions by cesium sputtering - SNICS II*. National Electrostatics Corp. WI 53562-0310 USA, P.O. Box 620310, Middleton 7540 Graber Rd., Mar. 2019.
- [255] J. P. De Souza, I. Danilov, and H. Boudinov. “Electrical isolation of GaAs by light ion irradiation damage”. In: *Radiation Effects and Defects in Solids* 147.1-2 (1998), pp. 109–120. DOI: 10.1080/10420159808226394.
- [256] S. V. Springham et al. “Micromachining using deep ion beam lithography”. In: *Nuclear Instruments and Methods in Physics Research Section B: Beam Interactions with Materials and Atoms* 130.1-4 (1997), pp. 155–159. DOI: 10.1016/s0168-583x(97)00275-9.
- [257] Frank D. Stacey. “Equations-of-state for close-packed materials at high pressures: geophysical evidence”. In: *Journal of Physics: Condensed Matter* 11.2 (1999), pp. 575–582. DOI: 10.1088/0953-8984/11/2/020.
- [258] Frank D. Stacey. “High pressure equations of state and planetary interiors”. In: *Reports on Progress in Physics* 68.2 (2005), pp. 341–383. DOI: 10.1088/0034-4885/68/2/r03.
- [259] Frank D. Stacey. “The K-primed approach to high-pressure equations of state”. In: *Geophysical Journal International* 143.3 (2000), pp. 621–628. DOI: 10.1046/j.1365-246x.2000.00253.x.
- [260] John F. Stanton, Jürgen Gauss, and Rodney J. Bartlett. “On the choice of orbitals for symmetry breaking problems with application to NO₃”. In: *The Journal of Chemical Physics* 97.8 (1992), pp. 5554–5559. DOI: 10.1063/1.463762.
- [261] Alrik Stegmaier. “Modelling proton beam writing in p-GaAs”. MA thesis. Universität Göttingen, May 2015.
- [262] J. I. Steinfeld, J. S. Francisco, and W. L. Hase. *Chemical Kinetics and Dynamics*. 2nd. Upper Saddle River, New Jersey: Prentice-Hall, 1998.
- [263] *Stopping powers and ranges for protons and alpha particles*. Tech. rep. 49. Bethesda, MD (United States): International Commission on Radiation Units and Measurements, May 1993.
- [264] G. P. Summers et al. “Damage correlations in semiconductors exposed to gamma, electron and proton radiations”. In: *IEEE Transactions on Nuclear Science* 40.6 (1993), pp. 1372–1379. DOI: 10.1109/23.273529.

Bibliography

- [265] Jianwei Sun, Adrienn Ruzsinszky, and John P. Perdew. “Strongly Constrained and Appropriately Normed Semilocal Density Functional”. In: *Physical Review Letters* 115.3 (July 2015). DOI: 10.1103/physrevlett.115.036402.
- [266] Jianwei Sun, Bing Xiao, and Adrienn Ruzsinszky. “Communication: Effect of the orbital-overlap dependence in the meta generalized gradient approximation”. In: *The Journal of Chemical Physics* 137.5 (2012), p. 051101. DOI: 10.1063/1.4742312.
- [267] Qiming Sun et al. “PySCF: the Python-based simulations of chemistry framework”. In: *WIREs Computational Molecular Science* 8.1 (2017). DOI: 10.1002/wcms.1340.
- [268] Qiming Sun et al. “Recent developments in the PySCF program package”. In: *The Journal of Chemical Physics* 153.2 (2020), p. 024109. DOI: 10.1063/5.0006074.
- [269] S. M. Sze and K. K. Ng. *Physics of Semiconductor Devices*. 3rd. Hoboken, New Jersey: John Wiley & Sons, Inc., 2007.
- [270] Y. Takeda and T. P. Pearsall. “Failure of Mattheissen’s Rule in the Calculation of Carrier Mobility and Alloy Scattering Effects in Ga_{0.47}In_{0.53}As”. In: *Electronics Lett.* 17 (1981), pp. 573–574.
- [271] Francis E. H. Tay et al. “A novel micro-machining method for the fabrication of thick-film SU-8 embedded micro-channels”. In: *Journal of Micromechanics and Microengineering* 11.1 (2000), pp. 27–32. DOI: 10.1088/0960-1317/11/1/305.
- [272] L. H. Thomas. “The calculation of atomic fields”. In: *Mathematical Proceedings of the Cambridge Philosophical Society* 23.5 (1927), pp. 542–548. DOI: 10.1017/s0305004100011683.
- [273] F. Thuselt and M. Rösler. “Gap shift in doped semiconductors at finite temperatures”. In: *physica status solidi (b)* 130.2 (1985), pp. 661–673. DOI: 10.1002/pssb.2221300230.
- [274] F. Thuselt and M. Rösler. “Universal approximation formulas for the gap shift in doped semiconductors”. In: *physica status solidi (b)* 130.2 (1985), K139–K144. DOI: 10.1002/pssb.2221300260.
- [275] D. I. Thwaites. “Bragg’s rule of stopping power additivity: a compilation and summary of results”. In: *Radiation Research* 95.3 (1983), p. 495. DOI: 10.2307/3576096.
- [276] David I. Thwaites. “Current status of physical state effects on stopping power”. In: *Nuclear Instruments and Methods in Physics Research Section B: Beam Interactions with Materials and Atoms* 12.1 (1985), pp. 84–89. DOI: 10.1016/0168-583x(85)90705-0.
- [277] Fei Tian et al. “Mechanical properties of boron arsenide single crystal”. In: *Applied Physics Letters* 114.13 (2019), p. 131903. DOI: 10.1063/1.5093289.
- [278] I. S. Tilinin. “Quasiclassical expression for inelastic energy losses in atomic particle collisions below the bohr velocity”. In: *Physical Review A* 51.4 (1995), pp. 3058–3065. DOI: 10.1103/physreva.51.3058.

Bibliography

- [279] T. Tillocher et al. “Optimization of submicron deep trench profiles with the STiGer cryoetching process: reduction of defects”. In: *J. Micromech. Microeng.* 21.8 (June 2011), p. 085005.
- [280] Micha Tomkiewicz. “Impedance spectroscopy of rectifying semiconductor-electrolyte interfaces”. In: *Electrochimica Acta* 35.10 (1990), pp. 1631–1635. DOI: 10.1016/0013-4686(90)80019-k.
- [281] V. Trivedi and S. J. Pearton. “Evaluation of rapid thermal processing systems for use in CMOS fabrication”. In: *Solid-State Electronics* 46.6 (2002), pp. 777–783. DOI: 10.1016/s0038-1101(02)00007-2.
- [282] C. Udalagama, A. A. Bettiol, and F. Watt. “Stochastic spatial energy deposition profiles for MeV protons and keV electrons”. In: *Physical Review B* 80.22 (2009), p. 224107. DOI: 10.1103/physrevb.80.224107.
- [283] M. Uhrmacher et al. “Energy calibration of the 500 kV heavy ion implanter ionas”. In: *Nuclear Instruments and Methods in Physics Research Section B: Beam Interactions with Materials and Atoms* 9.2 (1985), pp. 234–242. DOI: 10.1016/0168-583x(85)90688-3.
- [284] M. Uhrmacher et al. “Miss MaRPel – a 3 MV pelletron accelerator for hydrogen depth profiling”. In: *Journal of Alloys and Compounds* 404-406 (2005), pp. 307–311. DOI: 10.1016/j.jallcom.2004.09.092.
- [285] Evangelos Valamontes et al. “Realization and simulation of high-aspect-ratio micro/nanostructures by proton beam writing”. In: *Japanese Journal of Applied Physics* 47.11 (2008), pp. 8600–8605. DOI: 10.1143/jjap.47.8600.
- [286] David Vanderbilt. “Soft self-consistent pseudopotentials in a generalized eigenvalue formalism”. In: *Physical Review B* 41.11 (1990), pp. 7892–7895. DOI: 10.1103/physrevb.41.7892.
- [287] L. Vegard. “Die Konstitution der Mischkristalle und die Raumfüllung der Atome”. In: *Zeitschrift für Physik* 5.1 (1921), pp. 17–26. DOI: 10.1007/bf01349680.
- [288] I. Vurgaftman, J. R. Meyer, and L. R. Ram-Mohan. “Band parameters for III-V compound semiconductors and their alloys”. In: *Journal of Applied Physics* 89.11 (2001), pp. 5815–5875. DOI: 10.1063/1.1368156.
- [289] Oleg A. Vydrov and Troy Van Voorhis. “Nonlocal van der Waals density functional: the simpler the better”. In: *The Journal of Chemical Physics* 133.24 (2010), p. 244103. DOI: 10.1063/1.3521275.
- [290] P. Waage. “Experiments for Determining the Affinity Law”. In: *C. M. Forhandling: Videnskabs-Selskabet i Christiana* 92 (1864).
- [291] M. P. R. Waligórski, R. N. Hamm, and R. Katz. “The radial distribution of dose around the path of a heavy ion in liquid water”. In: *International Journal of Radiation Applications and Instrumentation. Part D. Nuclear Tracks and Radiation Measurements* 11.6 (1986), pp. 309–319. DOI: 10.1016/1359-0189(86)90057-9.

Bibliography

- [292] M. J. Walker. “Comparison of Bosch and cryogenic processes for patterning high-aspect-ratio features in silicon”. In: *Proc. SPIE, MEMS Design, Fabrication, Characterization, and Packaging* 89.4407 (Apr. 2001).
- [293] S. R. Walther et al. “Dopant channeling as a function of implant angle for low energy applications”. In: *1998 International Conference on Ion Implantation Technology. Proceedings (Cat. No.98EX144)*. IEEE, 1999. DOI: 10.1109/iit.1999.812068.
- [294] E. Warburg. “Ueber das Verhalten sogenannter unpolarisirbarer Elektroden gegen Wechselstrom”. In: *Annalen der Physik und Chemie* 303.3 (1899), pp. 493–499. DOI: 10.1002/andp.18993030302.
- [295] G. S. Was and R. S. Averback. “Radiation damage using ion beams”. In: *Comprehensive Nuclear Materials*. Elsevier, 2012, pp. 195–221. DOI: 10.1016/b978-0-08-056033-5.00007-0.
- [296] F. Watt et al. “Ion beam lithography and nanofabrication: a review”. In: *International Journal of Nanoscience* 04.03 (2005), pp. 269–286. DOI: 10.1142/s0219581x05003139.
- [297] F. Watt et al. “The National University of Singapore high energy ion nano-probe facility: Performance tests”. In: *Nuclear Instruments and Methods in Physics Research Section B: Beam Interactions with Materials and Atoms* 210 (2003), pp. 14–20. DOI: 10.1016/s0168-583x(03)01003-6.
- [298] Frank Watt et al. “Proton beam writing”. In: *Materials Today* 10.6 (2007), pp. 20–29. DOI: 10.1016/s1369-7021(07)70129-3.
- [299] E. Wendler and L. Wendler. “Empirical modeling of the cross section of damage formation in ion implanted III-V semiconductors”. In: *Applied Physics Letters* 100.19 (2012), p. 192108. DOI: 10.1063/1.4711810.
- [300] W. Wesch et al. “Defect production during ion implantation of various A III B V semiconductors”. In: *Journal of Applied Physics* 65.2 (1989), pp. 519–526. DOI: 10.1063/1.343134.
- [301] Ulrich Wietelmann, Michael Felderhoff, and Peter Rittmeyer. *Hydrides*. 2016. DOI: 10.1002/14356007.a13_199.pub2.
- [302] W. D. Wilson, L. G. Hagmark, and J. P. Biersack. “Calculations of nuclear stopping, ranges, and straggling in the low-energy region”. In: *Physical Review B* 15.5 (Mar. 1977), pp. 2458–2468. DOI: 10.1103/physrevb.15.2458.
- [303] A. B. Wittkower and H. D. Betz. “Equilibrium-charge-state distributions of energetic ions ($Z > 2$) in gaseous and solid media”. In: *Atomic Data and Nuclear Data Tables* 5.2 (1973), pp. 113–166. DOI: 10.1016/s0092-640x(73)80001-4.
- [304] Younan Xia and George M. Whitesides. “Soft lithography”. In: *Annual Review of Materials Science* 28.1 (1998), pp. 153–184. DOI: 10.1146/annurev.matsci.28.1.153.
- [305] Bo Xu, Qianqian Wang, and Yongjun Tian. “Bulk modulus for polar covalent crystals”. In: *Scientific Reports* 3.1 (2013). DOI: 10.1038/srep03068.

Bibliography

- [306] Zhimin Xu and Edmund Y. Lam. “Maximum a posteriori blind image deconvolution with Huber-Markov random-field regularization”. In: *Optics Letters* 34.9 (2009), p. 1453. DOI: 10.1364/ol.34.001453.
- [307] B. P. Yan, J. S. Luo, and Q. L. Zhang. “Study of band-gap narrowing effect and nonradiative recombination centers for heavily C-doped GaAs by photoluminescence spectroscopy”. In: *Journal of Applied Physics* 77.9 (1995), pp. 4822–4824. DOI: 10.1063/1.359406.
- [308] Huade Yao and A. Compaan. “Plasmons, photoluminescence, and band-gap narrowing in very heavily doped In/i-GaAs”. In: *Applied Physics Letters* 57.2 (1990), pp. 147–149. DOI: 10.1063/1.103967.
- [309] Y. Yao and J. A. van Kan. “Automatic beam focusing in the 2nd generation PBW line at sub-10nm line resolution”. In: *Nuclear Instruments and Methods in Physics Research Section B: Beam Interactions with Materials and Atoms* 348 (2015), pp. 203–208. DOI: 10.1016/j.nimb.2014.12.066.
- [310] Y. Yao, P. Santhana Raman, and J. A. van Kan. “Orthogonal and fine lithographic structures attained from the next generation proton beam writing facility”. In: *Microsystem Technologies* 20.10-11 (2014), pp. 2065–2069. DOI: 10.1007/s00542-014-2066-2.
- [311] B. S. Yarlagadda, J. E. Robinson, and Werner Brandt. “Effective-charge theory and the electronic stopping power of solids”. In: *Physical Review B* 17.9 (1978), pp. 3473–3483. DOI: 10.1103/physrevb.17.3473.
- [312] Eva Zarkadoula, German Samolyuk, and William J. Weber. “Effects of electron-phonon coupling on damage accumulation in molecular dynamics simulations of irradiated nickel”. In: *Materials Research Letters* 7.12 (2019), pp. 490–495. DOI: 10.1080/21663831.2019.1659435.
- [313] E. V. Zarochentsev, S. M. Orel, and V. N. Varyukhin. “Elastic constants of a stressed crystal. I. General theory”. In: *Physica Status Solidi (a)* 52.2 (1979), pp. 455–462. DOI: 10.1002/pssa.2210520213.
- [314] X. Zhang et al. “Comparison of electrical properties of aluminum oxide thin films on silicon and gallium arsenide substrates grown by atomic layer deposition”. In: *Surface and Coatings Technology* 228 (2013), S246–S248. DOI: 10.1016/j.surfcoat.2012.05.135.
- [315] Jianxiong Zhu et al. “Development trends and perspectives of future sensors and MEMS/NEMS”. In: *Micromachines* 11.1 (2019), p. 7. DOI: 10.3390/mi11010007.
- [316] J. F. Ziegler. “The electronic and nuclear stopping of energetic ions”. In: *Applied Physics Letters* 31.8 (1977), pp. 544–546. DOI: 10.1063/1.89771.
- [317] J. F. Ziegler, U. Littmark, and J. P. Biersack. *The stopping and range of ions in solids*. New York: Pergamon, 1985. ISBN: 008021603X.

Bibliography

- [318] James F. Ziegler, M. D. Ziegler, and J. P. Biersack. “SRIM – The stopping and range of ions in matter (2010)”. In: *Nuclear Instruments and Methods in Physics Research Section B: Beam Interactions with Materials and Atoms* 268.11-12 (June 2010), pp. 1818–1823. DOI: 10.1016/j.nimb.2010.02.091.
- [319] A. N. Zinoviev. “Interatomic potential at small internuclear distances. A simple formula for the screening constant”. In: *Nuclear Instruments and Methods in Physics Research Section B: Beam Interactions with Materials and Atoms* 406 (2017), pp. 465–469. DOI: 10.1016/j.nimb.2017.01.009.
- [320] A. N. Zinoviev, P. Yu. Babenko, and K. Nordlund. “Nuclear stopping powers for DFT potentials”. In: *Nuclear Instruments and Methods in Physics Research Section B: Beam Interactions with Materials and Atoms* 508 (2021), pp. 10–18. DOI: 10.1016/j.nimb.2021.10.001.
- [321] J. Patrick Zobel, Per-Olof Widmark, and Valera Veryazov. “The ANO-R basis set”. In: *Journal of Chemical Theory and Computation* 16.1 (Nov. 2019), pp. 278–294. DOI: 10.1021/acs.jctc.9b00873.
- [322] P. A. Zyla et al. “Review of Particle Physics”. In: *PTEP* 2020.8 (2020), p. 083C01. DOI: 10.1093/ptep/ptaa104.

List of Figures

1.1.	Number of scientific publications mentioning MEMS as indexed by <code>scholar.google.com</code> by year of publication in total and by the three largest publishers in the field.	8
1.2.	The first MEMS design, a resonant gate transistor, as published in a patent in 1965 (left) [177], in comparison to a modern design for a tunable coupling dual cavity for photonic integrated circuits from 2010 [47].	9
1.3.	Outline of the two primary steps of Proton beam writing in semiconductors (left) and resists (right). Both materials are modified in some way by Proton irradiation and can be selected such that either only defect rich or only defect poor material is removed in etching.	15
1.4.	Simulated trajectories of 100 projectiles (Electrons, Protons and Argon) in PMMA, Silicon and Gallium Arsenide. The gray layer represents a 30 μm thick layer of the target material and the particle energies are selected such that a majority of the layer is penetrated. The fanned out structure of Electron paths in the target are visible as well as the high particle energies required for the Argon beam to reach the required depths.	19
2.1.	Overview of the Pelletron MaRPel and a photo of the beam-lines in their current configuration. The ion beam is generated in the SNICS, accelerated to high energy in the high voltage tank and guided to one of three experiment beam-lines. The middle beam-line ends with the micro-beam chamber where PBW is performed.	24
2.2.	Schematic representation of the SNICS (ion source) used for PBW in Göttingen. The source works by ionizing Cs atoms and accelerating them towards a cooled cathode, where a sputtering process generates negatively charged ions that are accelerated out of the source.	26
2.3.	Energy deposited per atom in TiH_2 in collision cascades of Cs of varying kinetic energy in the cathode of a SNICS.	32
2.4.	Results of the Proton ray tracing simulations of the MaRPel accelerator with the micro-beam-line. On the left a top down view of the particle paths through the accelerator. In the center the distribution of Particles on the target with the quadrupole magnet after the 90 degree mass selection magnet at 0 strength and on the right at optimal strength.	35
2.5.	Overview of the micro-beam-line at MaRPel. The Proton beam enters from the top and passes through two sets of slits and the focusing quadrupole lenses into the target chamber, where the irradiation target is located. . .	37

List of Figures

2.6.	Photo of the micro-beam-line at the MaRPel. Left and right of the micro-beam-line are two other beam-lines. The target chamber is located in the bottom right and the Proton beam enters the beam-line on the top left corner of the picture.	38
2.7.	Frequency spectrum of the vibrations of turbo-pumps as measured by a microphone positioned at the surface of the pumps with different measures to dampen vibrations.	39
2.8.	Experimental demagnification for the quadruplet lens system at the micro-beam-line in Göttingen as a function of the mean distance of the lenses to the target surface. The beam sizes for these measurements on the target were between 2 and 5 mm in diameter.	40
2.9.	Picture of the quadruplet lens system at the micro-beam-line after the upgrades. In the front the cooling system is mounted. The lenses are pressed against several fittings by a spring mounting. The lenses can be adjusted with a set of micro-screws.	41
2.10.	Overview of the target chamber of the micro-beam-line. Visible is the sample holder, where the target is located. The sample holder is mounted on positioning stages. Several instruments are pointed towards the target surface and an Electron suppressor grid is mounted. The Proton beam enters from the left.	42
2.11.	Schematic representation of three sample holder designs. On the left a common design used in ion beam irradiation, in the middle a design similar to the one used in the CIBA Singapur and on the right the new design used at MaRPel.	44
2.12.	Cut away drawing of the newly designed sample holder. The samples (in red) are held against the lips of the front frame (blue) by the pressure screws (blue green). For samples of very different thicknesses (as shown here) spacing plates (dark green) and spacing frames (fuchsia) can be used. The assembly is held together by the frame screws (orange). At the front a Faraday cup (grey) is mounted that doubles as a stand for inserting the samples when the sample holder is set on a table.	45
2.13.	Photographs of the sample holder at MaRPel, here shown with a scintillator (modified with painted on cross hairs and two mounted Nickel grids), two samples and an isolated Copper plate mounted above the sample surface. Note the hook on the top for attaching a constant force spring, the plug for attaching a cable for current measurements and a single mounted spacer frame.	47
2.14.	Integrated x-ray intensity of the Nickel grid lines and the RBS spectrum of a Nickel edge on a GaAs sample as well a fit to these lines. Notable is the enhancement of the spectrum at the edge of the RBS signal.	49
2.15.	Test patterns considered here for benchmarking irradiation planning algorithm performance. All patterns have a resolution of 512×512 with the brightness determining the local irradiation amount (white being maximal and black being no irradiation).	51

List of Figures

3.1.	Stopping force for Silicon atoms in solid Silicon as predicted by SRIM 2013 [318]. Also shown are the sound velocities [155] and electronic orbital velocities of Silicon.	54
3.2.	Electronic stopping power (blue) and nuclear stopping power (orange) for different projectiles in Silicon as predicted by SRIM 2013 [318] in comparison to a compilation of experimental measurements (together with the reported uncertainties) [171] as a function of the projectile nuclear charge Z and kinetic energy E . Also shown are experimental data from anti-Proton stopping ($Z = -1$) [6, 168, 157, 170].	56
3.3.	Electronic stopping power (blue) and nuclear stopping power (orange) for Protons in different elemental materials as predicted by SRIM [318] in comparison to a compilation of experimental measurements (together with the reported uncertainties) [171] as a function of the target nuclear charge $Z \leq 54$ and projectile kinetic energy E	57
3.4.	Projectile and recoil distributions as well as distribution of ionization energy loss of 1 MeV Protons in Gallium Arsenide as a function of depth as simulated with SRIM 2013[318].	59
3.5.	Limiting energy at which nuclear reactions are expected to reach 4% of the Rutherford cross-section for Protons as a function of the nuclear charge of the target material Z	61
3.6.	Ranges of Protons in different solid targets as a function of the projectile energy for typical energies encountered in Proton beam writing as calculated with SRIM [318] and fit according to eq. 3.1 on page 61.	62
3.7.	Longitudinal straggling of Protons in different targets as simulated with SRIM [318] as a function of the laterally projected range (or penetration depth) and fit to this quantity.	63
3.8.	Distribution of final positions of 200, 1 MeV Protons in Silicon for a $\langle 100 \rangle$ oriented perfect crystal and an amorphous target of the same density. In the crystalline target channeling of the projectiles is visible.	64
3.9.	Radial screening functions for the Coulomb potentials of the neutral atoms of the periodic table as a function of the distance R to the nucleus as predicted from density functional theory and relaxed MP2 theory calculations. Also shown is a fit of shape $\exp\left(-\left(\frac{R}{a_0 Z^{n_Z}}\right)^{n_{R,0}+Z \cdot n_{R,1}}\right)$	66
3.10.	Screening lengths of the nuclear potentials by the Electrons as a function of the nuclear charge Z and as predicted from a fit of the function $\exp\left(-\left(\frac{R}{a(Z)}\right)^{n_R(Z)}\right)$, by Thomas-Fermi theory and as assumed by Ziegler's and Nakagawa's models.	67
3.11.	Effective screening function ϕ to the Coulomb potential of the nucleus of Carbon as a function of distance from the nucleus for different charge states q of the atom as determined from relaxed MP2 densities (solid lines) as well as the approximation proposed here (dashed lines).	70

List of Figures

3.12. Collision geometry of a projectile with an Hydrogen molecule used in this work. Hydrogen atoms are shown in blue , the projectile in orange and the trajectory for the potential calculation is shown in green	71
3.13. Screening functions to the bare nuclear potentials for the Born Oppenheimer potentials for Protons as calculated with pyscf and comparison with the Ziegler, Littmark, and Biersack [317] potential.	75
3.14. Electronic stopping power of Hydrogen and Uranium in different target materials with nuclear charge Z and the prediction by eq. 3.3 on page 76 with $n = 1$ and $n = 2$	77
3.15. Charge states of Carbon as a function of projectile velocity $\beta = \frac{v}{c}$ for different targets [303, 241] and as described from eq. 3.5 on page 78. . . .	79
3.16. Effective screening function of Hydrogen collisions with Gallium. The ground state is shown with thick lines and the first 10 excited states with thin lines. The simulation was performed in Orca with a X3LYP potential.	81
3.17. Stopping cross section for He stopping in He as calculated with the stopping model including the approximation for bond breaking in comparison to experimental measurements [171] on the left. On the right a plot of the used potential.	82
3.18. Stopping cross section for Silicon stopping in Gallium Arsenide as calculated with the stopping model including the approximation for bond breaking in comparison to several simulations as well as experimental measurements. . .	83
3.19. Evolution of the distribution of chain lengths relative to the initial mean chain length as a function of the effective density of reactive sites created due to irradiation with fast ions. Also shown is the mean chain length and the standard deviation in green.	87
4.1. Experimental [134, 133] and linearly interpolated relative permittivities of KOH- and HCl-solutions with water at room temperature for different concentrations.	96
4.2. Room temperature mobilities of Electrons and holes in Gallium Arsenide as a function of impurity concentrations and fit of the Caughey and Thomas model. Experimental data were taken from [253] and references therein. . .	99
4.3. Comparison between the experimentally [31, 308, 86, 146, 307, 126, 27] determined band gap of Gallium Arsenide as a function of the doping density and the newly proposed model.	102
4.4. Slice through a 3D structure in a negative resist during etching. The arrows indicate the deformation due to radiation damage caused swelling of the material. The colors indicate the local defect density.	105
4.5. Elastic constants of Diamond crystal structure group IV and Zincblende crystal structure III-V compound semiconductors as a function of the equilibrium volume per atom [153, 154, 182, 288] as well as an approximate exponential fit. Some of the values in a comprehensive review [288] were also found to have a unit conversion error and were corrected for this plot. .	107

List of Figures

4.6.	Energy per atom relative to the equilibrium value as a function of the reduced volume per atom for different semiconductors in the Diamond or Zincblende structure phase.	108
4.7.	The ratio of bulk modulus and pressure $\frac{B}{P}$ as a function of the atomic volume relative to the ground state $\frac{V}{V_0}$ for the semiconductors considered here.	109
4.8.	Comparison between experimental [156] pressure versus volume data of Gallium Arsenide with fits to them by the different equations of state as well as the ab-initio DFT simulations with the r2SCAN functional.	111
5.1.	Concentration of Mg and C in GaAs according to a simulation with SRIM and a semiconductor simulation of the experimental conditions described in the text. Also shown is the resulting free charge carrier density of holes and Electrons in the sample, as well as the defect and Hydrogen density introduced by irradiation with 400 keV Protons under a tilt angle of 7° with a dose of $10^{14} \frac{1}{\text{cm}^2}$. The continous lines correspond to the Magnesium implantantion, the dashed lines to Carbon.	113
5.2.	Sheet resistance as measured [33] for a semi-insulating Gallium Arsenide sample with a conductive layer created though ion implantation. Measurements were performed at varying degrees of irradiation with Protons. Shown are the experimental values and the model fit proposed here in comparison.	114
5.3.	Pourbaix diagram (phase diagram as a function of pH value and applied voltage with respect to a standard hydrogen electrode) of Gallium Arsenide as calculated with SPANA/MEDUSA [209]. Also shown is the region of stability of water (marked by the dissociation limit) and the position of the valence and conduction bands of Gallium Arsenide.	115
5.4.	Experimental conductivity (from the sources of [75]) of KOH solutions with water at 25°C as a function of the pH value of the solution.	116
5.5.	Current in the dark as a function of applied voltage across a p-doped Gallium Arsenide $\langle 100 \rangle$ surface in a KOH solution with a pH of 14.2 as measured with a standard Hydrogen electrode at room temperature.	118
5.6.	Experimental current through a $\langle 100 \rangle$ p-type Gallium Arsenide surface at pH 14.3 in the dark as a function of the applied potential (measured with a reversible Hydrogen electrode). See the text for an explanation of the three samples.	120
5.7.	IIS [95] simulated, normalized defect density of 400 keV Proton irradiated $\langle 100 \rangle$ Gallium Arsenide as a function of depth from the surface of the sample.	121
5.8.	Absolute value of the current as a function of the applied potential (measured here with a reversible Hydrogen electrode) and a reconstruction of the etching depth of the target as a Gallium Arsenide irradiated with 400 keV Protons is etched.	122
5.9.	Cyclic voltametry measurements for a Platinum electrode mounted in the etching cell.	123

List of Figures

5.10. Double logarithmic plot of the real and imaginary parts of the measured impedance Z of $\langle 100 \rangle$ p-type Gallium Arsenide in 26% KOH solution. . .	124
5.11. Warburg coefficient (representing the formation of a diffusive layer) of the p-type Gallium Arsenide - KOH solution interface as a function of the applied potential.	125
5.12. Double logarithmic plot of the real and imaginary parts of the measured impedance Z of $\langle 100 \rangle$ p-type Gallium Arsenide in 26% KOH solution with an applied DC potential of 1 V (RHE) for three samples irradiated to three different fluences by 3 MeV Protons.	126
5.13. Nyquist plot of p-type Indium Antimonide. On the left: unirradiated material for two different DC voltages. On the right: values after 3 MeV Proton irradiation to two different fluences at a potential of 0.8 V (RHE). .	127
5.14. Charge distributions at the Gallium and Arsenic rich $\langle 100 \rangle$ surface in water and KOH solution. Arsenic is shown in orange and Gallium in blue. The top row shows the Arsenic rich surface and the bottom row the Gallium rich surface. For a discussion of the changes see the text.	129
5.15. Cut through two long, 10 μm wide lines, irradiated by 2 MeV Protons to $2 \cdot 10^{11} \frac{\text{Protons}}{\text{cm}^2}$ (left) and $10^{12} \frac{\text{Protons}}{\text{cm}^2}$ (right) during etching in 10% KOH solution.	131
5.16. Cut through a long line, irradiated by 2 MeV Protons to $10^{12} \frac{\text{Protons}}{\text{cm}^2}$ during etching in 10% KOH solution. The beam profile of this beam was modeled by the convolution of a 5 μm wide Gaussian with a 10 μm windows function. .	132
5.17. SEM pictures of several lines written into p-type Gallium Arsenide in 4 μm steps. See the text for details.	133
6.1. Radial Electron density of Carbon as predicted by different methods. . . .	141
6.2. Radial Electron density of Silicon as predicted by different methods. . . .	142
6.3. Dissociation curve of triplet O_2 as computed with different all-Electron methods with the decontracted x2c-TZVP basis set in Orca and as computed with a pseudo-potential method and r2SCAN in cp2k . Lines are a guide to the eye and the horizontal line marks the energy of the Oxygen atoms at infinite separation.	144
6.4. Dissociation curve of singlet H_2 as computed with different all-Electron methods with the decontracted x2c-TZVP basis set in Orca and as computed with a pseudo-potential method and r2SCAN in cp2k . Lines are a guide to the eye and the horizontal line marks the energy of the Hydrogen atoms at infinite separation.	145
6.5. Energy per atom of Gallium Arsenide relative to the ground state as a function of the lattice constant a_0 as computed with an all-Electron method in Elk and a pseudo-potential method in CP2K	146

List of Tables

1.1. Markets for MEMS products in 2020 and their relative change since 2014 as well as their predicted growth until 2026 [55].	10
1.2. Overview of some of the early experiments and the materials in which Proton beam writing was successfully demonstrated as well as the time and place this happened.	22
2.1. Properties of the sputtering process in the cathode as a function of the Cs energy as roughly estimated with SRIM. Shown are the surface layer properties and sputtering details as a function of the Cs ion energies. . . .	29
2.2. Sputtering yield of negatively charged Hydrogen as a function of Cs kinetic energy and Electron affinity of the negatively charged target from the approximations discussed in the text.	30
2.3. Atoms in the collision cascade of the SNICS with Titanium Hydride (and Silver) filling and their ionization potentials and Electron affinities [90] in comparison.	31
3.1. Distribution of energy losses for different projectiles at 0° impact angle in Gallium Arsenide as simulated with SRIM [318].	60
3.2. Best fit values for screening functions $\phi(R) = \exp\left(-\left(\frac{R}{a(Z)}\right)^{n_R(Z)}\right)$ for the elements. Values in blue were inter- or extrapolated. The relative fit accuracy of the values is approximately 1/1000.	68
3.3. Common approximations for the screening function $\phi(x)$ used in nuclear stopping.	72
3.4. Effective screening lengths of interatomic collisions for nuclear stopping potentials with $a_0 = \left(\frac{9\pi^2}{128}\right)^{1/3}$	73
3.5. Root mean square deviations of the different combinations of screening functions and screening lengths from the calculated DFT screening functions of this work. For each combination of screening function and screening length, the root mean square deviation for all distances $R \leq 2$ Bohr, $R > 2$ Bohr and overall are shown from top to bottom. The lowest value in each category is shown in bold	74
3.6. Comparison of ground state Electron binding energies of carbon atoms [125, 90] with the best fit parameters from eq. 3.5 on page 78.	79

List of Tables

4.1. Overview of etching recipes of different resists used in Proton beam writing. The type determines if the target material behaves like a positive or negative resist.	89
4.2. Relative static permittivities of different materials.	95
4.3. Parameters for the Caughey and Thomas mobility model. Values marked in blue were estimated by comparison to similar materials and rough interpolation.	100
4.4. Band gaps [51, 191, 118] and density of states effective masses [288, 269, 118] of some semiconductors.	101
5.1. Fit values for the parameters for the modified Butler-Volmer current eq. 5.1 on page 119 for p-type Gallium Arsenide at pH 14.2.	119
6.1. Contributions to the Electronic total binding energies in Hartree of different atoms and estimates from DFT and MP2 for the decontracted x2c-TZVP basis set as calculated with <code>pyscf</code> and <code>Orca</code> . For an explanation of the different effects see the text.	140
6.2. Multi-pole moments and polarizability of H ₂ O at the experimental ground state geometry in atomic units as computed with different methods in a comparison to the experimental values. Values marked with “*” were calculated from numeric differentiation of dipole moments at finite fields. .	147

A. Basis sets

The basis sets used in this work in the CP2K format are given by:

H custom

```
6
1 0 1 1 1 1
          9.6545145 1 1
1 0 1 1 1 1
          4.197615 1 1
1 0 1 1 1 1
          1.82505 1 1
1 0 1 1 1 1
          0.7935 1 1
1 0 1 1 1 1
          0.345 1 1
1 0 0 1 1
          0.15 1
```

O custom

```
6
1 0 2 1 1 1 1
          9.6545145 1 1 1
1 0 2 1 1 1 1
          4.197615 1 1 1
1 0 2 1 1 1 1
          1.82505 1 1 1
1 0 2 1 1 1 1
          0.7935 1 1 1
1 0 2 1 1 1 1
          0.345 1 1 1
1 0 1 1 1 1
          0.15 1 1
```

K custom

```
6
1 0 1 1 1 1
          9.6545145 1 1
1 0 1 1 1 1
          4.197615 1 1
```

A. Basis sets

```

1 0 1 1 1 1
      1.82505 1 1
1 0 1 1 1 1
      0.7935 1 1
1 0 1 1 1 1
      0.345 1 1
1 0 1 1 1 1
      0.15 1 1

```

Ga custom

```

8
2 2 2 1 1
      51.072381705 1
2 2 2 1 1
      22.20538335 1
2 0 2 1 1 1 1
      9.6545145 1 1 1
2 0 2 1 1 1 1
      4.197615 1 1 1
2 0 2 1 1 1 1
      1.82505 1 1 1
2 0 2 1 1 1 1
      0.7935 1 1 1
2 0 2 1 1 1 1
      0.345 1 1 1
2 0 1 1 1 1
      0.15 1 1

```

As custom

```

8
2 2 2 1 1
      51.072381705 1
2 2 2 1 1
      22.20538335 1
2 0 2 1 1 1 1
      9.6545145 1 1 1
2 0 2 1 1 1 1
      4.197615 1 1 1
2 0 2 1 1 1 1
      1.82505 1 1 1
2 0 2 1 1 1 1
      0.7935 1 1 1
2 0 2 1 1 1 1
      0.345 1 1 1

```

A. Basis sets

2 0 1 1 1 1
0.15 1 1